Analysis of the spatial and spectral structures of localized eigenfunctions in Anderson models through the localization landscape theory

Perceval Desforges

INSTITUT POLYTECHNIQUE DE PARIS

NNT : 2021IPPAX027

Thèse de doctorat

Analysis of the spatial and spectral structures of localized eigenfunctions in Anderson models through the localization landscape theory

Thèse de doctorat de l'Institut Polytechnique de Paris
préparée à Ecole Polytechnique

École doctorale n°626 Ecole Doctorale de l'Institut Polytechnique de Paris (EDIPP)
Spécialité de doctorat : Physique

Thèse présentée et soutenue à Palaiseau, le 8 avril 2021, par

PERCEVAL DESFORGES

Composition du Jury :

Eric Akkermans Professeur, Technion, Physics Department	Rapporteur
Fabrice Mortessagne Directeur de recherche CNRS, Université de Nice, Institut de Physique de Nice	Rapporteur
Laurent Sanchez-Palencia Directeur de recherche CNRS, École Polytechnique, Centre de Physique Théorique	Président
Christophe Texier Professeur, Université Paris-Saclay, Laboratoire de Physique Théorique et Modèles Statistiques	Examinateur
Marcel Filoche Directeur de recherche CNRS, École Polytechnique, Laboratoire Physique de la Matière Condensée	Directeur de thèse

Analysis of the spatial and spectral structures of localized eigenfunctions in Anderson models through the localization landscape theory

Thèse de l'Institut Polytechnique de Paris

Perceval Desforges

August 22, 2021

Abstract

Dans un solide désordonné ou aléatoire, les fonctions d'onde des états électroniques peuvent s'écarter des états de Bloch étendus et au contraire, être localisées de manière exponentielle dans l'espace. Ce changement radical de la structure spatiale des fonctions d'onde a une forte influence sur les propriétés de transport du système et peut, par exemple, être responsable de la transition métal/isolant dans les alliages désordonnés. Dans les années récentes, un nouvel outil théorique appelé le *paysage de localisation* a émergé pour l'étude de cette localisation induite par le désordre. Dans cette thèse, nous utilisons la théorie du paysage de localisation afin d'étudier divers aspects de la localisation des ondes. Ce manuscrit commence donc par une brève introduction sur des différents développements historiques dans le sujet de la localisation d'Anderson qui concerne le travail abordé lors de cette thèse.

Tout d'abord, nous montrons comment extraire efficacement la structure spatiale de localisation à n'importe quelle dimension en adaptant l'algorithme dit de *watershed*. Cet algorithme s'appuie sur l'identification de minima locaux du paysage pour définir des régions de localisation. L'étape suivante consiste à utiliser les propriétés du paysage pour éliminer les régions qui ne sont pas capables d'accueillir une fonction propre localisée.

Puis nous passons à l'analyse des propriétés spectrales et calculons la distribution des valeurs propres (la densité intégrée des états) dans des modèles d'Anderson en *tight-binding* en utilisant de nouvelles approximations dérivées du paysage de localisation. Nous montrons que la théorie du paysage permet d'obtenir un très bon encadrement de la densité intégrée des états.

Nous étudions ensuite comment le paysage de localisation permet de comprendre l'existence d'un seuil de mobilité à plus haute énergie, en fonction de la dimension. Ces résultats semblent indiquer que le potentiel effectif joue un rôle crucial dans la localisation des fonctions propres en dimension supérieure et égale à 3.

Enfin, nous nous intéressons à un potentiel déterministe de désordre, le modèle d'Aubry-André, et explorons quelles informations sur le système peuvent être déduites du formalisme de localisation du paysage. Nous trouvons des résultats similaires que dans le cas de la localisation d'Anderson, mais souvent avec des constantes qui diffèrent.

Contents

Chapter 1

The role of disorder in quantum systems

In this chapter we first introduce the concept of Anderson localization. In section I we lay down the theoretical groundwork that we will need in the manuscript. We briefly cover important past works on the topic. This leads us to some of the remaining open questions. In section IV, we present the localization landscape theory which is a different and deterministic approach to Anderson localization. From there we overview the accomplishments of the localization landscape theory as well as several remaining points at issue.

I Anderson localization

I.1 Overview of electronic transport in disordered materials

What allows a quantum wave to pass through the greatest of barriers, and yet to be trapped in the weakest of disorders? This perplexing question was first considered by Anderson more than sixty years ago in his famous paper *Absence of Diffusion in Certain Random Lattices* [8]. Before examining this question further, we will review the relevant discoveries that led to the emergence of this phenomenon.

One of the first microscopic models of electron transport is the Drude model [26]. This is a classical model that considers the electrons as an ideal gas of point-like particles scattering off the different atoms forming the crystal. The average distance between two collisions on the lattice is the mean free path ℓ. In the presence of an electric field, the electrons move collectively at a stabilized speed which depends on the electric field and on ℓ.

This model was successful in describing the conductivity in metals at room temperature as well as the Hall effect. However, the behavior of insulators and semiconductors or the low temperature behavior was not explained by this model. After the emergence of quantum mechanics, the next step was to develop a quantum theory of electronic transport.

Combining the Drude model with the quantum mechanical Fermi-Dirac statistics, Sommerfeld developed a simple theory called the free electron model that accurately predicted additional features such as the shape of the electronic density of states. Interactions between the electrons were still neglected, as well as the interactions between the valence electrons and the ions. Nonetheless, many aspects remained unexplained, especially in the low temperature limit. Furthermore, this model offered no explanation for the conductive or insulating nature of materials: what fundamental property makes some of them metals and others insulators?

In 1928, Bloch developed the electronic band structure theory that complemented the free electron model. The electrons are described as non-interacting quantum waves with the same periodicity as the one of the crystal lattice. This is known as the Bloch theorem. The electronic wave functions are characterized by a wave vector $\vec{k}$ and a wavelength λ. In this model, the electrons are only allowed to fill certain bands of energy, according to Fermi-Dirac statistics. At zero temperature, the last energy band filled is called the

valence band while the lowest vacant energy band is called the conduction band. One defines the band gap as the difference in energy between the lowest state of the conduction band and the highest state in the valence band. Materials whose Fermi level lies in the conduction band are defined as metals. Those for which the Fermi level lies in the band gap are either insulators (with a large band gap, of the order of 10 eV) or semiconductors. This description of materials was the first to offer an explanation to the origin of the conducting or insulating properties of materials.

Under the action of an electric field, the electrons under the Fermi level may acquire enough energy to go over it, which creates an electrical current. In metals, any small electric field will put the electrons in motion, since the Fermi level is in the conduction band. In insulators where the band gap is very large, only very strong electric fields will put a small amount of electrons in motion. Semiconductors are in between, where a strong enough electric field will allow current to flow. They can also be doped, which can shift the Fermi level closer to either the valence or conduction bands. Contrary to metals, semiconductors' conductivity increases with temperature since the states at the bottom of the conduction band are in the exponential part of the Fermi-Dirac factor, making their number very dependent on the temperature. A key takeaway from this model is that electrons in perfect crystals move as if they were in a vacuum ignoring the crystal, but with a renormalized mass, noted m^*.

If there is a vacant spot in the valence band, an electron in the conduction band can emit a photon or a phonon and descend to the valence band. Its energy will necessarily be greater than or equal to the band gap, with it more likely to be close to the band gap. In the case of a photon, since energy and frequency are linked ($E = \hbar\nu$), the emission spectrum of semiconductors is therefore narrow enough to appear as a pure color to the human eye.

This model is the backbone upon which other models are built on to understand the electronic states in materials. The study of the spatial and spectral structure of the eigenstates of the Hamiltonian of electrons in solid systems is necessary for comprehending the transport properties of these electrons. Implementing Boltzmann's kinetic theory to the system by considering interactions between the electrons and phonons gives a good description of the transport properties of metals. This is also known as the semi-classical model of electron dynamics. For a more in-depth introduction on electronic transport in materials, the reader can consult Ashcroft and Mirmin's *"Solid States Physics"* [12].

These models are effective in describing the electric properties of materials that have crystalline structures. However, in reality no crystal is perfect. The existence of small defects or impurities, which can be missing atoms in the crystal or atoms replaced by different atoms (substitution defects), means we can no longer assume that the wave functions of the electrons are Bloch states. A possibility is then to treat the disorder as a perturbation to produce corrections to the eigenstates. The disorder must necessarily be quite small for this sort of calculation. This description is adequate for low concentration of impurities, for instance for lightly doped semiconductors.

For many materials, treating the disorder as a small perturbation is fundamentally inadequate. For example, the different elements of metallic alloys can have concentrations of the same order of magnitude, and be randomly distributed in the crystal. In this case, instead of having small defects in an ordered crystal, the different elements of the crystal occupy random sites and there is no underlying structure. Similarly, certain semiconductor alloys such as indium gallium nitride (InGaN) are specifically designed to emit at a certain wavelength by tuning the concentration of indium with respect to gallium (more gallium increases the band gap which decreases the emitted wavelength).

Another approach to describing the electronic structure of materials is the tight-binding model. The idea behind it is the opposite of the Bloch model. Here, the electrons are considered to be bound to their respective atoms, and therefore the atomic orbitals are used as the basis states of the Hamiltonian. Because they are so strongly bound, the overlap with the neighboring atoms is very small. Therefore, the electrons can be described as bound to an isolated atom, with a slight perturbation due to its neighbors. The wave function of the electrons in this model is projected on a discrete basis: the various localized sites of the lattice. The Hamiltonian for such a model is:

$$H = \sum_i \epsilon_i a_i^\dagger a_i - t \sum_{<i,j>} \left(a_i^\dagger a_j + h.c. \right), \tag{1.1}$$

where ϵ_i corresponds to the energy at the site i, $a_i^\dagger$ and a_i are the creation and annihilation second quantization operators that respectively create and destroy an electron at site i, and t is the hopping

term that represents the coupling or the overlap between two neighboring states. The $< i, j >$ symbol indicates that the sum is run over nearest neighbors, and *h.c.* stands for Hermitian conjugate. These are the basic elements of the tight-binding model with nearest neighbor coupling.

I.2 Anderson localization

In 1958, Anderson imagined a tight-binding model where the on-site energies would be random [8]. This model was meant to be the simplest capturing the fluctuations of the potential due to a random quenched disorder in the system. An example of such a system is displayed in Figure 1.1. In his original paper, the on-site energies follow a general random law $P(E)\mathrm{d}E$, the width of this distribution being W (which we will very often call $V_{\max}$ in this manuscript). The two parameters of the model are the potential strength $V_{\max}$ and the overlap between neighboring sites t. The ratio $V_{\max}/t$ is a dimensionless parameter that represents the strength of the disorder.

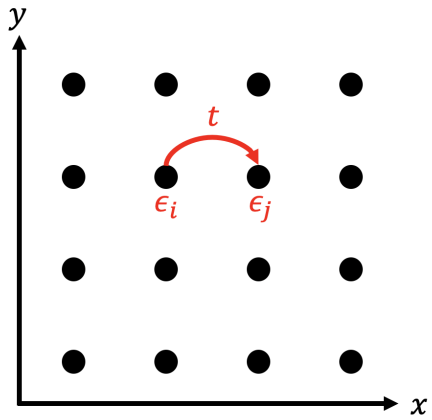

Figure 1.1: Two-dimensional Anderson tight-binding model with nearest neighbor hopping.

Studying the wave function at a site i at a time τ, $\psi_i(\tau)$, Anderson argued that if this quantity goes to 0 at infinite time, the wave will have completely delocalized, i.e. it will have spread out on the entire domain. However if this quantity stays finite, it means that the wave function remains localized: it did not spread out in the entire domain. Anderson showed that for sufficiently large ratios of $V_{\max}/t$, the eigenfunctions remain localized (in reality, it was shown later on that this critical disorder strength does not always exist and depends on other factors such as the embedding dimension of the system). Physically speaking, for strong enough disorders and weak overlap between neighboring sites, the eigenfunctions do not propagate in the medium. This critical ratio was later defined as the *mobility edge* by Mott in his papers from the 1960s [59, 60].

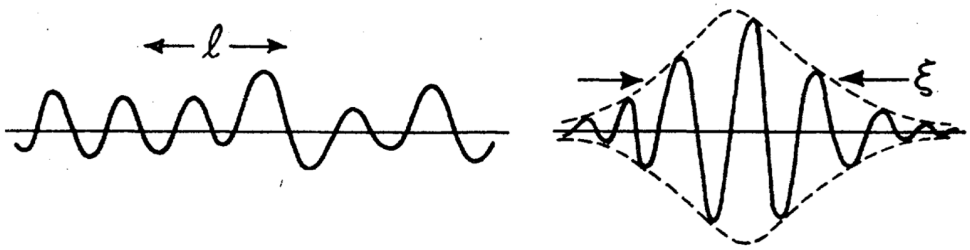

Figure 1.2: The two different states for a quantum wave function. Left: Delocalized states with mean free path ℓ. Right: Exponentially localized state of localization length ξ. Reprinted from [52].

Furthermore, Anderson showed that the eigenfunctions decay exponentially from site to site (see Figure 1.2). This brings into play another parameter, the localization length ξ, which governs this exponential decay: $\psi \sim \exp(-x/\xi)$. This is the first description of Anderson localization, also known as strong localization.

Since then, this phenomenon has been studied extensively, and shown to exist in other systems. Most notably, the continuous Hamiltonian equivalent of the Anderson tight-binding model is:

$$\hat{H}\psi = \left(-\frac{\hbar^2}{2m}\Delta + V\right)\psi, \tag{1.2}$$

where Δ is the Laplacian operator, $\hbar$ is the reduced Planck constant, m is the mass of the electron, V is the random potential, and ψ are the continuous wave functions.

Let us take an example. Consider a two-dimensional system following equation (1.2). In the absence of a potential, the solutions to such an equation are plane waves, with some examples represented in Figures 1.3.

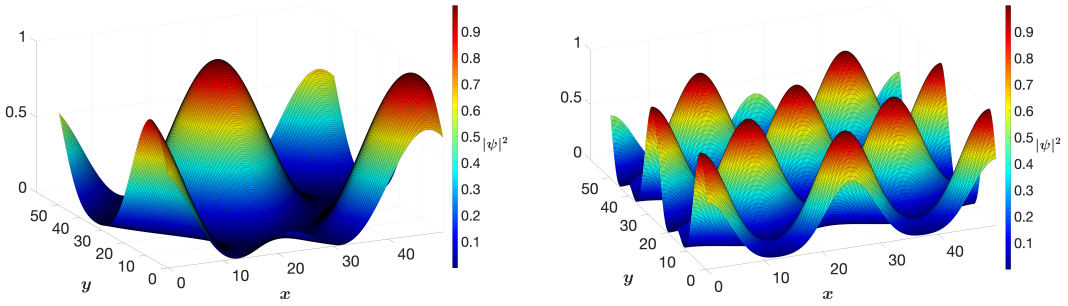

(a) (b)

Figure 1.3: (a) Example of the probability density of a delocalized eigenfunction of the Schrödinger operator without any potential. This is an excited mode. (b) Example of a delocalized eigenfunction of the Schrödinger operator without any potential. This is the tenth excited mode.

In Figure 1.4 we have represented a two-dimensional potential following a Boolean random law and taking values in $[0, 10]$. If we solve equation (1.2) with this potential, the solutions are not plane waves and are now localized, as can be seen in Figure 1.5.

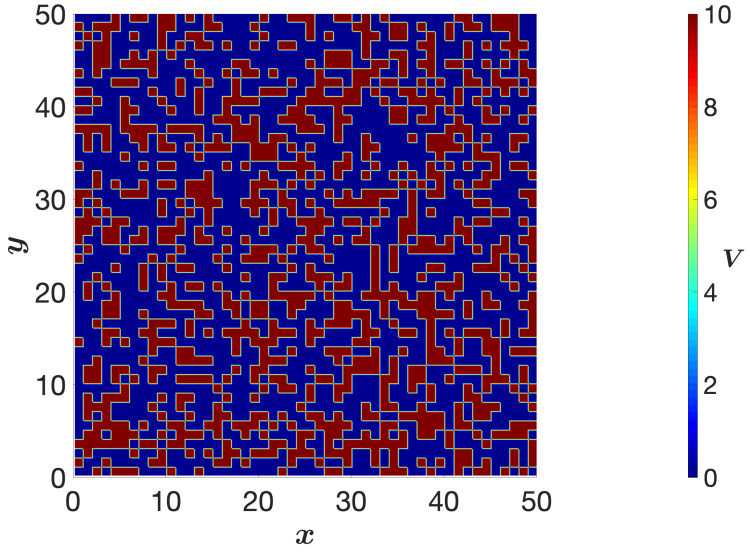

Figure 1.4: A 2D potential with a Boolean random law. The potential is piece-wise constant, taking values 0 with a 60% chance (in blue) and $V_{\max} = 10$ with 40% chance (in red).

As can be seen in Figure 1.4, the $V = 0$ part of this Boolean potential percolates. A classical particle starting from this region with any positive energy in the center of the domain could travel to the edge

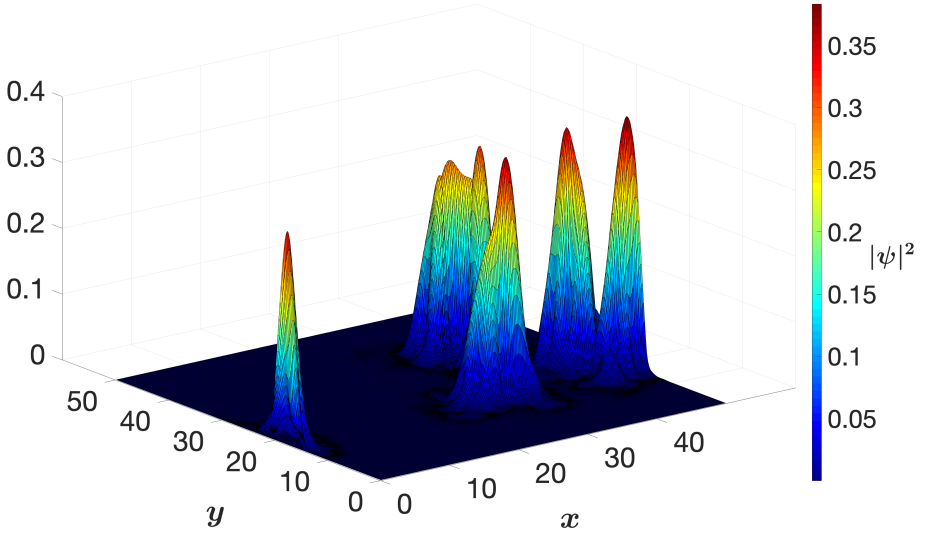

Figure 1.5: The first 5 eigenfunctions that are solutions to the Schrödinger equation (1.2). They each occupy a distinct area in the domain.

without being stopped. And yet the eigenfunctions of the Anderson Hamiltonian with this potential are localized. This behavior can only be understood with a wave-like description of the particles.

In order to understand how waves localize instead of propagating through a medium, and the role wave interference plays in in this process, let us consider a simplified description of an electron traveling from a point A to a point B, as depicted in Figure 1.6. In Feynman's path integral formulation, calculating the probability amplitude P for the electron to travel from A to B requires considering all paths from A to B and sum the probability amplitudes of each individual path C_i:

$$P = \left| \sum_i C_i \right|^2 = \sum_i |C_i|^2 + \sum_{i \neq j} C_i C_j^* \tag{1.3}$$

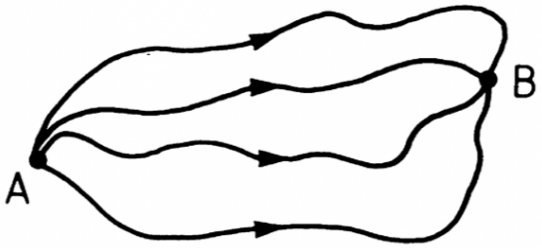

Figure 1.6: An example of the different paths an electron can take to go from point A to point B. In the quantum theory setting, all paths must be considered and summed to calculate the probability for the electron movement. Reprinted from [73].

Two terms contribute to the total probability. The first corresponds to the addition of contributions from the paths that do not interact with each other, it is therefore classical by nature. The second corresponds to interferences between the different paths, it is due to the wave nature of the quantum particle. In general, the sum in the second term averages to zero since the various phase contributions usually cancel each other out. In those cases, the probability ends up being: $P = \sum_i |C_i|^2 = P_{class}$.

There is an exception to this case. If the starting and end points are identical, or for self-crossing paths as shown in Figure 1.7, a path going one way will positively interfere with a path going the other way, due to the time-reversal symmetry of the Hamiltonian. Furthermore, the electron must

maintain coherence along its path. The contribution of these two paths to the probability is now given by: $P_{=}2|C|^2 + 2C_iC_j^* = 4|C|^2 = 2P_{class}$. In this case, it is therefore twice as likely for a quantum particle to return to its starting point than for a classical particle.

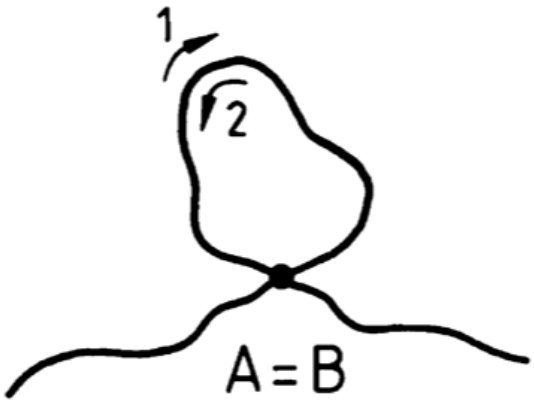

Figure 1.7: An example of a self-crossing path. The starting and end points are identical, which leads to a constructive interference. Reprinted from [73].

This phenomenon is called *coherent backscattering*, and is the origin of the phenomenon called *weak localization* which has been extensively studied in various papers [4, 6, 57]. The following works offer an excellent review of the topic [15, 20, 52, 5]. When light is shined into a medium with randomly placed scatterers, some of the light comes back, and there is a sharp peak in intensity at exactly the angle at which the initial light was shined. This example shows that wave interference is crucial for generating localization of eigenfunctions in disordered media.

Anderson localization has been treated in many different ways since its inception. Historically, there have been numerous different ways to characterize the localization/delocalization transition, but we will focus on three for the purpose of this manuscript. The first is to use the localization length as a measure of how localized the eigenstates were. Another way is to study the conductivity, which goes to zero as disorder increases in the localization regime. And finally a more mathematical approach is to consider the statistics of the distribution of the eigenvalues. The goal is not to present an exhaustive review of the literature [70, 52, 27, 1], but to develop specific points that pertain to the rest of the manuscript. We have just presented Anderson localization and weak localization. We will now examine the scaling theory of localization, as it established central results on the transition between localized and delocalized states depending on the dimensionality. This will be followed by a presentation of random matrix theory as it has elaborated tools to quantify how localized eigenfunctions are. Afterwards we will look at Lifshitz's model of disorder and the Lifshitz tails, which are a feature in the integrated density of states of disordered systems. And finally we will give an overview of the main questions left concerning localization and how we plan to address them.

I.3 Scaling theory

Concurrently with the first steps of Anderson localization, renormalization group theories emerged for studying transitions and critical phenomena. It did not take very long for others to formulate a scaling theory of localization: Thouless was the first to present these ideas in a paper in 1974 [70]. The foundations of the scaling theory were built upon and clearly formulated by Abrahams, Anderson, Licciardello and Ramakrishnan a few years later [2].

In localization/delocalization transition phenomena different length scales are involved. The smallest length scales are the de Broglie wavelength λ and the correlation length of the disorder ζ. If $\zeta < \lambda$, the details of the disorder are not seen by the electron [61]. If $\lambda < \zeta$, it is the opposite, which is the case for example in optical speckle potentials [16]. The larger length scales are the mean free path ℓ and the localization length ξ. Depending on the details of the system, (the type of disorder, the dimensionality) these two length scales can take on different values. For instance, in 3D with low disorder strength, $\xi = \infty$ while in 1D, for weak disorder, a transfer matrix calculation gives $\xi = 2\ell$.

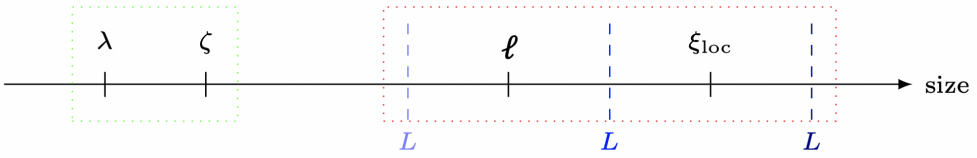

Figure 1.8: The different length scales involved in the localization/delocalization transition. The three areas separated by the dotted lines correspond to the three different regimes: ballistic, diffusive and localized (from left to right). Reprinted from [61].

The scaling theory of localization describes how changing the system size allows to pass from one regime to another. If the system size L is smaller than the mean free path ℓ the particles do not have time to diffuse and the movement is therefore ballistic. For $\ell < L < \xi$, the transport is diffusive with weak localization corrections. The localized regime is reached when $L > \xi$. If the localization length is infinite then the localization regime can never be reached. The different length scales and their relation with one another are displayed in Figure 1.8.

The general idea behind scaling theories is that the exact nature of the eigenfunctions and eigenvalues of a hypercube of size L^d (d being the dimension) will be determined by its specific properties such as the realization of disorder. A scaling theory provides a procedure that enables us to retrieve information on these finite sized systems at the thermodynamic limit. Let us consider the cube of side-length L and let us make copies of it in order to stack them up to assemble a hypercube of size $(2L)^d$. How do the system properties change in this operation?

The first step of the scaling theory is to determine a parameter that characterizes the transition that is to be studied (in our case the localization/delocalization transition). This parameter should depend on as few variables as possible, ideally only one. As mentioned before for the Anderson transition, different quantities measure how localized the eigenfunctions are. Let us establish such a criterion. Considering the aforementioned hypercube of size L^d, if the system is closed, the eigenfunctions of the different hypercubes will not intermix, and the average spacing between the eigenvalues is determined by $\Delta E = \left(\rho L^d\right)^{-1}$, with ρ the density of states. Now if the system is open, the time it would take for a particle to diffuse from that hypercube to the other is $\tau_D = \frac{L^2}{D}$ where D is the diffusion constant. Through its diffusion, that particle's energy resolution δE is such that $\delta E \tau_D \sim \hbar$.

When $\Delta E \gg \delta E$, the eigenfunctions' energy resolution is very small, meaning that their frequency resolution is also. This implies that the eigenfunctions are spatially extended. They therefore overlap considerably and the eigenvalues are close to each other. We are in the delocalized regime. On the other hand, if $\Delta E \ll \delta E$, the overlap between in the eigenfunctions is very small compared to how far apart the eigenvalues are. This is the localized regime. The ratio of these two quantities is our criterion: $\Delta E/\delta E$. Thouless further argued that the conductance G is linearly related to the quantity $\Delta E/\delta E$ [70]. Furthermore, we can express this quantity in units of $e^2/\hbar$:

$$g = \frac{G}{e^2/\hbar} = \frac{\Delta E}{\delta E}. \tag{1.4}$$

g is referred as the dimensionless conductance. It is important to realize that as we are doubling the system size, the new value of the conductance depends only on the old value. The idea behind scaling theory is to study the β function which measures how the conductance evolves with the system size:

$$\beta(g) = \frac{\mathrm{d}\ln g}{\mathrm{d}\ln L}. \tag{1.5}$$

The main hypothesis we make here is that this function is only dependent on g. $\beta(g)$ gives all the information that is needed in order to determine the behavior of the eigenfunctions as the system size goes to infinity. Indeed, if β is negative, that means as the size is increased, the conductance decreases,

eventually going to 0. While if it is positive, the conductance will increase. We can determine the asymptotic behavior of β by using the known expressions of g for small and large values of g.

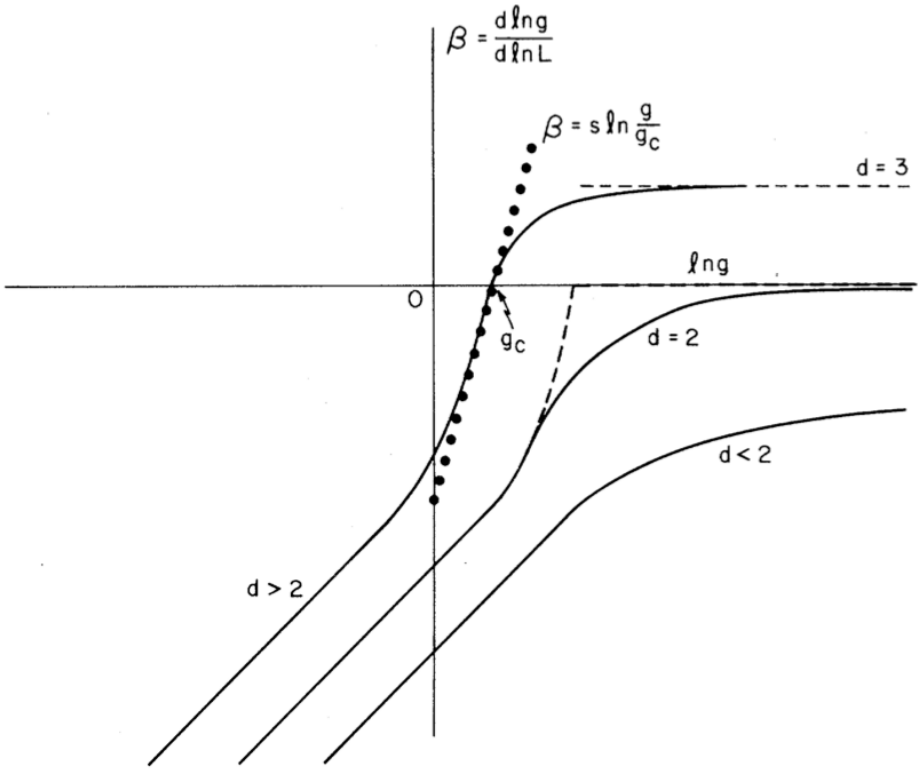

Figure 1.9: The evolution of the β function for three different dimensions. The slope of β at g_c is related to the critical exponents. If there was a minimal conductivity in 2D, β would go to 0 at a distinct value, instead of asymptotically going to 0. β would behave like the dashed curve that prolongs from the $d = 2$ curve. Reprinted from [2].

One can derive formulas for g, and therefore for $\beta(g)$ in the strongly localized regime: $\beta(g) = \ln \frac{g}{g_0} = -\frac{L}{\xi}$ using the fact that g decays exponentially, and in the delocalized regime: $\beta(g) = d - 2$ using Ohm's law.

After obtaining the asymptotic behavior of the β function for both small and large g, and assuming $\beta(g)$ behaves reasonably, we can link these two asymptotics together as simply as possible, i.e., monotonically. As can be seen in Figure 1.9, β stays negative for $d = 1$ and $d = 2$. No matter the initial conditions, the process of doubling the system size as detailed above always decreases g. At the thermodynamic limit, the conductance always vanishes, meaning that the eigenfunctions are all localized. In 3D however, β is negative for small g, and positive for large g. This means that there is a critical value g_c where $\beta(g_c) = 0$. For g above this value, the scaling process increases the conductance, while for g under this value, the eigenfunctions become more and more localized as the system size is increased.

According to the scaling theory of localization, there is no minimal finite value for the conductivity: $\sigma_{\min} = 0$. This was one of the first results of the theory. The other main prediction was the value for the critical exponents for the localization transition in 3D.

In the theory of critical phenomena, a transition is characterized by a certain order parameter. As mentioned before, one can choose different parameters, but one that makes sense in the localized phase is the localization length ξ. In the Anderson model, this parameter depends on the potential strength W:

$$\xi \sim (W - W_c)^{-\nu}\,, \tag{1.6}$$

where W_c is the critical potential strength and ν is the critical exponent. To obtain a value for ν, we start by expanding the expression for $\beta(g)$ around the critical point g_c. The simplest models have given $\nu \approx 1.63$ which is quite close to values found through various numerical simulations: $\nu = 1.58 \pm 0.01$ [61, 68, 33].

This comparison of length scales raises another question. All previous considerations have been expressed in the thermodynamic limit, i.e., in an infinitely sized sample. In practice however, systems are of finite size. Usually this is not a problem as the length scales involved are much smaller than real sized samples. For instance, 2D Anderson localization remains difficult to observe experimentally as the localization length is very large: $\xi_{2D} \sim l \exp\left(\frac{\pi}{2} k_F l\right)$ [52, 48] (where k_F is the Fermi wave vector). For instance, in a cold atoms experiment [16], with $\ell = 100\ \mu m$ and $k_F = 2.5\ \mu m^{-1}$, this gives $\xi_{2D} \sim \ell e^{400}$, which is obviously much larger than the system size. The dependence on the mean free path is exponential, so in systems with weak disorder the size is often smaller than this length. This creates an additional difficulty in the observation of the mobility edge: how to differentiate a truly delocalized state from a localized state with excessively large localization length? The concept of *effective mobility edge*, which can be defined as the energy over which the localization length of the eigenfunctions are greater than the system size, has emerged to characterize this phenomenon. In finite-size systems, eigenfunctions over the effective mobility edge will appear delocalized. The origin of the effective mobility, which in practice mainly concerns speckle potentials in cold atoms, comes from correlations in the disordered potential [65, 28].

Predicting the exact values for the mobility edge and the effective mobility edge is one of the open questions left today in Anderson localization.

I.4 Random matrix theory

In 1955, Wigner introduced the random matrix theory in order to model the spectra of the nuclei of heavy atoms [75]. Since then, the use of random matrices has spread to other domains in physics such as the physics of disordered systems. The idea behind this theory is that the statistics of the spectrum of a random operator are heavily dependent on the symmetries of that operator and on whether its eigenfunctions are localized or delocalized.

The argument goes as follows: consider a very localized system where the different eigenfunctions have very little overlap with one another. Pushing this argument to the extreme, the matrix will essentially be diagonal with off-diagonal elements either very small or 0. In this case, the system being disordered, the diagonal elements are the eigenvalues and are determined randomly. The level spacings are defined as the difference between consecutive eigenvalues: $s_n = E_{n+1} - E_n$. As the energy at each site is determined randomly, the spacings can be interpreted as a Poisson process, and therefore follow a Poisson distribution [66]:

$$P_P(s) = \frac{1}{\delta} \exp\left(-\frac{s}{\delta}\right), \tag{1.7}$$

where $\delta = \langle s \rangle$ is the average value of the s_n. Physically, this indicates that when the eigenfunctions are localized, they behave independently: there is no repulsion between the different eigenvalues.

However, when the the eigenstates are delocalized the statistics of the spacings are different and depend on the symmetries of the Hamiltonian [7, 35]. The most studied operators belong either to the Gaussian Orthogonal Ensemble (GOE), the Gaussian Unitary Ensemble (GUE), or the Gaussian Symplectic Ensemble (GSE). In each case, the elements of the matrix associated to the operator are random variables following a normal distribution. Depending on the ensemble, there is an added constraint: the matrix must be orthogonal for the GOE, unitary for the GUE, and symplectic for the GSE. An orthogonal matrix corresponds to a Hamiltonian with time-reversal symmetry, a unitary matrix to a Hamiltonian without time-reversal symmetry, and a symplectic matrix to a Hamiltonian with time-reversal symmetry but no spin rotational symmetry. The statistics of the level spacings of the spectra of each type of matrix are different. The following formulae are obtained for 2×2 matrices, but describe the statistics of larger matrices very well. This is called the *Wigner surmise*.

$$P_{\mathrm{GOE}}(s) = \frac{\pi}{2} s \exp\left(-\frac{\pi}{4} s^2\right), \tag{1.8}$$

$$P_{\mathrm{GUE}}(s) = \frac{32}{\pi^2} s^2 \exp\left(-\frac{\pi}{4} s^2\right), \tag{1.9}$$

$$P_{\mathrm{GSE}}(s) = \frac{2^{18}}{3^6 \pi^3} s^4 \exp\left(-\frac{64}{9\pi} s^2\right). \tag{1.10}$$

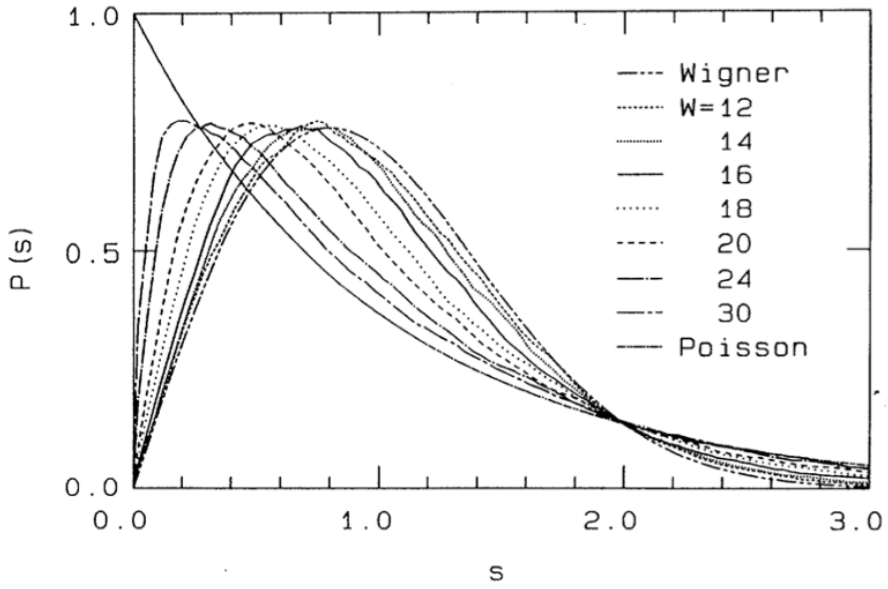

Figure 1.10: For three-dimensional systems, as the disorder strength increases, the eigenstates go from delocalized to localized. Therefore the probability distributions of the level spacings go from Poisson-like to Wigner-like. Reprinted from [66].

The Anderson model usually exhibits time-reversal symmetry, so the statistics of the GOE are relevant in this case. Certain models add a magnetic field interaction which destroys time-reversal symmetry. In that case, the GUE statistics are relevant.

According to these statistics, for delocalized eigenstates, it is very unlikely for two consecutive eigenvalues to be close to each other since the probability density of the spacings at 0 vanishes. It is just as unlikely for two consecutive eigenvalues to be infinitely apart, there is therefore a value of the spacing where the probability is maximal. Figure 1.10 displays the transition between the Wigner surmise and the Poisson statistics.

The distribution of the energy spacings is another useful tool in studying the localization/delocalization transition, as determining these distributions requires only the calculation of the eigenvalues and not the eigenfunctions, which is considerably more computationally costly.

II Other manifestations of localization

In this section we will present other examples of disordered systems where localization occurs. Each case is interesting to us because they either exhibit new characteristics of localization (the Lifshitz tails) or demonstrate localization in novel ways (the Aubry-André model). The latter can then be used as a test bed for the localization landscape theory.

II.1 Lifshitz tails

In parallel to Anderson, Lifshitz developped his own model of disorder known as the Lifshitz model [55, 56]. In this model, instead of considering a tight-binding model, the model is continuous, with repulsive impurities added at specific points of the lattice:

$$-\frac{\hbar^2}{2m}\Delta\psi + V(\vec{r})\psi + \sum_j U(\vec{r} - \vec{r_j})\psi = E\psi, \tag{1.11}$$

where V is the periodic potential due to the crystal and U is the potential due to the impurities, which is summed over the various sites j of impurities.

In the absence of disorder for free electrons, the dispersion relation is quadratic. This leads to a density of states following a power law: $\rho \sim E^{d/2-1}$. Since the aforementioned dispersion relation does not hold in the presence of disorder, neither does the expression for the density of states. Instead, Lifshitz showed that the integrated density of states (or counting function) at the bottom of the spectrum tends towards $-d/2$:

$$\lim_{E \to E_0} \frac{\ln\left(\ln\left(N(E)\right)\right)}{\ln\left(E - E_0\right)} = -\frac{d}{2}. \tag{1.12}$$

This behavior is called the Lifshitz tails, and has interested mathematicians and physicists alike. The former were at first interested in determining which types of potentials were responsible for the appearance of these tails. Initially, it was only proven for this particular type of potential, but later on others generalized these results. Pastur, Benderskii [14] and Kirsch [45] expanded the theory to a large class of potentials. In 1985, Simon showed that the Lifshitz tails occurred in Anderson type potentials [67]. Klopp studied the weak disorder limit of the Anderson model and found an expression for these Lifshitz tails [46, 47]. For further information on the mathematical side of the topic, the read can refer to these comprehensive reviews [44, 62, 50].

From the experimental physicist's perspective, these tails in the integrated density of states have an impact on other observables. For disordered crystals, Urbach observed that the absorption curve also exhibits exponentially decreasing tails [72]. He then proposed a phenomenological law to account for this:

$$\alpha(h\nu) = \alpha_0 e^{(h\nu - E_1)/E_U(T)}, \tag{1.13}$$

where α_0 is a constant, E_1 is the energy limit of the extended band-like states, and E_U the Urbach energy. These parameters are to be determined experimentally. Several works have attempted to establish a universal theory for these tails [25, 42]. A possible explanation lies in thermal disorder or in the disorder induced localization of the electrons and holes, but there is still debate as to which phenomenon is the leading cause of the Urbach tails.

Throughout this thesis we will be concerned only with the mathematical aspect of these exponential tails. A more precise behavior than equation (1.12) is sought after, especially its dependency on the parameters of the random law governing the disorder.

II.2 The Aubry-André model

In this introduction, we have always treated Anderson localization through the prism of independently and identically distributed (i.i.d.) random potentials. Anderson localization is always studied statistically since the potentials depend on the realization of disorder. It does not make sense to try to solve the eigen-equations analytically since there is no expression for the potential.

However randomness is not a necessary condition to produce localization. Another class of potentials known as quasi-periodic or pseudo-random exhibit some aspects of localization. In tight-binding models, these potentials have a cosine term but with a spatial frequency that is incommensurate with the lattice spacing. In this way, values are never repeated and seem random.

We consider a discrete Hamiltonian $H_\omega^{\lambda,\alpha}$ in 1D :

$$H_\omega^{\lambda,\alpha}\psi_n = \psi_{n+1} + \psi_{n-1} + 2\lambda\cos\left[2\pi\left(\omega + n\alpha\right)\right]\psi_n = E\psi_n, \tag{1.14}$$

which depends on three parameters, the potential strength λ, the spatial frequency α, and the phase ω.

In practice, the lattice spacing is taken equal to 1, and therefore the frequency must be an irrational number so that the spatial frequency is incommensurate with the lattice spacing. In physics, Aubry and André were the first to propose such a model, and showed localization of the eigenfunctions [13]. The model had been introduced to study specific phenomena, the Peierls instabilities, but has since been used as a foil to the Anderson model since it behaves similarly.

Independently, Hofstadter developed a comparable equation while working on two-dimensional Bloch electrons in a magnetic field [36], which also had an incommensurate potential. Hofstadter's paper is

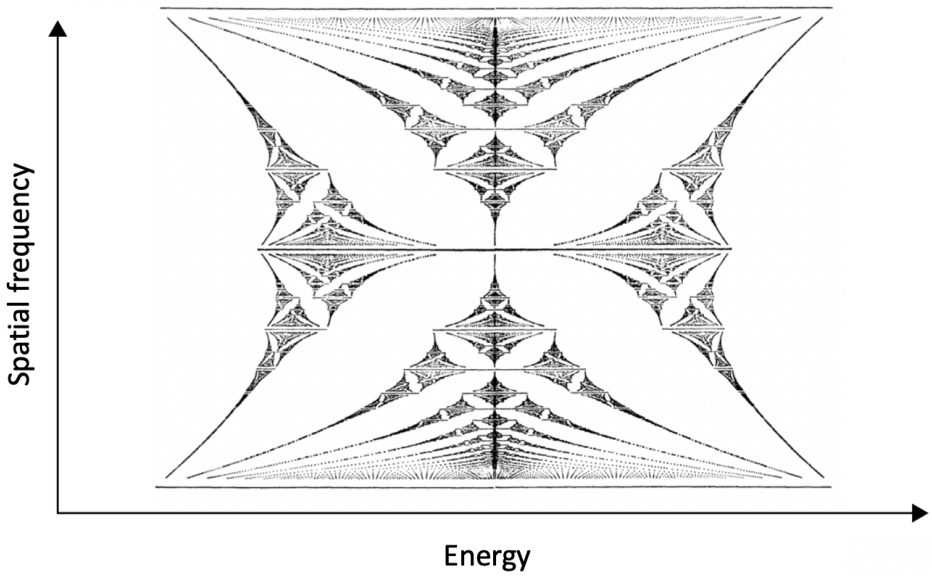

Figure 1.11: The Hofstadter "butterfly" plot. The x axis represents the energy; the y axis represents the irrational frequency α. Reprinted from [36].

famous for predicting the "butterfly" figure represented in Figure 1.11. It is a representation of the spectra for the different values of the frequency α, for the specific value of the potential strength $\lambda = 1$. This set has a fractal-like structure. This model was shown to be a special case of the Aubry-André model afterwards [41]. It has been extensively studied, and many of its properties are known. All the eigenfunctions are either localized or delocalized [39], depending on the value of λ (delocalized for $\lambda < 1$, localized for $\lambda > 1$), regardless of the dimension [17] (in $\mathbb{Z}^d$). Furthermore, Jitomirskaya and collaborators have shown that the eigenfunctions possess a hierarchical structure determined by the continued fraction expansion of the irrational frequency α [40]. From the physics perspective, these quasi-periodic potentials are an excellent way to study localization experimentally in a cold atoms setting [64], as well as being a base model to research more complex phenomena from a theoretical point of view such as many-body localization [38], higher dimensional transitions [24], topological zero energy phases [34] and their transport properties [69].

The Aubry-André model is therefore an excellent case study of computable wave localization. Many of its properties are known and well understood which makes it ideal to compare and contrast with Anderson localization.

III Several remaining open questions

We would like to summarize some of the remaining essential questions in the field of Anderson localization that will be addressed in this thesis:

- The precise asymptotic behavior of the Lifshitz tails depending on the disorder parameters is an ongoing question. The current description of the exponential decay of the counting function involving the limit of the logarithm of the logarithm of the counting function is in a weak form.
- High-energy localization is well understood in one dimension thanks to transfer matrix calculations: quantities such as the localization length can be derived [43, 48, 58, 71]. Less results are known in two dimensions, and we still do not understand the mechanisms behind the emergence of a mobility edge at higher dimensions.
- Finally, one of the main questions is the analytical characterization and description of the mobility edge, the critical exponents, as well as the effective mobility edge. The mobility edge is one of the defining feature of localization. And yet we are not fully capable of predicting and characterizing it depending on the features of the disorder of the system. The same goes for the critical exponents.

Perhaps as important is the effective mobility edge. Being able to differentiate the two mobility edges is critical for the study of the true mobility edge. Indeed, experimentally and numerically, one is often confronted with the situation where delocalization seems to be observed because the system size is not large enough.

IV The localization landscape: a deterministic approach to localization

As was seen in the previous sections, approaches to Anderson localization have largely been statistical. The properties of the system are averaged over many realizations of the disorder. However, because of this, little can be said on the localization structure for particular realizations of disorder.

The localization landscape theory departs completely from this paradigm. It is a deterministic approach to study the localization properties of the eigenfunctions. In this way, information can be acquired directly from the system under study. One useful application is for relating theory with experiments, since more often than not experimental physicists can only measure the properties of one or a few samples.

IV.1 The spatial properties of the localization landscape

The localization landscape theory was first introduced in 2012 [31] with the aim of explaining the mechanisms at work in weak or Anderson localization. The idea was to consolidate many different vibrating systems in a universal mathematical framework.

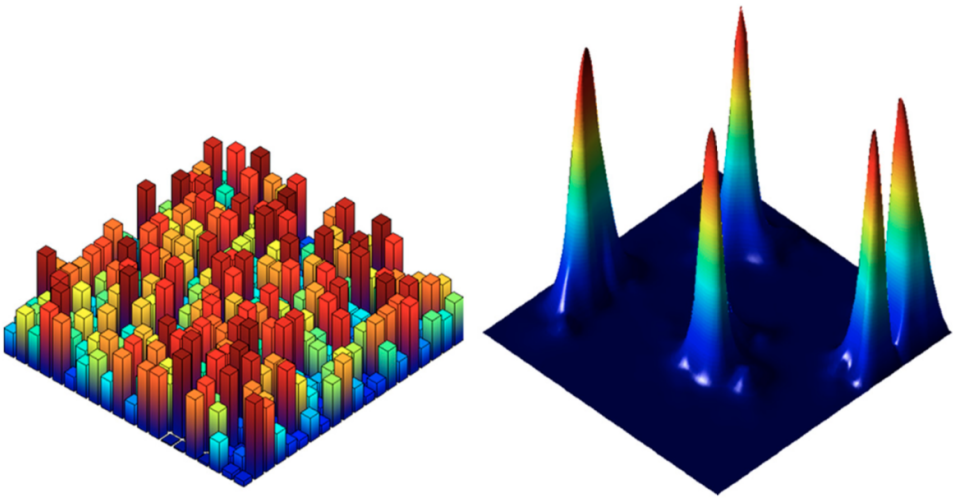

Figure 1.12: Left: Example of a random potential on a 2D domain. The domain is divided into 20×20 squares, and on each square the potential is piecewise constant with values uniformly distributed between 0 and $V_{max} = 8000$. Right: The associated eigenfunctions of the Schrödinger equation. There is no clear and obvious relationship between the two. Reprinted from [31].

Let us start with a simple example. In Figure 1.12, the random potential seems to give no information whatsoever on the location of the eigenfunctions. Intuitively, one can guess that the low energy eigenfunctions will appear spatially in places where the potential is lowest. However, an eigenfunction also requires space to exist, meaning that the determining factor is not the location of the minimum, but more the location of the minimum of some sort of potential averaged on a length scale that is to be determined.

We define $H = -\Delta + V$ as the operator of the system on the domain Ω and consider the Green's function $G(x, y)$ such that $H_x G(x, y) = \delta_y(x)$. Thus, for any function v, we have $\int_\Omega H_x G(x, y) v(x) \mathrm{d}x = \int_\Omega \delta_y(x) v(x) \mathrm{d}x = v(y)$. Here, H is a self-adjoint elliptic operator and the Green's function is symmetric.

We now show how to define a new function u that explains the localization structure of the eigenfunctions. Considering an eigenfunction ψ of eigenvalue λ, we can show the first fundamental inequality for the localization landscape:

$$|\psi(x)| \leq E\|\psi\|_{\infty} u(x), \tag{1.15}$$

where

$$u(x) \equiv \int_{\Omega} |G(x,y)|dy, \tag{1.16}$$

is the definition of the localization landscape. If the Green's function is positive (which is the case of all Hamiltonians $H = -\Delta + V$ with positive potential), then the expression of u is simplified:

$$u(x) = \int_{\Omega} G(x,y)\mathrm{d}y, \tag{1.17}$$

and u is now the solution to the following equation:

$$\int_{\Omega} H_x G(x,y)\mathrm{d}y = H_x \int_{\Omega} G(x,y)\mathrm{d}y = H_x u(x) = \int_{\Omega} \delta_y(x)\mathrm{d}y = 1 \tag{1.18}$$

This last equation is the most commonly found definition of the localization landscape in the literature, i.e.,

$$Hu = (-\Delta + V)u = 1. \tag{1.19}$$

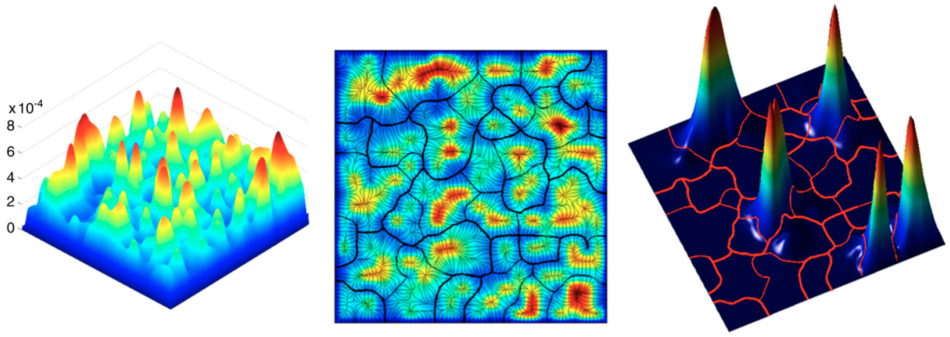

Figure 1.13: Left: The localization landscape calculated from the random potential of Figure 1.12. Center: A top view of the aforementioned localization landscape. Red corresponds to peaks while blue to valleys. The thick blue lines delineate several subregions in the domain. Right: The five first eigenfunctions superimposed on the valleys defined previously. These eigenfunctions each fit exclusively in a single sub-region enclosed within the valleys. Reprinted from [31].

From inequality (1.15), one can recognize that areas where u is "very small" define locations where ψ is "small" as well. In Figure 1.13, the localization sub-regions are well defined by the valleys (the $((d-1)$-dimensional set of curves whose points are local minima [22]) of the localization landscape. At higher energies the inequality (1.15) does not restrict the eigenfunctions anymore.

Further work on the landscape has led to the discovery of the effective confining potential, which unlocks even more properties for the localization landscape theory [11]. Considering the original Schrödinger equation $(-\Delta + V)\,\psi = E\psi$, let us define the auxiliary function $\psi \equiv u\phi$. The equation is transformed in the following way:

$$(-\Delta + V)\,(u\phi) = Eu\phi \tag{1.20}$$

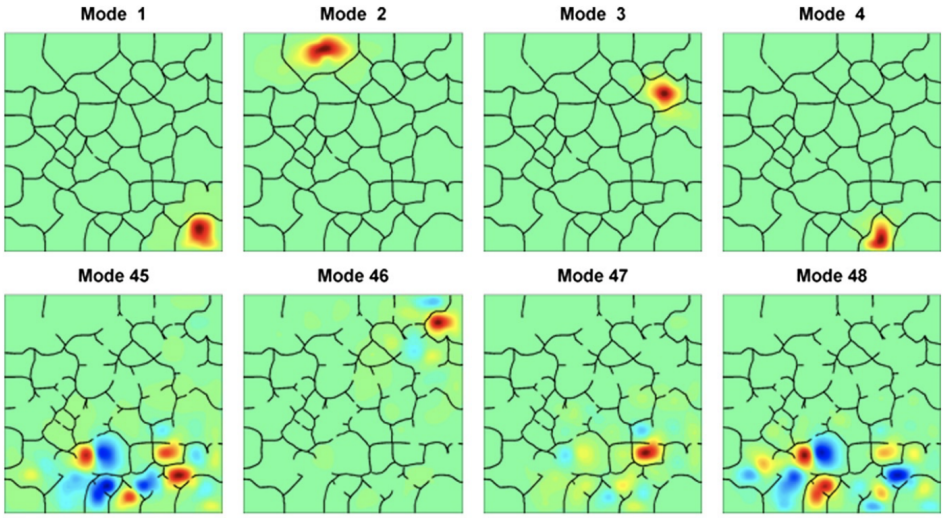

Figure 1.14: Several eigenfunctions are represented here. As the eigenfunctions' energy increases, the barriers between the sub-regions open up. The eigenfunctions are no longer confined in the small initial sub-regions. Reprinted from [31].

from which we obtain:

$$-\Delta\phi - 2\frac{\nabla u}{u}\cdot\nabla\phi + \frac{1}{u}\phi = E\phi \tag{1.21}$$

which finally gives us:

$$-\frac{1}{u^2}\boldsymbol{\nabla}\cdot\left(u^2\boldsymbol{\nabla}\phi\right) + W\phi = E\phi, \tag{1.22}$$

where we have defined $W \equiv \frac{1}{u}$. This quantity is homogeneous to an energy. The new function ϕ thus obeys a Schrödinger-like equation where the differential Laplacian operator has been replaced by $\frac{1}{u^2}\boldsymbol{\nabla}\cdot\left(u^2\boldsymbol{\nabla}\right)$, and the original potential has been replaced by W, which we will call the *effective confining potential*. The reason behind this name is justified by the following identity satisfied by any quantum state $|\psi\rangle$:

$$\langle\psi|\hat{H}|\psi\rangle = \left\langle u\nabla\left(\frac{\psi}{u}\right)\middle| u\nabla\left(\frac{\psi}{u}\right)\right\rangle + \langle\psi|\hat{W}|\psi\rangle\,. \tag{1.23}$$

From this equation one can observe that instead of being the sum of a kinetic and a potential energy, the energy is now split in two different terms: the first one is akin to a reduced kinetic energy while the second is likened to an effective potential energy, hence the name given to W.

The new Schrödinger-like operator has exactly the same spectrum as the original Hamiltonian. The eigenfunctions of the transformed equation divided by u are the same as those of the initial equation. There is a one-to-one correspondence between the solutions to the analogous equation and those of the original equation.

This fact casts a new light on the mechanism of localization. It appears in fact as a more classical localization in the new potential defined by W. The valleys of the localization landscape are the crestlines of the effective confining potential which determine the sub-regions of localization. When the energy E of an eigenfunction is larger than the crestlines of the effective confining potential surrounding the sub-region of localization of the eigenfunction, it is not longer confined by it. The eigenfunctions can then spread out into other sub-regions. The larger the energy, the more the eigenfunction can spread out, until finally the entire domain is accessible and therefore it is delocalized, as can be seen in Figure 1.14.

Following these findings, a series of papers have explored additional properties of the localization landscape. The first one established approximations of the fundamental eigenvalues and eigenfunctions of the

different localization regions defined by the landscape [32], while others detail different applications of these approximations [63, 54].

Among these findings, one can mention that, in each localization sub-region Ω_i able to host a localized eigenfunction, the fundamental of that region ψ_0^i is well approximated by the restriction of the landscape u to that sub-region:

$$\psi_0^i \approx \frac{u}{\|u\|} \tag{1.24}$$

Moreover, the energy of the fundamental, E_0^i, can also be approximated by the landscape:

$$E_0^i \approx \frac{\int_{\Omega_i} u(\vec{r})\mathrm{d}^d r}{\int_{\Omega_i} u^2(\vec{r})\mathrm{d}^d r} \tag{1.25}$$

A recent exhaustive study in various dimensions (1D and 2D) and for different random potentials (uniform, binary, etc.) has not only corroborated the approximation of the fundamental eigenfunctions by the landscape, but has also found a more general relation between the landscape and the energies of the local fundamentals [9]. The authors showed that these eigenvalues are approximately proportional to the minimum of the effective confining potential in the localization sub-regions with a factor depending only on the dimensionality of the system:

$$E_0^i \approx \left(1 + \frac{d}{4}\right) \times \min_{\Omega_i} W \tag{1.26}$$

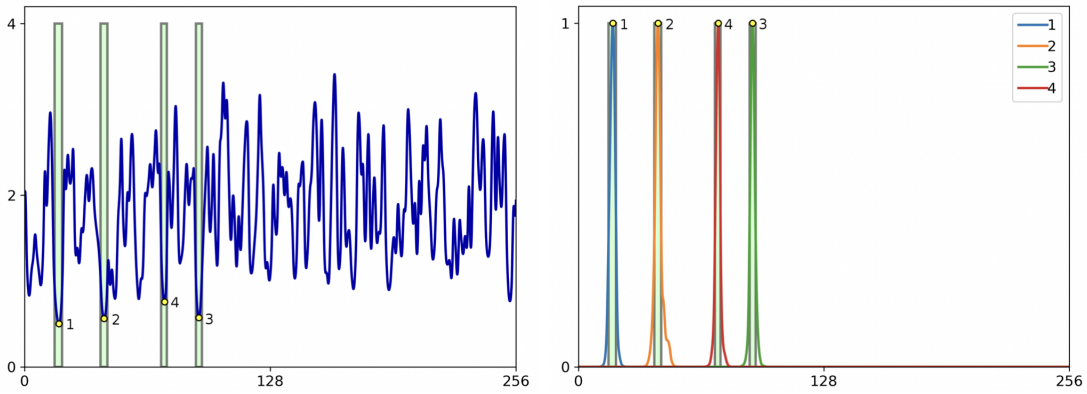

(a) (b)

Figure 1.15: (a) Example of an effective confining potential. The first four minima are labeled in ascending order. The authors estimated the width of the eigenfunctions with the size of the regions. (b) The actual eigenfunctions are displayed on top of the predictions. They are labeled in ascending order of their energy. Reprinted from [9]

In Figure 1.15, we see an example of how we can use the localization landscape to predict the shape of the fundamental eigenfunctions in each localization region as well as the order in increasing value of the eigenvalues. One aspect that we have glossed over is how should these sub-regions be defined. While it is simple enough in 1D, it is actually more complex in 2D or 3D than we have let on. The crestlines of the effective confining potential are a good first estimate of the borders of the localization sub-regions. This topic will be explored more thoroughly in the next chapter.

The authors of the study [9] also compared the eigenvalues with the minima of the effective confining potential and found the relation (1.26). The agreement between the computed eigenvalues and the approximations obtained from the local minima was calculated to be within 2%. This equation is a very robust method for estimating the fundamental eigenvalues of Schrödinger operators with random potentials.

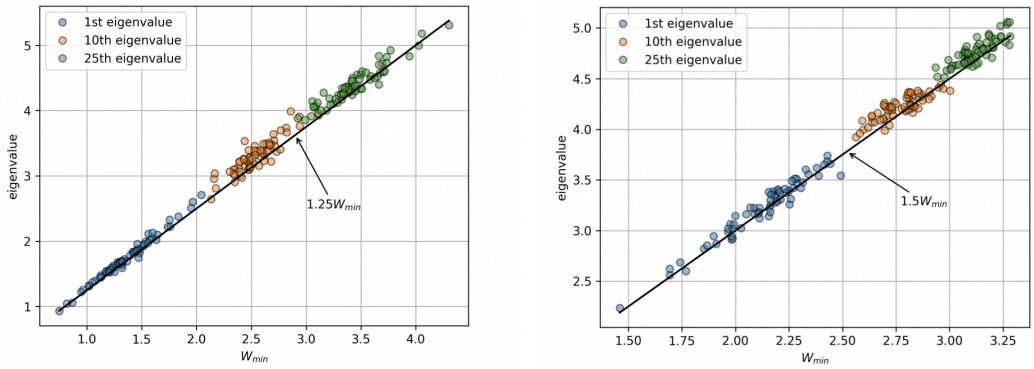

(a) (b)

Figure 1.16: (a) The 1st, 10th, and 25th eigenvalues and minima of the effective confining potential for many different realizations of a random potential in 1D, plotted against their associated local minimum. (b) Similar computation for 2D. Reprinted from [9]

IV.2 Spatial and spectral structures of eigenfunctions

The effective confining potential not only helps predict the localization sub-regions, but also can be used to construct an Agmon distance ρ_E which controls the exponential decay of the localized eigenfunctions [11, 3]. For a given energy E, the Agmon distance $\rho_E(\vec{r_1}, \vec{r_2})$ between any two points $\vec{r_1}$ and $\vec{r_2}$ is defined as:

$$\rho_E(\vec{r}_1, \vec{r}_2) = \min_{\gamma} \left(\int_{\gamma} \sqrt{(W(\vec{r}) - E)_+} \mathrm{d}s \right), \tag{1.27}$$

where $(x)_+ = \max(x, 0)$, and the minimum is taken over all possible paths that go from $\vec{r}_1$ to $\vec{r}_2$.

An eigenfunction whose peak is centered at $\vec{r}_0$ decays as:

$$|\psi(\vec{r})| \lesssim e^{-\rho_E(\vec{r}_0, \vec{r})}. \tag{1.28}$$

According to the inequality (1.28), the decay only occurs when $W < E$. In Figure 1.17 the eigenfunction decays mostly in the barriers of W and not in its valleys.

Another important quantity that appears frequently is the integrated density of states, or counting function, $N(E)$ which is defined as the number of states smaller than the energy E. As the counting function is difficult to compute, it is possible to obtain its asymptotic behavior using Weyl's law.

The idea behind Weyl's law comes from some of the basic principles of Fourier analysis. A function with a small extension in space necessarily has a large extension in spatial frequency, and vice versa. For a wave's Fourier transform to be supported on a single frequency, it must be spread out on the entire domain. This is the idea behind the uncertainty principle.

Every eigenfunction, due to their orthogonality, occupies a box of size of order one in phase space, i.e. sets where $|x - x_0| < \delta$ and $|k - k_0| < \delta^{-1}$. Calculating the volume of the subset of phase space where the energy is less than a certain value E should give the counting function $N(E)$, as this subset should be able to fit in $N(E)$ boxes of size 1. This especially works asymptotically at high values of energy [74, 19, 37]:

$$N(E) \approx \frac{1}{(2\pi)^d} \iint_{H(\vec{x}, \vec{k}) \leq E} \mathrm{d}^d x \mathrm{d}^d k. \tag{1.29}$$

If one considers a Hamiltonian of the form $H = \frac{\hbar^2 k^2}{2m} + V(x)$, the double integral reduces to a single integral in the following way:

$$N_V \equiv \frac{1}{(2\pi)^d} \iint_{\frac{\hbar^2 k^2}{2m} + V(x) \leq E} \mathrm{d}^d x \mathrm{d}^d k. \tag{1.30}$$

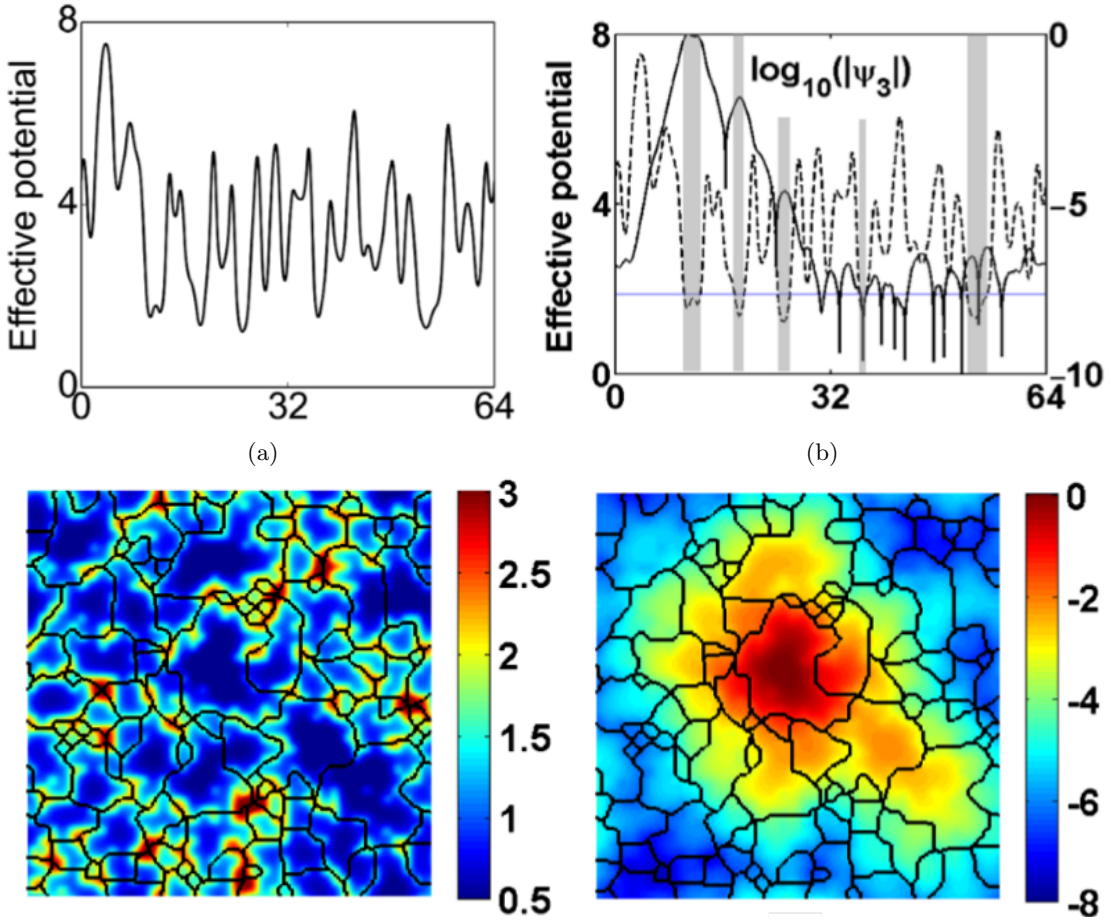

Figure 1.17: (a) An effective confining potential in 1D. (b) The same effective confining potential in the background, with the third excited eigenstate in log scale. The horizontal blue line corresponds to the energy of the eigenfunction. The vertical gray bars correspond to the wells of W for this state, i.e. the areas where $E < W(x)$. (c) The effective confining potential in 2D. The boundaries correspond to the crests of the potential, and define localization regions. (d) The fundamental eigenfunction in log scale. The boundaries of the effective confining potential are featured as well. Reprinted from [11]

Which gives in 1D:

$$N_V = \frac{\sqrt{2m}}{\pi\hbar} \int_{V(x)\leq E} \sqrt{(E - V(x))_+}\, \mathrm{d}x. \tag{1.31}$$

As seen before, W operates as an effective potential energy with wells and barriers that delineate the localization sub-regions of the eigenfunctions. Using the effective confining potential instead of the original potential considerably improves the approximation given by Weyl's law [11], as can be seen in Figure 1.18, even at low energy. At higher energies, both laws are asymptotically equivalent to the integrated density of states.

We have seen that transforming the eigenvalue equation in order to exhibit the W term reveals another role of the landscape with many new properties. While, initially, most of these claims were only partially substantiated theoretically and mostly conjectural, many were also proven rigorously in a recent paper [10].

More recently, an even more powerful relationship between the localization landscape and the counting function has been unveiled [23]. For a given value E, let us divide the domain into d-cubes (intervals in 1D, squares in 2D, cubes in 3D...) of sidelength $1/\sqrt{E}$, which is the natural scaling of the Laplacian.

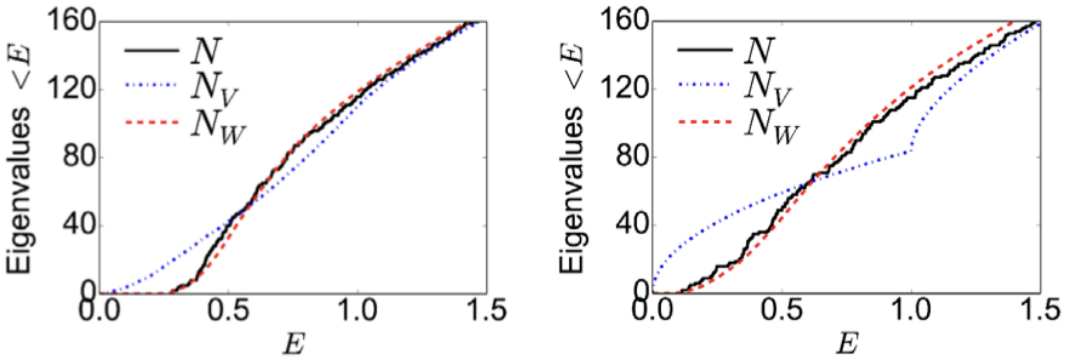

(a) (b)

Figure 1.18: (a) The counting function (or integrated density of states) of a continuous 1D system with random piecewise constant potential taking values uniformly in $[0, 1]$. The actual integrated density of states is displayed in black, the Weyl's law approximation with V in dashed blue lines, and the approximation with W in dashed red lines. (b) Similar but for a boolean potential taking values 0 and 1. Reprinted from [11]

We define the function $N_u(E)$ (which we will call the landscape law counting function) as the number of d-cubes where the minimum of W in that d-cube is smaller than E. In other words:

$$N_u(E) \equiv \left(\text{number of cubes of size } \frac{1}{\sqrt{E}} \text{ where } W \leq E \right). \tag{1.32}$$

This counting function has two important properties. First, throughout the spectrum, the expected value of the landscape law counting function satisfies a double inequality governing the expected value of the actual counting function:

$$C_5 N_u\left(C_6 E\right) \leq N(E) \leq N_u\left(C_4 E\right), \tag{1.33}$$

where the constants C_5 and C_6 depend only on the dimension and on the expectation value of the random potential, and C_4 only on the dimension. The optimal values of these constants are not known at the moment.

Secondly, the landscape law counting function allows to predict more precisely the behavior of the asymptotic scaling of the counting function near 0. In the case of a random piecewise constant potential with i.i.d variable following the same cumulative distribution function F, we obtain the inequality:

$$\gamma_3 E^{d/2} F(\tilde{c_P} E)^{\gamma_4 E^{-d/2}} \leq N(E) \leq \gamma_1 E^{d/2} F(c_P E)^{\gamma_2 E^{-d/2}} \text{ for } E < E^* \tag{1.34}$$

where E^*, c_P, γ_1, and γ_2 are constants depending on the dimension and on the expectation value of the random variable, and $\tilde{c_P}$, γ_3, and γ_4 are constants that only depend on the dimension.

Because of the presence of the cumulative distribution function, this inequality demonstrates the exact dependence of the Lifshitz tails on the random law. For instance, in the case of a uniform random law taking values in $[0, 1]$, the inequality gives:

$$\gamma_3 E^{d/2} e^{\gamma_4 E^{-d/2} \log E} \leq N(E) \leq \gamma_1 E^{d/2} e^{\gamma_2 E^{-d/2} \log E}, \tag{1.35}$$

while for a binary random law taking values 0 or 1 the inequality loses the logarithmic dependence on E inside the exponent:

$$\gamma_3 E^{d/2} e^{-\gamma_4 E^{-d/2}} \leq N(E) \leq \gamma_1 E^{d/2} e^{-\gamma_2 E^{-d/2}}. \tag{1.36}$$

Once again, the constants involved are not known as of yet, but nonetheless these inequalities provide the asymptotic behavior of the counting function. Furthermore, if these constants were to be either determined exactly by theory or approximated numerically, one would get closer to understanding the fine behavior of the Lifshitz tails.

IV.3 Remaining challenges for the localization landscape theory

The localization of waves is a very general phenomenon that can occur in many various types of systems, which can be classical or quantum [18, 51, 29, 30, 49]. One of the strengths of the localization landscape formalism is its adaptability to different equations [21, 30, 53]. One of the only requirements is the presence of a positive elliptic operator, which are abundant in electrostatics, wave mechanics and continuum mechanics.

The main question we will attempt to answer in this thesis is: what information does the localization landscape bring on the spatial and spectral structures of the eigenfunctions in a disordered potential?

These preceding sections have laid the foundation for the topics that this thesis will address:

- How do we accurately and reliably determine the sub-regions that actually host localized eigenfunctions?
- How do we predict the spectrum of the Hamiltonian in a disordered potential, asymptotically (near 0) or not?
- What can be said about the high energy behavior of the eigenstates?
- Finally, we will look at a deterministic example: the Aubry-André model.

Bibliography

[1] E. Abrahams. *50 Years of Anderson Localization*. World Scientific, 2010. doi:10.1142/7663.

[2] E. Abrahams, P. W. Anderson, D. C. Licciardello, and T. V. Ramakrishnan. Scaling theory of localization: Absence of quantum diffusion in two dimensions. *Phys. Rev. Lett.*, 42:673–676, 1979. doi:10.1103/PhysRevLett.42.673.

[3] S. Agmon. *Lectures on Exponential Decay of Solutions of Second-Order Elliptic Equations: Bounds on Eigenfunctions of N-Body Schrödinger Operations. (MN-29)*. Princeton University Press, 1982. URL: http://www.jstor.org/stable/j.ctt13x1d8z.

[4] E. Akkermans and R. Maynard. Weak localization of waves. *Journal de Physique Lettres*, 46(22):1045–1053, 1985. doi:10.1051/jphyslet:0198500460220104500.

[5] E. Akkermans and G. Montambaux. *Mesoscopic Physics of Electrons and Photons*. Cambridge University Press, 2007. doi:10.1017/CBO9780511618833.

[6] E. Akkermans, P. Wolf, R. Maynard, and G. Maret. Theoretical study of the coherent backscattering of light by disordered media. 49, 01 1988. doi:10.1051/jphys:0198800490107700.

[7] G. W. Anderson, A. Guionnet, and O. Zeitouni. *An Introduction to Random Matrices*. Cambridge Studies in Advanced Mathematics. Cambridge University Press, 2009. doi:10.1017/CBO9780511801334.

[8] P. W. Anderson. Absence of diffusion in certain random lattices. *Phys. Rev.*, 109:1492–1505, 1958. doi:10.1103/PhysRev.109.1492.

[9] D. N. Arnold, G. David, M. Filoche, D. Jerison, and S. Mayboroda. Computing spectra without solving eigenvalue problems. *SIAM J. Sci. Comput.*, 41:B69–B92, 2017. URL: https://arxiv.org/abs/1711.04888.

[10] D. N. Arnold, G. David, M. Filoche, D. Jerison, and S. Mayboroda. Localization of eigenfunctions via an effective potential. *Commun. Part. Diff. Eq.*, 44(11):1186–1216, 2019. doi:10.1080/03605302.2019.1626420.

[11] D. N. Arnold, G. David, D. Jerison, S. Mayboroda, and M. Filoche. Effective confining potential of quantum states in disordered media. *Phys. Rev. Lett.*, 116:056602, 2016. doi:10.1103/PhysRevLett.116.056602.

[12] N. Ashcroft and N. Mermin. *Solid State Physics*. Saunders College Publishing, Fort Worth, 1976. URL: https://www.bibsonomy.org/bibtex/27759092df316587a126f200107b24a85/brouder.

[13] S. Aubry and G. André. Analyticity breaking and Anderson localization in incommensurate lattices. *Ann. Isr. Phys. Soc.*, 3:133–164, 1980.

[14] M. Benderskii and L. Pastur. On the spectrum of the one-dimensional Schrödinger equation with a random potential. *Mat. Sb.*, 11:245–256, 1970. doi:10.1070/SM1970v011n02ABEH002068.

[15] G. Bergmann. Weak localization in thin films: a time-of-flight experiment with conduction electrons. *Physics Reports*, 107(1):1–58, 1984. doi:https://doi.org/10.1016/0370-1573(84)90103-0.

[16] J. Billy, V. Josse, Z. Zuo, A. Bernard, B. Hambrecht, P. Lugan, D. Clément, L. Sanchez-Palencia, P. Bouyer, and A. Aspect. Direct observation of Anderson localization of matter waves in a controlled disorder. *Nature*, 453:891–4, 2008. doi:10.1038/nature07000.

[17] J. Bourgain. Anderson localization for quasi-periodic lattice Schrödinger operators on $\mathbb{Z}^d$, d arbitrary. *Geo. and Func. Anal.*, 17(682), 2007. doi:https://doi.org/10.1007/s00039-007-0610-2.

[18] X. Boutillon and K. Ege. Vibroacoustics of the piano soundboard: Reduced models, mobility synthesis, and acoustical radiation regime. *J. Sound Vib.*, 332(18):4261 – 4279, 2013. doi:https://doi.org/10.1016/j.jsv.2013.03.015.

[19] T. Carleman. *Complete Works*. Malmo Litös, 1960.

[20] S. Chakravarty and A. Schmid. Weak localization: The quasiclassical theory of electrons in a random potential. *Physics Reports*, 140(4):193–236, 1986. doi:https://doi.org/10.1016/0370-1573(86)90027-X.

[21] Y. Chalopin, F. Piazza, S. Mayboroda, C. Weisbuch, and M. Filoche. Universality of fold-encoded localized vibrations in enzymes. *Scientific Reports*, 9, 2019. doi:10.1038/s41598-019-48905-8.

[22] J. Damon. *Properties of Ridges and Cores for Two-Dimensional Images*, volume 10. Kluwer Academic Publishers, 1999. doi:10.1023/A:1008379107611.

[23] G. David, M. Filoche, and S. Mayboroda. The landscape law for the integrated density of states. *arXiv*, 2019. URL: https://arxiv.org/abs/1909.10558.

[24] T. Devakul and D. A. Huse. Anderson localization transitions with and without random potentials. *Phys. Rev. B*, 96(214201), 2017. doi:http://dx.doi.org/10.1103/PhysRevB.96.214201.

[25] J. D. Dow and D. Redfield. Toward a unified theory of Urbach's rule and exponential absorption edges. *Phys. Rev. B*, 5:594–610, 1972. doi:10.1103/PhysRevB.5.594.

[26] P. Drude. Zur elektronentheorie der metalle. *Ann. Phys.*, 306(3):566–613, 1900. doi:10.1002/andp.19003060312.

[27] F. Evers and A. D. Mirlin. Anderson transitions. *Rev. Mod. Phys.*, 80:1355–1417, 2008. doi:10.1103/RevModPhys.80.1355.

[28] G. M. Falco, A. A. Fedorenko, J. Giacomelli, and M. Modugno. Density of states in an optical speckle potential. *Phys. Rev. A*, 82:053405, 2010. doi:10.1103/PhysRevA.82.053405.

[29] S. Félix, B. Sapoval, M. Filoche, and M. Asch. Enhanced wave absorption through irregular interfaces. *EPL*, 85(1):14003, 2009. doi:10.1209/0295-5075/85/14003.

[30] M. Filoche and S. Mayboroda. Strong localization induced by one clamped point in thin plate vibrations. *Phys. Rev. Letters*, 103:254301, 2009. doi:10.1103/PhysRevLett.103.254301.

[31] M. Filoche and S. Mayboroda. Universal mechanism for Anderson and weak localization. *Proc. Natl. Acad. Sci. USA*, 109(37):14761–14766, 2012. doi:10.1073/pnas.1120432109.

[32] M. Filoche, M. Piccardo, Y.-R. Wu, C.-K. Li, C. Weisbuch, and S. Mayboroda. Localization landscape theory of disorder in semiconductors. I. Theory and modeling. *Phys. Rev. B*, 95:144204, 2017. doi:10.1103/PhysRevB.95.144204.

[33] B. G. G. Lemarié and D. Delande. Universality of the Anderson transition with the quasiperiodic kicked rotor. *Europhys. Lett.*, 87:37007, 2009. doi:10.1209/0295-5075/87/37007.

[34] S. Ganeshan, K. Sun, and S. D. Sarma. Topological zero-energy modes in gapless commensurate Aubry-André-Harper models. *Phys. Rev. Lett.*, 110(180403), 2013. doi:https://doi.org/10.1103/PhysRevLett.110.180403.

[35] T. Guhr, A. Müller–Groeling, and H. A. Weidenmüller. Random-matrix theories in quantum physics: common concepts. *Phys. Rep.*, 299(4):189 – 425, 1998. doi:https://doi.org/10.1016/S0370-1573(97)00088-4.

[36] D. R. Hofstadter. Energy levels and wave functions of Bloch electrons in rational and irrational magnetic fields. *Phys. Rev. Lett.*, 14(6), 1976. doi:10.1103/PhysRevB.14.2239.

[37] L. Hörmander. The spectral function of an elliptic operator. *Acta Math.*, 121:193–218, 1968. doi:10.1007/BF02391913.

[38] S. Iyer, V. Oganesyan, G. Refael, and D. A. Huse. Many-body localization in a quasiperiodic system. *Phys. Rev. B*, 87:134202, 2013. doi:https://doi.org/10.1103/PhysRevB.87.134202.

[39] S. Jitomirskaya. Metal-insulator transition for the almost Mathieu operator. *Ann. of Maths.*, 150(3), 1999. URL: https://arxiv.org/abs/math/9911265.

[40] S. Jitomirskaya and W. Liu. Universal hierarchical structure of quasiperiodic eigenfunctions. *Ann. of Maths.*, 187(3), 2018. doi:https://doi.org/10.4007/annals.2018.187.3.3.

[41] M. Johansson and R. Riklund. Self-dual model for one-dimensional incommensurate crystals including next-nearest-neighbor hopping, and its relation to the Hofstadter model. *Phys. Rev. B*, 43(16), 1991. doi:10.1103/PhysRevB.43.13468.

[42] S. John, C. Soukoulis, M. H. Cohen, and E. N. Economou. Theory of electron band tails and the Urbach optical-absorption edge. *Phys. Rev. Lett.*, 57:1777–1780, 1986. doi:10.1103/PhysRevLett.57.1777.

[43] M. Kappus and F. Wegner. Anomaly in the band centre of the one-dimensional Anderson model. *Z. Phys.*, 45(1):15–21, 1981. doi:10.1007/BF01294272.

[44] W. Kirsch and B. Metzger. The integrated density of states for random Schrödinger operators. *in: F. Gesztesy, P. Deift, C. Galvez, P. Perry, W. Schlag (Editors): Spectral Theory and Mathematical Physics: A Festschrift in Honor of Barry Simon's 60th Birthday.*, page 649–696, 2007. doi:10.1090/pspum/076.2/2307751.

[45] W. Kirsch and B. Simon. Lifshitz tails for periodic plus random potentials. *J. Stat. Phys.*, 42:799–808, 1986. doi:10.1007/BF01010445.

[46] F. Klopp. Weak disorder localization and Lifshitz tails. *Comm. Math. Phys.*, 232:125–155, 2002. doi:10.1007/s00220-002-0727-y.

[47] F. Klopp. Weak disorder localization and Lifshitz tails: Continuous Hamiltonians. *Ann. Henri Poincaré*, 3:711–737, 2002. doi:10.1007/s00023-002-8633-6.

[48] B. Kramer and A. MacKinnon. Localization: theory and experiment. *Rep. Prog. Phys.*, 56(12):1469–1564, 1993. doi:10.1088/0034-4885/56/12/001.

[49] U. Kuhl, O. Legrand, and F. Mortessagne. Microwave experiments using open chaotic cavities in the realm of the effective Hamiltonian formalism. *Fortschritte der Physik / Progress of Physics*, 61(2 - 3):404 – 419, 2013. published online 2012-07-30. doi:10.1002/prop.201200101.

[50] W. König. *The Parabolic Anderson Model, Random Walk in Random Potential*. Pathways in Mathematics. Springer, 2016. URL: https://www.springer.com/gp/book/9783319335957#aboutBook.

[51] D. Laurent, O. Legrand, P. Sebbah, C. Vanneste, and F. Mortessagne. Localized modes in a finite-size open disordered microwave cavity. *Phys. Rev. Lett.*, 99:253902, 2007. doi:10.1103/PhysRevLett.99.253902.

[52] P. Lee and T. Ramakrishnan. Disordered electronic systems. *Rev. Mod. Phys.*, 57:287–337, 1985. doi:10.1103/RevModPhys.57.287.

[53] G. Lefebvre, A. Gondel, M. Dubois, M. Atlan, F. Feppon, A. Labbé, C. Gillot, A. Garelli, M. Ernoult, S. Mayboroda, M. Filoche, and P. Sebbah. One single static measurement predicts wave localization in complex structures. *Phys. Rev. Lett.*, 117:074301, 2016. doi:10.1103/PhysRevLett.117.074301.

[54] X. Li, X. Li, and S. D. Sarma. Mobility edges in one-dimensional bichromatic incommensurate potentials. *Phys. Rev. B*, 96(085119), 2017. doi:10.1103/PhysRevB.96.085119.

[55] I. Lifshitz. Structure of the energy spectrum of impurity bands in disordered solid solutions. *J. Exp. Theor. Phys.*, 17:1159–1170, 1963.

[56] I. Lifshitz. Energy spectrum structure and quantum states of disordered condensed systems. *Phys.-Uspekhi*, 7(4):549–573, 1965. doi:10.1070/pu1965v007n04abeh003634.

[57] R. Maynard, E. Akkermans, and P. Wolf. Coherent backscattering and weak localization phenomena in optics and in metals: Analogies and differences. Les Houches 1986 - Session XLVI: Chance and Matter, 1986. URL: https://phsites.technion.ac.il/eric/wp-content/uploads/sites/6/2013/07/SessionXLVI_1987.pdf.

[58] S. A. Molčanov. The structure of eigenfunctions of one-dimesional unordered structures. *Mathematics of the USSR-Izvestiya*, 12(1):69–101, 1978. doi:10.1070/im1978v012n01abeh001841.

[59] N. F. Mott. Conduction in glasses containing transition metal ions. *J. Non Cryst. Solids*, 1:1–17, 1968. doi:10.1016/0022-3093(68)90002-1.

[60] N. F. Mott. Conduction in non-crystalline materials. *Philos. Mag.*, 19(160):835–852, 1969. doi:10.1080/14786436908216338.

[61] C. Müller and D. Delande. Disorder and interference: localization phenomena. Les Houches 2009 - Session XCI: Ultracold Gases and Quantum Information, 2010. doi:10.1093/acprof:oso/9780199603657.003.0009.

[62] L. Pastur and A. Figotin. *Spectra of Random and Almost-Periodic Operators*. Grundlehren der mathematischen Wissenschaften. Springer, 1992. URL: https://www.springer.com/gp/book/9783642743481.

[63] M. Piccardo, C.-K. Li, Y.-R. Wu, J. S. Speck, B. Bonef, R. M. Farrell, M. Filoche, L. Martinelli, J. Peretti, and C. Weisbuch. Localization landscape theory of disorder in semiconductors. II. Urbach tails of disordered quantum well layers. *Phys. Rev. B*, 95:144205, 2017. doi:10.1103/PhysRevB.95.144205.

[64] G. Roati, C. D'Errico, L. Fallani, M. Fattori, C. Fort, M. Zaccanti, G. Modugno, M. Modugno, and M. Inguscio. Anderson localization of a non-interacting Bose-Einstein condensate. *Nature*, 453(7197):895–U36, 2008. doi:10.1038/nature07071.

[65] L. Sanchez-Palencia, D. Clément, P. Lugan, P. Bouyer, G. V. Shlyapnikov, and A. Aspect. Anderson localization of expanding Bose-Einstein condensates in random potentials. *Phys. Rev. Lett.*, 98:210401, 2007. doi:10.1103/PhysRevLett.98.210401.

[66] B. Shklovskii, B. Shapiro, B. Sears, P. Lambrianides, and H. Shore. Statistics of spectra of disordered systems near the metal-insulator transition. *Phys. Rev. B*, 47:11487–11490, 1993. doi:10.1103/PhysRevB.47.11487.

[67] B. Simon. Lifschitz tails for the Anderson model. *J. Stat. Phys.*, 38(1-2):65–76, 1985. doi:10.1007/BF01017848.

[68] K. Slevin and T. Ohtsuki. Corrections to scaling at the Anderson transition. *Phys. Rev. Lett.*, 82:382–385, 1999. doi:10.1103/PhysRevLett.82.382.

[69] M. J. Stephen and E. Akkermans. Transport properties of an incommensurate system. *Phys. Rev. B*, 33:3837–3843, 1986. doi:10.1103/PhysRevB.33.3837.

[70] D. Thouless. Electrons in disordered systems and the theory of localization. *Phys. Rep.*, 13:93–142, 1974. doi:10.1016/0370-1573(74)90029-5.

[71] D. Thouless. Introduction to localization. *Phys. Rep.*, 67(1):5 – 8, 1980. doi:https://doi.org/10.1016/0370-1573(80)90072-1.

[72] F. Urbach. The long-wavelength edge of photographic sensitivity and of the electronic absorption of solids. *Phys. Rev.*, 92:1324–1324, 1953. doi:10.1103/PhysRev.92.1324.

[73] D. Vollhardt and P. Wölfle. Chapter 1 - Self-consistent theory of Anderson localization. In W. Hanke and Y. Kopaev, editors, *Electronic Phase Transitions*, volume 32 of *Modern Problems in Condensed Matter Sciences*, pages 1 – 78. Elsevier, 1992. doi:https://doi.org/10.1016/B978-0-444-88885-3.50006-8.

[74] H. Weyl. Ramifications, old and new, of the eigenvalue problem. *Bull. Amer. Math. Soc.*, 56(2):115–139, 1950. URL: https://projecteuclid.org:443/euclid.bams/1183514553.

[75] E. P. Wigner. Characteristic vectors of bordered matrices with infinite dimensions. *Ann. Math.*, 62(3):548–564, 1955. URL: http://www.jstor.org/stable/1970079.

Chapter 2

Extracting the spatial structure of localization

I The sub-regions of localization

One feature of the localization landscape is to provide a deterministic method for approximating the eigenfunctions and eigenvalues of a given realization of disorder [2, 3, 8, 9]. In these papers, the localization landscape has been found to define sub-regions where localization occurs. The authors used the valley lines of the localization landscape to define these sub-regions in two dimensions.

Let us recall the fundamental property of the localization landscape, i.e. $|\psi(x)| \leq E\ u(x)$ for a given eigenfunction ψ of eigenvalue E. For this specific eigenpair, the eigenfunction is only bound in the surfaces (in 2D) or volumes (in 3D) where $u(x) \leq 1/E$ (these surfaces or volumes are also called sublevel sets).

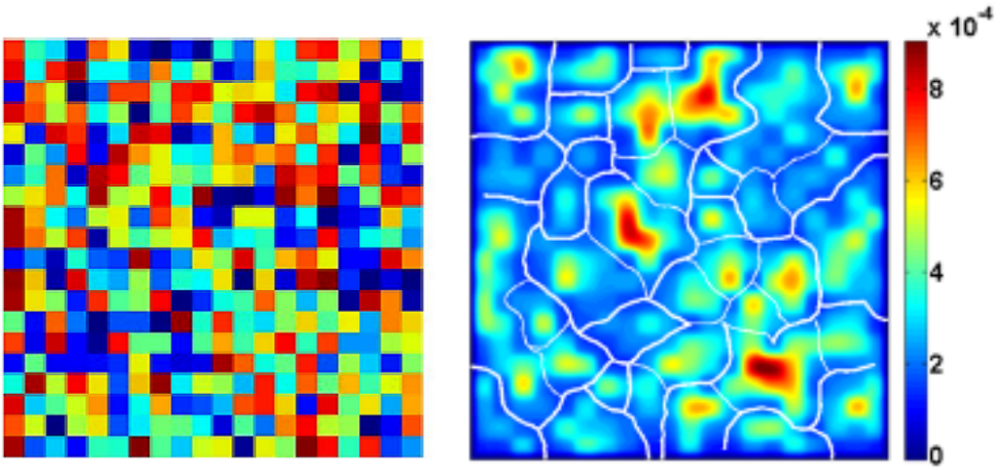

(a) (b)

Figure 2.1: Example of a random potential and its localization landscape. (a) The domain is divided in 20×20 elementary square cells. The potential is piecewise constant taking values according to a uniform random law between 0 and 8000. (b) The localization landscape determined from the potential. The valley line network of the localization landscape delineates the different sub-regions of localization for a certain eigenpair (ψ, E). Reprinted from [9].

Through the localization landscape inequality, the various eigenfunctions are compelled to be small along the lines (in 2D) or surfaces (in 3D) where u is locally minimal. These lines or surfaces are defined as the valleys of the landscape. They form a network that is the basis for understanding the localization

properties of the operator. Figure 2.1 depicts the valley line network. This network partitions the domain into disjoint regions, as can be seen in Figure 2.1.

We define $\mathcal{N}(E)$ the effective valley network at energy E [8], as the subset of the valley line network (in 2D) where $1/u(x) \leq E$. The effective valley network shows how the valley line network opens up as the energy increases, as can be seen in Figure 2.2. With increasing energy, the various sub-regions defined by the network merge. For each eigenpair, there is an associated effective valley network, and thus a specific partition of the domain consisting in more or less large sub-regions of localization.

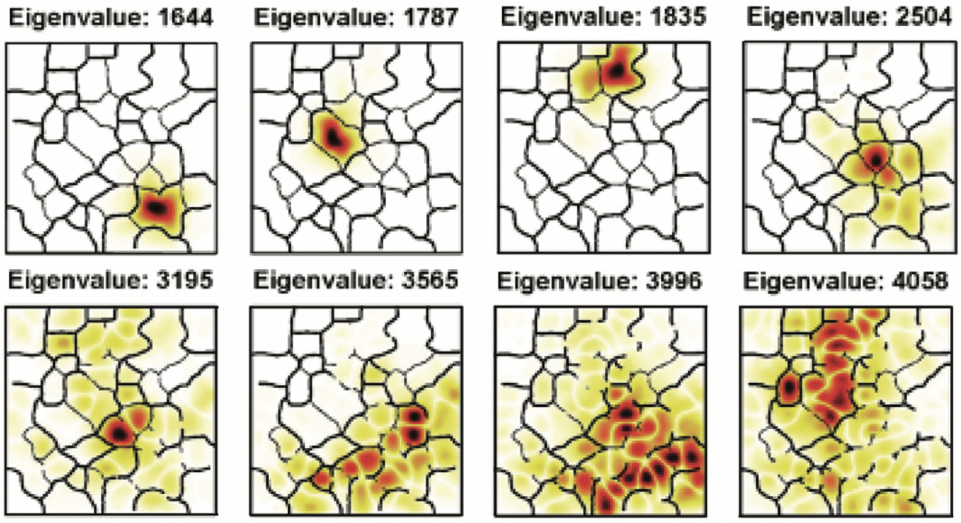

Figure 2.2: Representation of the evolving effective valley network for the same localization landscape as shown in Figure 2.1. 8 eigenfunctions are displayed (numbers 1, 2, 3, 11, 31, 45, 56, and 59). As the eigenvalue increases, the network opens up. Reprinted from [9].

Unfortunately, sub-regions defined this way do not always accurately depict the regions of localization. The reason for this is that this definition of sub-regions does not consider whether the effective confining potential is deep enough to host a localized stationary wave. Indeed, if a sub-region defined this way is very "shallow" (we will clarify and define this notion more precisely later on), we can see that no eigenfunction can be hosted by such a sub-region.

In this chapter we will first present the algorithm we have developed for determining the localization sub-regions. To this end, we start by looking at an algorithm that finds the valley line network, called the *watershed* algorithm. We then find and implement a criterion that determines whether a sub-region defined by the valley line network is capable of hosting a localized eigenfunction. Then, we construct a procedure that merges small sub-regions together so that the newly formed sub-regions may be able to host localized eigenfunctions. And finally, the last step of our algorithm is to eliminate excess sub-regions that, even after the merging procedure, are still unable to host a localized eigenfunction.

We will then assess the effectiveness of this new algorithm quantitatively. And finally, we will look at a real case of the implementation of this algorithm for a complicated domain shape.

In the following we will mainly work with the effective confining potential instead of the localization landscape. Since W is the reciprocal of u, finding the valley line network of the landscape is the same as finding the crest line network of the effective confining potential.

II The watershed algorithm

II.1 The initial watershed

II.1.a Basic principles

The most commonly used algorithm in image processing to segment an image into different parts is the *watershed* algorithm [6]. To understand how it works and the reason for this name, the reader should envision a graphical representation of a function with one variable ($y = f(x)$). Then, the reader should imagine a water source flooding each local minimum. When the various pools growing around each minimum meet, the boundaries define the borders and therefore the sub-regions as well.

For more clarity, here is a one-dimensional example of how the algorithm operates:

- First, the local minima of the function must be identified and labeled differently. In this example, we use three different colors, red, blue, and green, to label the local minima. These local minima are the starting points of the sub-regions that are to be constructed (see figure 2.3).

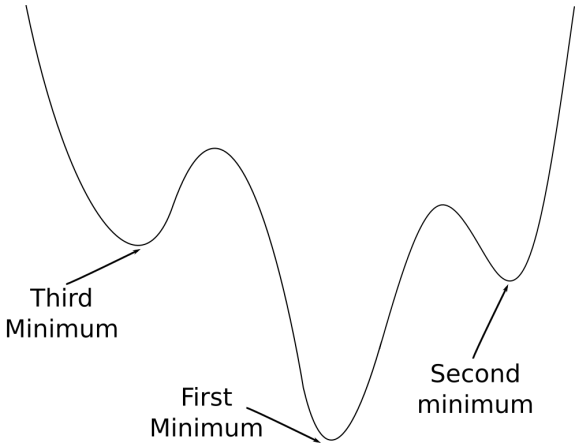

Figure 2.3: Identify and label the local minima.

- Next, the level of water is slowly raised so that all neighboring points with a value of the function smaller than the "level of water" are labeled as well. (hence the name, watershed). In practice, this means going through the neighboring points of the local minima and labeling them the same way as their local minimum, defining the beginning of a sub-region. We then repeat this process by considering the neighboring points of the set of points we have just defined (see Figure 2.4c).
- As these differently labeled sets of points increase in size, the points at which the sets meet define the barriers between the future sub-regions (see figure 2.4e). These points are labeled differently then the other points so as to mark them as barrier points. In practice, once a point has been labeled, it cannot be labeled differently.
- Finally, once the algorithm is finished, all of the points of the domain have been labeled. Each set of points with the same label defines a sub-region. The points that have been labeled as barrier points separate the different sub-regions. These are also known as border points, or crest points.

In the domain of image processing, there are different methods that can be employed to reduce over-segmenting, but no method is clearly better than the other. In our case, we have to develop a method in order to answer the specific problems at hand, i.e. determining the sub-regions of wave localization.

One has two options to reduce over-segmenting. The first method is to reduce the number of sub-regions identified at the start of the procedure. This can be done in different ways. For example, one can search for local minima that are minima on larger sets of points. One can also impose a minimal distance between two different starting points. The easiest way is to manually exclude local minima from the list of starting points until the resulting partition of the domain looks satisfactory. The second method is to merge the different sub-regions together depending on a specific criterion at the end of the procedure. These two methods are not exclusive.

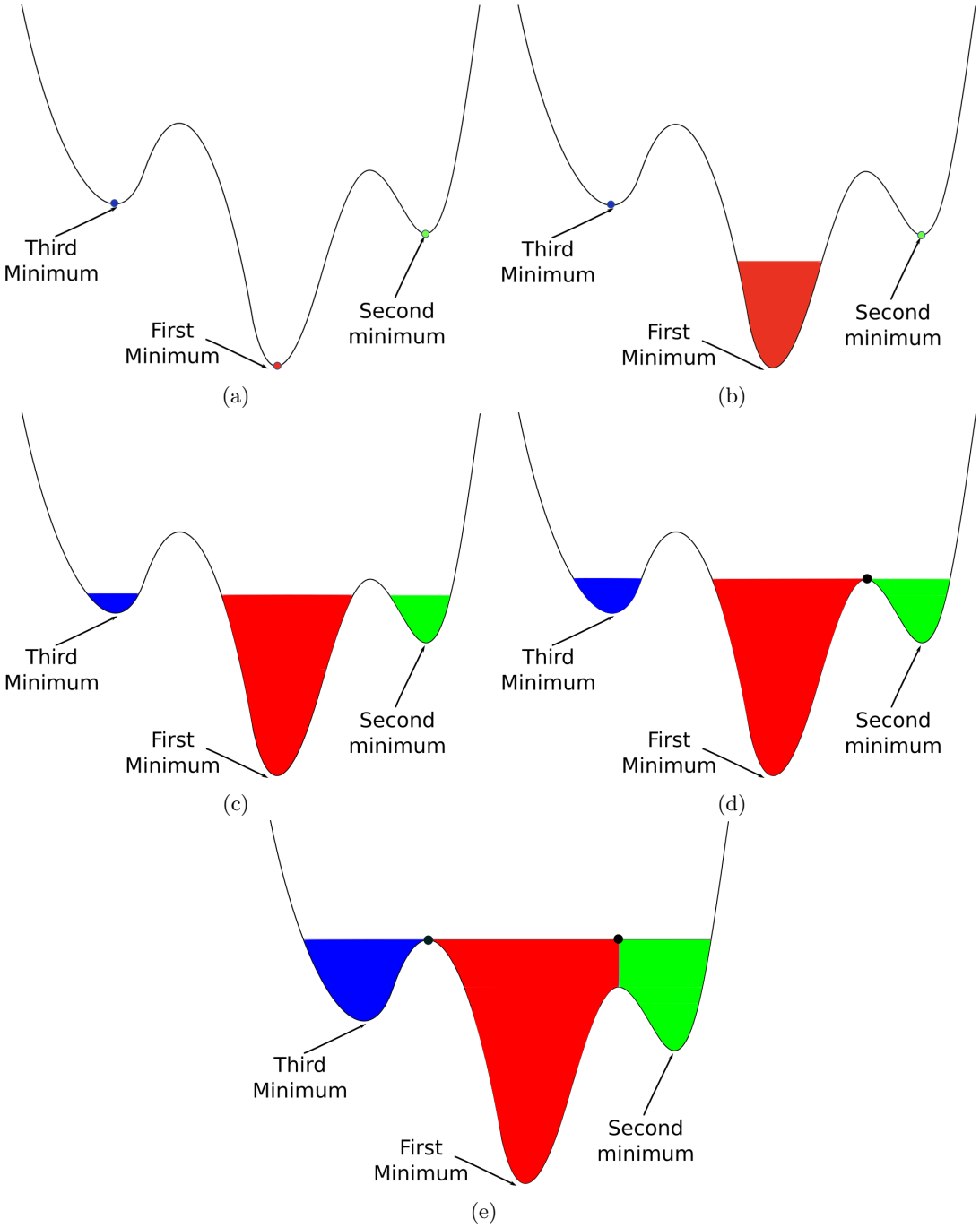

Figure 2.4: The different steps of the algorithm. (a) First the minima are labeled. (b) Then the water level is raised. All points under this level are labeled (painted) in the same way as the neighboring local minimum. (b) As the level rises, sets of points are labeled differently. (d) When two sets of points meet, they define a barrier between them. (e) The water level is raised until all the barriers have been defined.

For the purpose of this thesis, we have exclusively studied the merging of the sub-regions, as we had a physical criterion to do so. Let us first see how a standard watershed algorithm partitions the domain.

II.1.b Results of the basic watershed

In this chapter, we will be studying a 2D system since interesting topological problems arise above (and including) 2 dimensions. In 1D it is quite trivial to determine local minima and maxima and define

sub-regions of localization. In dimension larger than 1, the shapes of the sub-regions can become more complex.

For our simulations, we consider piece-wise $L \times L = 50 \times 50$ periodic 2D random potentials with cells of side-length 1 (see Figure 2.5a). We use two different potentials, the first one following a uniform law taking values in the interval $[0; V_{\max}]$, and the second following a Boolean law taking values in $\{0, V_{\max}\}$ with $V_{\max} \in \{4, 8, 12\}$. We then compute the landscape using the programming language FreeFem++ [12], via a finite element method. The landscape is approximated on a basis of P1 functions. For the mesh, we choose as basic elements triangles defined by squares of size $h \times h = 0.2 \times 0.2$ then divided in two. The number of degrees of freedom of our system is therefore $N = L \times L \times h^{-2} = 50 \times 50 \times 25 = 62500$. The potential is represented in Figure 2.5a.

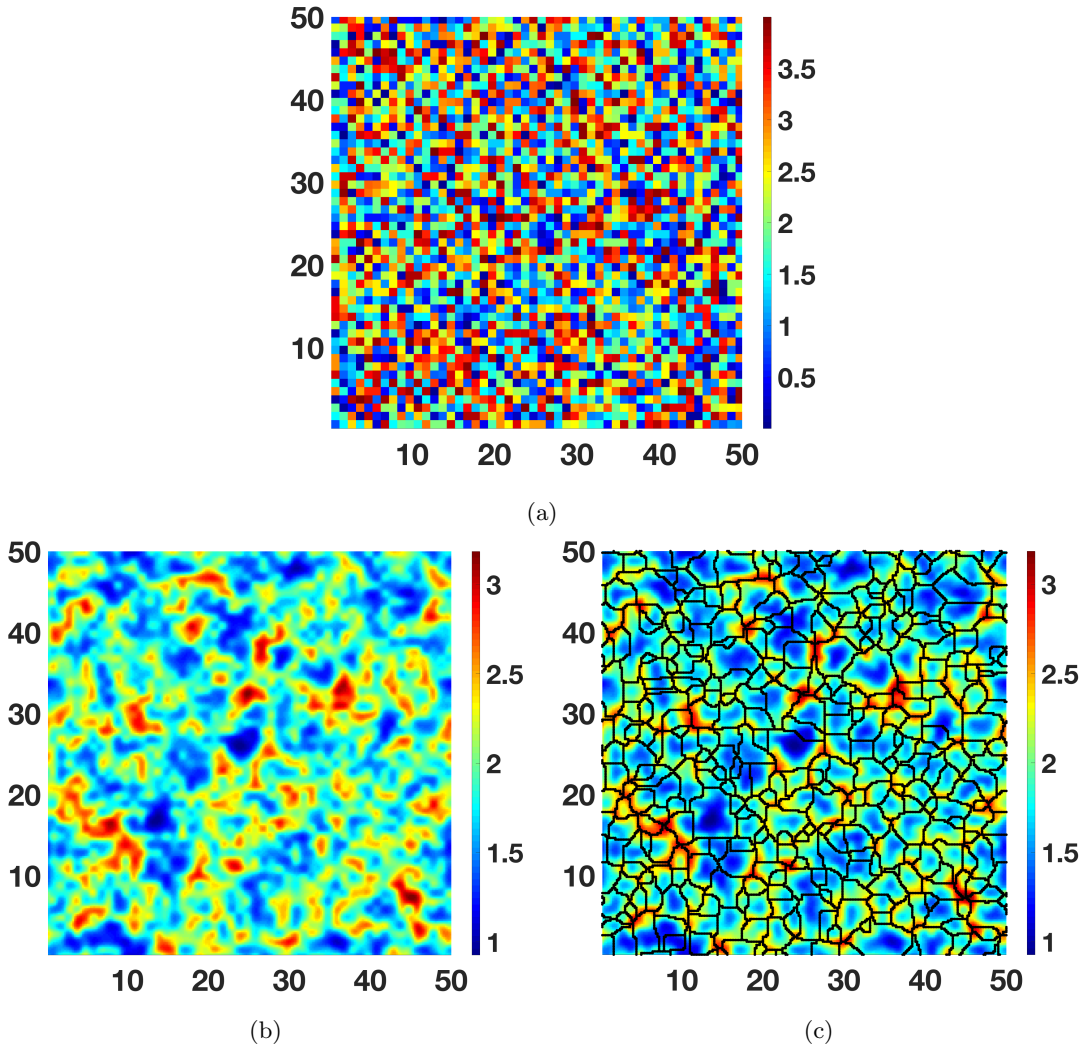

Figure 2.5: (a) Example of a potential following a uniform random law taking values in $[0, 4]$. (b) The effective confining potential of the corresponding potential. (c) The same effective confining potential with the boundaries computed from the standard watershed algorithm.

We have also imposed periodic boundary conditions in order to avoid boundary effects. The resulting effective confining potential is shown in Figure 2.5, with the initial result of the watershed algorithm.

At first glance, the resulting partition in Figure 2.6b appears far too segmented. The superimposed eigenfunctions are clearly localized, but the algorithm does not always properly identify their localization sub-regions. For instance, in the example above, the first, second, and fourth eigenfunctions lie in their localization sub-region, while the third and fifth do not. The origin of this problem lies in the small fluctuations (ripples) of the effective confining potential that can be observed in Figure 2.7, which is a 3D topographical view of the effective confining potential with the partition of the domain computed from

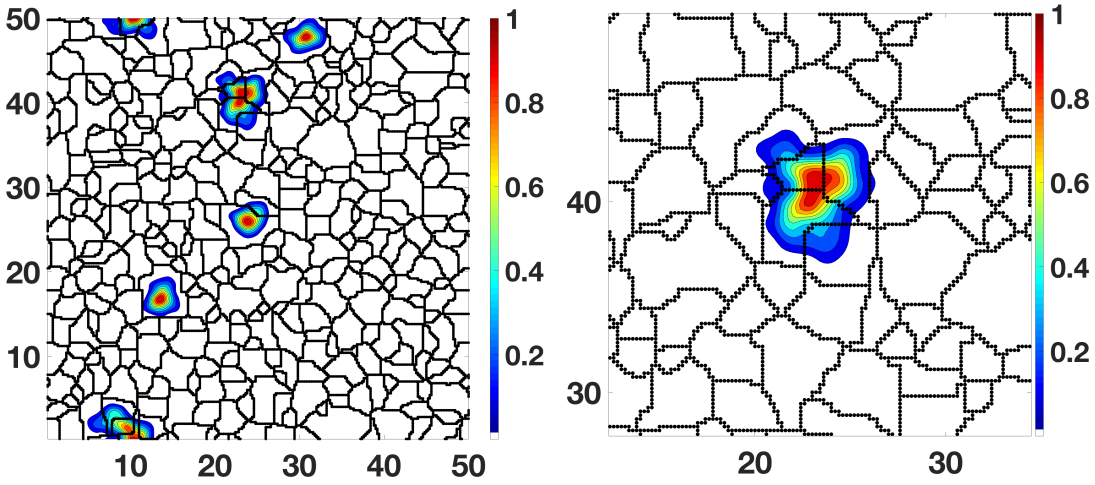

(a) (b)

Figure 2.6: (a) The five first eigenfunctions are displayed on top of the network of sub-regions defined by the watershed algorithm. The coordinates of the maximum of each consecutive eigenfunction are: $\{23.8; 26\}$, $\{13.6; 16.8\}$, $\{10.4; 50.0\}$, $\{30.8; 47.8\}$, $\{23.2; 41.2\}$. Their eigenvalues are respectively: 1.40, 1.41, 1.48, 1.51, 1.55. (b) A close-up look at the fifth eigenfunction. Its sub-region of localization has clearly been over-segmented into multiple sub-regions.

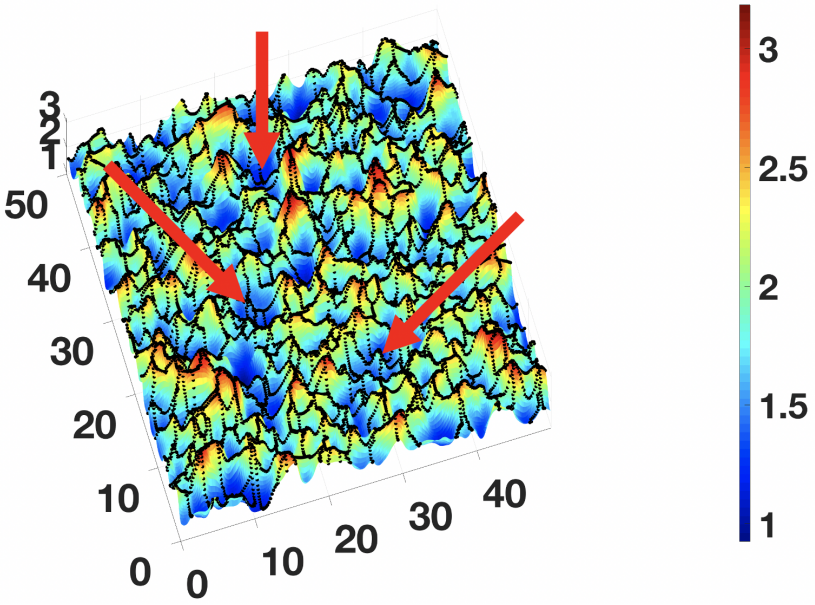

Figure 2.7: A 3D view of the effective confining potential and the borders defined by the watershed algorithm. The arrows point towards the large basins that have been over-segmented into multiple sub-regions due to small fluctuations and ripples of the effective confining potential.

the watershed algorithm. One observes large basins that should clearly host a localization sub-region, but they have been over-segmented into many sub-regions.

The next step is to find an effective protocol to merge the initial sub-regions found by the watershed algorithm.

II.2 Merging the sub-regions

II.2.a First implementation

We will use the image of a quantum particle in an effective potential to assist us. For a quantum particle to be trapped in a well of the effective confining potential, its energy must be smaller that the potential barriers surrounding it. Since the barriers are thick, we assume that tunneling effects can be neglected at this stage.

How do we express this idea quantitatively? The localization landscape formalism fortunately provides a good estimate for an eigenfunction's eigenvalue, dependent on the local minimum of the effective confining potential in that sub-region [2]:

$$E_0^i \approx (1 + \frac{d}{4}) \min_{\Omega_i} W. \tag{2.1}$$

Therefore, for a potential well to contain an eigenfunction, the crest points bordering the potential well must all be larger than the eigenvalue of the fundamental mode of that sub-region, which is equal to $(1 + \frac{d}{4})$ times the local minimum of the effective confining potential. Mathematically, the condition is:

$$E_0^i < \min_{\partial\Omega_i}(W) \;\Rightarrow\; \min_{\Omega_i}(W) \times \left(1 + \frac{d}{4}\right) < \min_{\partial\Omega_i}(W)\,. \tag{2.2}$$

This condition allows us to formulate a criterion for merging the different sub-regions determined by the initial watershed algorithm. Figure 2.8 shows an example of a situation where two sub-regions separated by a small barrier are to be merged.

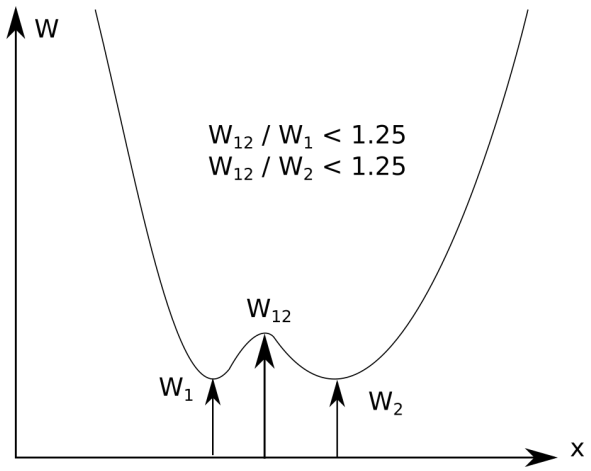

Figure 2.8: A ripple inside a 1D potential well. The two smaller wells inside the larger are unable to host an eigenfunction since the potential barrier separating them is too small.

The problem reduces to a graph where only the local minima of each sub-region $\min_{\Omega_i}(W)$ (which correspond to the nodes) and the minima on the crest along the shared border of the sub-regions $\min_{\partial\Omega_i \cap \partial\Omega_j}(W)$ (which correspond to the lines of the graph) are important. An example graph is depicted in Figure 2.9.

One may be tempted to simply merge sub-regions that are too "shallow" to host an eigenfunction with surrounding sub-regions. However, this approach not only is dependent on the order in which sub-regions are merged, but also causes small sub-regions to be merged with deep sub-regions that are already capable of hosting an eigenfunction, i.e. sub-regions where all of its crest points are larger than $(1 + \frac{d}{4})$ times the local minimum of the effective confining potential. The sub-regions are then much too large compared to the actual sizes of the localized eigenfunctions. This is the situation portrayed in Figure 2.10.

We therefore require that the condition 2.2 must be verified by both sub-regions in order to merge them together. The ratio between the lowest crest point on the border between two sub-regions and the local

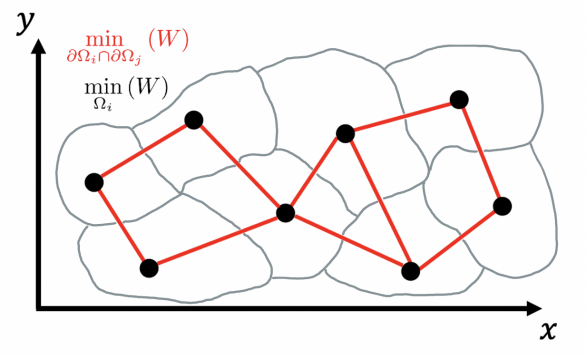

Figure 2.9: Example of a graph network for reducing the problem. The nodes correspond to $\min_{\Omega_i}(W)$ and the lines to $\min_{\partial\Omega_i \cap \partial\Omega_j}(W)$. The gray lines correspond to the borders between the sub-regions.

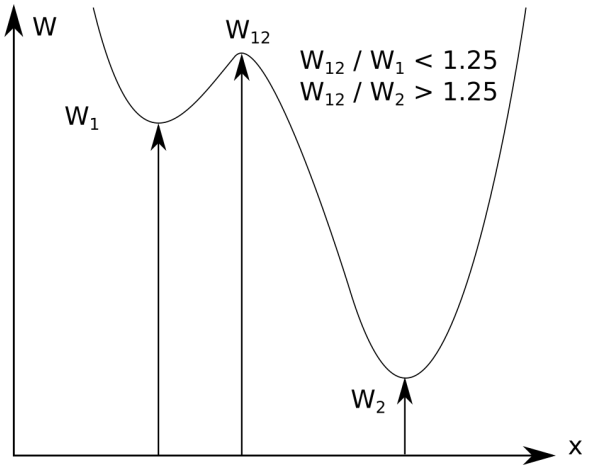

Figure 2.10: A deep 1D potential well bordered by a shallow 1D potential well. As the deep well is capable of hosting an eigenfunction, these two sub-regions are not to be merged.

minima must be smaller than $(1 + \frac{d}{4})$. This leads to the following criterion:

$$\frac{\min_{\partial\Omega_i \cap \partial\Omega_j}(W)}{\min_{\Omega_i}(W)} < 1 + \frac{d}{4}. \tag{2.3}$$

Using this principle, we can now devise an algorithm that proceeds through every sub-region, combining them with their neighbors if need be:

- First, we sort the sub-regions by increasing value of their local minima.
- Next, we create a function that links every pair of neighboring sub-regions to the minimum of their corresponding mutual border.
- We then iterate through all the sub-regions, comparing them with their neighbors according to the criterion. If it is met, we combine them, and put the sub-region back into the queue (see Figure 2.11).

The final result features less sub-regions, with some being very large (see Figure 2.12). The low energy eigenfunctions are now well contained in this new partition (see Figure 2.13).

The order in which the algorithm merges the sub-regions is important. Indeed, when two sub-regions are merged, the new local minimum is now defined as the smallest of the two former minima. So the sub-region with the greatest local minimum which would have been a priori able to merge with other sub-regions, is unable to merge now that it has been merged with a lower sub-region. See for example

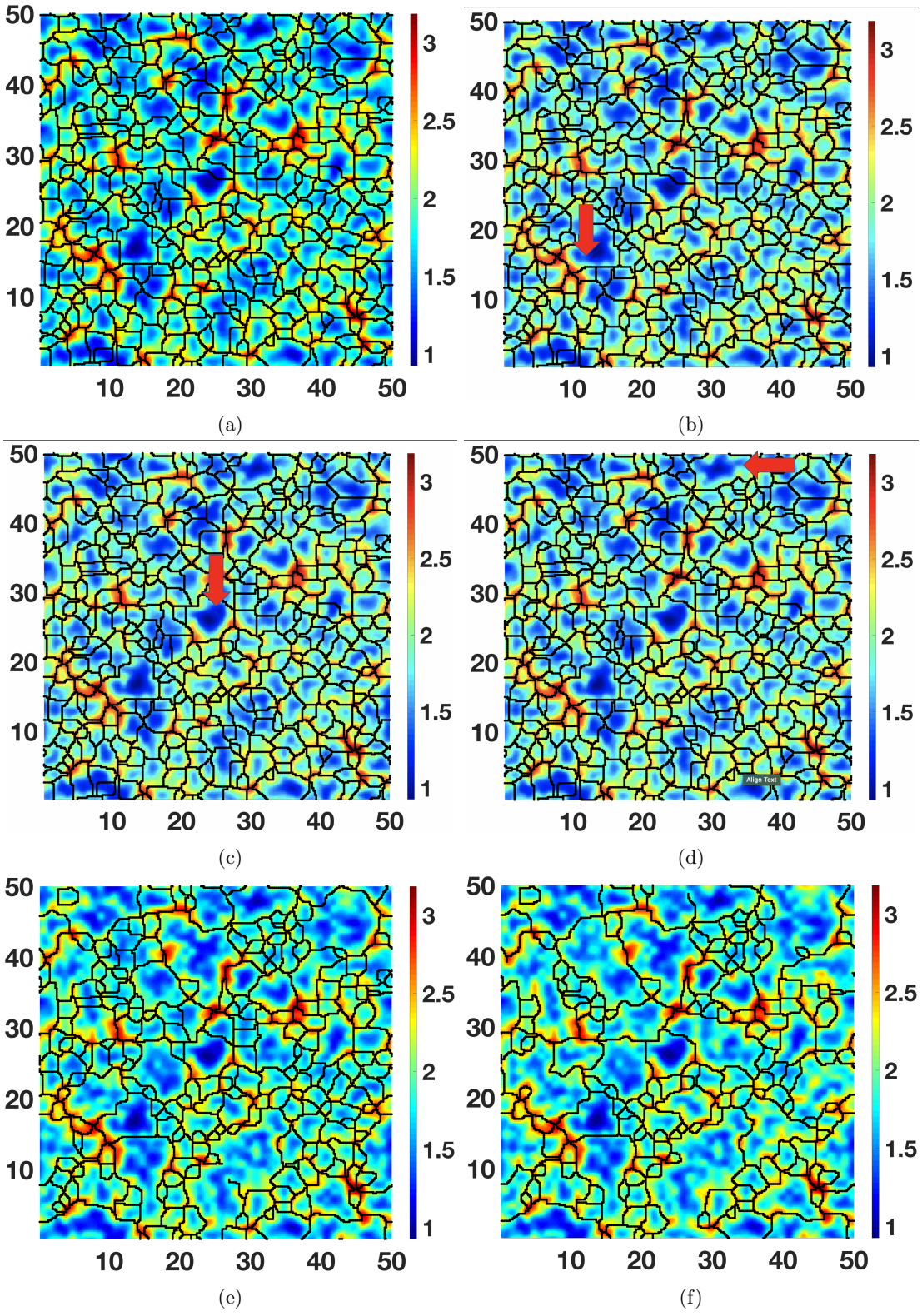

Figure 2.11: (a) The initial partition of the domain. (b) The first merge occurs at the sub-region of coordinates: $\{13.6; 16.8\}$. (c) The second merge occurs at the sub-region of coordinates: $\{23.8; 26\}$. (d) The third merge occurs at the sub-region of coordinates: $\{30.8; 47.8\}$. (e) The 50^{th} step of the algorithm. (f) The 100^{th} step of the algorithm.

the situation depicted in Figure 2.14. If the middle sub-region labeled 2 is first merged with the right sub-region labeled 3, it can then be merged with the left sub-region labeled 1. However, if we first merge

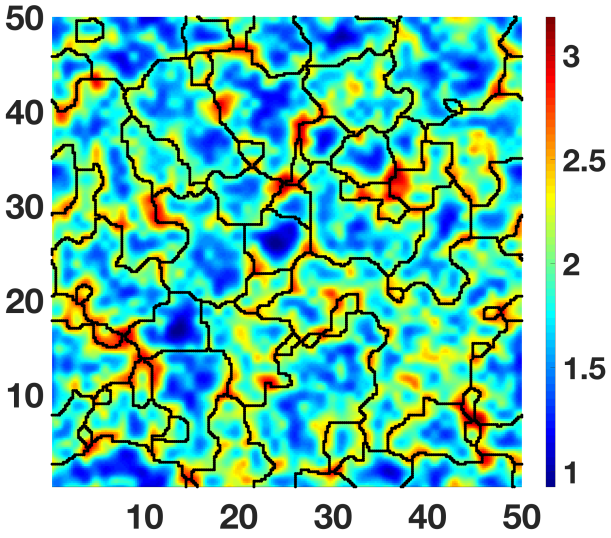

Figure 2.12: The final step of the merging process. The sub-regions are now much larger.

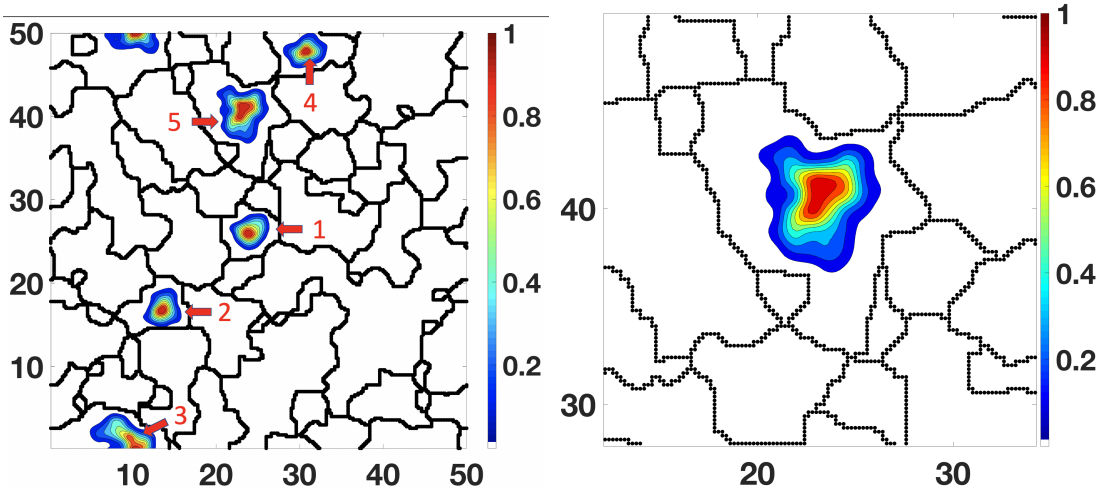

(a) (b)

Figure 2.13: (a) The five first eigenfunctions are displayed on top of the network of sub-regions defined by the watershed algorithm followed by the merging procedure. The coordinates of the maximum of each consecutive eigenfunction are: $\{23.8; 26\}$, $\{13.6; 16.8\}$, $\{10.4; 50.0\}$, $\{30.8; 47.8\}$, $\{23.2; 41.2\}$. Their eigenvalues are respectively: 1.40, 1.41, 1.48, 1.51, 1.55. (b) A close-up look at the fifth eigenfunction. The previously defined sub-regions of localization have been merged into one single sub-region fully encapsulating the eigenfunction.

the sub-regions 1 and 2, the sub-region 3 will be excluded.

Our goal is to devise an algorithm that accurately predicts the localization sub-regions. For this purpose, since the most localized eigenfunctions are those of lowest energy, we decided to first merge the sub-regions with the smallest local minima. This insures that the most confining sub-regions are the most accurately determined.

II.2.b Refining the merging condition

The merging procedure we just defined (see Figure 2.12) is quite lenient, in that two well defined sub-regions will be merged if only a single point on their common border dips under the criterion we decided. We would like to restrict the merging criterion slightly to avoid this situation.

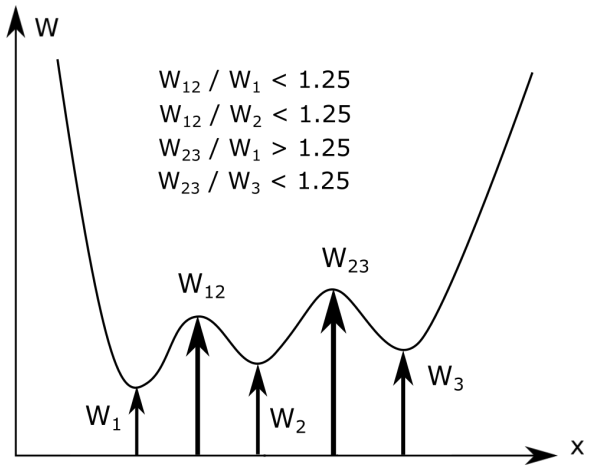

Figure 2.14: Three potential wells with different depths and different barrier heights separating them. Comparing them one on one, these wells meet the criterion to be merged. However, once sub-regions 1 and 2 have been merged, the last barrier separating the two remaining sub-regions is too high. The order of merging determines the final result.

The basis of the "$(1 + \frac{d}{4})$" condition is that an eigenfunction surrounded by a high enough potential barrier will be localized inside it. However, this is a classical view while the objects that we are confining are wave functions. From a wave perspective, we can consider that a wave cannot "escape" a confining potential through an aperture that is much smaller than its wavelength.

In order to account for this, instead of considering the minimum along a crest line, we consider the average over a certain number of points of the crest line around this minimum. This average is taken over a length that corresponds to the localization length of the localized eigenfunctions. For our example, this corresponds to a distance of 2 on the figures (which amounts to 10 points) and has been determined by measuring the size of the fundamental eigenfunction of the system. Qualitatively, this partition seems to produce sub-regions that are closer in size to the localized eigenfunctions that we have shown before (see Figure 2.15).

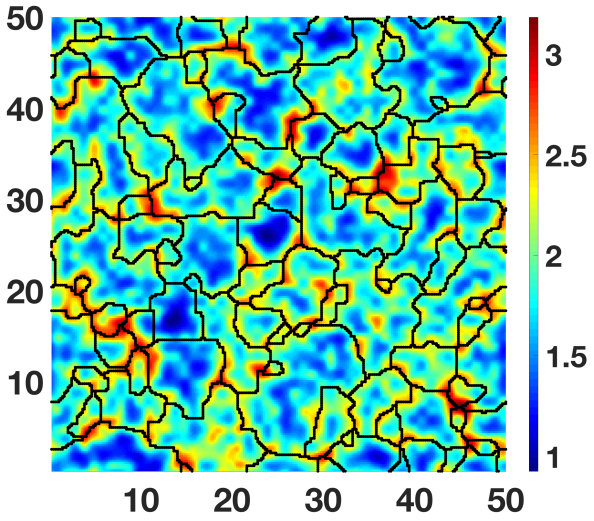

Figure 2.15: Result of the merging process while considering the average value of the crest line between two sub-regions around its minimum.

The low energy eigenfunctions seem to be well contained inside these sub-regions (see Figure 2.13a). Even as the energies of the eigenfunctions increase and the eigenfunctions start delocalizing on more than one sub-region, they stay contained inside the boundaries determined by the watershed algorithm.

The parameter governing the distance over which the crest line must be averaged around its minimum has been determined by computing the lowest energy eigenfunction and measuring its localization length.

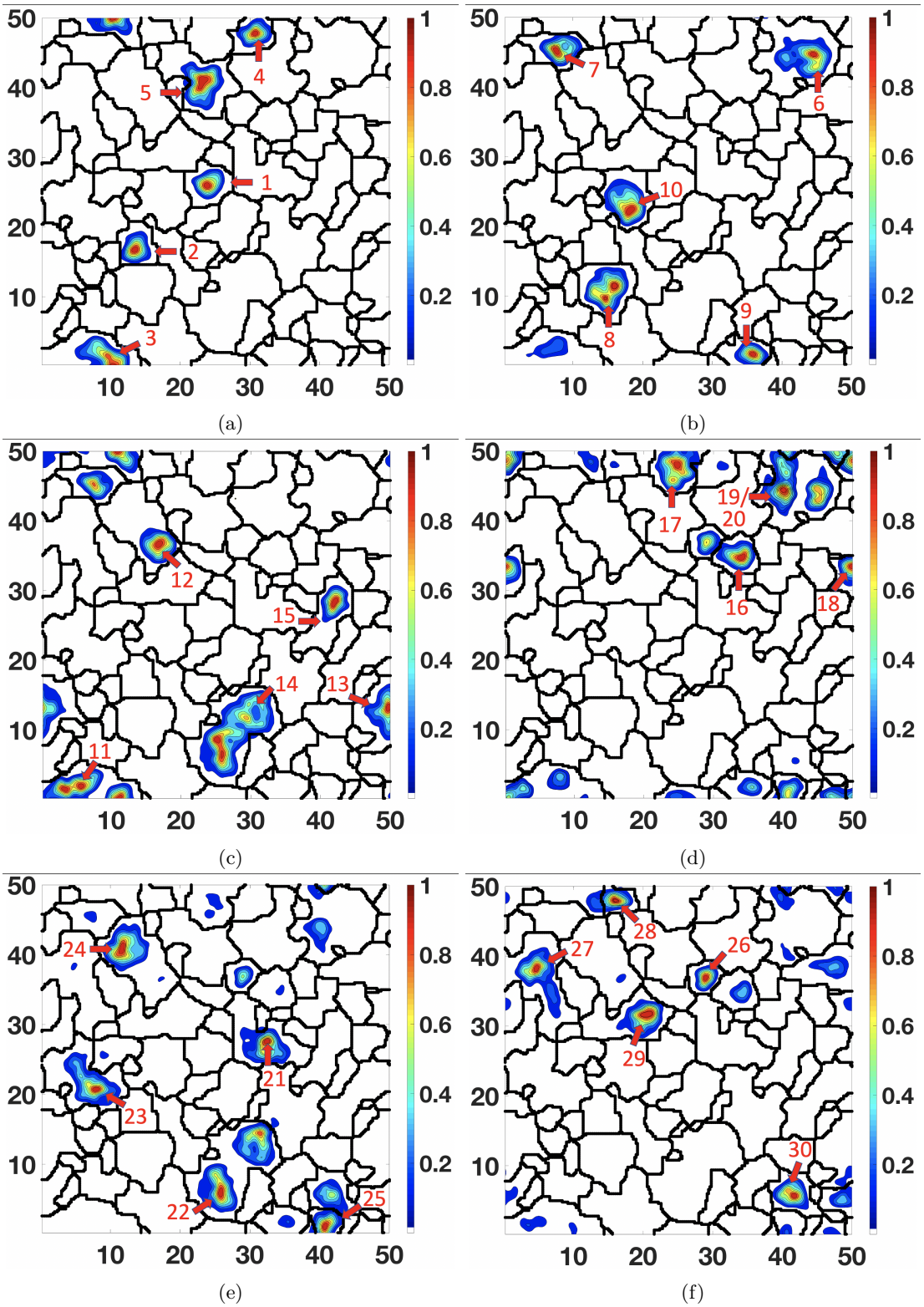

Figure 2.16: The 30 first eigenfunctions are represented 5 at a time. (a) Eigenvalues: 1.40, 1.41, 1.48, 1.51, 1.55. (b) Eigenvalues: 1.59, 1.62, 1.63, 1.64, 1.65. (c) Eigenvalues: 1.66, 1.68, 1.68, 1.70, 1.70. (d) Eigenvalues: 1.71, 1.72, 1.73, 1.74, 1.75. (e) Eigenvalues: 1.75, 1.75, 1.75, 1.78, 1.79. (f) Eigenvalues: 1.79, 1.81, 1.83, 1.84, 1.85.

Admittedly, we would rather not have to resort to computing eigenfunctions for this procedure, however in this model there is no prediction for the localization length which is not the case for other 2D models [11].

II.3 Eliminating excess sub-regions

One of the future goals of the localization landscape (that is not the objective of this thesis) is to establish a transport theory by hopping mechanism between the localization sub-regions. Hopping mechanisms between impurities is a very common method to model transport in disordered systems [5, 14, 15].

The idea behind this model is that, at low injection, the electrons hop from one localization sub-region to another when an electric field is applied. The various sub-regions defined by the partition of the domain form a network of sites upon which the electrons travel. The hopping probability could be defined in different ways such as depending on the height of the potential barrier separating the sub-regions, or from the Agmon distance between the sub-regions [4]. Our goal is therefore to define a network of sub-regions where each one is capable of hosting at least one localized eigenfunction, as in Figure 2.9.

The algorithm we have developed is effective in identifying the sub-regions of localization, but there are some disturbing features still present (which can be seen in Figure 2.15), namely that the partition defines tiny spurious sub-regions. These small sub-regions are very unlikely to host a localized eigenfunction as they are high in energy and the potential barrier surrounding them is low comparatively to their local minimum.

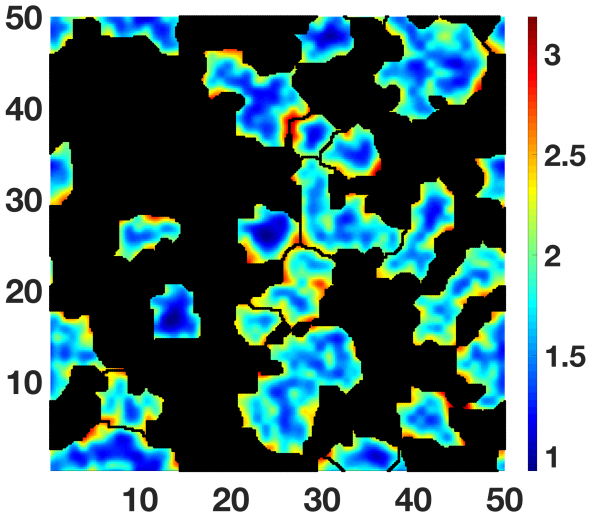

Figure 2.17: The result of removing the excess sub-regions. Compared to the actual sub-regions of localization (see Figure 2.13), many of them seem to be excluded although they host localized eigenfunctions.

We therefore want to eliminate these excess sub-regions from the graph network. In order to do so, for each node on the graph, we compare the ratio between its local minimum and the minimum of the border between it and its neighboring sub-regions ($\min_{\partial\Omega_i \cap \partial\Omega_j}(W)$) with the criterion $(1 + \frac{d}{4})$ (see Equation (2.3)). The minimum on a border between two sub-regions is calculated in the same way as before which means that the average around the minimum is the actual value that is considered.

Unfortunately, this has the effect of removing far too many sub-regions (see Figure 2.17). For instance, the seventh eigenfunction depicted in Figure 2.16b is clearly localized but its sub-region of localization has been grayed out by the algorithm.

The criterion must therefore be modified and relaxed to obtain the results we would expect. We consider three different criteria: the minimum, the average, or the maximum of the minima of the border points. Regarding the graph network, this corresponds to considering for each node either the minimum, the average, or the maximum of the links. In Figure 2.18, we have represented the results of the watershed using the average and the maximum of the links. This new criterion excludes less sub-regions. The topographic view shows that the sub-regions that have been excluded are those very high in energy that resemble plateaus.

Compared with the sub-regions occupied by the localized eigenfunctions (see Figure 2.13b), the new sub-regions match the locations where the eigenfunctions localize (see Figure 2.16). None of the excluded

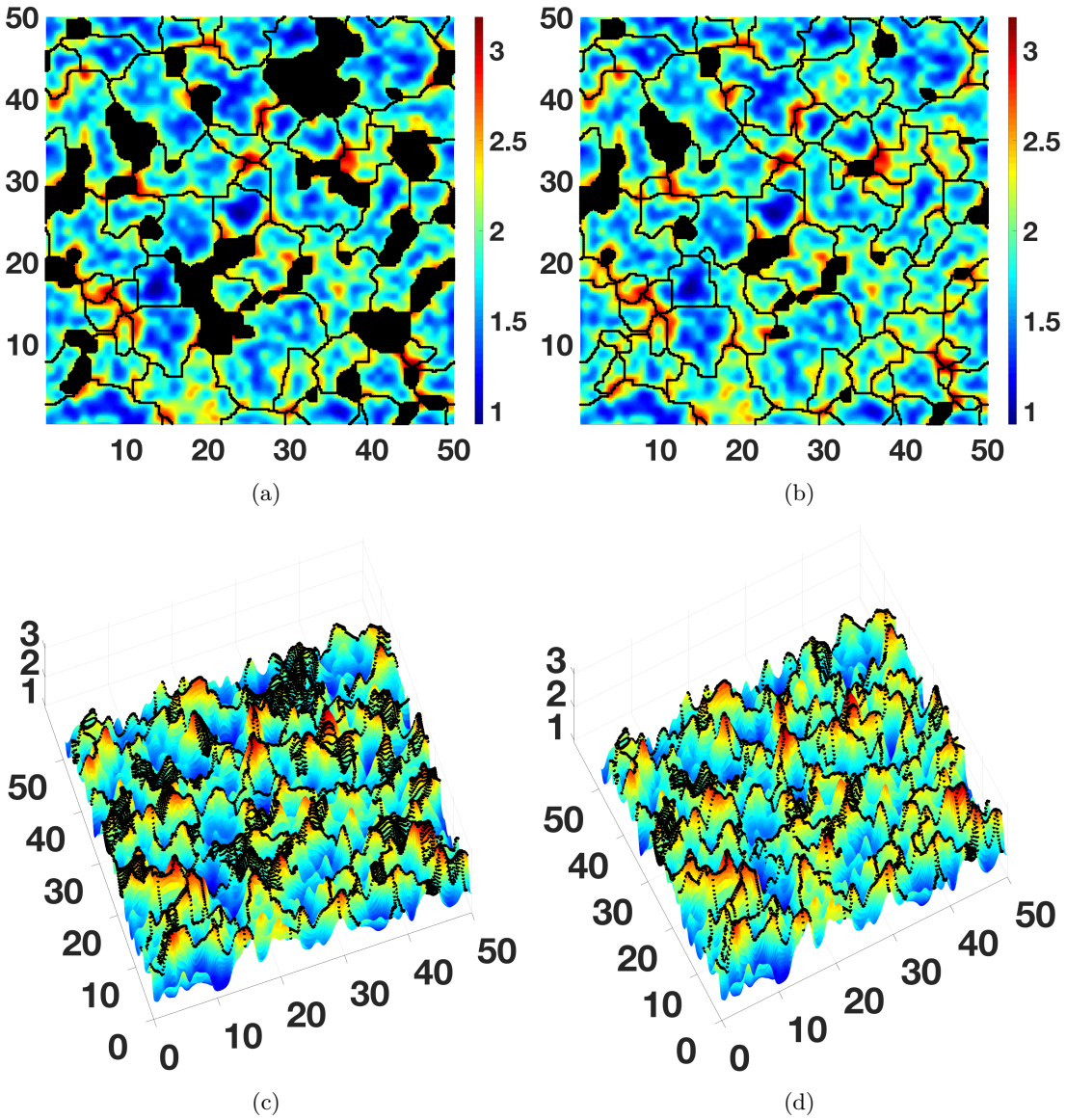

Figure 2.18: (a) Result of the exclusion process taking the average of the crest minima. (b) The result of the exclusion process taking the maximum of the crest minima. (c) Result of the exclusion process taking the average of the crest minima (topographic view). (d) Result of the exclusion process taking the maximum of the crest minima (topographic view).

sub-regions host any of the lowest energy eigenfunctions. Obviously, at high energy this is not true anymore as the localization length of the eigenfunctions becomes larger than the domain size. These two methods produce similar satisfying results. The criterion where we consider only the maximum of the crest minima excludes less sub-regions, but these extra sub-regions do not seem to be very relevant for the localization of eigenfunctions.

This concludes the presentation of the watershed algorithm before moving on to a quantitative assessment of its performance. To summarize, the algorithm starts in a very standard fashion by identifying and labeling the local minima. These minima define the candidate sub-regions. Then the domain is "flooded": points are added incrementally to the existing sub-regions. At the end of the procedure, the initial watershed lines are drawn. Next, the sub-regions are merged one after another according to the $(1 + \frac{d}{4})$ criterion, so that each final sub-region is capable of hosting an eigenfunction. And finally, some sub-regions are excluded according to the same criterion and following the same reasoning. This is the procedure we follow to determine the sub-regions of localization from the effective confining potential.

III Assessing the effectiveness of the algorithm

This new partition is qualitatively satisfying. We will now devise a way to quantitatively measure how effective a given partition is in regard to defining the sub-regions of localization. For this analysis, we will be using all aforementioned parameters (type of mesh, type of potential, etc.). We will vary the potential strength from 4 to 8 to 12, and use both random uniform and random binary laws.

Ideally, the size of the eigenfunctions should be at most the same size as the sub-regions. The standard way to measure the size over which the eigenfunction is localized is to use the participation ratio defined as

$$\mathrm{PR} = \frac{\left(\int |\psi|^2 \mathrm{d}x\right)^2}{|\Omega| \int |\psi|^4 \mathrm{d}x} \tag{2.4}$$

which we have normalized by the system size. We have:

$$\mathrm{PR} \approx \begin{cases} 1 & \text{delocalized} \\ \frac{\xi^d}{\Omega} & \text{localized} \end{cases}$$

Roughly speaking, the PR represents the fraction of the domain that is occupied by the eigenfunction. Therefore, when multiplied by the system size, it represents the size of the effective support of the eigenfunction.

We compute the participation ratios of the 50 first eigenfunctions for 10 different realizations of the random potential, and compare them with the sizes of the sub-regions determined by the watershed algorithm in Figure 2.19. We compare three different cases: the watershed without the merging procedure (Figure 2.19a), the full watershed using the average of the crest minima which we will call exclusion method 1 (Figure 2.19b), and the full watershed using the maximum of the crest minima which we will call exclusion method 2 (Figure 2.19c). The red line corresponds to the bissector of the plane, i.e., where the size of the eigenfunctions deduced from the PR are the same size as the sub-regions they are located in.

Let us first comment on the differences between the figures before and after the merging procedure. While it may seem that the original watershed produces sub-regions that are more likely to be the same size as the eigenfunctions, having points under the red curve is not satisfactory. The reason being that we do not want the algorithm to underestimate the size of the eigenfunctions, since this underestimation reduces the accuracy of the eigenfunction approximation obtained from the localization landscape ($\psi_0^i \approx \frac{u}{\|u\|}$ [10]). It is therefore better for the sizes of the sub-regions to be overestimated than underestimated. In that regard, the process of merging the sub-regions produces better results. The watershed underestimates the size of the sub-regions 47.8% of the time without the merging procedure, and only 8.8% and 8.2% with the merging procedures using the average and the maximum of the minima of the crest points respectively.

	Uniform random law			Binary random law		
$V_{\max}$	no merging	exclusion method 1 (average)	exclusion method 2 (maximum)	no merging	exclusion method 1 (average)	exclusion method 2 (maximum)
4	47.8%	8.8%	8.2%	12.2%	4.6%	4.6%
8	11.8%	2%	2%	1.2%	0.4%	0.4%
12	3%	0.2%	0.2%	0.4%	0.2%	0.2%

Table 2.1: The percentage of sub-regions underestimated by the different algorithms for various parameters.

Now comparing the merging procedures between them, the difference is small but significant. Indeed from Figure 2.19b we can see that the sizes of some sub-regions are evaluated at 0. This happens when

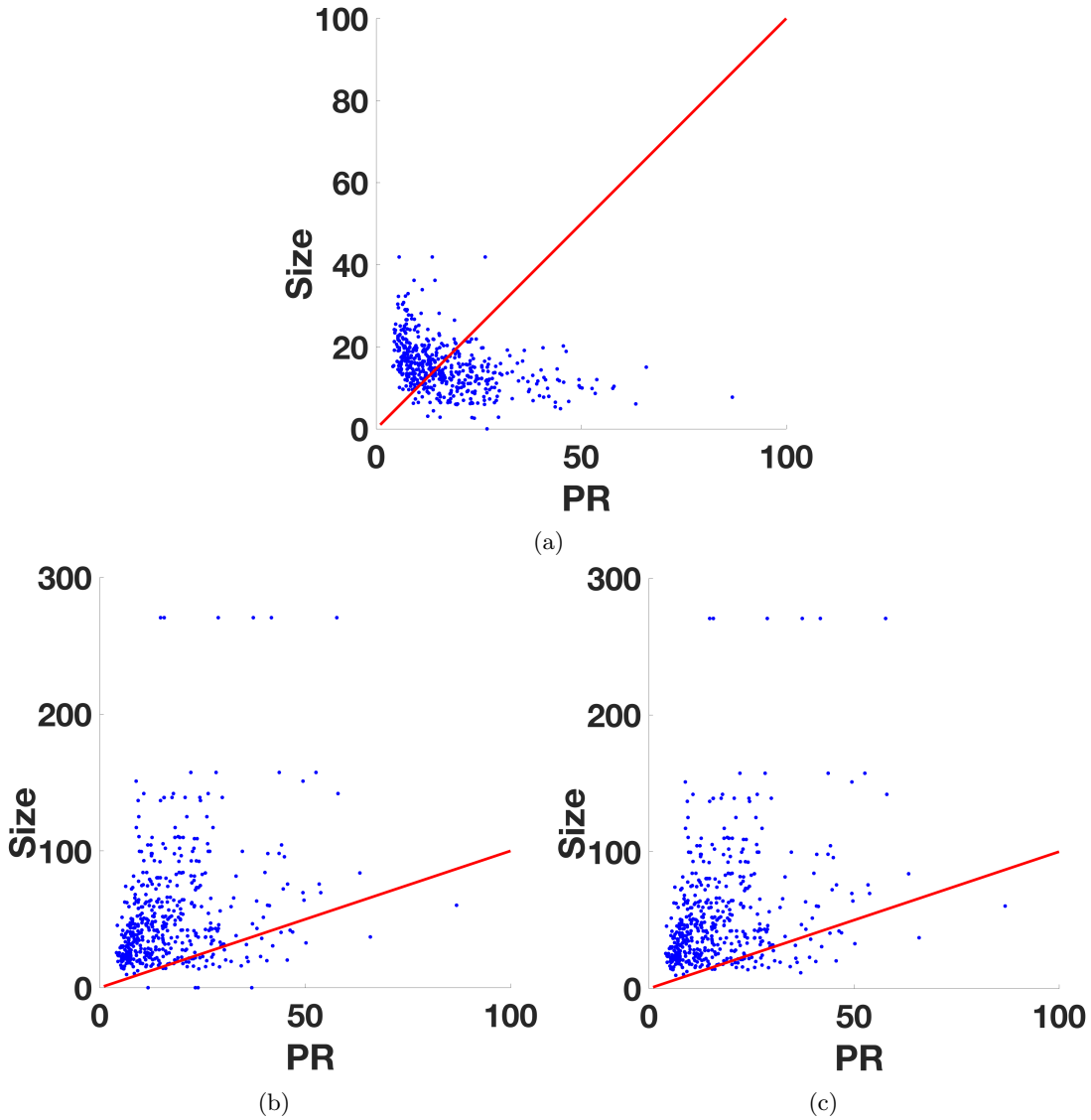

Figure 2.19: Participation ratio of the first 50 eigenfunctions for 10 different realizations of disorder versus the size of the localization sub-regions determined by: (a) The original watershed algorithm without merging; (b) The watershed algorithm using the average of the crest minima to exclude sub-regions; (c) The watershed algorithm using the maximum of the crest minima to exclude sub-regions. The red line represents the 'PR=Size' curve.

a sub-region is excluded although it hosts an eigenfunction. This however does not happen very often, but is more likely when the strength of the potential is low.

It is apparent that the merging procedure is therefore beneficial in identifying the sub-regions of localization. While especially effective at low potential strengths and with a uniform random law, the merging procedure improves the identification of sub-regions for all sets of parameters.

Another statistical measure of the improvement achieved through the merging procedure is obtained by computing the norm of the eigenfunction restricted to its sub-region, i.e., the sub-region where the eigenfunction is maximal. We also call this the restricted norm, $\|\psi\|_{\Omega_i}$. This value tells us what is the fraction of an eigenfunction present in a given sub-region.

Once again, let us start by comparing the situation between merging and no merging, regardless of the exclusion procedure. From Figure 2.20, it seems that, on average, the points have migrated upwards (i.e. that the eigenfunctions occupy a greater portion of their sub-region) between Figure 2.20a and Figures 2.20b and 2.20c. Especially at low energies, all eigenfunctions end up with a restricted norm close to 1. For the same reason as before, this is proof that the newly defined sub-regions are larger and

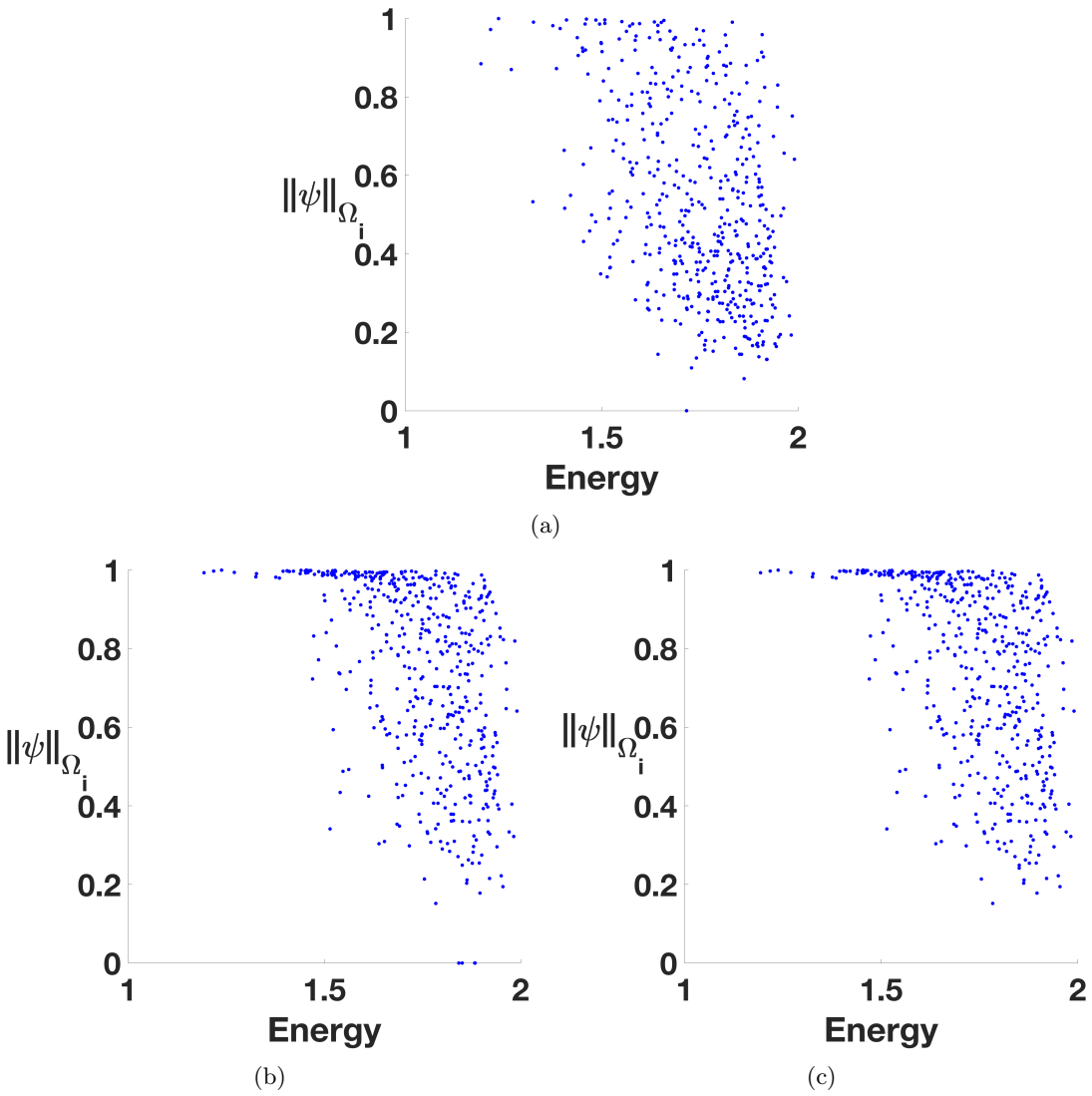

(a)

(b)

(c)

Figure 2.20: The restricted norm of the first 50 eigenfunctions for 10 different realizations of disorder versus the eigenvalue for: (a) The original watershed algorithm without merging. (b) The watershed algorithm using the average of the crest minima to exclude sub-regions. (c) The watershed algorithm using the maximum of the crest minima to exclude sub-regions.

better represent the sub-regions of localization.

	Uniform random law			Binary random law		
$V_{\max}$	no merging	exclusion method 1 (average)	exclusion method 2 (maximum)	no merging	exclusion method 1 (average)	exclusion method 2 (maximum)
4	0.54	0.73	0.74	0.78	0.85	0.85
8	0.77	0.88	0.88	0.90	0.93	0.93
12	0.84	0.93	0.93	0.92	0.94	0.94

Table 2.2: Average value of the restricted norm of the eigenfunctions for the different algorithms and various values of the parameters.

This observation is confirmed through histogram plots (Figure 2.21) which represent the distribution of the values of the restricted norm of the eigenfunctions. The difference between merging and not merging is much clearer here. While the distribution is more or less uniform without the merging procedure, adding it creates a spike in the distribution towards 1 which is evidence that merging the sub-regions is

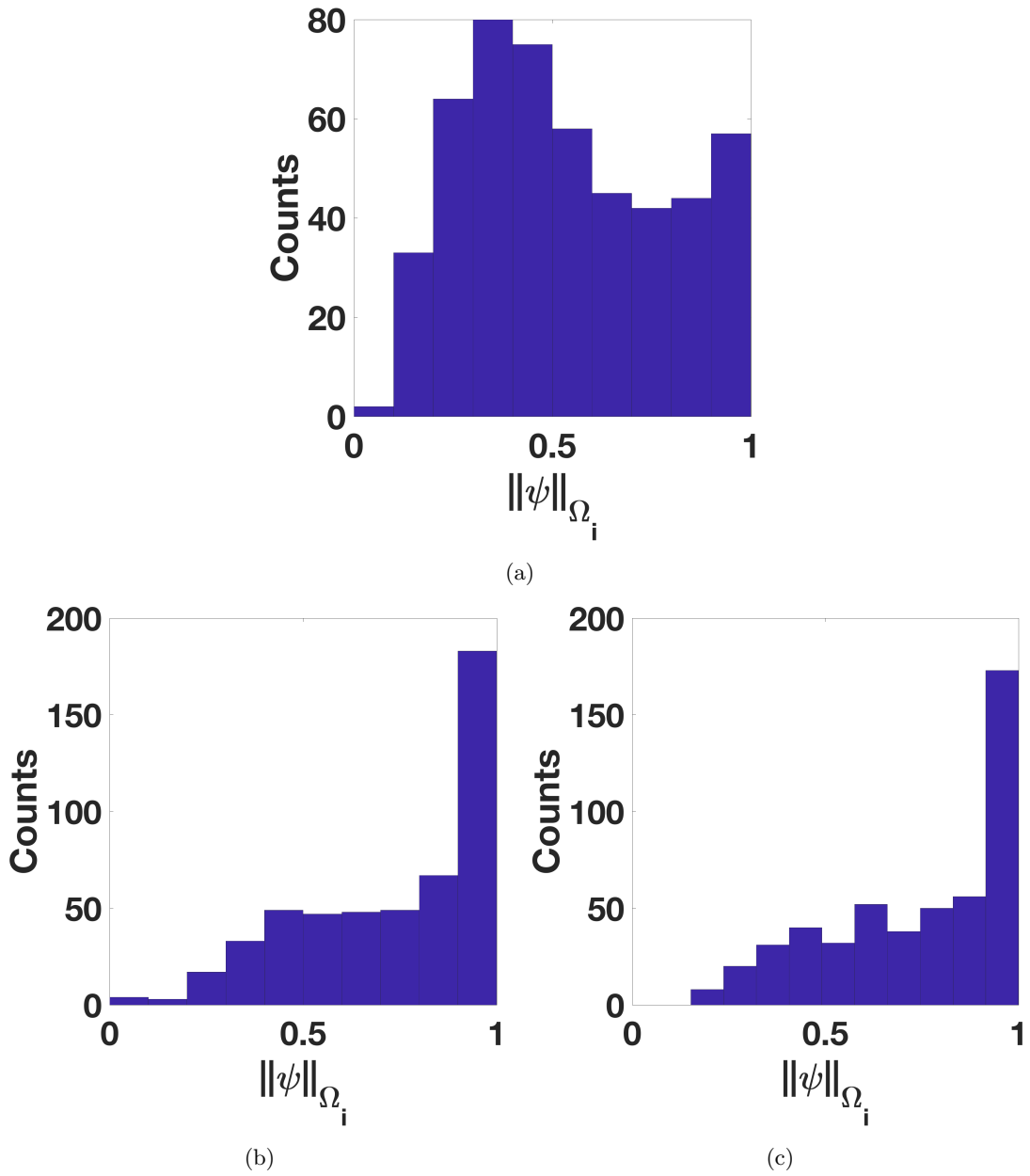

Figure 2.21: Histograms of the restricted norm of the first 50 eigenfunctions for 10 different realizations of disorder. (a) The original watershed algorithm without merging. (b) The watershed algorithm using the average of the crest minima to exclude sub-regions. (c) The watershed algorithm using the maximum of the crest minima to exclude sub-regions.

important for the identification of the sub-regions of localization.

Comparing the different merging procedures reveals subtle differences once again. The histograms in Figure 2.21 and the scatter plots of Figure 2.20 show that a few eigenfunctions have a restricted norm close to 0 when taking the average of the crest minima when excluding sub-regions. These eigenfunctions do not have a restricted norm close to 0 when the maximum is taken. However, the data from Table 2.2 show that this improvement between exclusion method 1 and 2 is limited to the case of low potential strengths and uniform random laws.

The above table also shows the significant improvement brought by the merging procedure, especially at low potential strengths. We observe that the difference is not as important at higher potential strengths. These additional features added to the watershed algorithm are expected to be very beneficial in improving the computation of the localization sub-regions.

IV A case study: mechanical vibrations in clamped plates

We now present a case where we adapted the watershed algorithm to irregular meshes. This work (which is the continuation of other studies on the localization of mechanical waves [7, 13]) has been performed in collaboration with Patrick Sebbah and Kun Tang from Bar Ilan University. Essentially, the system under study is a metallic plate with geometric irregularities. The plate is set in vibration and the different vibrational modes are measured. The harmonic solutions can be written as $w(x, y, t) = W(x, y) \exp(i\omega t)$ where we have separated the spatial and temporal variables. The eigenmodes of vibration W_k satisfy the equation:

$$\frac{1}{\alpha^2}\Delta^2 W_k = \omega_k^2 W_k, \tag{2.5}$$

where

$$\alpha = \sqrt{\frac{12\rho\,(1-\nu^2)}{Eh^2}}, \tag{2.6}$$

is a constant depending on the the density of the plate ρ, the Poisson ratio of the material ν, the Young modulus of the material E, and the plate thickness h. ω_k is the angular frequency of the vibrations.

Similarly to the quantum case, the eigenmodes become localized with enough disorder, and the subregions of localization are difficult to predict. As can be seen in Figure 2.22, the metallic plate is clamped in certain places somewhat randomly. The landscape predicts where the eigenmodes localize.

The localization landscape corresponding to the eigenvalue problem (2.5) is the solution of the Dirichlet problem:

$$\frac{1}{\alpha^2}\Delta^2 u = 1. \tag{2.7}$$

It is therefore proportional to the out-of-plane static deformation under uniform load (we remind the reader that the landscape is related to the Green's function by: $u(x, y) = \int G(x', y', x, y)\mathrm{d}x\mathrm{d}y$), which makes it easy to measure. More background on the use of the landscape for these sort of systems can be found in the literature [7, 8, 13].

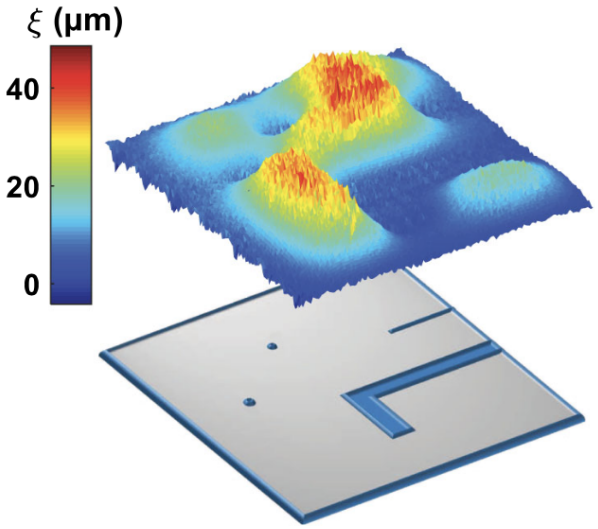

Figure 2.22: Bottom: Sketch of the metallic plate. The blue segments and points correspond to the areas where the plate is clamped. Top: The associated localization landscape. Reprinted from [13].

In Tang and Sebbah's experiment, a metallic plate was randomly clamped in different points. The computed effective confining potential of this setup can be seen in Figure 2.23. Since the landscape

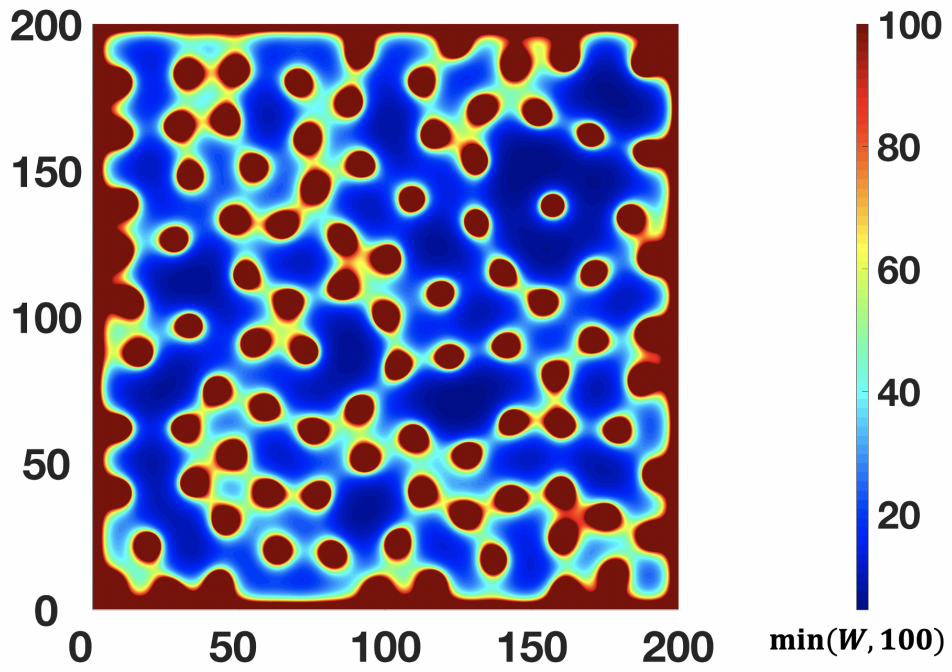

Figure 2.23: The effective confining potential calculated from the landscape provided by Tang and Sebbah. For clarity, values over 100 are removed. This is the picture obtained using a square mesh to model the system.

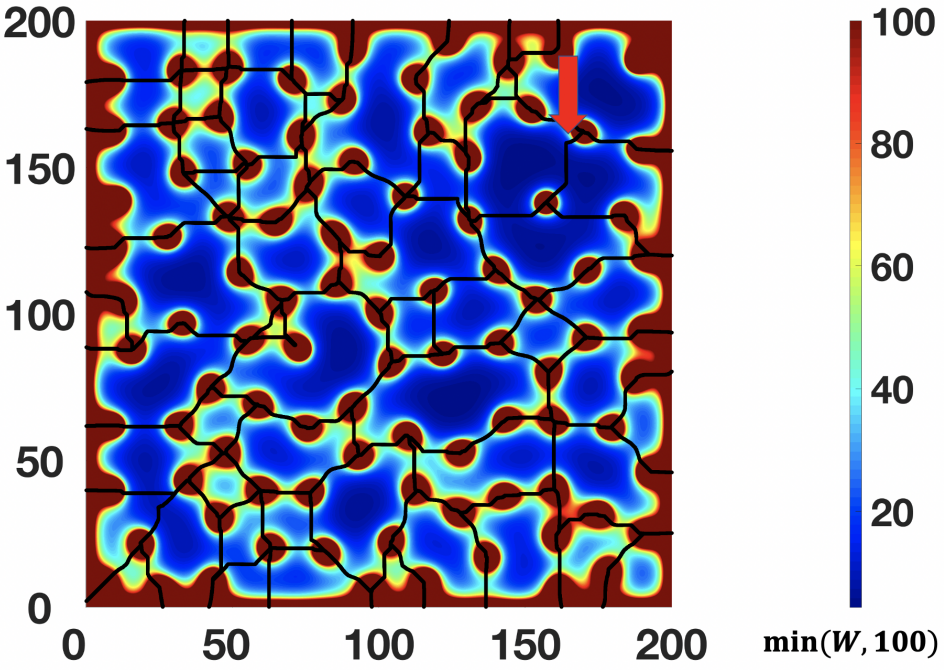

Figure 2.24: The watershed partition computed from the above effective confining potential. The red arrow points towards a border line that is not smooth.

vanishes at the clamped points and on the borders of the domain, the potential W should diverge, but it is capped at 100 at these points on the figure for the sake of clarity.

From this effective confining potential we wish to determine the sub-regions of localization by using the watershed algorithm we have developed. One important difference between this wave equation and the quantum case lies in the relation between the local fundamental mode and the respective local

minimum of the effective confining potential. Instead of having $E_0^i \approx (1+\frac{d}{4}) \min_{\Omega_i} W$, this relation is now: $\omega_{0,i} \approx 1.27/\sqrt{\min_{\Omega_i}(W)}$ with $\omega_{0,i}^2 = E_0^i$ (see Supplementary Material in [13]).

The resulting partition from the watershed algorithm (see Figures 2.24 and 2.25) is a good start, but improvements could be made. Indeed, one of the problems of using a square mesh is that the lines delineating different sub-regions must necessarily follow the grid, and so are either straight or jagged. The red arrow points to a border line that is not smooth, and that does not really follow the gradient of the curve. This is not the only border line that is problematic. The problem is that the clamped points are represented as disks on the domain, and the mesh is not fine enough to resolve the curvature of these disks.

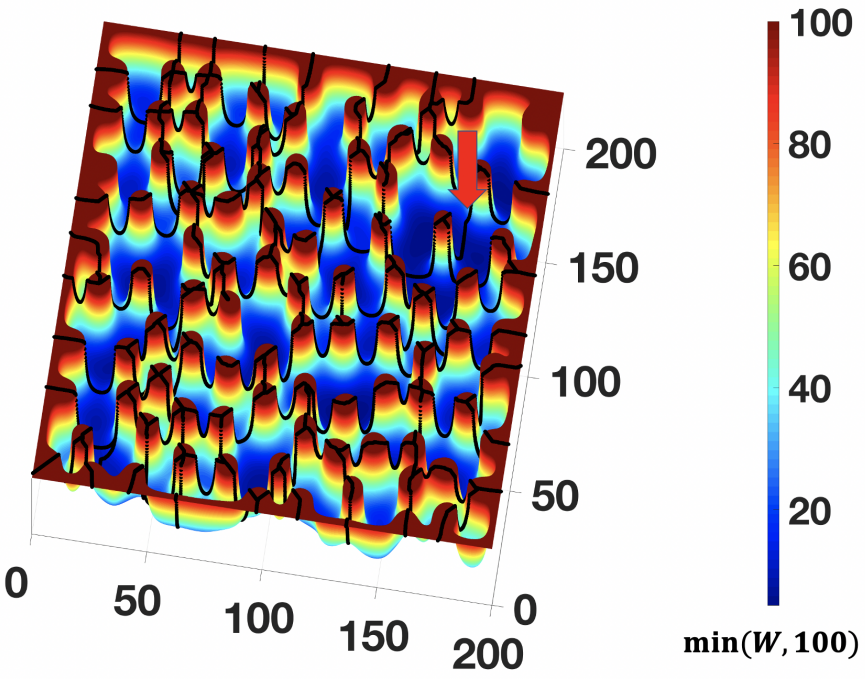

Figure 2.25: The watershed partition superimposed on the landscape. The red arrow points towards a border line that is not smooth.

The algorithm we have developed was adapted to a grid type mesh, where each point has exactly $2d$ neighbors (4 in the case of our 2D system). These types of meshes are the simplest to implement and work well, required that the geometry of the problem is simple. For instance in the Anderson model, the lattice is $\mathbb{Z}^d$, therefore the distances between neighboring sites remain constant.

This choice however is not always optimal. For example, when studying randomly distributed impurities, or a solid that does not form a crystal (like a glass), modeling the system by a grid is not possible. In some cases, using a grid either forces to make approximations or to use a mesh refined to the point that computation times become unrealistic.

For problems where a regular mesh is not adequate, the finite element method is suitable for any kind of mesh. The literature on the finite element method is extensive: a good review can be found in the book by Zienkiewicz, Taylor, and Zhu [1]. Our algorithm was developed for solutions using finite differences methods, and not finite elements methods. The algorithm, nonetheless, can be well adapted for these types of problems.

For this problem, we therefore used an adaptive triangular mesh that is finer in areas where more detail is needed. An example of this can be seen in Figure 2.26. The mesh gets progressively finer the closer it gets to the clamped points. This is required by the vanishing boundary conditions on the landscape on the borders of the domain and at the edges of the clamped points and also because the differential equation is now a fourth order equation instead of a second order one. It then increases over short distances away from the boundaries and the clamped points. In areas where we know the landscape is constant, or does not vary much, the mesh becomes larger again, so as to not waste computing power.

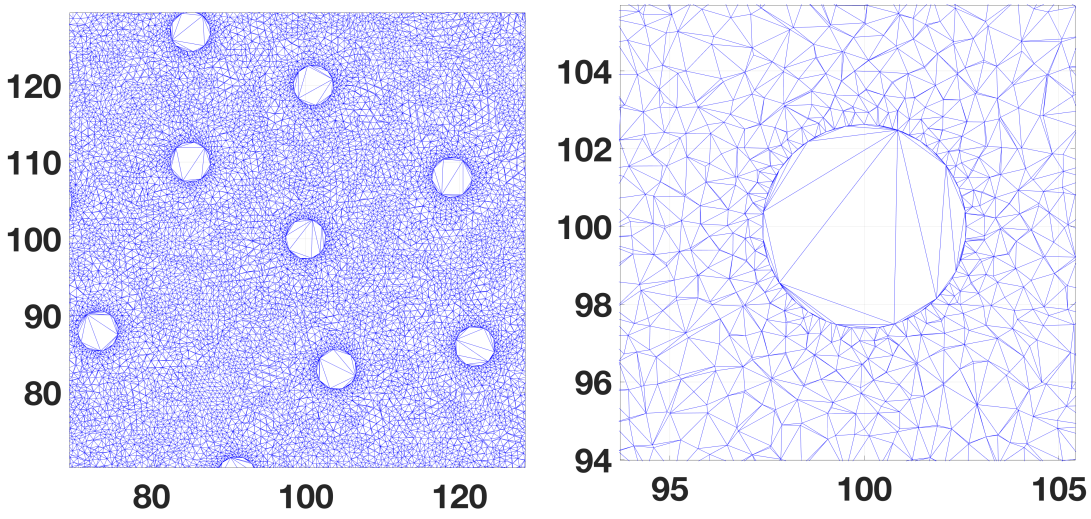

(a) (b)

Figure 2.26: (a) The adaptive mesh of the domain. (b) A close-up look on an area where the mesh size varies significantly.

We had to adapt the watershed algorithm to work on any type of mesh. The same foundation of the algorithm can be used. The only crucial difference is how the algorithm evaluates neighboring points. Beforehand, it was quite straightforward. The neighbors of any point were its adjacent points on the grid. Now each point has its own set of neighbors defined by the connections between the vertices of the mesh. The algorithm needs only to consider this when identifying local minima. Every other step is identical.

The result can be observed in Figure 2.27. The lines delineating the sub-regions are no longer straight and follow the curvature of the landscape better. We superimpose this network with three different modes (the second, sixth and ninth) in Figure 2.28 in different scales. The "log gradient" portion of the figure corresponds to the norm of the gradient of the eigenfunction in logarithmic scale. What is remarkable is the agreement between the network obtained from the algorithm and the lines where the gradient of the eigenfunction is maximum. These lines correspond to points where the eigenfunction drops off, where the decay of the eigenfunction is the largest.

This figure also highlights the importance of adapting the mesh to the domain. In this case, the system has irregularities (the randomly placed clamped points) which makes an irregular mesh more suitable.

In conclusion, the watershed algorithm can now be adapted to irregular meshes obtained from the finite element method, which is essential for modeling a wider variety of problems.

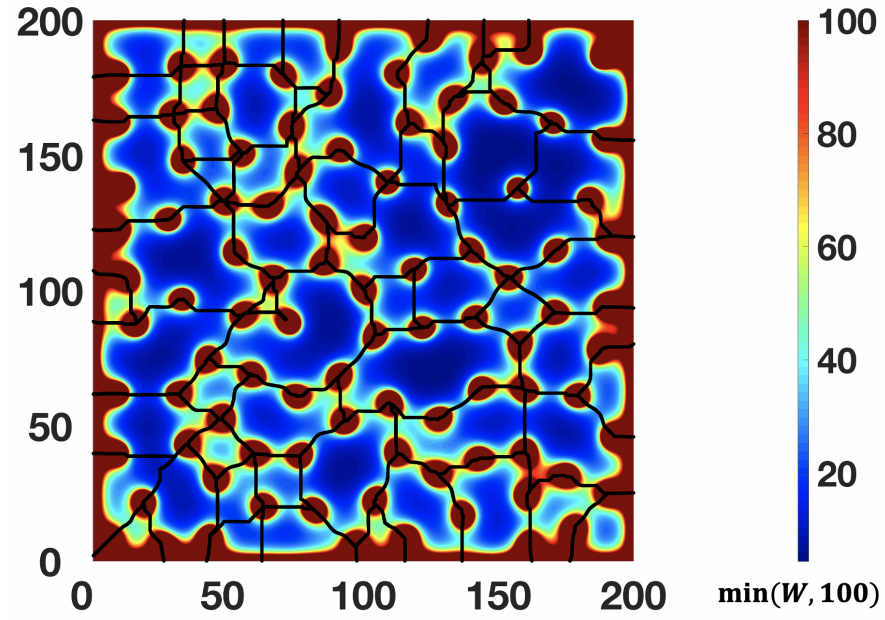

(a)

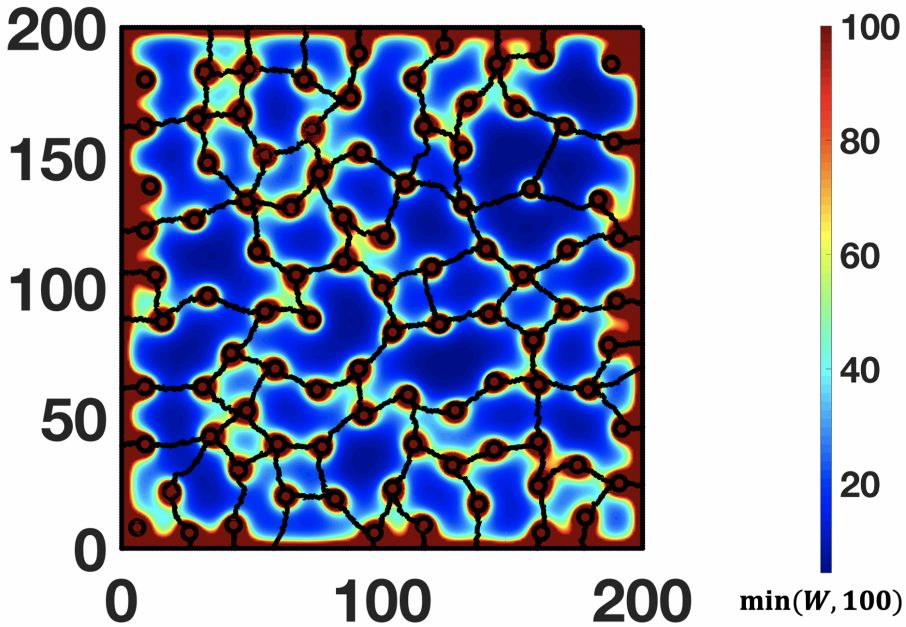

(b)

Figure 2.27: (a) The effective confining potential with the initial watershed partition. (b) The same effective confining potential with the new watershed partition.

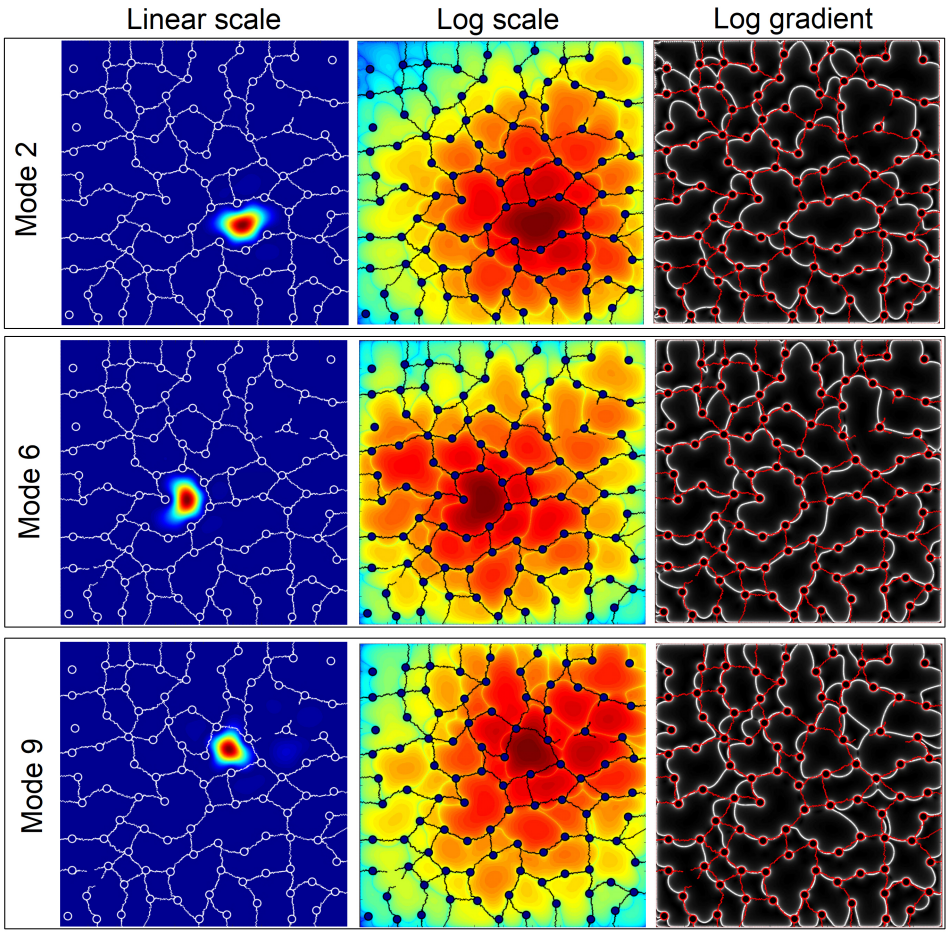

Figure 2.28: The second, sixth and ninth vibration modes with the effective valley network obtained from the watershed algorithm. Left: linear scale. Center: logarithmic scale. Right: the norm of the gradient of the eigenfunctions in logarithmic scale. (Courtesy of Kun Tang.)

V Conclusion

We have reviewed the workings of the watershed algorithm with the aim of defining the localization sub-regions as accurately as possible. The main steps of the algorithm are the identification and labeling of the local minima, the computation of the initial sub-regions, the merging of these sub-regions, and finally the exclusion of the superfluous sub-regions.

This algorithm is, before anything else, an image processing tool that must be tuned for the task at hand. For instance, the merging criterion we established can change value depending on what type of system is being studied (1.5 for 2D Anderson, 1.75 for 3D Anderson, $\omega_{0,i} \approx 1.27/\sqrt{\max_{\Omega_i}(u)}$ for 2D pinned plates, etc.).

Developing a universal method for merging the localization sub-regions for Anderson localization is an important step in the study of the spatial structure of the eigenfunctions. This has numerous applications, such as the study of electronic transport by hopping mechanism on a network of localization sub-regions, the approximation of localized eigenfunctions restricted to the localization sub-regions, or the computation of the eigenfunctions using iterative methods using the preceding approximation. We expect this algorithm to participate in future studies of Anderson localized eigenfunctions.

Bibliography

[1] The finite element method: Its basis and fundamentals. In O. Zienkiewicz, R. Taylor, and J. Zhu, editors, *The Finite Element Method: its Basis and Fundamentals (Seventh Edition)*, page iii. Butterworth-Heinemann, Oxford, seventh edition edition, 2013. doi:10.1016/B978-1-85617-633-0.00020-4.

[2] D. N. Arnold, G. David, M. Filoche, D. Jerison, and S. Mayboroda. Computing spectra without solving eigenvalue problems. *SIAM J. Sci. Comput.*, 41:B69–B92, 2017. URL: https://arxiv.org/abs/1711.04888.

[3] D. N. Arnold, G. David, M. Filoche, D. Jerison, and S. Mayboroda. Localization of eigenfunctions via an effective potential. *Commun. Part. Diff. Eq.*, 44(11):1186–1216, 2019. doi:10.1080/03605302.2019.1626420.

[4] D. N. Arnold, G. David, D. Jerison, S. Mayboroda, and M. Filoche. Effective confining potential of quantum states in disordered media. *Phys. Rev. Lett.*, 116:056602, 2016. doi:10.1103/PhysRevLett.116.056602.

[5] S. D. Baranovskii. Theoretical description of charge transport in disordered organic semiconductors. *Phys. Status Solidi B*, 251(3):487–525, 2014. doi:10.1002/pssb.201350339.

[6] S. Beucher and C. Lantuéjoul. Use of watersheds in contour detection. volume 132, 1979. URL: https://www.researchgate.net/publication/230837989_Use_of_Watersheds_in_Contour_Detection.

[7] M. Filoche and S. Mayboroda. Strong localization induced by one clamped point in thin plate vibrations. *Phys. Rev. Letters*, 103:254301, 2009. doi:10.1103/PhysRevLett.103.254301.

[8] M. Filoche and S. Mayboroda. Universal mechanism for Anderson and weak localization. *Proc. Natl. Acad. Sci. USA*, 109(37):14761–14766, 2012. doi:10.1073/pnas.1120432109.

[9] M. Filoche and S. Mayboroda. *The landscape of Anderson localization in a disordered medium*, volume 601, pages 113–121. Contemp. Math., 2013. doi:10.1090/conm/601/11916.

[10] M. Filoche, M. Piccardo, Y.-R. Wu, C.-K. Li, C. Weisbuch, and S. Mayboroda. Localization landscape theory of disorder in semiconductors. I. Theory and modeling. *Phys. Rev. B*, 95:144204, 2017. doi:10.1103/PhysRevB.95.144204.

[11] V. Gasparian and A. Suzuki. Localization length in two-dimensional disordered systems: Effects of evanescent modes. *Journal of physics. Condensed matter : an Institute of Physics journal*, 21:405302, 10 2009. doi:10.1088/0953-8984/21/40/405302.

[12] F. Hecht. New development in FreeFem++. *J. Numer. Math.*, 20(3-4):251–265, 2012. URL: https://freefem.org/.

[13] G. Lefebvre, A. Gondel, M. Dubois, M. Atlan, F. Feppon, A. Labbé, C. Gillot, A. Garelli, M. Ernoult, S. Mayboroda, M. Filoche, and P. Sebbah. One single static measurement predicts wave localization in complex structures. *Phys. Rev. Lett.*, 117:074301, 2016. doi:10.1103/PhysRevLett.117.074301.

[14] A. Miller and E. Abrahams. Impurity conduction at low concentrations. *Phys. Rev.*, 120:745–755, 1960. doi:10.1103/PhysRev.120.745.

[15] N. Tessler, Y. Preezant, N. Rappaport, and Y. Roichman. Charge transport in disordered organic materials and its relevance to thin-film devices: A tutorial review. *Adv. Mater.*, 21(27):2741–2761, 2009. doi:10.1002/adma.200803541.

Chapter 3

Lifshitz Tails

I The Lifshitz tails

I.1 Introduction

In single-particle quantum systems subject to random potential, the Integrated Density of States (IDOS, or counting function, defined as the number of eigenvalues per unit volume smaller than a given energy and denoted hereafter as $N(E)$) departs significantly at low energy from the high energy asymptotic behavior known as Weyl's formula. According to the latter, in the absence of any potential, $N(E)$ scales as $E^{d/2}$ where d is the ambient dimension. However, in the presence of a disordered or random potential the IDOS exhibits a very slowly growing tail at low energy. In 1964, Lifshitz proposed a model based on scattered impurities where the integrated density of states would drop off exponentially as E approaches its minimum value E_0, forming what is known as a *Lifshitz tail* [21, 20]:

$$N(E) \sim C \exp\left(-c(E-E_0)^{-\frac{d}{2}}\right) . \tag{3.1}$$

Since then, understanding the precise behavior of the density of states in the presence of disorder has been the subject of a very rich literature (for an extended review on the topic, the reader can refer to [19, 28, 15, 13, 18]). The existence of Lifshitz tails for the Poisson random potential was proved in [5, 9, 24, 27]. Later Kirsch and Martinelli gave a proof close to Lifshitz's intuition for a large class of random potentials in the continuous setting in [14], while Simon generalized the argument to the tight binding model [30]. These are only a few isolated results and we do not aim to provide an exhaustive list of the literature. It is important to mention however that there exist exact asymptotic results on Lifshitz tails for specific models [30, 23, 6, 18]. Nonetheless, we are still lacking a general understanding for all models, and the only mathematical statement that could be rigorously proven in *full generality* does not have the form of Eq. (3.1) but rather the weaker form:

$$\lim_{E\to E_0} \frac{\ln(|\ln(N(E))|)}{\ln(E-E_0)} = -\frac{d}{2} \quad . \tag{3.2}$$

These results are asymptotic in the limit of vanishing $E - E_0$. Away from the asymptotic behavior at low energy, Klopp and Elgart showed that in the weak disorder limit these Lifshitz tails extend roughly up to the average of the potential [16, 17, 10]. To this day, many unsolved questions remain concerning these Lifshitz tails: (i) Can one improve the known results by deriving a general estimate on $\ln(N(E))$ and not on $\ln(|\ln(N(E))|)$? (ii) If so, how does disorder enter the estimate? For instance, can one quantify existing results showing logarithmic corrections for random uniform disorder as compared to binary disorder [25, 29]? (iii) Can one derive precise estimate for the full spectrum instead of asymptotic near the lower bound of the spectrum?

In this article, we present a new function, denoted by $N_u(E)$ and called *Landscape Law* [8], that provides the first estimates from above and below of the actual counting function throughout the spectrum. This function is obtained from the *localization landscape*, a theoretical tool introduced in 2012 and developed in the recent years [12, 3]. Not only do these estimates cover the entire range of energy for any type of

potential or disorder in continuous models, but they also provide the asymptotic behavior of $\ln(N(E))$ at low energy for random uniform or binary disorder, thus removing a log from the previously known results. In particular, they recover the logarithmic correction in the case of the uniform Anderson model. We investigate numerically the optimal constants involved in the bounds, and observe their similarity for both binary and uniform Anderson models. Finally, we test whether these mathematically proven bounds from above and below could in fact be merged into one single approximate formula based on N_u, thus providing a very fast and efficient way of predicting the behavior of the IDOS on the entire spectrum even in a random or complicated system.

I.2 Numerical Model

We consider a d-dimensional tight-binding model. The corresponding Hamiltonian is

$$\hat{H} = \sum_i V_i a_i^\dagger a_i - t \sum_{\langle i,j \rangle} \left(a_i^\dagger a_j + h.c. \right), \tag{3.3}$$

where $\langle i, j \rangle$ denotes the sum over nearest neighbors, t is the hopping term, V_i is the on-site random potential (on a grid of lattice parameter 1), and $a_i^\dagger$ and a_i are the creation and annihilation operators, respectively. From now on, t will be taken equal to 1, thus setting the energy scale. The V_i are i.i.d. variables and follow a random law which can be either uniform or binary in $[0,\ V_{\max}]$. The localization landscape u in this system is defined as the solution to $\hat{H}u = 1$, the right-hand side being the constant vector. In order to ensure that the landscape is positive everywhere, the potential V is uplifted by a quantity $2d$, where d is the embedding dimension. Consequently, the lowest bound E_0 of the spectrum in all subsequent examples is $E_0 = 0$ and the spectrum lies in the interval $[0,\ V_{\max} + 4d]$. It has been shown in [22] that the function $W \equiv 1/u$ defines an effective potential for all quantum states in the tight-binding model, and that this potential provides a remarkably accurate estimate of the energy of the lower-energy states.

Using this effective potential, the function $N_u(E)$ is defined as follows: for a given energy E, we partition the entire domain into d-cubes (intervals in 1D, squares in 2D,...) of side length $E^{-1/2}$. $N_u(E)$ is then defined as the fraction of such cubes for which the minimum of W over the cube is smaller than E:

$$N_u(E) \equiv \frac{1}{|\Omega|} \times \Big(\text{ number of cubes of size } \frac{1}{\sqrt{E}} \text{ where } \min(W) \leq E \Big). \tag{3.4}$$

For the continuous model, it has been mathematically proven in [8] that there exist constants C_4, C_5, C_6 such that N_u satisfies the following inequalities:

$$C_5 N_u\left(C_6 E\right) \leq N(E) \leq N_u\left(C_4 E\right), \tag{3.5}$$

where $N(E)$ is the IDOS per unit volume. The constants C_5 and C_6 depend only on the dimension d and on the average of the potential, and C_4 depends only on the dimension. When the potential is random, this inequality is verified for the expectations of the IDOS (note that these expectations become finite deterministic quantities in the limit of an infinite domain). To our knowledge, these inequalities are the first universal bounds for the counting function $N(E)$ of a Schrödinger Hamiltonian throughout the entire spectrum. In other words, unlike Weyl's formula or Lifshitz tails, they are not asymptotic. The proof is rather technical and is based on the analysis of the low values of the effective potential W. A sketch of the proof is given in Supplementary Material. We are currently preparing a version of this proof for discrete tight-binding models [4].

An example of the sharpness and the predictive power of this inequality is provided in Fig. 3.1 which displays the actual IDOS $N(E)$ (blue) and the landscape law $N_u(E)$ (red) for one realization of a random i.i.d. binary disorder with periodic boundary conditions. The potential can take the values either 0 or $V_{\max} = 1$ with equal probability on each site of a one-dimensional domain of $N = 10^5$ sites. $N(E)$ is computed using the LDL^T factorization and Sylvester's law of inertia [26]. One can see how the two curves, plotted on a log-log scale, follow each other very closely. On this log-log plot, the upper and lower bounds of (3.5) would correspond simply to horizontal and vertical translations of the graph of $N_u(E)$.

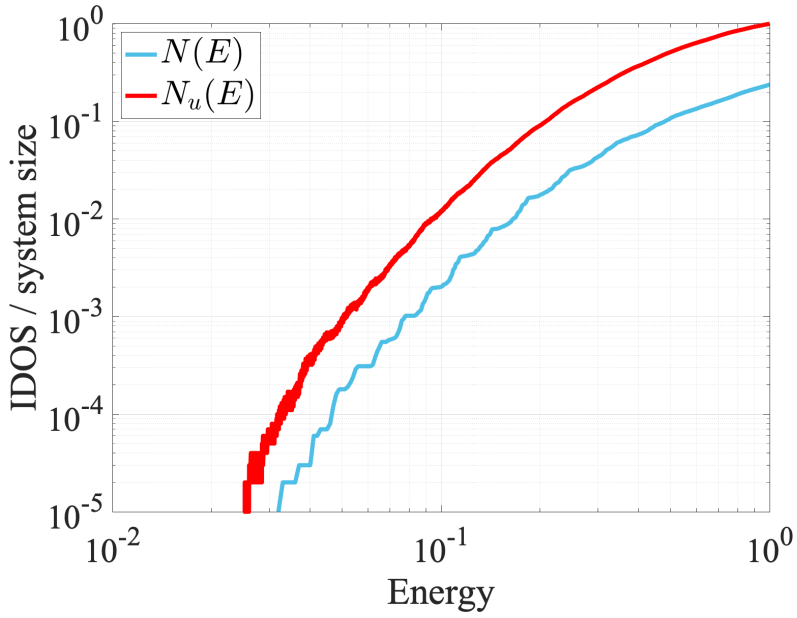

Figure 3.1: Counting function $N(E)$ (blue) and landscape law $N_u(E)$ (red) for one realization of a one-dimensional binary Anderson tight-binding model. The number of sites is $N = 10^5$ and the values of the on-site potential are either 0 or 1.

While Ref. [8] proves the existence of constants C_4, C_5, C_6 fulfilling (3.5), it does not bring any insight on their sharpest values. Indeed, strictly speaking, [8] gives a "tube" containing the IDOS (in log-log plot), and while it is remarkable that the tube diameter does not depend on the energy, it could be quite wide if the constants are very different. The goal of this study is threefold: first, to demonstrate the accuracy of the Landscape Law in approximating the actual IDOS. Secondly, we indicate how to determine numerically the sharpest values for the constants entering the bounds in (3.5). This is of particular relevance for C_4 which is predicted to be universal, i.e., to depend only on the dimension d and not on the particular potential. Thirdly, we assess the possibility to provide an optimal approximation to the IDOS $N(E)$ (rather than a tube), i.e., to find a constant $C_{5,\text{fit}}$ such that $N(E) \approx C_{5,\text{fit}} N_u(C_6 E)$.

II Sharpest values

One starts with the same system as in Fig. 3.1, but this time $N(E)$ is averaged over 1000 realizations. Figure 3.2a displays the corresponding $N(E)$ and $N_u(E)$ together with their standard deviations represented as error bars (the bottom bars are not displayed when they are larger than the value itself, i.e., when they cross the horizontal axis). In order to determine the constants C_4, C_5, C_6, we first restrict our study to the domain $E > 0.02$ to avoid the noise at very low energy. We observe that the graph of $N_u(E)$ is always above the graph of $N(E)$, which means that $C_4 < 1$. This fact derives from the definition of N_u, and we will discuss it further down. The value of the constant C_4 corresponds in log-log scale to the largest possible right-shift of the graph of N_u (or in other words to the smallest possible value of C) such that $N(E) \leq N_u(CE)$. Here, this value is found to be $C_4 \approx 0.79$ (or $1/C_4 \approx 1.26$). To find the values of C_5 and C_6, we first look for the optimal value C such that $N(E)/N_u(CE)$ is as constant as possible. This is achieved by taking the minimum of the standard deviation of $\ln(N(E)/N_u(CE))$ when varying C. Figure 3.2b displays this standard deviation for values of C ranging from 0.5 to 1. One observe a clear minimum at $C_6 \approx 0.90$ (or $1/C_6 \approx 1.11$). Finally the minimum of the graph of $N(E)/N_u(C_6 E)$ provides us the sharpest value of C_5 (see Fig. 3.2c): it is here $C_5 \approx 0.18$. However, one can observe that if we were looking for a best fit for C_5 (instead of a lower bound for (3.5)), then the best fit would be closer to $C_{5,\text{fit}} \approx 1/4.08$ (obtained by computing the average of $\ln(N(E)/N_u(C_6 E))$ for $E > 0.02$). With these constants, the agreement between the actual IDOS and the rescaled formula based on the localization landscape is excellent throughout the computed spectrum (see Fig. 3.2d). This means that

the inequalities in (3.5) can almost be transformed into an equality:

$$N(E) \approx C_{5,\text{fit}}\, N_u(C_6 E)\,. \tag{3.6}$$

The same methodology is then applied to one-dimensional uniform Anderson tight-binding model ($N = 10^5$), and to two-dimensional binary and uniform Anderson tight-binding models. Figure 3.3 displays the results for a uniform Anderson model of disorder amplitude $V_{\max} = 1$. Here also, we observe that the landscape law $N_u(E)$ follows very closely the actual IDOS $N(E)$. After computation, the value found for C_4 in this case is $C_4 \approx 0.78 = 1/1.28$. Further analysis of the standard deviation of the values of $N_u(CE)/N(E)$ as a function of C (see Fig. 3.3b) yields $C_6 \approx 0.84 = 1/1.19$. Plotting now $N_u(C_6E)/N(E)$ as a function of E (Fig. 3.3c), one observes that it oscillates slowly between 3 and 5 in the noiseless part of the graph. A possible choice for C_5 is then $C_5 = 1/4.85$, but the best fit is obtained for $C_{5,\text{fit}} = 1/3.94$, as confirmed in Fig. 3.3d.

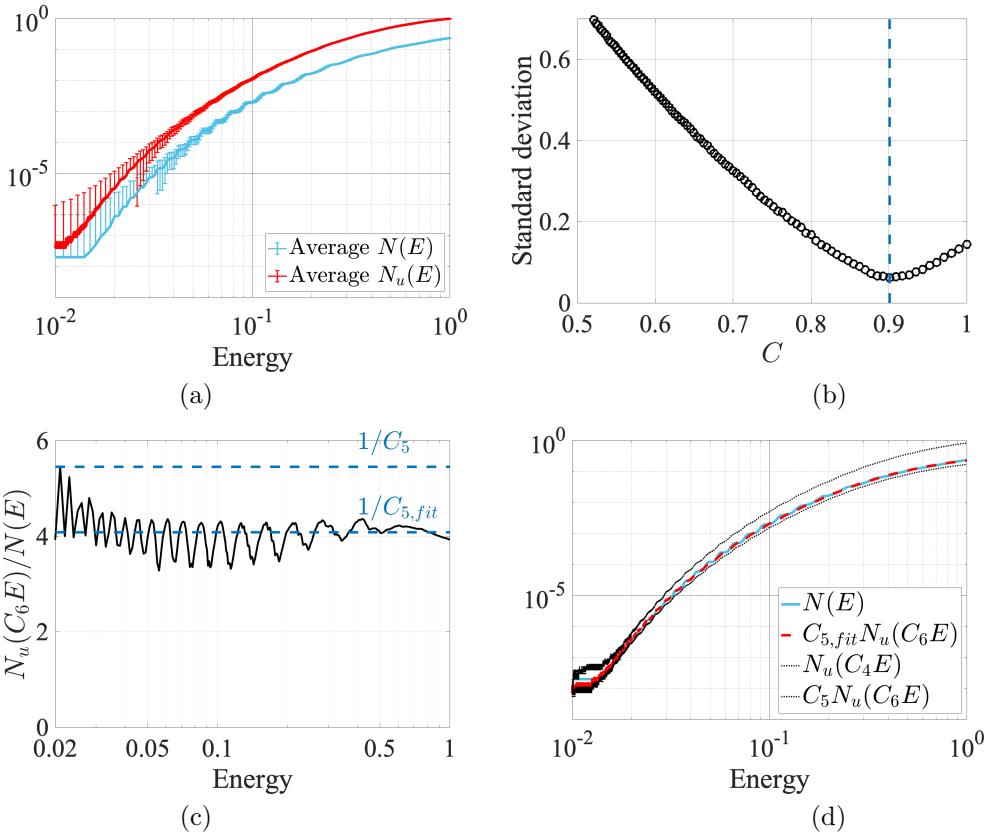

Figure 3.2: (a) $N(E)$ (blue) averaged over 1000 random realizations, and averaged landscape law $N_u(E)$ (red), for a one-dimensional binary Anderson tight-binding model of size $N = 10^5$ and $V_{\max} = 1$. The error bars show the standard deviation over the 1000 realizations (the bottom bars are not displayed when they are larger than the value itself, i.e., when they cross the horizontal axis). (b) Standard deviation of the distribution of values of $\ln(N_u(CE)/N(E))$ for various values of C. The minimum around $C = 0.90 \approx 1/1.11$ provides the value of C_6. (c) Plot of $N_u(C_6E)/N(E)$. The maximum shows that one can take $C_5 = 1/5.45$. A best fit for $N(E)$ is obtained by taking the average value $C_{5,\text{fit}} \approx 1/4.08$. (d) Final comparison between the original $N(E)$ (blue), the best fit $C_{5,\text{fit}}\, N_u(C_6E)$ (dashed red), and the two bounds from above of below in Eq. (3.5) $N_u(C_4E)$ and $C_5 N_u(C_6E)$ (dotted lines). Note that the best fit is so close to the actual IDOS that the blue line is almost invisible.

In order to check the validity of our approach, we have investigated the role of the domain size for these one-dimensional Hamiltonians (we could not run such a study in 2D because the computation time did not allow us to explore a large enough range of domain sizes). Domain sizes $N = 10^3$, 10^4, and 10^5 were simulated, for both Anderson binary and Anderson uniform models. We also tested several

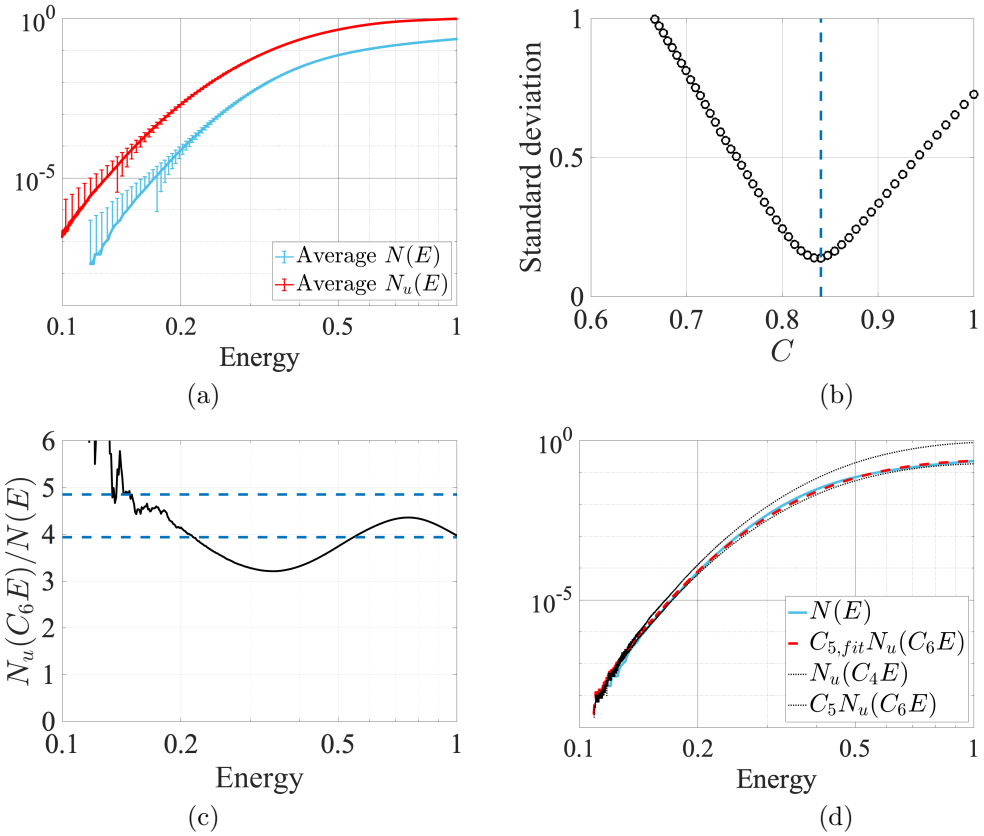

Figure 3.3: (a) $N(E)$ (blue) averaged over 1000 random realizations, and averaged landscape law $N_u(E)$ (red), for a one-dimensional uniform Anderson tight-binding model of size $N = 10^5$ and $V_{\max} = 1$. (b) Standard deviation of the distribution of values of $\ln(N_u(CE)/N(E))$ for various values of C. The minimum around $C = 0.84 \approx 1/1.19$ provides the value of C_6. (c) Plot of $N_u(C_6E)/N(E)$. The maximum shows that one can take $C_5 = 1/4.85$. A best fit for $N(E)$ is obtained by taking the average value $C_{5,\text{fit}} \approx 1/3.94$. (d) Final comparison between the original $N(E)$ (blue), the best fit $C_{5,\text{fit}}\, N_u(C_6E)$ (dashed red), and the two bounds from above of below $N_u(C_4E)$ and $C_5N_u(C_6E)$ (dotted lines).

values of the potential amplitude, $V_{\max} = 1$, 2, and 4. For instance, Fig. 3.4 displays the analysis of the Anderson uniform model for $V_{\max} = 4$. Once again, one can observe that the fit is excellent throughout the spectrum, justifying looking for constants that satisfy Eq. (3.6) (see Table 3.1 for the summary of these results).

We then turned our study of two-dimensional systems. The considered domain is a square of side length $L = 1500$ which corresponds to $N = 2.25 \times 10^6$ sites. Given that this system size is more than 10 times the size of the studied one-dimensional systems, we could average only over 100 realizations for computational reasons. The fact that the side length of the system has been reduced by three orders of magnitude when going from 1D to 2D shifted considerably the lower bound of the energy range that could be explored. In the following simulations, we were unable to go below $E_{\min} \approx 0.2$.

Figure 3.5 displays the analysis for a 2D binary Anderson model. The constants extracted from the analysis are $C_4 = 1/1.53$, $C_{5,\text{fit}} = 1/14.5$, $C_6 = 1/1.42$. The agreement between $N(E)$ and the rescaled landscape law is still good in the whole energy range, even though one can see now that the ratio $N_u(C_6E)/N(E)$ oscillates much more than in the one-dimensional case (see Fig. 3.2c). This observation is even more marked in the case of the 2D uniform Anderson case (see Fig. 3.6). One can observe that the upper and lower bounds are significantly apart in this case, especially at larger energy. This reflects the fact that the prefactor of $N_u(E)$ has to be different at low and at high energy in order to approximate $N(E)$ accurately.

Table 3.1 summarizes the values obtained for the constants in all cases. For the three one-dimensional cases displayed in Figs 3.2-3.4, we performed an error bar analysis by splitting the 1000 realizations into

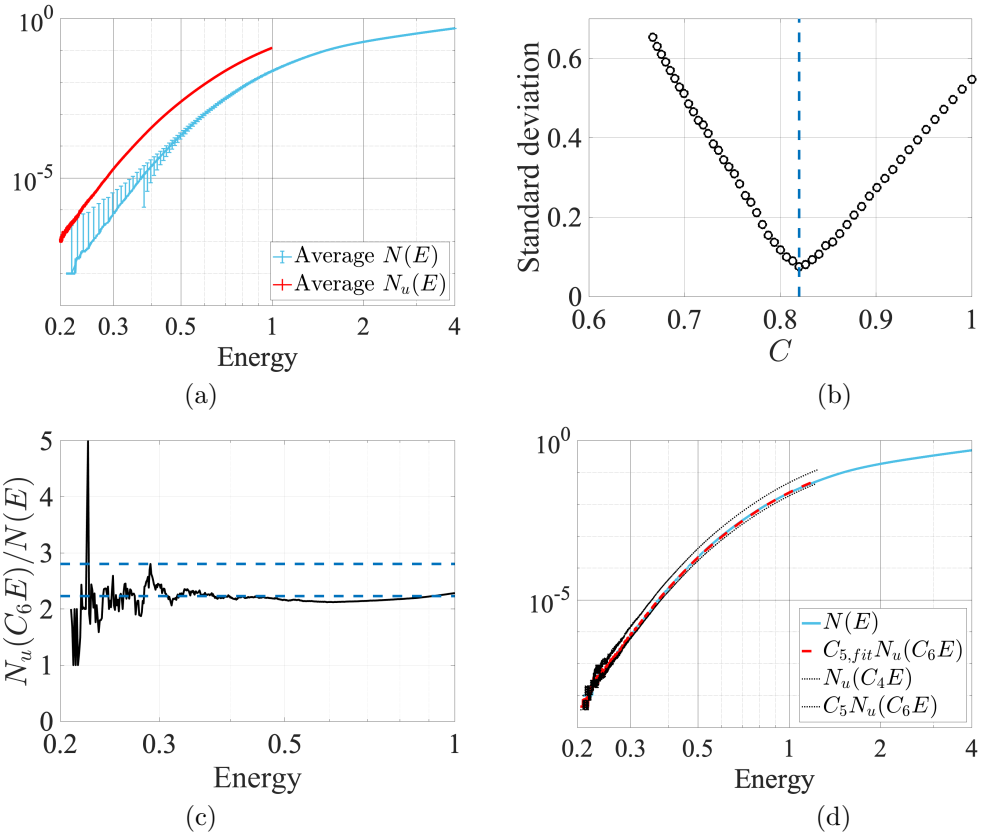

Figure 3.4: (a) $N(E)$ (blue) averaged over 1000 random realizations, and averaged landscape law $N_u(E)$ (red), for a one-dimensional uniform Anderson tight-binding model of size $N = 10^5$ and $V_{\max} = 4$. (b) Standard deviation of the distribution of values of $\ln(N_u(CE)/N(E))$ for various values of C. The minimum around $C = 0.82 \approx 1/1.22$ provides the value of C_6. (c) Plot of $N_u(C_6E)/N(E)$. The maximum in the noiseless part of the graph shows that one can take $C_5 = 1/2.77$. A best fit for $N(E)$ is obtained by taking the average value $C_{5,\text{fit}} \approx 1/2.23$. (d) Final comparison between the original $N(E)$ (blue), the best fit $C_{5,\text{fit}}N_u(C_6E)$ (dashed red), and the two bounds from above of below $N_u(C_4E)$ and $C_5N_u(C_6E)$ (dotted lines).

20 samples of 50 realizations, and computing the constants separately for each sample. The numbers to the right of the symbol $\pm$ correspond to twice the standard deviation.

This table triggers several comments. First, the values of the constants C_4, C_5, $C_{5,\text{fit}}$, C_6 do not seem to depend at all on the domain size (for the same potential law). For instance, for $V_{\max} = 1$ and a binary disorder, the values of C_4^{-1} are 1.26, 1.27, 1.26, for $L = 10^5$, 10^4, 10^3, respectively, while for the same $V_{\max}$ and a uniform disorder the corresponding values are 1.28, 1.28, and 1.27. Similarly, the values of C_6^{-1} are 1.11, 1.1, 1.08 for the same domain sizes for a binary disorder and 1.19, 1.18, and 1.16 for a uniform disorder. The values of $C_{5,\text{fit}}^{-1}$ are 4.08, 4.15, 4.27 for a binary disorder, and 3.94, 4.05, 4.29 for a uniform disorder. Finally, the values of C_5^{-1} are 5.45, 8.18, 5.96 for the binary disorder and 4.85, 7.81, 8.86 for a uniform disorder. These last values are slightly more dispersed, and the reason is that they are determined by the maxima of the curves in frames (c) (Figs 3.2-3.6) which depend on the accuracy of the data in the lower part of the spectrum. This dispersion justifies looking for the values of $C_{5,\text{fit}}$ which are much more reliable than the ones of C_5.

Secondly, the values of $1/C_4$ are quite close to the value $1 + d/4$, where d is the ambient dimension. This value arises in the localization landscape approach as the ratio between a local fundamental eigenvalue inside a localization region and the local minimum of the effective potential $W = 1/u$ [2, 1]. From the definition of $N_u(E)$, at a given energy E, a d-cube of side length $E^{-1/2}$ contributes to $N_u(E)$ only if $\min(W)$ inside the cube is smaller than E. In that situation, one would expect a local fundamental eigenvalue roughly at $(1 + d/4)W_{\min}$. Consequently, there is a natural multiplicative shift in energy

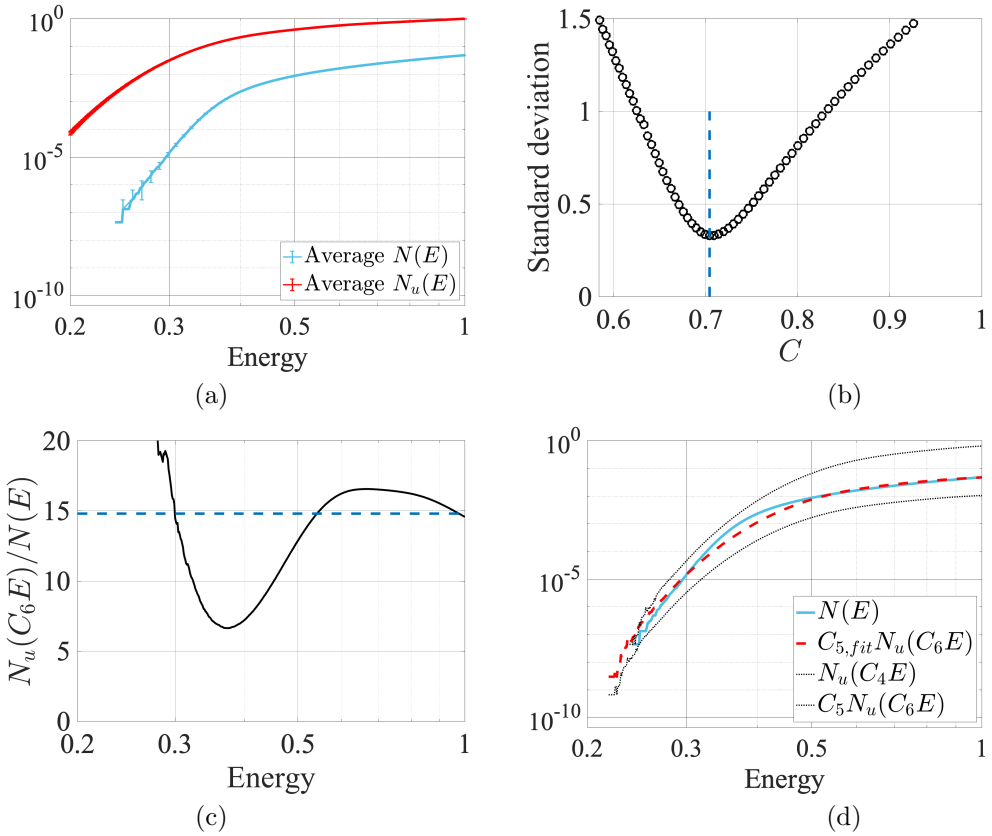

Figure 3.5: (a) $N(E)$ (blue) averaged over 100 random realizations, and averaged landscape law $N_u(E)$ (red), for a two-dimensional binary Anderson tight-binding model of size $N = (1500)^2$. (b) Standard deviation of the distribution of values of $\ln(N_u(CE)/N(E))$ for various values of C. The minimum around $C = 0.7 \approx 1/1.42$ provides the value of C_6. (c) Plot of $N_u(C_6E)/N(E)$. Its maximum for $E > 0.3$ shows that one can take $C_5 = 1/66.4$ which is also almost the best fit $C_{5,\text{fit}} \approx 1/14.8$. (d) Final comparison between the original $N(E)$ (blue), the best fit $C_{5,\text{fit}}\, N_u(C_6E)$ (dashed red), and the two bounds from above of below $N_u(C_4E)$ and $C_5N_u(C_6E)$ (dotted lines).

between $N(E)$ and $N_u(E)$, by a factor $1 + d/4$. This is what is found in our 1D and 2D simulations. One has to note that this shift has already been observed in a very different model, namely the "pieces model" in which a one-dimensional system is partitioned into sub-intervals of random length following a Poisson law [7, 11].

Thirdly, the values of C_6 follow rather closely those of C_4, being only slightly larger ($C_6^{-1} < C_4^{-1}$). We observe that the values of C_6 are closer to those of C_4 for Anderson uniform models.

Fourthly, the results displayed in Table 3.1 help us understand the influence of the disorder strength $V_{\max}$. To that end, we have set $V_{\max} = 1$, 2, or 4 for Anderson binary and Anderson uniform models in 1D and 2D. The theory developed in [8] states that the constants involved in the bounds and which depend on the potential, should in fact not depend of its maximum value but rather on its average value. However, in both Anderson binary and Anderson uniform models, the average value of the potential is $\langle V \rangle = V_{\max}/2$, so it is still directly determined by the disorder strength. In all computed cases, we observe that the values of C_4 and C_6 remain almost unchanged while the value of $C_{5,\text{fit}}$ appears to be roughly proportional to $V_{\max}^{1/2}$, which is a natural scaling in the problem at hand.

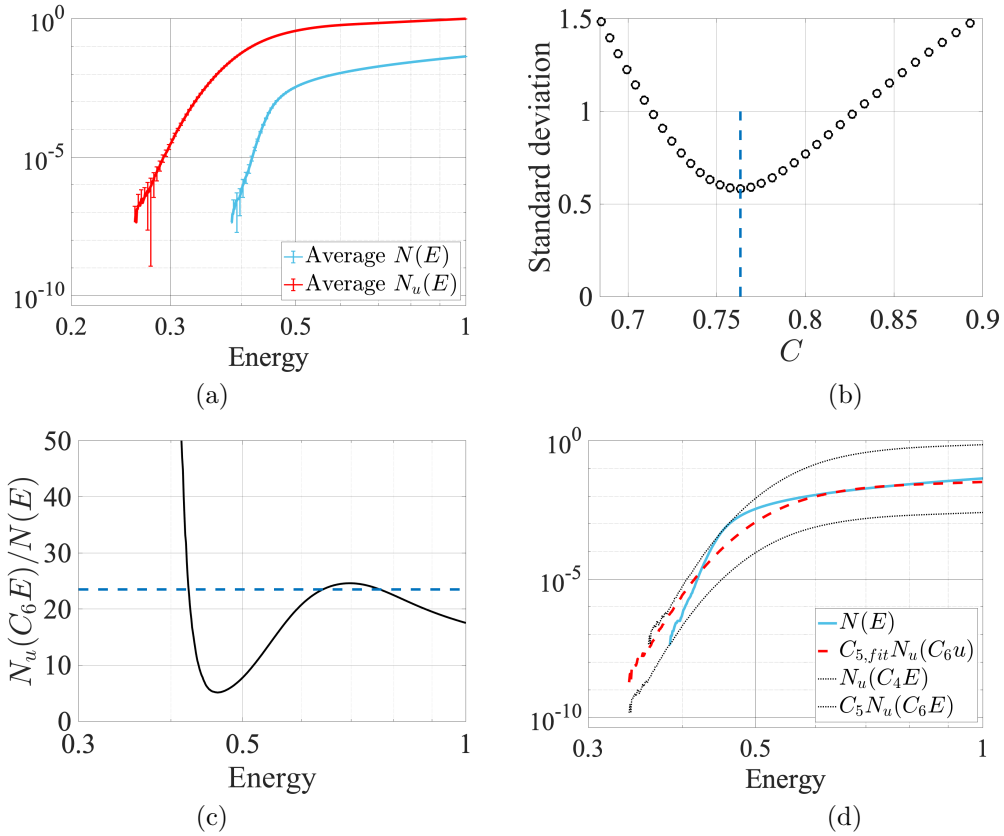

Figure 3.6: (a) $N(E)$ (blue) averaged over 100 random realizations, and averaged landscape law $N_u(E)$ (red), for a two-dimensional uniform Anderson tight-binding model of size $N = (1500)^2$. (b) Standard deviation of the distribution of values of $\ln(N_u(CE)/N(E))$ for various values of C. The minimum around $C = 0.76 \approx 1/1.31$ provides the value of C_6. (c) Plot of $N_u(C_6E)/N(E)$. Its maximum for $E > 0.4$ shows that one can take $C_5 = 1/298$ while the best fit leads to $C_{5,\text{fit}} \approx 1/23.5$. (d) Final comparison between the original $N(E)$ (blue), the best fit $C_{5,\text{fit}}$ $N_u(C_6E)$ (dashed red), and the two bounds from above of below $N_u(C_4E)$ and $C_5N_u(C_6E)$ (dotted lines).

Model		L	$V_{\max}$	$1/C_4$	$1/C_5$	$1/C_{5,\text{fit}}$	$1/C_6$
1D	binary	10^5	1	1.26	5.45	4.08	1.11
			2	1.3	3.78	3.03	1.2
			4	1.26	2.91	2.04	1.32
		10^4	1	1.27	8.18	4.15	1.1
		10^3		1.26	5.96	4.27	1.08
	uniform	10^5	1	1.28	4.85	3.94	1.19
			2	1.24	8.14	3.36	1.19
			4	1.24	2.77	2.23	1.22
		10^4	1	1.28	7.81	4.05	1.18
		10^3		1.27	8.86	4.29	1.16
2D	binary	1500	1	1.53	46.4	14.5	1.42
			2	1.54	33.8	9.00	1.44
	uniform		1	1.39	111	20.1	1.31
			2	1.47	3.34	1.62	1.48

Table 3.2: Summary of the values found for the constants C_4, C_5, $C_{5,\text{fit}}$, and C_6. L is the sidelength (so that the system size is $|\Omega| = L^d$), and $V_{\max}$ is the maximum value of the potential.

Model		L	$V_{\max}$	$1/C_4$	$1/C_5$	$1/C_{5,\text{fit}}$	$1/C_6$
1D	bin.	10^5	1	1.26 ± 0.05	5.45 ± 5	4.08 ± 0.15	1.11 ± 0.02
			2	1.3	3.78	3.03	1.2
			4	1.26	2.91	2.04	1.32
		10^4	1	1.27	8.18	4.15	1.1
		10^3		1.26	5.96	4.27	1.08
	uni.	10^5	1	1.28 ± 0.02	4.85 ± 4.3	3.94 ± 0.2	1.19 ± 0.02
			2	1.24	8.14	3.36	1.19
			4	1.24 ± 0.03	2.77 ± 1.2	2.23 ± 0.05	1.22 ± 0.01
		10^4	1	1.28	7.81	4.05	1.18
		10^3		1.27	8.86	4.29	1.16
2D	bin.	1500	1	1.53	66.4	14.8	1.42
			2	1.54	33.8	9.00	1.44
	uni.		1	1.39	298	23.5	1.31
			2	1.47	4.64	1.83	1.48

Table 3.1: Summary of the values found for the constants C_4, C_5, $C_{5,\text{fit}}$, and C_6. The Anderson models are one- or two-dimensional, with binary or uniform random laws. L is the side length (so that the system size is $|\Omega| = L^d$), and $V_{\max}$ is the disorder strength. For the 3 cases presented in Figs 3.2-3.4, error bars were computed. The numbers displayed after the $\pm$ symbol correspond to two standard deviations. The 2D computations performed were with too few realizations to derive meaningful statistics.

III Low energy scaling law

One can mention an alternative way of relating $N(E)$ and $N_u(E)$ at the bottom of the spectrum, and therefore of extracting the constants involved in Eq. (3.6). This consists of using a corollary of the Landscape Law pertaining to the scaling at low energies for all random i.i.d. potentials. In Ref. [8], it is shown that, in the case of an Anderson tight-binding model where the on-site potential values $\{V_i\}$ follow a random law of cumulative distribution function F (i.e., the probability to have $V_i \leq E$ is $F(E)$), there exist constants γ_1, γ_2, γ_3, γ_4, c_1, c_2 such that

$$\gamma_3 F\left(c_2 E\right)^{\gamma_4 E^{-\frac{d}{2}}} \leq \frac{N(E)}{E^{\frac{d}{2}}} \leq \gamma_1 F\left(c_1 E\right)^{\gamma_2 E^{-\frac{d}{2}}} . \tag{3.7}$$

More specifically, in the case of binary and uniform random laws, one has $F(E) = 1/2$ and $F(E) = E$ for $0 < E < 1$, respectively. Therefore, with a slight change of the meaning of γ_4,

$$\gamma_3\, e^{\gamma_4 E^{-\frac{d}{2}}} \leq N(E)\, E^{-\frac{d}{2}} \leq \gamma_1\, e^{\gamma_2 E^{-\frac{d}{2}}} , \tag{3.8}$$

$$\gamma_3 e^{\gamma_4 E^{-\frac{d}{2}} |\ln(E)|} \leq N(E)\, E^{-\frac{d}{2}} \leq \gamma_1 e^{\gamma_2 E^{-\frac{d}{2}} |\ln(E)|} . \tag{3.9}$$

Let us consider the binary Anderson model. The inequality (3.8) can be rewritten as

$$\begin{aligned} \gamma_4 + \ln(\gamma_3) E^{\frac{d}{2}} &\leq E^{\frac{d}{2}} \ln\left(N(E)\, E^{-\frac{d}{2}}\right) \\ &\leq \gamma_2 + \ln(\gamma_1) E^{\frac{d}{2}} . \end{aligned} \tag{3.10}$$

In other words, the quantity $E^{\frac{d}{2}} \ln\left(N(E)\, E^{-\frac{d}{2}}\right)$ can be bounded between two affine functions of $E^{\frac{d}{2}}$. In

the uniform Anderson model, a similar expression holds with a logarithmic correction:

$$\gamma_4 + \ln(\gamma_3)\frac{E^{\frac{d}{2}}}{|\ln(E)|} \leq \frac{E^{\frac{d}{2}}}{|\ln(E)|}\ln\left(N(E)\,E^{-\frac{d}{2}}\right) \leq \gamma_2 + \ln(\gamma_1)\frac{E^{\frac{d}{2}}}{|\ln(E)|}\,. \tag{3.11}$$

Figure 3.7 displays the graphs of these quantities near $E = 0$ in three different cases already examined: (i) a 1D binary Anderson model (cf. Fig. 3.2), (ii) a 1D uniform Anderson model (cf. Fig. 3.3), and (iii) a 2D uniform Anderson model (cf. Fig. 3.6). In each case, the values of γ_1, γ_2, γ_3, γ_4 are extracted from the scaling behavior of $N(E)$ and $N_u(E)$ (the linear scaling relations expressed in Eqs. (3.10) and (3.11) are shown in dotted lines in the graphs), and then used to compute the effective values of C_5 and C_6 relating N to N_u. The findings are grouped in Table 3.3. One has to underline that the huge computation time required to reach very low values of E limited the accuracy and the range of the data on which the scaling behavior could be efficiently be tested, and led to significant error bars. It precluded us from performing this analysis in the 2D uniform Anderson model. Even in the 2D binary Anderson model (Fig. 3.7c), the scaling is observed for a very limited range of energies. Yet, we observe in 1D the scaling predicted by the mathematical proof in [8] (see Fig. 3.7a,b). The parameters C_5 and C_6 are consistent with the values reported in Table 3.1, confirming that N_u can be used through Eq. (3.6) to approximate $N(E)$ throughout the spectrum. Finally, in 2D (Fig. 3.7c), the discrepancy in the values of C_5 clearly indicates that one cannot find a single prefactor satisfying Eq. (3.6), and that this prefactor has in fact to be modified into a very slowly varying function from $E = 0$ to the largest eigenvalue.

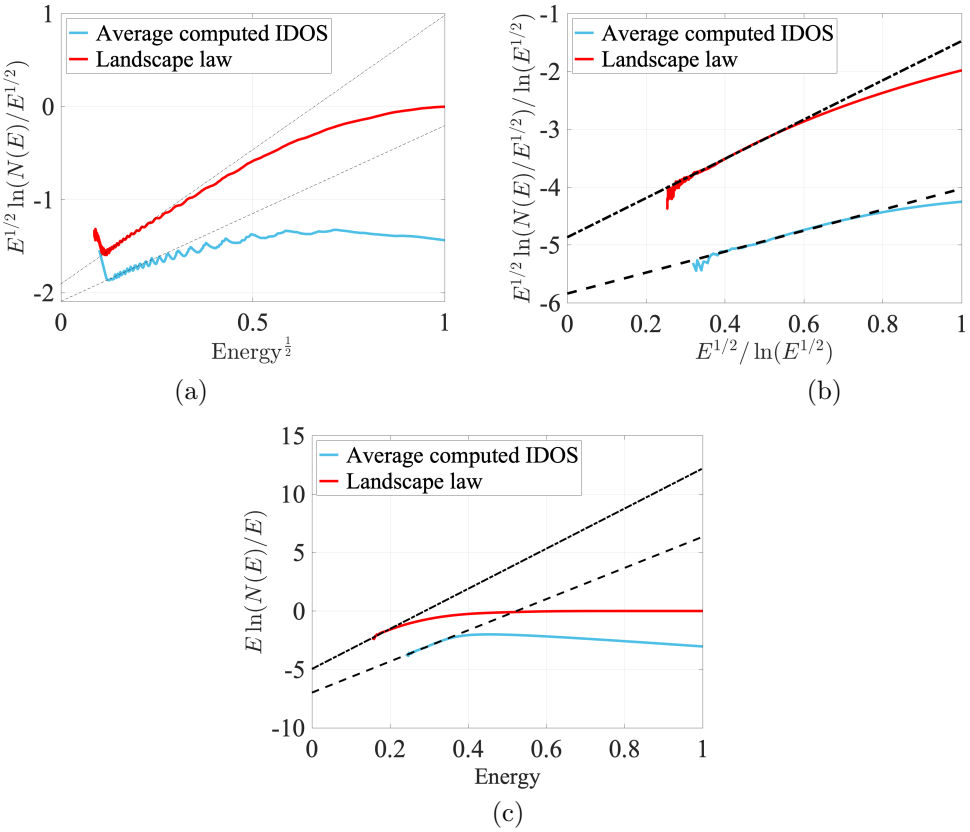

Figure 3.7: Scaling behavior of $N(E)$ and $N_u(E)$ near $E = 0$. The straight lines correspond to the asymptotic linear behaviors appearing in Eqs. (3.10) and (3.11). (a) 1D binary Anderson model. (b) 1D uniform Anderson model. (c) 2D binary Anderson model.

The general picture that emerges from this exhaustive numerical study is that $N_u(E)$ follows very closely the behavior of the actual IDOS $N(E)$ throughout the entire energy range while being at the same time much easier to compute and to handle. Although it is not always possible to approximate $N(E)$ through one single expression such as Eq. 3.6, one can wonder whether we could obtain a very good estimate with

			Table I		scaling	
	Model	$V_{\max}$	$1/C_{5,\text{fit}}$	$1/C_6$	$1/C_5$	$1/C_6$
1D	binary	1	4.08	1.11	2.55	1.2
	uniform	1	3.95	1.19	4.05	1.44
2D	binary	1	14.5	1.42	0.84	1.62

Table 3.3: Comparisons between the constants $C_{5,\text{fit}}$ and C_6 from Table 3.1 and the constants C_5 and C_6 obtained from the scaling analysis near $E = 0$.

almost universal constants. First, we remind that the values found for the constant C_6 are all very close to $1/(1 + d/4)$, for a reason expressed in [1]. A natural universal approximation for $N(E)$, without any fitting parameter, could thus be proportional to $N_u\left(E/(1 + d/4)\right)$. To test this hypothesis, we plot the ratio $N(E)/N_u\left(E/(1 + d/4)\right)$ vs. E for all cases reported in Table 3.1, see Fig. 3.8.

We observe that in 1D, all curves for all tested potentials (binary or Anderson models, different disorder strengths, different system sizes) follow the same pattern, i.e., a slow evolution from a value close to 2 at low energy to a value close to 4 at larger energy. In 2D, the structure is similar with a wider dynamics, from about 1 to about 16. This means that while the IDOS $N(E)$ spans several orders of magnitude (about 6 to 10 in our examples), the function $N_u(E/(1+d/4))$ remains always remarkably close to $N(E)$. The prefactor appears to be different in the low and high energy regime, although it seems within reach, at least in 1D, to derive a very slowly varying function of the energy that would account for this change of prefactor. This change of prefactor between the low and the high energy regimes can be understood. One knows that, at least in the continuous setting, $N(E)/N_u(E)$ is equivalent to $\omega_d/(2\pi)^d$ at higher energy (so independent of the potential), with ω_d the volume of the unit ball in dimension d. Therefore, as soon as $E > V_{\max}$, all cubes satisfy the condition in Eq. (3.4) and $N_u(E) = E^{d/2}$. On the other hand, in the low energy limit, one expects $N(E)$ to behave as $N_u(E/(1 + d/4))$ which implies a different prefactor depending on the type of potential.

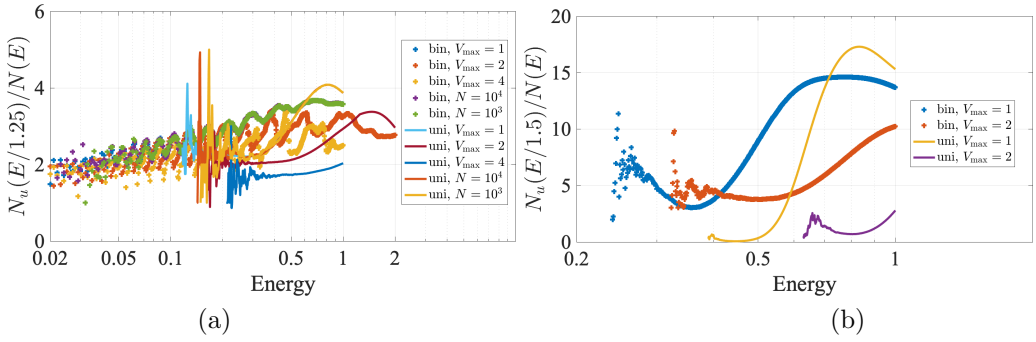

(a) (b)

Figure 3.8: Ratio $N_u\left(E/(1 + d/4)\right)/N(E)$ plotted as a function of the energy E. (Top) For all 1D models reported in Table 3.1. (Bottom) The same plot for all 2D models reported in Table 3.1.

IV Conclusion

In conclusion, we have presented here a new function called the Landscape Law which, for the first time, provides bounds from above and below for the integrated density of states of quantum systems on the entire spectrum. This Landscape Law, derived from the localization landscape, is not only much faster to compute than the entire IDOS especially in random or disordered systems, but it also captures the scaling behavior of Anderson models near the bottom of the spectrum in full generality, for instance accounting for the logarithmic correction distinguishing the binary and uniform Anderson models. In one dimension, the bounds are so close that a single formula approximates the IDOS throughout the entire spectrum, with only a prefactor C_5 and a multiplicative shift on the energy C_6 (consistent with the "$1 + d/4$"

formula found in [1]). In two dimensions, the bounds still provide a satisfactory approximation to the IDOS, but they cannot be merged into a single formula. Instead, one needs to adjust the prefactor from the bottom to the top of the spectrum. In summary, the Landscape Law promises to be a remarkable tool for investigating the properties of IDOS in many random or disordered potentials, with or without spatial correlations, not only theoretically but also numerically. In particular, it opens the perspective of assessing accurately the density of states in systems of very large sizes without having to compute any eigenvalues.

This concludes our study on the properties of the localization landscape on the low energy portion of the spectrum, which started in Chapter 2 where we focused on the information the localization landscape gives on the spatial structure of the eigenfunctions, and ended in this chapter which was focused on the spectral structure. We now move on to the higher energy behavior of the eigenfunctions as we try to understand the reasons for localization when the effective potential no longer confines the eigenfunctions.

Bibliography

[1] D. N. Arnold, G. David, M. Filoche, D. Jerison, and S. Mayboroda. Computing spectra without solving eigenvalue problems. *SIAM J. Sci. Comput.*, 41:B69–B92, 2017. URL: https://arxiv.org/abs/1711.04888.

[2] D. N. Arnold, G. David, M. Filoche, D. Jerison, and S. Mayboroda. Localization of eigenfunctions via an effective potential. *Commun. Part. Diff. Eq.*, 44(11):1186–1216, 2019. doi:10.1080/03605302.2019.1626420.

[3] D. N. Arnold, G. David, D. Jerison, S. Mayboroda, and M. Filoche. Effective confining potential of quantum states in disordered media. *Phys. Rev. Lett.*, 116:056602, 2016. doi:10.1103/PhysRevLett.116.056602.

[4] D. N. Arnold, M. Filoche, S. Mayboroda, W. Wang, and S. Zhang. The landscape law for tight binding Hamiltonians, 2021. arXiv:2101.03282.

[5] M. Benderskii and L. Pastur. On the spectrum of the one-dimensional Schrödinger equation with a random potential. *Mat. Sb.*, 11:245–256, 1970. doi:10.1070/SM1970v011n02ABEH002068.

[6] M. Biskup and W. Konig. Long-time tails in the parabolic Anderson model with bounded potential. *Ann. Probab.*, 29(2):636–682, 2001.

[7] A. Comtet and C. Texier. Comment on "effective confining potential of quantum states in disordered media". *Phys. Rev. Lett.*, 124:219701, 2020. doi:10.1103/PhysRevLett.124.219701.

[8] G. David, M. Filoche, and S. Mayboroda. The landscape law for the integrated density of states. *arXiv*, 2019. URL: https://arxiv.org/abs/1909.10558.

[9] M. D. Donsker and S. S. Varadhan. Asymptotics for the Wiener sausage. *Commun. Pure Appl. Math.*, 28(4):525–565, 1975.

[10] A. Elgart et al. Lifshitz tails and localization in the three-dimensional Anderson model. *Duke Math. J.*, 146(2):331–360, 2009.

[11] M. Filoche, D. Arnold, G. David, D. Jerison, and S. Mayboroda. Filoche et al. reply:. *Phys. Rev. Lett.*, 124:219702, 2020. doi:10.1103/PhysRevLett.124.219702.

[12] M. Filoche and S. Mayboroda. Universal mechanism for Anderson and weak localization. *Proc. Natl. Acad. Sci. USA*, 109(37):14761–14766, 2012. doi:10.1073/pnas.1120432109.

[13] A. Grabsch, C. Texier, and Y. Tourigny. One-dimensional disordered quantum mechanics and Sinai diffusion with random absorbers. *J. Stat. Phys.*, 155(2):237–276, 2014. doi:10.1007/s10955-014-0957-3.

[14] W. Kirsch and F. Martinelli. Large deviations and Lifshitz singularity of the integrated density of states of random Hamiltonians. *Commun. Math. Phys.*, 89(1):27–40, 1983.

[15] W. Kirsch and B. Metzger. The integrated density of states for random Schrödinger operators. *in: F. Gesztesy, P. Deift, C. Galvez, P. Perry, W. Schlag (Editors): Spectral Theory and Mathematical Physics: A Festschrift in Honor of Barry Simon's 60th Birthday.*, page 649–696, 2007. doi:10.1090/pspum/076.2/2307751.

[16] F. Klopp. Weak disorder localization and Lifshitz tails. *Comm. Math. Phys.*, 232:125–155, 2002. doi:10.1007/s00220-002-0727-y.

[17] F. Klopp. Weak disorder localization and Lifshitz tails: Continuous Hamiltonians. *Ann. Henri Poincaré*, 3:711–737, 2002. doi:10.1007/s00023-002-8633-6.

[18] W. König. *The Parabolic Anderson Model, Random Walk in Random Potential*. Pathways in Mathematics. Springer, 2016. URL: https://www.springer.com/gp/book/9783319335957#aboutBook.

[19] I. Lifshits, S. Gredeskul, and L. Pastur. *Introduction to the Theory of Disordered Systems*. Wiley, New York, 1988.

[20] I. Lifshitz. Energy spectrum structure and quantum states of disordered condensed systems. *Phys.-Uspekhi*, 7(4):549–573, 1965. doi:10.1070/pu1965v007n04abeh003634.

[21] I. M. Lifshitz. The energy spectrum of disordered systems. *Adv. Phys.*, 13(52):483–536, 1964. doi:10.1080/00018736400101061.

[22] M. L. Lyra, S. Mayboroda, and M. Filoche. Dual landscapes in Anderson localization on discrete lattices. *EPL*, 109:47001, 2015. doi:http://dx.doi.org/10.1209/0295-5075/109/47001.

[23] G. Mezincescu. Internal Lifschitz singularities of disordered finite-difference Schrödinger operators. *Commun. Math. Phys.*, 103(1):167–176, 1986.

[24] S. Nakao. On the spectral distribution of the Schrödinger operator with random potential. *Japan. J. Math. New series*, 3(1):111–139, 1977.

[25] T. M. Nieuwenhuizen and J. M. Luck. Singularities in spectra of disordered systems: an instanton approach for arbitrary dimension and randomness. *EPL*, 9(5):407–413, 1989. doi:10.1209/0295-5075/9/5/001.

[26] B. N. Parlett. *The Symmetric Eigenvalue Problem*. Society for Industrial and Applied Mathematics, 1998. arXiv:https://locus.siam.org/doi/pdf/10.1137/1.9781611971163, doi:10.1137/1.9781611971163.

[27] L. Pastur. Behavior of some Wiener integrals as t $\to \infty$ and the density of states of Schrödinger equations with random potential. *Theoret. Math. Phys.*, 32(1):615–620, 1977.

[28] L. Pastur and A. Figotin. *Spectra of Random and Almost-Periodic Operators*. Grundlehren der mathematischen Wissenschaften. Springer, 1992. URL: https://www.springer.com/gp/book/9783642743481.

[29] A. Politi and T. Schneider. Corrections to the lifshitz tail and the long-time behaviour of the trapping problem. *Europhysics Letters (EPL)*, 5(8):715–720, 1988. doi:10.1209/0295-5075/5/8/009.

[30] B. Simon. Lifschitz tails for the Anderson model. *J. Stat. Phys.*, 38(1-2):65–76, 1985. doi:10.1007/BF01017848.

Chapter 4

High Energy Localization

I Introduction

In the preceding chapters, we have focused on the properties of the low energy eigenfunctions. This is because, in the localization landscape formalism, the effective confining potential gives an almost classical interpretation of the energy of the localized eigenfunctions at the bottom of the spectrum. These eigenfunctions correspond to localized modes in a given sub-region through the equation (1.23) which we recall here [3, 4, 5, 12, 13]:

$$\langle\psi|\hat{H}|\psi\rangle = \left\langle u\nabla\left(\frac{\psi}{u}\right)\middle| u\nabla\left(\frac{\psi}{u}\right)\right\rangle + \langle\psi|\hat{W}|\psi\rangle\,. \tag{4.1}$$

The energy is almost contained in the effective potential term for low-energy eigenfunctions. However, under certain conditions, namely in 1D and 2D for Anderson-like potentials, the eigenfunctions remain localized at higher energies. On the contrary, in 3D, depending on the amplitude of disorder, a localization/delocalization transition might exist (Anderson transition). In that situation, the eigenfunctions delocalize above a certain energy threshold, also called *the mobility edge*. Although scaling theory has been used to show the existence of this mobility edge [1], there is as of yet no theory that predicts analytically this threshold, nor the critical exponents that govern the divergence of the localization length in the vicinity of the threshold.

In this chapter, we explore the high energy localization through the lens of the localization landscape approach. Below is the reduced eigen-equation (1.22) which is obtained by the conjugaison operation of the Hamiltonian ($\frac{1}{u}\,\hat{H}\,u$):

$$-\frac{1}{u^2}\boldsymbol{\nabla}\cdot\left(u^2\boldsymbol{\nabla}\phi\right) + W\phi = E\phi, \tag{4.2}$$

where $\psi \equiv u\phi$. Obviously, the localization of ψ is equivalent to the localization of ϕ. The second term of the left-hand side is the aforementioned effective potential term responsible for the low-energy localization, while the first term of the left-hand side can be understood as a Laplace-Beltrami operator.

Previously, we have ignored the effects of the first term on the localization of the eigenfunctions, arguing that this first term corresponds to an effective kinetic energy while the second term corresponds to an effective potential energy. For the study of the high-energy localization, we will this time do the opposite: ignore the potential term (since at high enough energies it can be neglected) and look at the localization properties of the eigenfunctions of the newly defined operator.

We will from now investigate the properties of the equation (which we will call the reduced equation):

$$-\frac{1}{u^2}\boldsymbol{\nabla}\cdot\left(u^2\boldsymbol{\nabla}\phi\right) = E\phi. \tag{4.3}$$

(4.3) defines a spectral problem. In this chapter we will study the properties of these eigenfunctions and their level statistics for 1D, 2D and 3D systems in order to observe the localization/delocalization

transition. We will use the finite element method for the numerical computations. Once again we will rely on the PETSc and SLEPc libraries for C++ [9, 8, 19, 31].

II The one-dimensional case: absence of transition and small localization lengths

We will start by studying the one-dimensional case where the most results are known. Indeed, in tight-binding models transfer matrix and perturbation methods have shown that localization occurs no matter the potential strength and have also provided an expression for the localization length [20, 21, 24, 33].

II.1 Study of the eigenfunctions and their localization length

The goal of this first part is to assess the eigenfunctions' localization at high energies whether we consider the original or the reduced equation.

The domain size is 10,000 and the discretization is such that there are 10 points per unit length, which means that there are a total of 100,000 points in the mesh. The potential is piece-wise constant on each interval of length 1 and its values follow a uniform random law taking values in $[0, 1]$. In Figure 4.1, we see the change in the eigenfunctions of the original equation as the energy increases. They are always localized but their localization length increases. As can be seen in the right column where the figures are zoomed in on intervals of size 200, the eigenfunctions' effective support increases as their energy increases. In Figure 4.2, we display the change in the properties of the eigenfunctions at different energies. This time, at very small energies, the eigenfunctions are delocalized completely. They then localize sharply as the energy increases. Beyond that, they remain localized, but with a localization length that increases with energy.

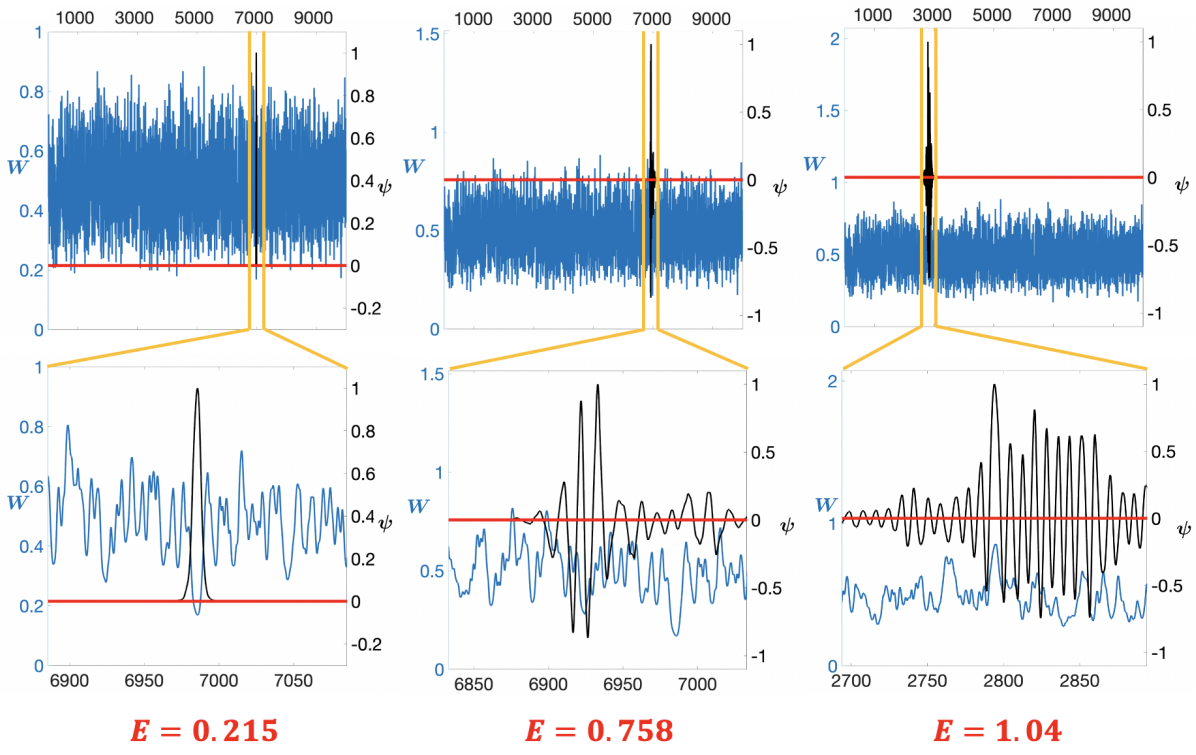

Figure 4.1: Three eigenfunctions (in black) with the effective confining potential (in blue). The graphs of the eigenfunctions are centered vertically on their energy with respect to the effective confining potential. In the top row we have displayed the entire domain, while the bottom row is a zoomed in view (constant interval of size 200). Left: $E = 0.215$. Center: $E = 0.758$. Right: $E = 1.04$.

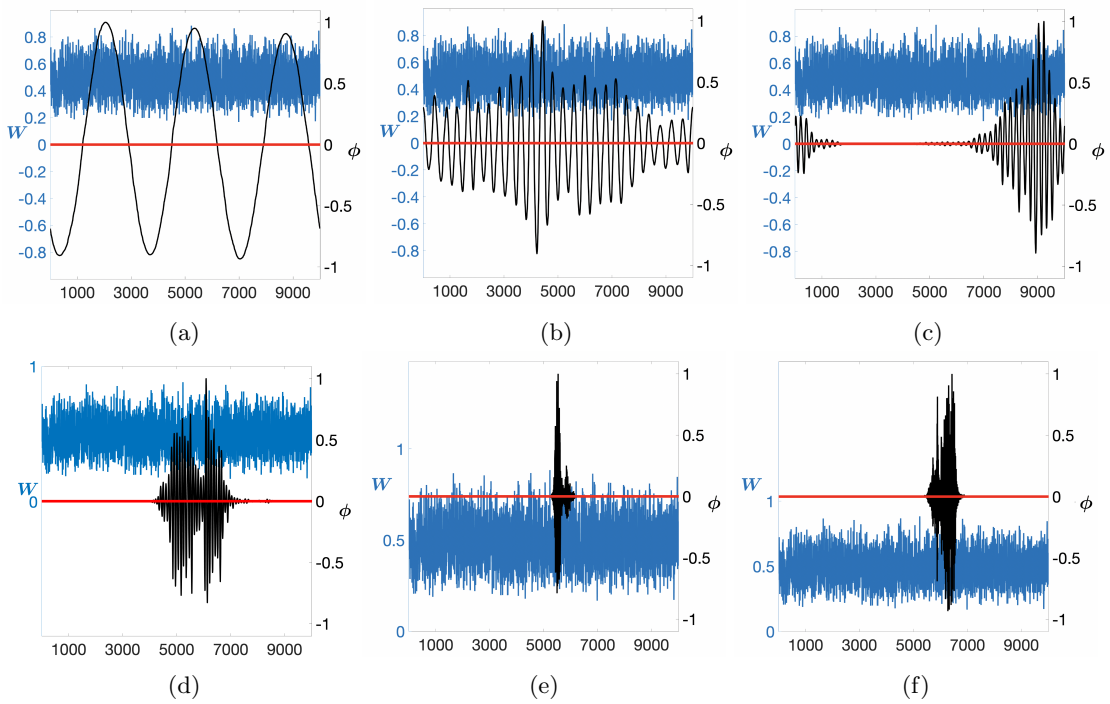

Figure 4.2: Six eigenfunctions (in black) with the effective confining potential (in blue). The graphs of the eigenfunctions are centered vertically on their energy with respect to the effective confining potential. (a) $E = 3 \cdot 10^{-6}$. (b) $E = 1.89 \cdot 10^{-4}$. (c) $E = 7.63 \cdot 10^{-4}$. (d) $E = 3.07 \cdot 10^{-3}$. (e) $E = 0.740$. (f) $E = 1.04$.

These few examples seem to indicate that the eigenfunctions of the reduced equations are all localized above a small energy and have a localization length that increases with their energy.

Computing the localization length can be tricky. It is defined as the rate of the exponential decay of the envelope of the localized wave functions: $\psi(r) \sim e^{-|r/\xi|}$. While the eigenfunction in Figure 4.2c has a clearly defined exponentially decaying envelope, the eigenfunction in Figure 4.2d has secondary peaks which makes this computation difficult.

In order to overcome this difficulty, we use the participation ratio, defined as:

$$\mathrm{PR}_n = \frac{\left(\int |\psi_n|^2 \mathrm{d}x\right)^2}{|\Omega| \int |\psi_n|^4 \mathrm{d}x}, \tag{4.4}$$

which we have normalized by the system size.

We now compute the participation ratio of all eigenfunctions at the bottom of the spectrum for various parameters of our problem (dimensions, strength of potential, original or reduced equation). For the purpose of this analysis (and for all other analyses in this chapter) we limit ourselves in our computations to at most the 10% first eigenfunctions, as the numerical results for the rest have much larger errors [34].

We have calculated the participation ratio for all eigenfunctions from $E = 0$ to $E \approx 25$ (Figure 4.3). Figures 4.3a and 4.3b correspond to the original and reduced equations, respectively, with $V_{\max} = 1$. We now have confirmation of what we observed in Figures 4.1 and 4.2: the low-energy eigenfunctions are localized, and their localization lengths increase with energy (the participation ratio increases with the localization length). The very first eigenfunctions, in the case of the reduced equation, are delocalized at very low energies as can be seen in Figure 4.4. This equation can be rewritten as:

$$-\frac{1}{u^2} \boldsymbol{\nabla} \cdot \left(u^2 \boldsymbol{\nabla} \phi\right) = E\phi. \tag{4.5}$$

$$\Leftrightarrow -\Delta\phi - \left(\boldsymbol{\nabla} \log u^2\right) \cdot \boldsymbol{\nabla}\phi = E\phi \tag{4.6}$$

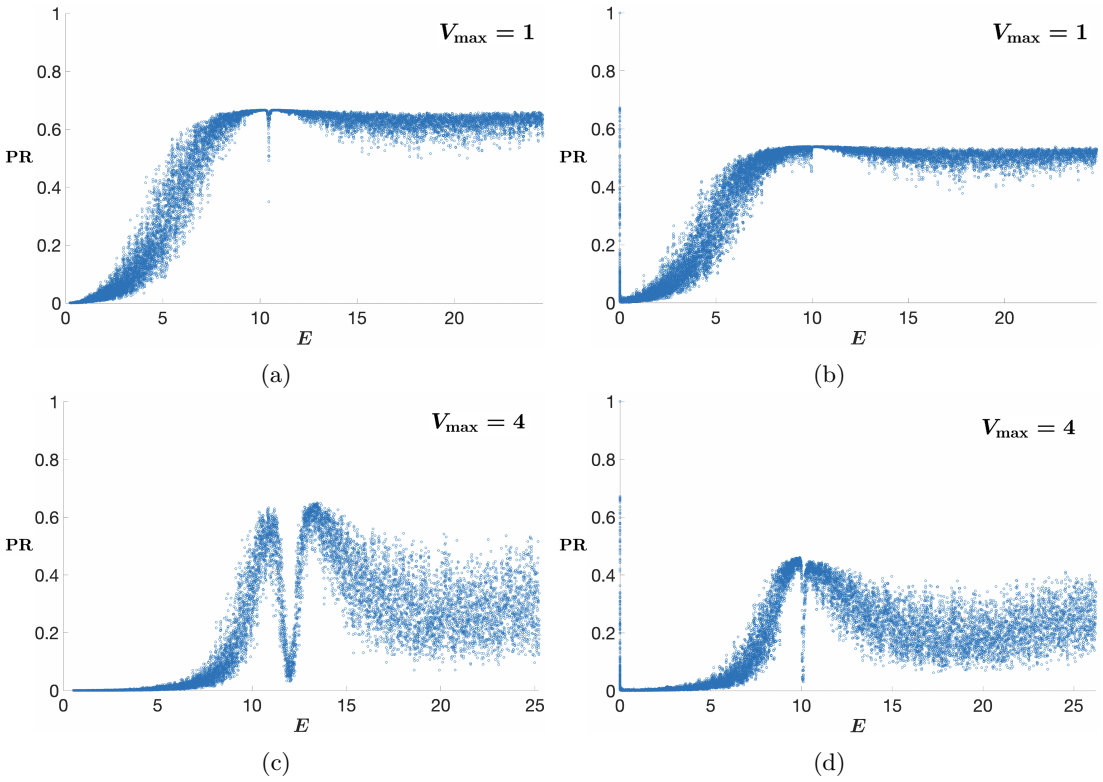

Figure 4.3: The PR of all eigenfunctions from $E = 0$ to around $E = 25$ for different parameters. (a) Original equation and $V_{\max} = 1$. (b) Reduced equation and $V_{\max} = 1$. (c) Original equation and $V_{\max} = 4$. (d) Reduced equation and $V_{\max} = 4$.

There is an immediate obvious solution to equation 4.6 which is the constant solution of eigenvalue 0. This solution is the most delocalized function that can exist, and has an PR of the order of 1. According to their PRs (Figures 4.3b and 4.3d), the eigenfunctions then transition from delocalized states to localized states very rapidly (for energies of the order of 10^{-3}).

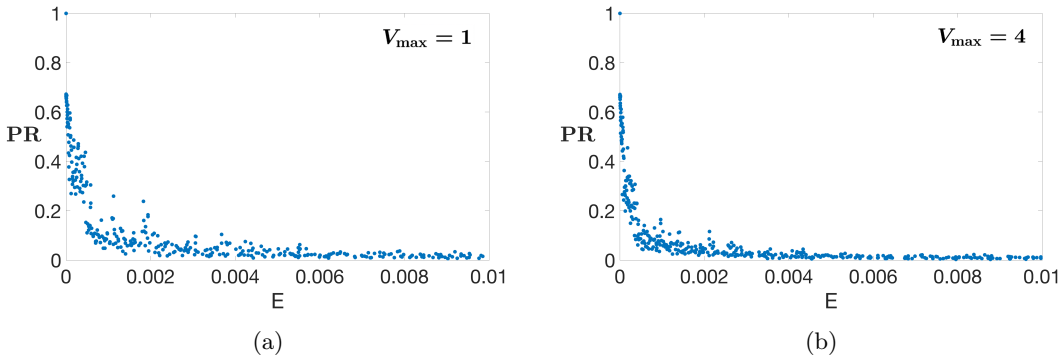

Figure 4.4: The PR of all eigenfunctions from $E = 0$ to $E = 0.01$ of the reduced equation for (a) $V_{\max} = 1$ and (b) $V_{\max} = 4$.

There is a particularity in Figure 4.3 we want to stress here. It is more obvious in Figure 4.3c and 4.3d, but there is a drop in the participation ratio around $E = 10$. This would seem to indicate that the eigenfunctions localize once again at a certain energy. Figure 4.5 shows the behavior of the eigenfunctions near this anomalous energy. We can see from these figures that indeed the localization length of these eigenfunctions decreases with increasing energy at this particular range. As of yet we have been unable to explain this phenomenon. We cannot exclude numerical errors, but this behavior has been consistently reproduced over our simulations.

Finally, in Figure 4.6, we have represented a condensed version of our data on the PRs. We calculated

the PRs for 7 different potential strengths and for 5 different realizations of disorder. Then, we computed the average of the PRs of the eigenfunctions of energy in intervals of size 0.01. Regardless of the potential strength and of the type of equation (original or reduced), the PRs remain low, which suggests that the eigenfunctions are localized. The PRs increase with $E/V_{\max}$, since the localization length of the eigenfunctions increases with their energy.

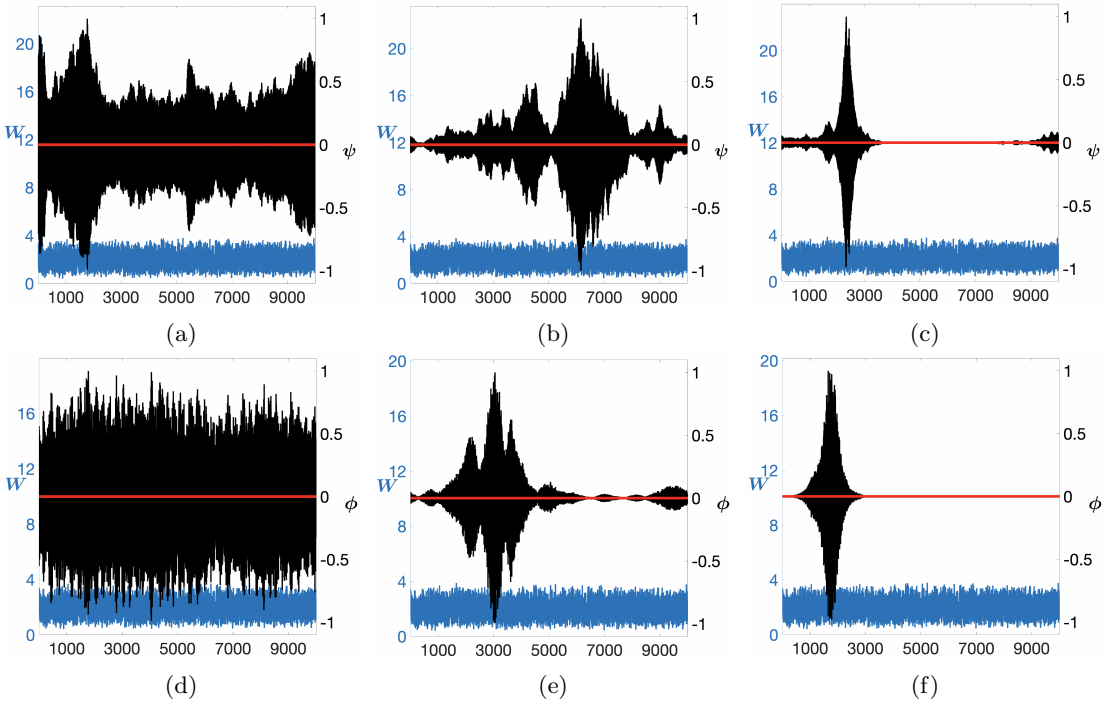

Figure 4.5: Sample eigenfunctions of both the original and reduced equation for $V_{\max} = 4$ (top row: original equation; bottom row: reduced equation). (a) Original equation: $E = 11.57$. (b) Original equation: $E = 11.81$. (c) Original equation: $E = 12.01$. (d) Reduced equation: $E = 9.99$. (e) Reduced equation: $E = 10.04$. (f) Reduced equation: $E = 10.09$.

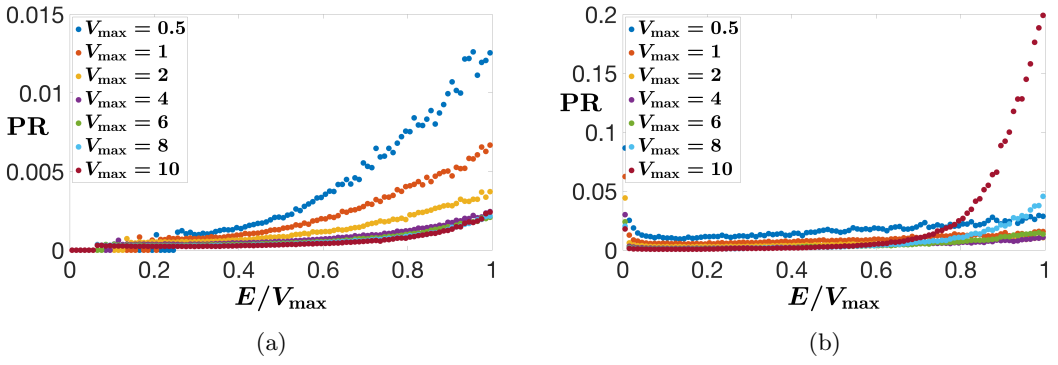

Figure 4.6: The PR of the (a) original and (b) reduced equations for $V_{\max} = 0.5, 1, 2, 4, 6, 8,$ and 10. We compare eigenfunctions of same reduced energy $E/V_{\max}$. Each point is the average of the PRs of all eigenfunctions whose energy are in the same interval of size 0.01 and for 5 different realizations of disorder.

II.2 The distribution of the energy spacings and their ratios: characterizing the localizing phase

II.2.a Energy spacings

Our conjecture is this: removing the effective confining potential term in the Anderson equation does not change the localization properties of the eigenfunctions in 1D. To test this assumption, we now explore the statistics of the eigenvalues, as previously explained in Chapter 1. We recall that one possible way to test the onset of localization or delocalization is through the distribution of the energy spacings by fitting the computed distribution with the Poisson and Wigner distributions [2, 18, 32, 10] or of their ratios by comparing the average of these distributions with the known averages [7, 11, 17, 27].

We use mostly the same data as for the calculation of the participation ratios. We compute all the eigenvalues in a certain interval, and then calculate the differences of the subsequent eigenvalues: $s_n = E_n - E_{n-1}$. These are the *energy spacings*. We then divide these spacings by their average $\delta = \langle s \rangle$ to normalize the distribution.

There are many different types of distributions the energy spacings can follow. We will focus mainly here on two, the first one being the Poisson distribution: $P_P(s) = \frac{1}{\delta} \exp\left(-\frac{s}{\delta}\right)$, which is characterized by no repulsion between subsequent levels (since the most probable value for the difference between subsequent levels is 0). The Poisson distribution therefore corresponds to localized eigenfunctions, since they do not "interact" with each other. Conversely, the Wigner distribution, $P_{\mathrm{GOE}}(s) = \frac{\pi}{2} s \exp\left(-\frac{\pi}{4} s^2\right)$ is characterized by repulsion between the subsequent eigenvalues. This distribution is therefore linked to delocalized eigenfunctions.

We compute these distributions for the original and the reduced equations for various values of the potential strength. After computing these statistics, we fit them with either the Poisson distribution or the Wigner distribution by calculating the coefficient of determination R^2. We also compare the average spacing δ for each parameter.

The statistics of the eigenfunctions for the 1D equation are displayed in Figure 4.7.

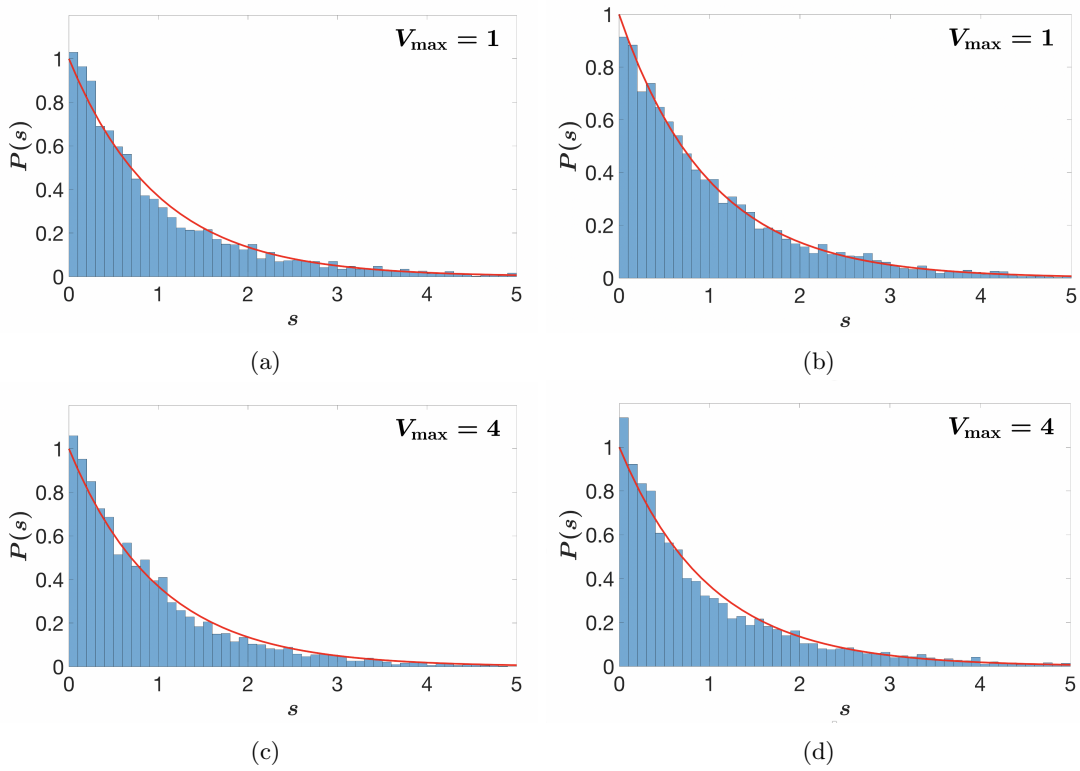

Figure 4.7: Statistics of the energy spacings (in blue bars) of about 10,000 eigenfunctions starting at the beginning of the spectrum for different potential strengths. We have also displayed the exact Poisson distribution in red. A summary of the values of δ and R^2 is displayed in Table 4.1. (a) Original equation and $V_{\max} = 1$. (b) Reduced equation and $V_{\max} = 1$. (c) Original equation and $V_{\max} = 4$. (d) Reduced equation and $V_{\max} = 4$.

Given the first eigenfunctions for the reduced equations are always delocalized, we have excluded them from our analysis, so as to not mix different types of eigenfunctions together. We have therefore excluded the 1000 first eigenvalues for the reduced equation.

The results from Figure 4.7 and Table 4.1 are quite clear, all of these statistics fit the Poisson distribution, with the smallest $R^2 = 0.9792$. Interestingly, the average spacing δ increases with the potential strength for the original equation, stays quite constant for the reduced equation.

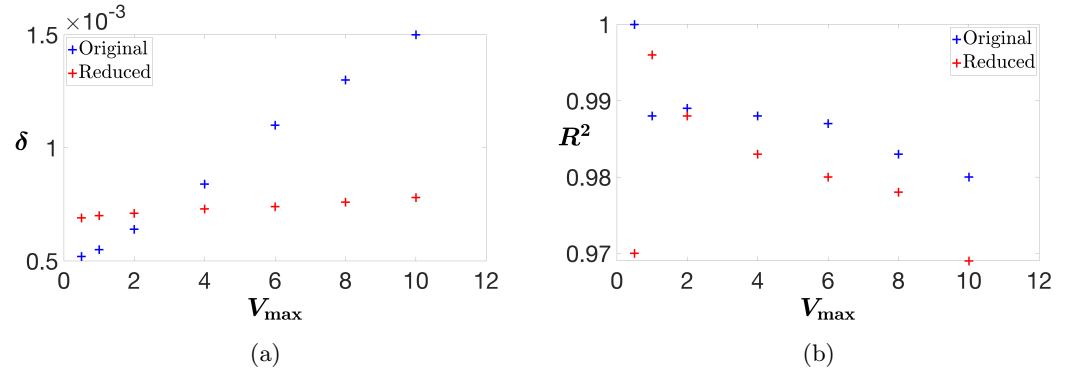

Figure 4.8: The values found for δ and R^2 for the various potential strengths

	Original		Reduced	
$V_{\max}$	δ	R^2	δ	R^2
0.5	$5.2\ 10^{-4}$	1.00	$6.9\ 10^{-4}$	0.970
1	$5.5\ 10^{-4}$	0.988	$7.0\ 10^{-4}$	0.996
2	$6.4\ 10^{-4}$	0.989	$7.1\ 10^{-4}$	0.988
4	$8.4\ 10^{-4}$	0.988	$7.3\ 10^{-4}$	0.983
6	$1.1\ 10^{-3}$	0.987	$7.4\ 10^{-4}$	0.980
8	$1.3\ 10^{-3}$	0.983	$7.6\ 10^{-4}$	0.978
10	$1.5\ 10^{-3}$	0.980	$7.8\ 10^{-4}$	0.969

Table 4.1: Summary of the values found for δ and R^2.

II.2.b The energy spacings ratios

The problem with the definition of the energy spacings is that the average $\delta = \langle s \rangle$ is supposed to represent the "local" average gap, which is difficult to determine when considering a very large range of eigenvalues [27]. To overcome this challenge, we define the *energy spacings ratios* as:

$$r_n = \min(s_n, s_{n+1}) / \max(s_n, s_{n+1}). \tag{4.7}$$

The distribution of the ratios differ from the distributions of the spacings. For localized eigenfunctions the distribution is: $P_l(r) = 2/(1+r)^2$ with support $[0, 1]$ and its average is $\langle r \rangle_P = 2\ln 2 - 1 \approx 0.386$ [7, 6]. The distribution of the ratios for delocalized eigenstates is not known analytically although it does resemble the Wigner distribution mentioned before. We do know the numerical value for the average of the ratios: $\langle r \rangle \approx 0.5295$.

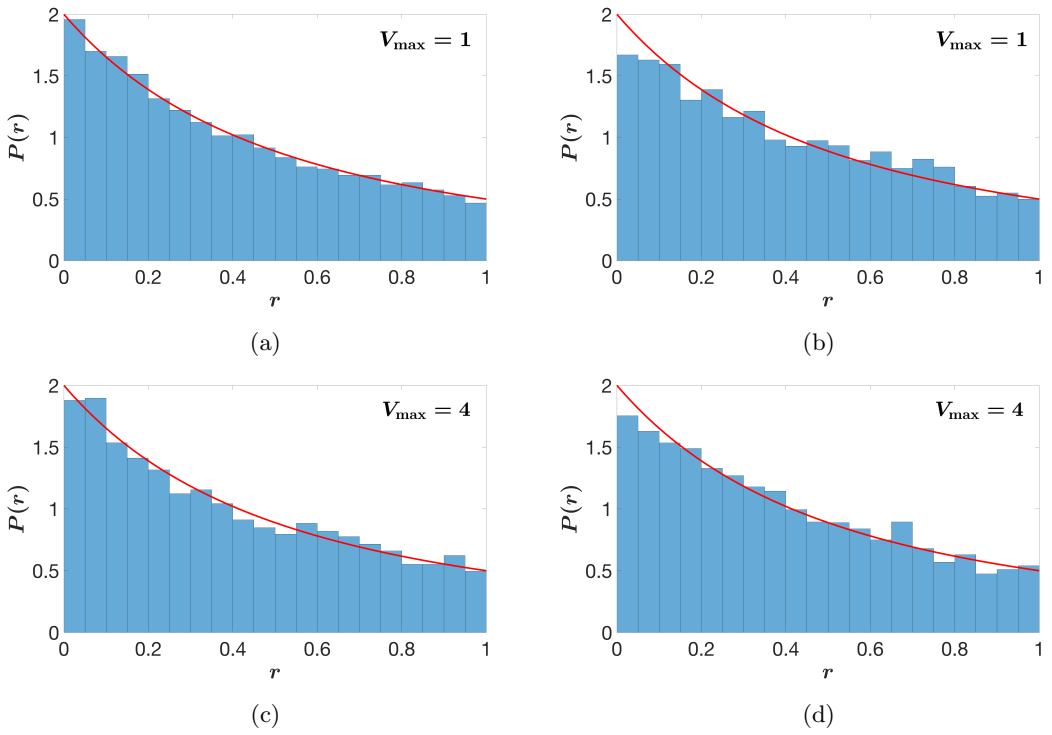

Figure 4.9: Statistics of the energy spacings ratios (in blue bars) of about 5,000 eigenfunctions starting at the beginning of the spectrum for different potential strengths. We have also displayed the exact $2/(1+r)^2$ distribution in red. A summary of the values of $\langle r \rangle$ and R^2 is displayed in Table 4.2. (a) Original equation and $V_{\max} = 1$. (b) Reduced equation and $V_{\max} = 1$. (c) Original equation and $V_{\max} = 4$. (d) Reduced equation and $V_{\max} = 4$.

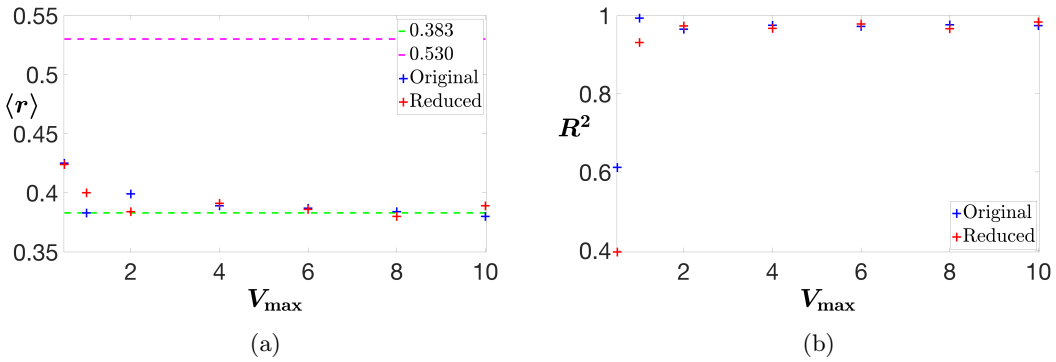

Figure 4.10: The values found for $\langle r \rangle$ and R^2 for the various potential strengths

We have repeated the same analysis as in subsection II.2.a but this time considering the energy spacings ratios. In Figure 4.9 we have displayed the histograms of these ratios for both the original and reduced equations for $V_{\max} = 1$ and 4. A summary of the values computed for $\langle r \rangle$ and R^2 is shown in Figure 4.10 and Table 4.2. These results are similar to the results for the analysis of the spacings, but not as conclusive for the low potential strength case. Indeed, for $V_{\max} = 0.5$, the fit is not accurate, and the values of $\langle r \rangle$ are far off from the exact value of 0.383. For potential strengths greater than 0.5 however, the coefficients of determination are all close to 1, and the values of $\langle r \rangle$ are off by at most 2%. Evidently for potential strengths that are too weak, the eigenstates appear delocalized because of finite size effects: the domain is too small compared to their localization length. We have once again further evidence that in 1D, the eigenfunctions of the original and reduced equations are all localized (barring the first few eigenfunctions of the reduced equation).

	Original		Reduced	
$V_{\max}$	$\langle r \rangle$	R^2	$\langle r \rangle$	R^2
0.5	0.425	0.612	0.424	0.396
1	0.383	0.993	0.400	0.931
2	0.399	0.965	0.384	0.973
4	0.389	0.975	0.391	0.967
6	0.387	0.972	0.386	0.978
8	0.384	0.976	0.380	0.966
10	0.380	0.974	0.389	0.983

Table 4.2: Summary of the values found for $\langle r \rangle$ and R^2.

To summarize the results of this section, we have shown first qualitative evidence and then quantitative evidence that in 1D, both the original and reduced eigen-equations have localized eigenstates. We have done the former by observing the spatial distribution of the eigenfunctions, and the latter by computing the PRs of the eigenfunctions as a surrogate for the localization length, and by studying the distributions of both the energy spacings and their ratios.

III The two-dimensional case

In two dimensions, the scaling theory suggests that there is no localization/delocalization transition, and that all the eigenfunctions remain localized [1, 14, 23]. However, there is no explicit formula for the localization length except for a few specific cases [15, 16]. We do know that it increases exponentially with the mean free path [22]. However, for computational reasons, it is much more difficult to compute in domains of large side-length. It is however possible to compensate this by increasing the potential strength.

In this section we reiterate the analysis already performed in the 1D case. We will start by looking qualitatively at the eigenfunctions, followed by a more quantitative approach where we will compute the PRs and the distributions of the energy spacings and their ratios.

III.1 Study of the eigenfunctions and their localization length

Our objective here is to show visually that the eigenfunctions of both the original and reduced equations are localized throughout the spectrum. We chose a domain size of $L^2 = 100 \times 100$ and a mesh size of 0.2×0.2 for a total of 250,000 degrees of freedom. The potential is piece-wise constant on each square of side-length 1 and its values follow a uniform random law taking values in $[0, 100]$. We have increased the potential strength compared to the 1D case since our domain is smaller and we therefore require the eigenfunctions to be more localized.

In Figure 4.11, as in the 1D case, we see the change in the eigenfunctions of the original equation as the energy increases. They are always localized but their localization length increases. In Figure 4.12, we display 4 eigenfunctions of the reduced equation. As in the one-dimensional case, at very small energies, the eigenfunctions are delocalized completely. They then localized sharply as the energy increases. Beyond that, they remain localized, but with an increasing localization length.

We have shown qualitative evidence that the eigenfunctions of both the original and reduced equations remain localized throughout the spectrum, but we would like quantitative evidence. In the same fashion as in the preceding section, we will use the participation ratio as a surrogate to study the localization length, as it is even more difficult to compute in the 2D case than in the 1D case.

Figure 4.14 summarizes our results. Each point represents the average PR of all eigenfunctions in an energy interval of size 0.01 around E. We would like to explore higher potential strengths, however, the

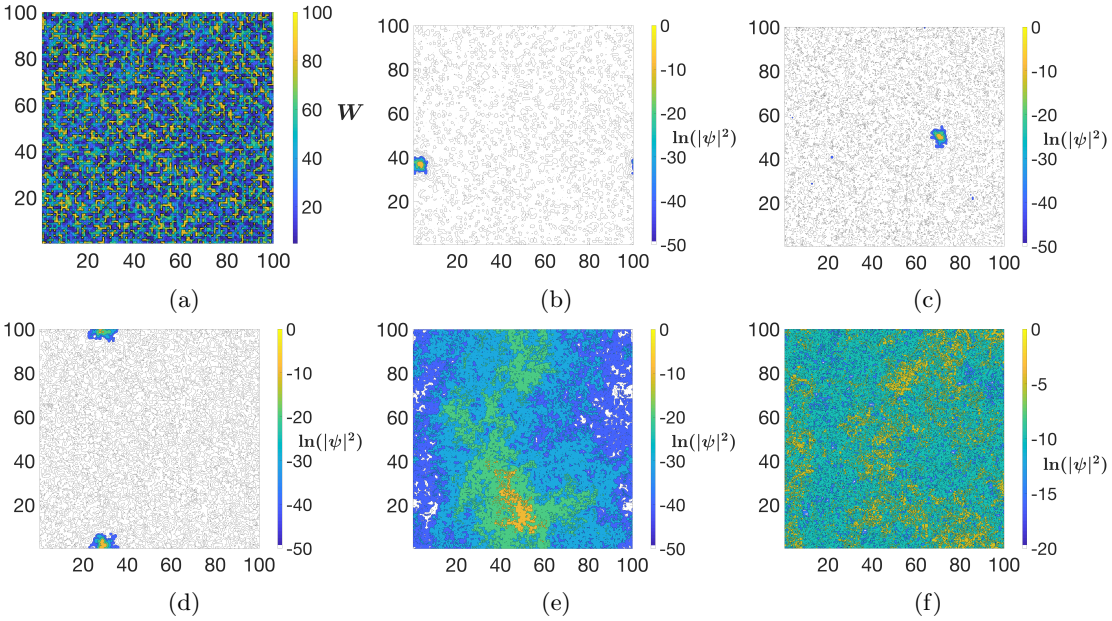

Figure 4.11: (a) The effective confining potential for a piece-wise. The other frames display sample eigenfunctions. (b) $E = 7.53$. (c) $E = 11.8$. (d) $E = 20.7$. (e) $E = 54.8$. (f) $E = 75.0$.

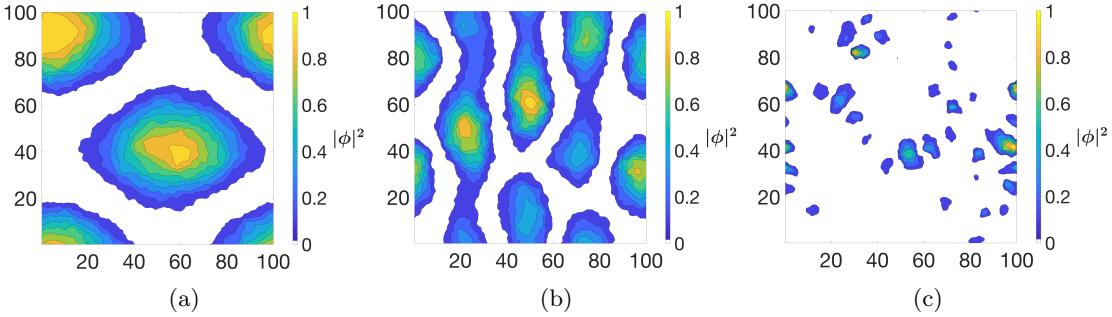

Figure 4.12: Sample eigenfunctions of the reduced equation. (a) $E = 0.00157$. (b) $E = 0.00638$. (c) $E = 0.0494$.

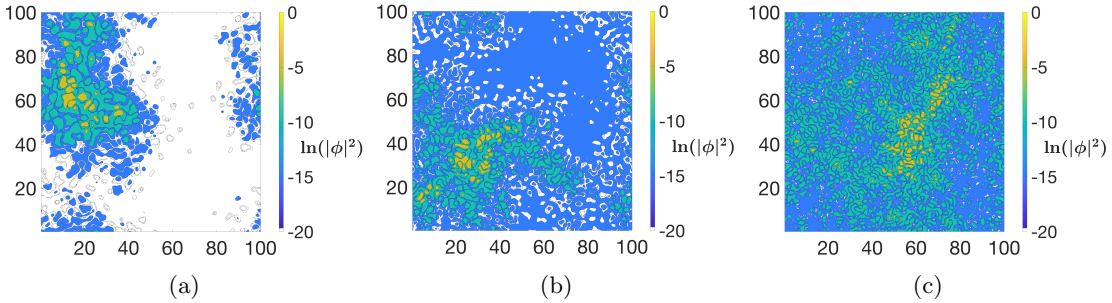

Figure 4.13: Sample eigenfunctions of the reduced equations in log scale. (a) $E = 0.834$. (b) $E = 2.49$. (c) $E = 4.25$.

amount of eigenfunctions that needs to be computed in order to reach eigenfunctions of energy $V_{\max}$ is much larger than for lower potential strengths. Indeed, the eigenvalues are included in an interval that depends on the potential strength and the mesh size. The eigenvalues of a 2D tight-binding system with random potential are found in the interval $[-4t, 4t + V_{\max}]$ where t is the hopping term and if we assume a positive potential. If t is fixed, increasing the potential strength increases the number of eigenvalues that are in the interval $[0, V_{\max}]$. T By analogy with this tight-binding system, the same phenomenon is

happening in our 2D continuous problem, where the mesh size plays the role of the hopping term. We are reaching the maximum amount of eigenfunctions we can compute using this computational method [34]. The solution would be to use higher order finite elements or to use a finer mesh, but this increases the computation times too much.

The results we have in Figure 4.14 are not very conclusive. For the original equation, the eigenfunctions start out localized, and their PR (and therefore their localization length) increases before reaching an upper limit due to the finite size of the domain. For the reduced equation, the data suggest that localization lengths of the eigenfunctions are comparable to the size of the domain (because their PRs are of the order of 1).

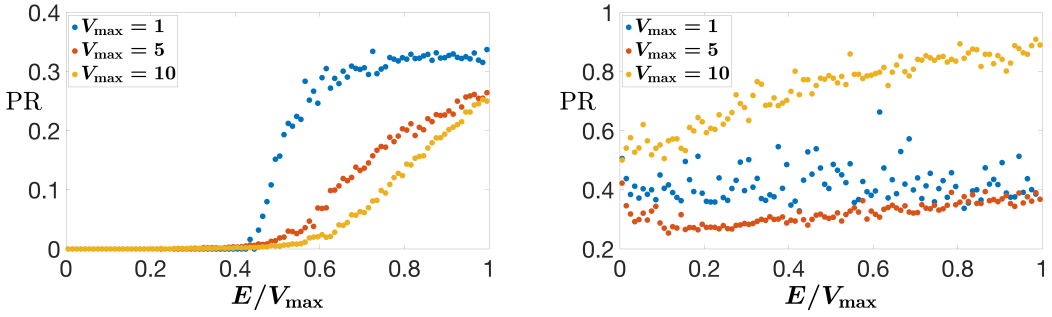

(a) (b)

Figure 4.14: PR of the (a) original and (b) reduced equations for $V_{\max} = 1, 5$, and 10. We compare eigenfunctions of same reduced energy $E/V_{\max}$. Each point is the average of the PRs of all the eigenfunctions whose energy are in the same interval of size 0.01.

III.2 The distribution of the energy spacings and their ratios

We analyze now the distribution of the energy spacings and their ratios as already explained in the previous section. The goal here is to investigate the localization properties of the eigenfunctions for large enough potential strength.

III.2.a The energy spacings

The statistics of the spacings of the eigenvalues for the 2D equation are displayed in Figures 4.15 and 4.17. In Figure 4.15 we have computed the spacings of the first 10,000 eigenvalues (skipping the first 1,000 for the reduced equation) for both the original and reduced equations and for $V_{\max} = 1, 10$, and 100. Figure 4.16 and Table 4.3 summarize the results for δ, R_P^2 (which is the coefficient of determination with respect to the Poisson distribution), and R_W^2 (which is the coefficient of determination with respect to the Wigner distribution). As expected for the original equation, as the potential strength increases, the Poisson distribution becomes a better and better fit for the data (the coefficient of determination increases). For the reduced equation, we observe a similar but slower trend. The problem is that we

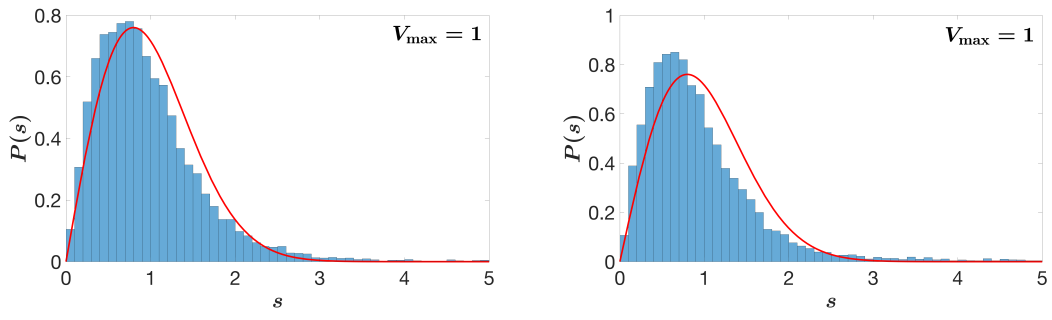

(a) (b)

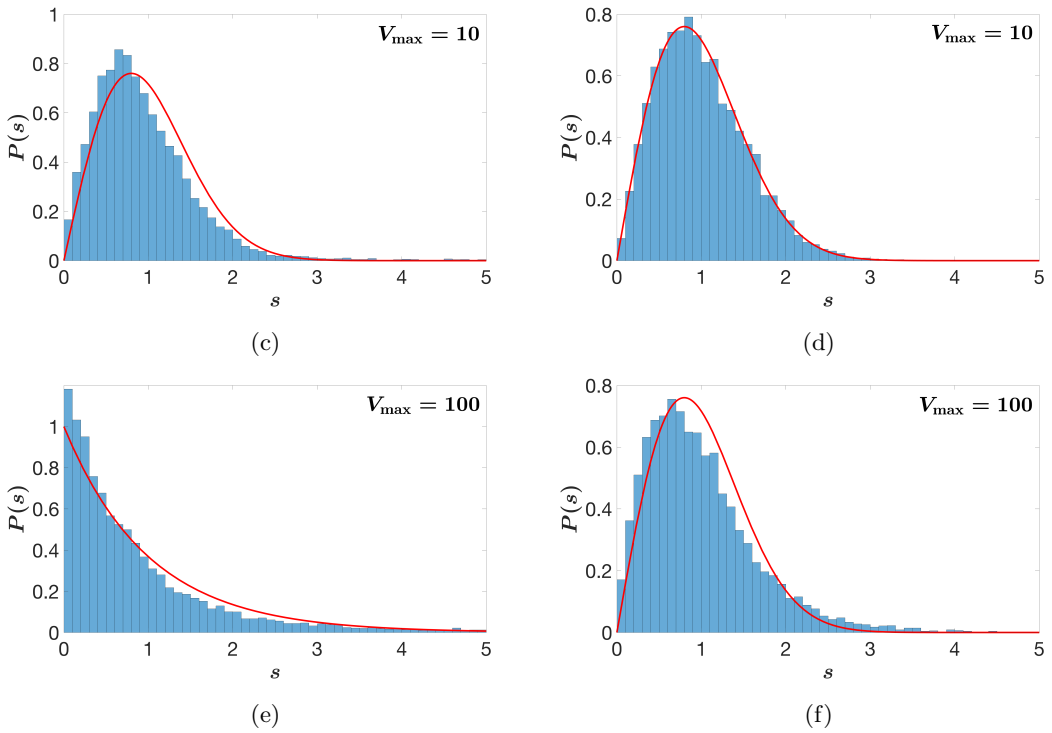

Figure 4.15: Statistics of the energy spacing of the first 10,000 eigenvalues (in blue bars) for different parameters. We have also displayed the exact Poisson or Wigner distribution in red. (a) Original equation and $V_{\max} = 1$. (b) Reduced equation and $V_{\max} = 1$. (c) Original equation and $V_{\max} = 10$. (d) Reduced equation and $V_{\max} = 10$. (e) Original equation and $V_{\max} = 100$. (f) Reduced equation and $V_{\max} = 100$.

are considering a large amount of eigenvalues. It is possible that only the very first eigenfunctions are localized with a localization length smaller than the domain size. The other eigenfunctions therefore appear delocalized and carry the spectral signature of delocalization.

In Figure 4.17, we have displayed the same distributions of the spacings with the same parameters, only this time we have only considered the first 1000 eigenvalues (once again skipping the 1000 first for the reduced equation). This way we keep only the most localized eigenfunctions. Figure 4.18 and Table 4.4 summarizes the results for δ, R_P^2, and R_W^2. The trend is now much clearer. With increasing potential strength, the fit of the data by the Poisson distribution improves (the coefficient of determination increases), regardless of the equation type (original or reduced) although this transition occurs at a lower potential strength for the original equation compared to the reduced equation (around $V_{\max} = 10$ for the former, and $V_{\max} = 100$ for the latter). This suggests that in 2D, the eigenfunctions of both the original and reduced equations are localized.

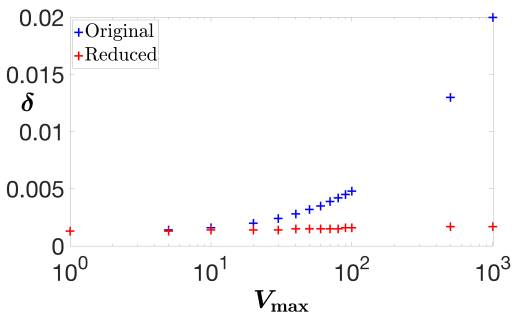

(a)

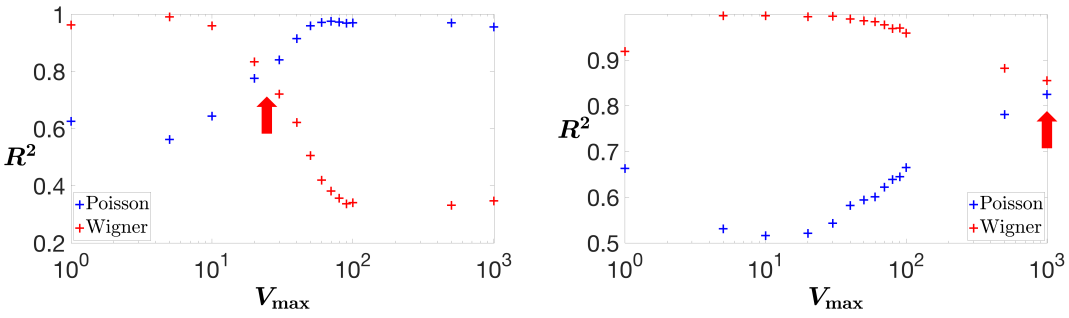

(b) (c)

Figure 4.16: The values found for δ and R^2 for the various potential strengths. (a) Average energy spacing δ for both the original and the reduced equation, against the potential strength. (b) R^2 for the original equation. The arrow points at the potential strength where the curves cross, which indicates a transition. (c) R^2 for the reduced equation. The arrow points at the potential strength where the curves cross, which indicates a transition.

	Original			Reduced		
$V_{\max}$	δ	R_P^2	R_W^2	δ	R_P^2	R_W^2
1	$1.3\ 10^{-3}$	0.626	0.963	$1.3\ 10^{-3}$	0.663	0.919
5	$1.4\ 10^{-3}$	0.562	0.991	$1.3\ 10^{-3}$	0.531	0.997
10	$1.6\ 10^{-3}$	0.644	0.960	$1.4\ 10^{-3}$	0.516	0.997
20	$2.0\ 10^{-3}$	0.776	0.834	$1.4\ 10^{-3}$	0.521	0.995
30	$2.4\ 10^{-3}$	0.841	0.721	$1.4\ 10^{-3}$	0.543	0.996
40	$2.8\ 10^{-3}$	0.915	0.622	$1.5\ 10^{-3}$	0.582	0.990
50	$3.2\ 10^{-3}$	0.960	0.506	$1.5\ 10^{-3}$	0.594	0.986
60	$3.5\ 10^{-3}$	0.972	0.420	$1.5\ 10^{-3}$	0.601	0.984
70	$3.9\ 10^{-3}$	0.976	0.382	$1.5\ 10^{-3}$	0.622	0.977
80	$4.2\ 10^{-3}$	0.973	0.357	$1.5\ 10^{-3}$	0.639	0.969
90	$4.5\ 10^{-3}$	0.969	0.337	$1.6\ 10^{-3}$	0.645	0.970
100	$4.8\ 10^{-3}$	0.970	0.341	$1.6\ 10^{-3}$	0.665	0.959
500	$1.3\ 10^{-2}$	0.970	0.332	$1.7\ 10^{-3}$	0.781	0.882
1000	$2.0\ 10^{-2}$	0.975	0.347	$1.7\ 10^{-3}$	0.825	0.855

Table 4.3: Summary of the values found for δ and R^2.

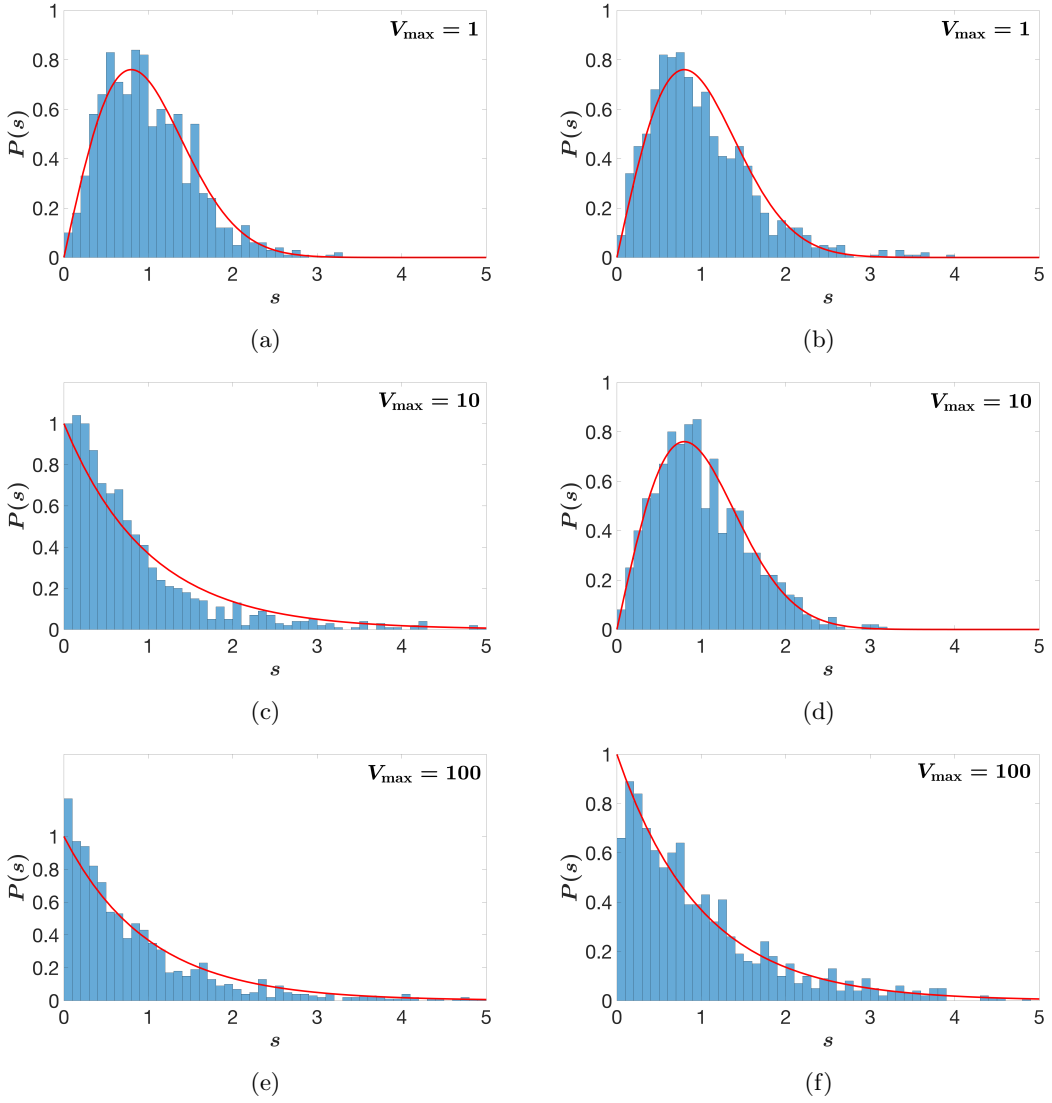

Figure 4.17: Statistics of the energy spacing of the first 1,000 eigenvalues (in blue bars) for different parameters. We have also displayed the exact Poisson or Wigner distribution in red. (a) Original equation and $V_{\max} = 1$. (b) Reduced equation and $V_{\max} = 1$. (c) Original equation and $V_{\max} = 10$. (d) Reduced equation and $V_{\max} = 10$. (e) Original equation and $V_{\max} = 100$. (f) Reduced equation and $V_{\max} = 100$.

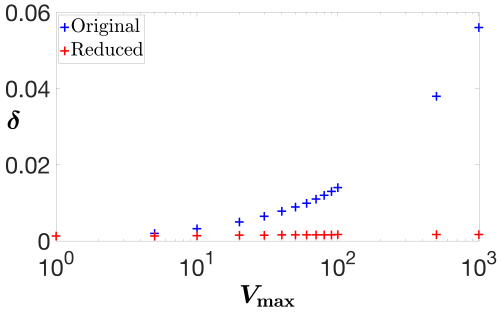

(a)

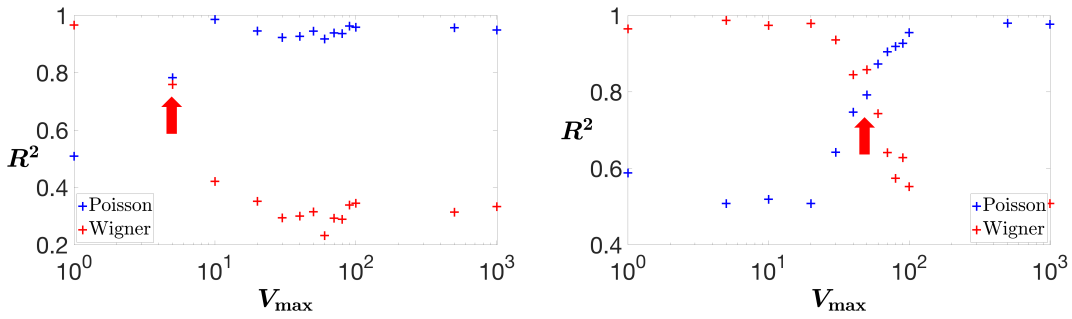

(b) (c)

Figure 4.18: The values found for δ and R^2 for the various potential strengths when only considering the 1,000 first eigenvalues. (a) Average energy spacing δ for both the original and the reduced equation, against the potential strength. (b) R^2 for the original equation. The arrow points at the potential strength where the curves cross, which indicates a transition. (c) R^2 for the reduced equation. The arrow points at the potential strength where the curves cross, which indicates a transition.

	Original			Reduced		
$V_{\max}$	δ	R_P^2	R_W^2	δ	R_P^2	R_W^2
1	$1.3\ 10^{-3}$	0.509	0.966	$1.3\ 10^{-3}$	0.588	0.965
5	$2.0\ 10^{-3}$	0.783	0.759	$1.3\ 10^{-3}$	0.508	0.987
10	$3.2\ 10^{-3}$	0.956	0.421	$1.4\ 10^{-3}$	0.519	0.974
20	$5.0\ 10^{-3}$	0.946	0.352	$1.5\ 10^{-3}$	0.508	0.979
30	$6.5\ 10^{-3}$	0.923	0.294	$1.5\ 10^{-3}$	0.642	0.936
40	$7.8\ 10^{-3}$	0.927	0.300	$1.6\ 10^{-3}$	0.747	0.845
50	$8.9\ 10^{-3}$	0.945	0.315	$1.6\ 10^{-3}$	0.792	0.858
60	$9.9\ 10^{-3}$	0.918	0.232	$1.6\ 10^{-3}$	0.873	0.743
70	$1.1\ 10^{-2}$	0.939	0.293	$1.6\ 10^{-3}$	0.905	0.641
80	$1.2\ 10^{-2}$	0.937	0.289	$1.6\ 10^{-3}$	0.919	0.574
90	$1.3\ 10^{-2}$	0.963	0.339	$1.6\ 10^{-3}$	0.927	0.628
100	$1.4\ 10^{-2}$	0.959	0.345	$1.7\ 10^{-3}$	0.955	0.552
500	$3.9\ 10^{-2}$	0.967	0.314	$1.7\ 10^{-3}$	0.980	0.496
1000	$5.6\ 10^{-2}$	0.949	0.333	$1.7\ 10^{-3}$	0.977	0.508

Table 4.4: Summary of the values found for δ and R^2 when considering only the first 1,000 eigenvalues.

III.2.b Energy spacings ratios

In a similar fashion as in the preceding section, we now study the energy spacings ratios. We use the same data and compute the ratios from the spacings, and compare the average value of the ratios $\langle r \rangle$ with the two characteristic values for the localized and delocalized phases (0.383 and 0.5295).

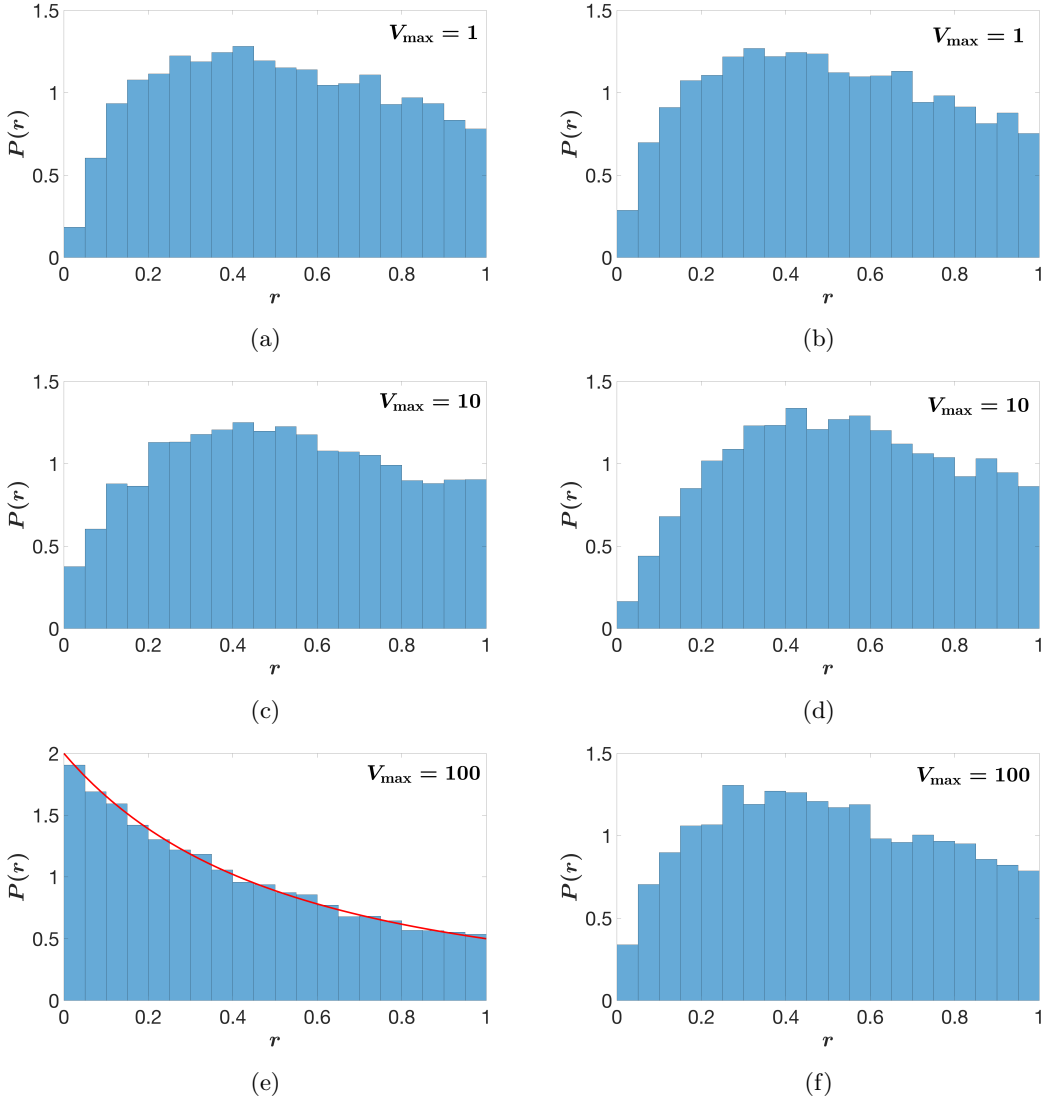

Figure 4.19: Statistics of the energy spacing ratios of the first 10,000 eigenvalues (in blue bars) for different parameters. We have also displayed the $2/(1+r)^2$ distribution in red when appropriate. (a) Original equation and $V_{\max} = 1$. (b) Reduced equation and $V_{\max} = 1$. (c) Original equation and $V_{\max} = 10$. (d) Reduced equation and $V_{\max} = 10$. (e) Original equation and $V_{\max} = 100$. (f) Reduced equation and $V_{\max} = 100$.

Figure 4.19 shows the distribution of the ratios for a few selected potential strengths ($V_{\max} = 1, 10$, and 100) and for both the original and reduced equations. Figure 4.20 summarizes the values of $\langle r \rangle$ we have found. The trend is the same as for the distribution of the spacings: the average of the ratios gets closer and closer to 0.383 as $V_{\max}$ increases for the original equation.

In summary, in this section we have shown (albeit less conclusively than in the 1D case) that the eigenfunctions of the reduced equation are also localized, although their localization length is greater than that of the eigenfunctions of the original equation. This evidence is less conclusive because localization lengths of 2D localized eigenfunctions increase quickly with the energy of the eigenfunctions, and we can only work with limited domain sizes.

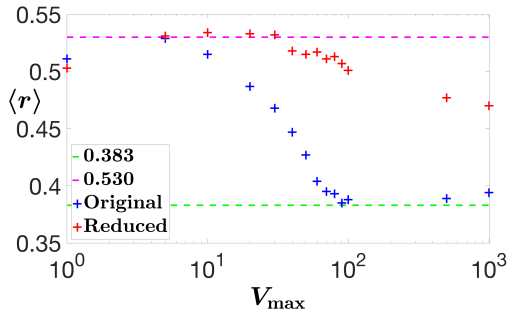

Figure 4.20: The values found for $\langle r \rangle$ and R^2 for the various potential strengths.

IV The three-dimensional case: the localization-delocalization transition

We now move on to three-dimensional systems. For Anderson-type potentials, these systems are known to undergo a localization/delocalization transition at a threshold called the mobility edge [1, 25, 26]. Our question for this section is this: does the reduced equation also exhibit a phase transition between localized and delocalized states?

We first proceed qualitatively in the same way as before by looking at the spatial distribution of the eigenfunctions. We then move on to more quantitative tools. We do not use the participation ratios, as they do not tell us much for the same reasons they were unhelpful in 2D. We will instead rely on the distributions of the energy spacings and their ratios to distinguish localized from delocalized phases. Finally we implement a new tool called finite-size scaling analysis which enables us to identify a possible localization-delocalization transition for the eigenfunctions of the reduced equation.

IV.1 Spatial structure of the eigenfunctions

We start our investigation by representing the spatial distributions of sample eigenfunctions of both the original and reduced equations.

The domain size is $L^3 = 20 \times 20 \times 20$ and the mesh size is $0.2 \times 0.2 \times 0.2$ for a total of 1,000,000 degrees of freedom. The potential follows a uniform random law taking values in $[0, 100]$. In Figure 4.21, we see the change in the eigenfunctions of the unmodifed equation as the energy increases. They start out localized but become more and more delocalized. This is the behavior we would expect in an infinitely-sized system.

In Figure 4.22, we have displayed sample low, medium and high energy eigenfunctions of the reduced equation for a potential following a uniform random law taking values in $[0, 100]$. All three eigenfunctions are delocalized in the entire domain, even though the potential strength is high. We will now move on the

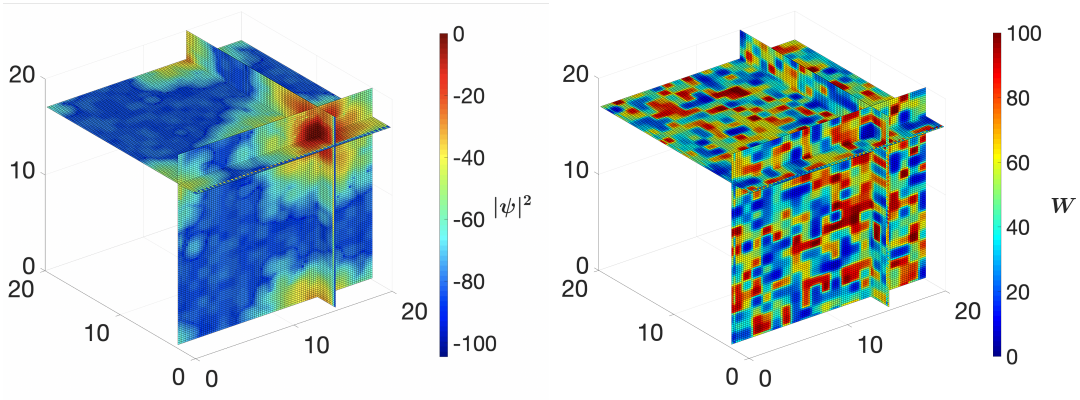

(a) (b)

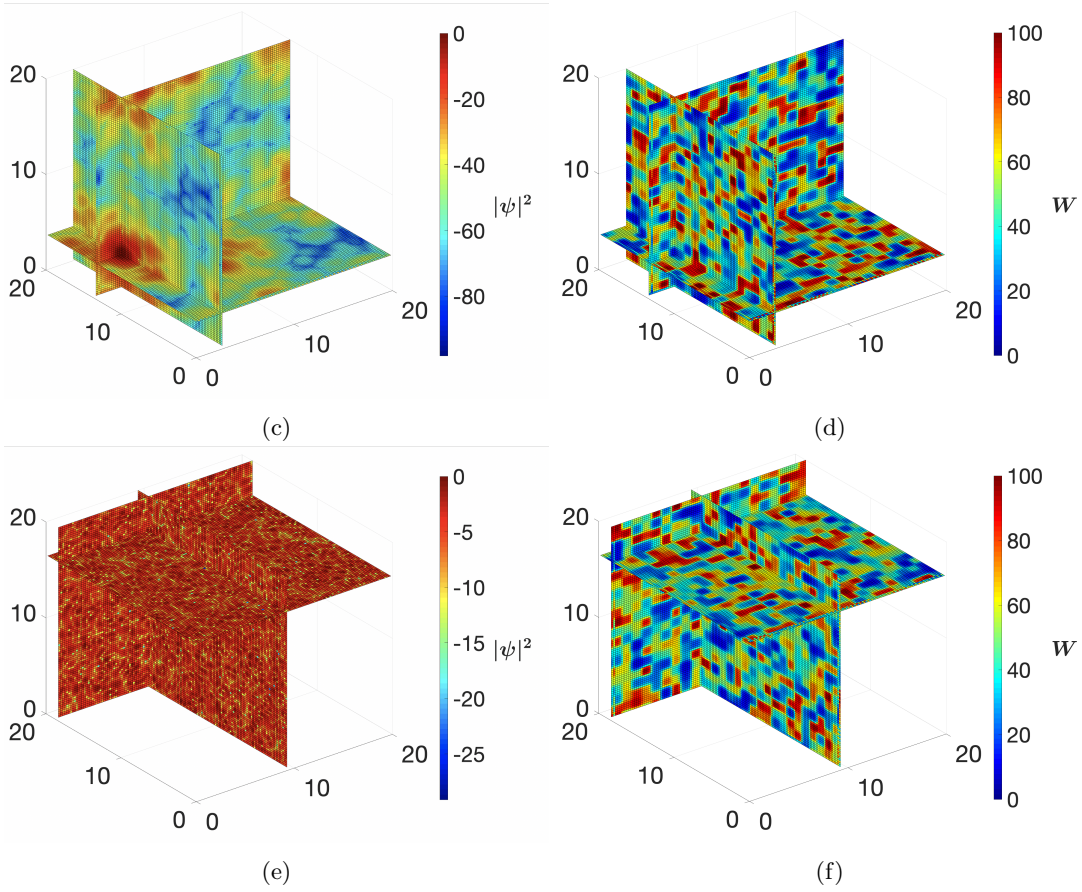

Figure 4.21: The following figures are 3D representations of the eigenfunctions ((a), (c), and (e)) and of the effective confining potential ((b), (d), and (f)) for a potential following a uniform random law taking values in $[0, 100]$. These functions are represented on slices of the total domain, one slice parallel to the Oxy plane, another parallel to the Oyz plane, and the last parallel to the Oxz plane. The point at the intersection of these slices is chosen to be the maximum of the represented eigenfunction (on the left). We then display on the right the effective confining potential with the same slices. The eigenvalues are: (a) $E = 11.7$; (c) $E = 20.8$; (e) $E = 100.0$.

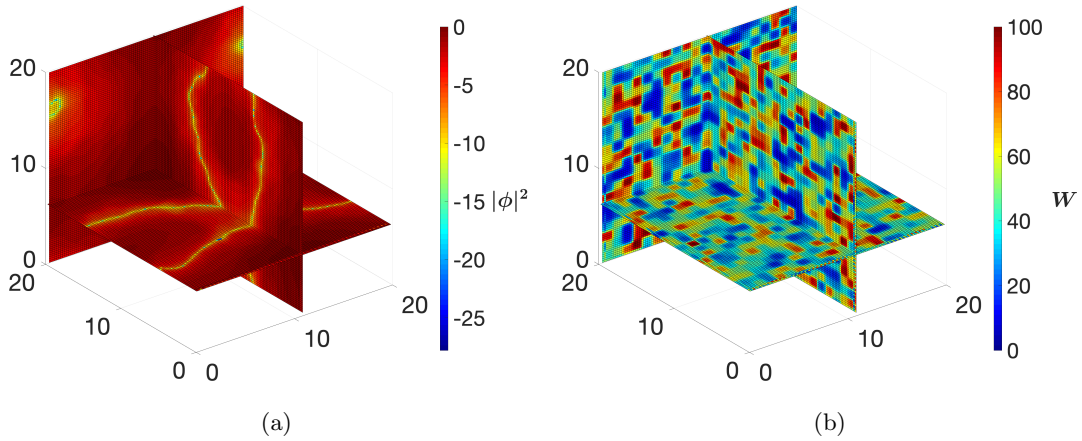

the study of the spectral structure of the eigenfunctions for a more quantitative measure of how localized the eigenfunctions are.

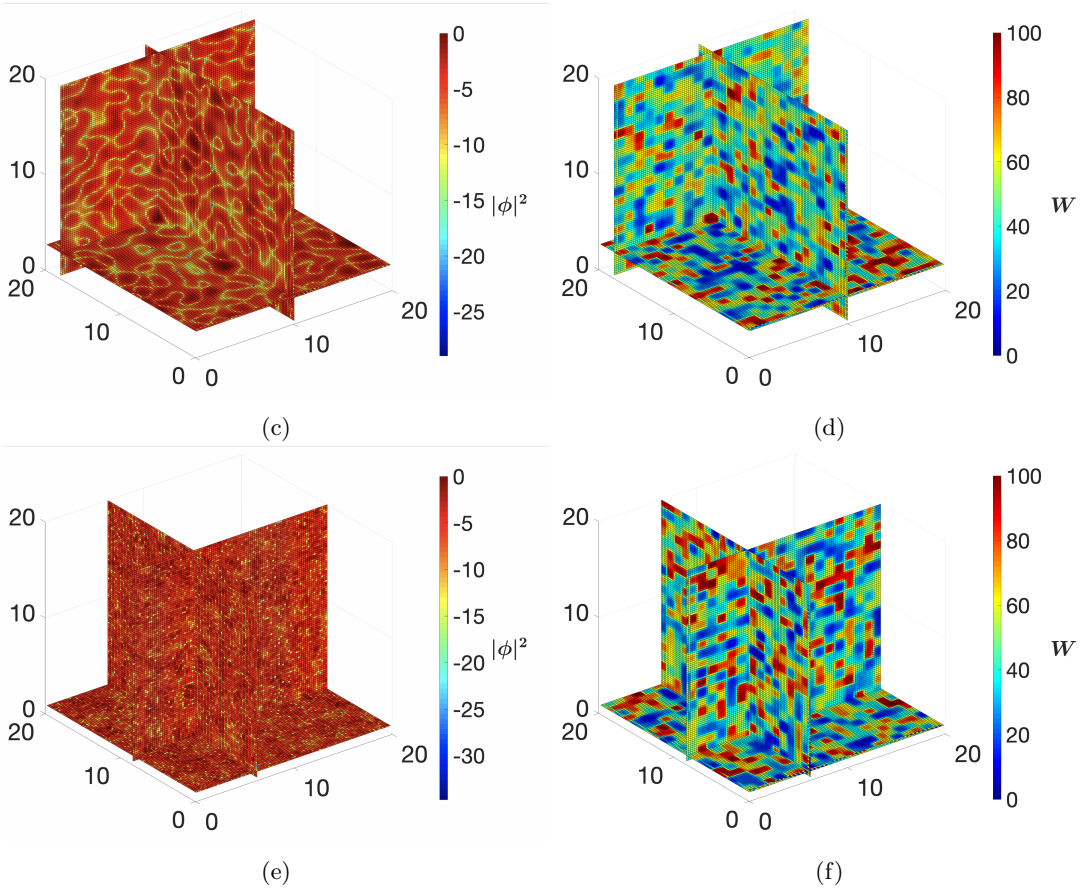

Figure 4.22: The following figures are 3D representations of the eigenfunctions ((a), (c), and (e)) and of the effective confining potential ((b), (d), and (f)) for a potential following a uniform random law taking values in $[0, 100]$. These functions are represented on slices of the total domain, one slice parallel to the Oxy plane, another parallel to the Oyz plane, and the last parallel to the Oxz plane. The point at the intersection of these slices is chosen to be the maximum of the represented eigenfunction (on the left). We then display on the right the effective confining potential with the same slices. The eigenvalues are: (a) $E = 6.9 \times 10^{-2}$; (c) $E = 10.0$; (e): $E = 100.0$.

IV.2 Distribution of the energy spacings and their ratios

As mentioned at the beginning of this section, we will not attempt to study the localization lengths by computing the PRs, since it would require us to compute too high energy eigenfunctions with therefore a large error. Instead we will move on directly to the study of the distributions of the spacings and their ratios.

IV.2.a The energy spacings

We start our analysis in the same way as before: we compare the distributions of the energy spacings for the first 10,000 eigenvalues of both the original and reduced equations. In Figure 4.23 we have displayed a few examples of the computed distributions. Figure 4.24 and Table 4.5 summarize our results. Looking at the progression of both R_P^2 and R_W^2 as the potential strength increases, we see that in the case of the original equation, the distributions shift from Poisson-like behavior to Wigner-like behavior. On the contrary, the distributions of the spacings of the eigenfunctions of the reduced equation do not evolve and remain Wigner-like.

Once again, in Figure 4.25, we have displayed the same distributions of the spacings with the same parameters, only this time we have only considered the first 1000 eigenvalues (once again skipping the 1000 first for the reduced equation). Figure 4.26 and Table 4.6 summarize the results for δ, R_P^2, and R_W^2.

The trend is the same as in the preceding table, and indicates that over a certain potential strength the eigenfunctions of the original equation transition to delocalized to localized states. This change is not observable for the eigenfunctions of the reduced equation.

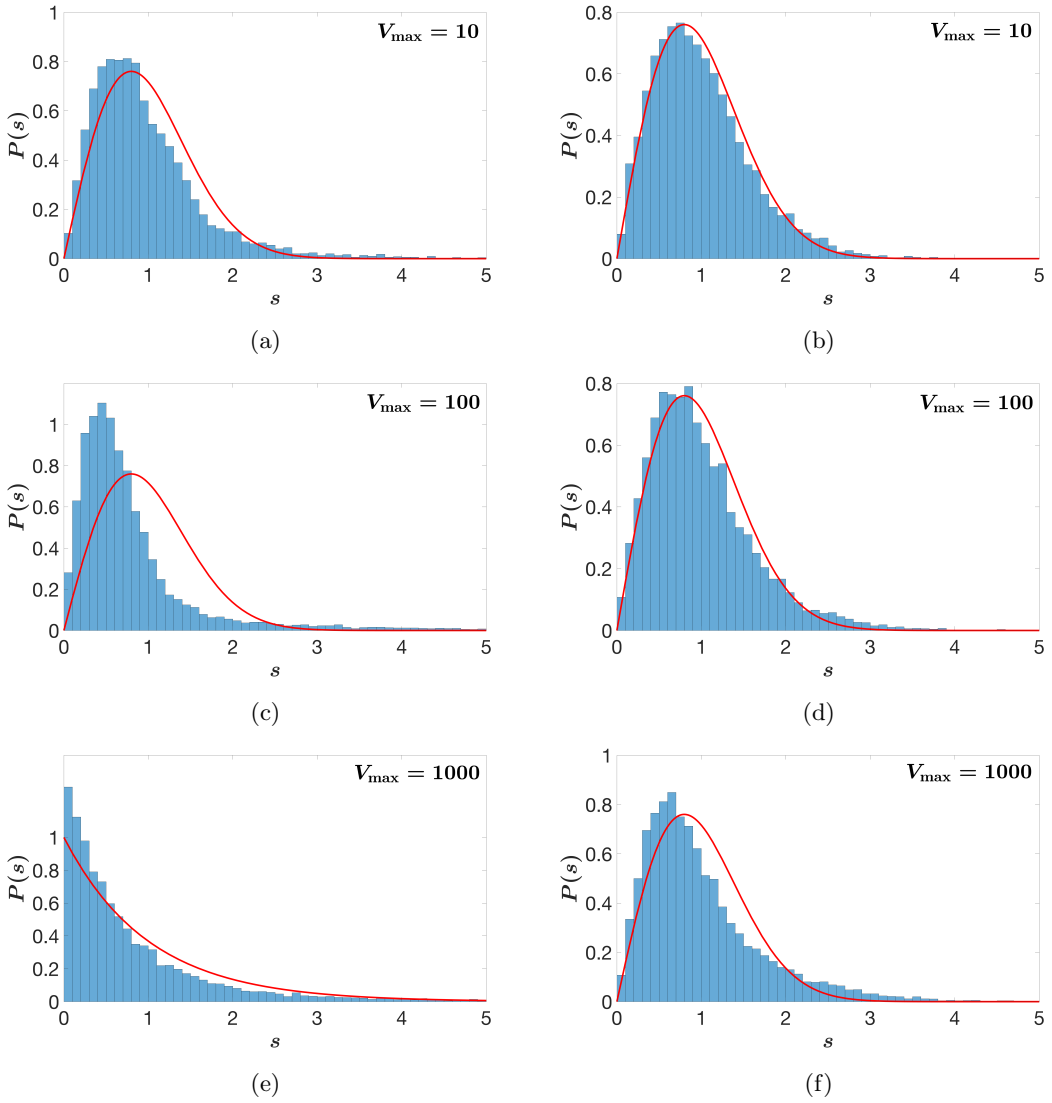

Figure 4.23: Statistics of the energy spacing of the first 10,000 eigenvalues (in blue bars) for different parameters. We have also displayed the exact Poisson or Wigner distribution in red. (a) Original equation and $V_{\max} = 10$. (b) Reduced equation and $V_{\max} = 10$. (c) Original equation and $V_{\max} = 100$. (d) Reduced equation and $V_{\max} = 100$. (e) Original equation and $V_{\max} = 1000$. (f) Reduced equation and $V_{\max} = 100$.

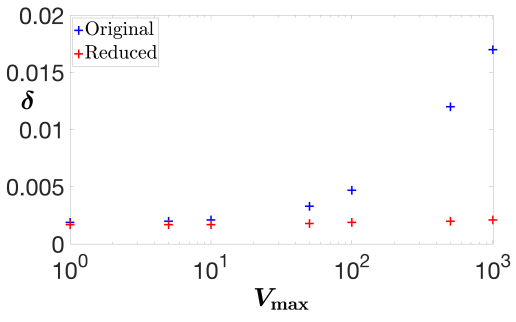

(a)

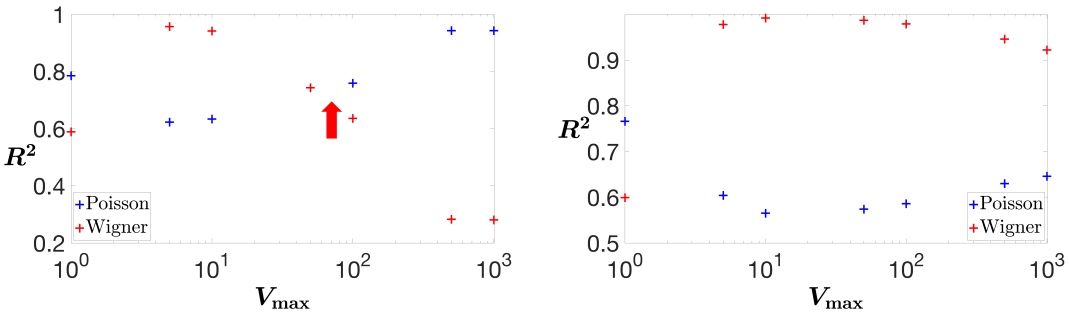

(b) (c)

Figure 4.24: The values found for δ and R^2 for the various potential strengths. (a) Average energy spacing δ for both the original and the reduced equation, against the potential strength. (b) R^2 for the original equation. The arrow points at the potential strength where the curves cross, which indicates a transition. (c) R^2 for the reduced equation.

	Original			Reduced		
$V_{\max}$	δ	R_P^2	R_W^2	δ	R_P^2	R_W^2
1	$1.9\ 10^{-3}$	0.785	0.589	$1.7\ 10^{-3}$	0.766	0.599
5	$2.0\ 10^{-3}$	0.623	0.957	$1.7\ 10^{-3}$	0.604	0.978
10	$2.1\ 10^{-3}$	0.634	0.942	$1.7\ 10^{-3}$	0.565	0.992
50	$3.3\ 10^{-3}$	0.743	0.743	$1.8\ 10^{-3}$	0.574	0.987
100	$4.7\ 10^{-3}$	0.759	0.636	$1.9\ 10^{-3}$	0.586	0.979
500	$1.2\ 10^{-2}$	0.943	0.283	$2.0\ 10^{-3}$	0.630	0.946
1000	$1.7\ 10^{-2}$	0.943	0.281	$2.1\ 10^{-3}$	0.646	0.922

Table 4.5: Summary of the values found for δ and R^2.

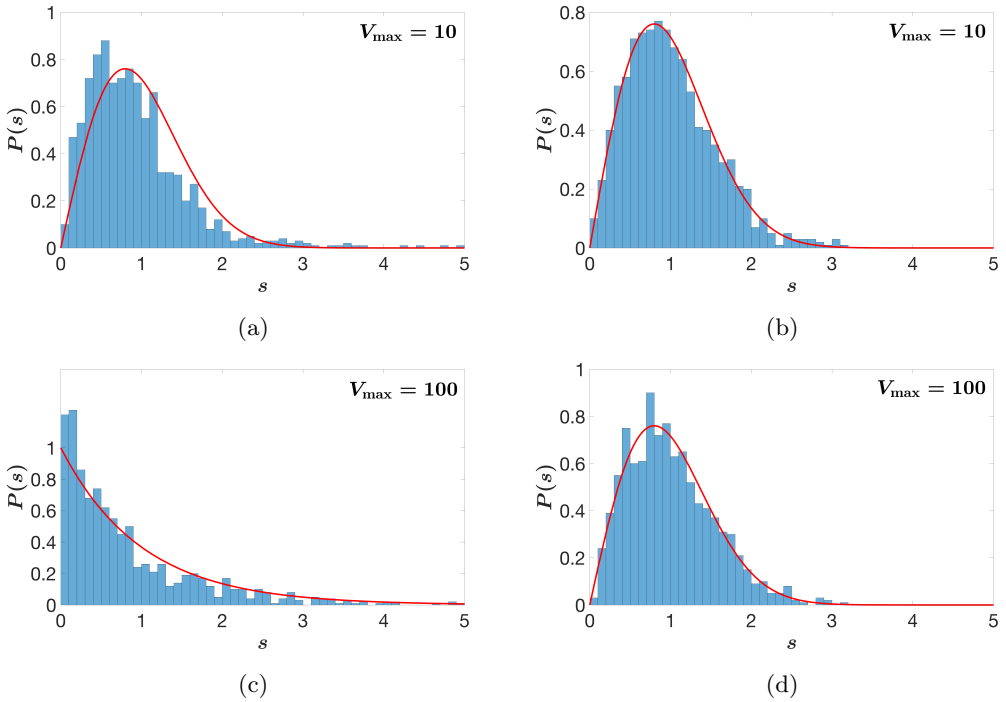

(a) (b)

(c) (d)

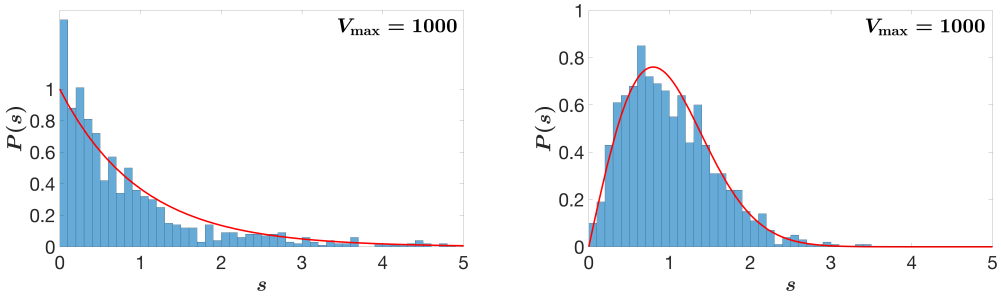

(e) (f)

Figure 4.25: Statistics of the energy spacing of the first 1000 eigenvalues (in blue bars) for different parameters. We have also displayed the exact Poisson or Wigner distribution in red. (a) Original equation and $V_{\max} = 10$. (b) Reduced equation and $V_{\max} = 10$. (c) Original equation and $V_{\max} = 100$. (d) Reduced equation and $V_{\max} = 100$. (e) Original equation and $V_{\max} = 1000$. (f) Reduced equation and $V_{\max} = 1000$.

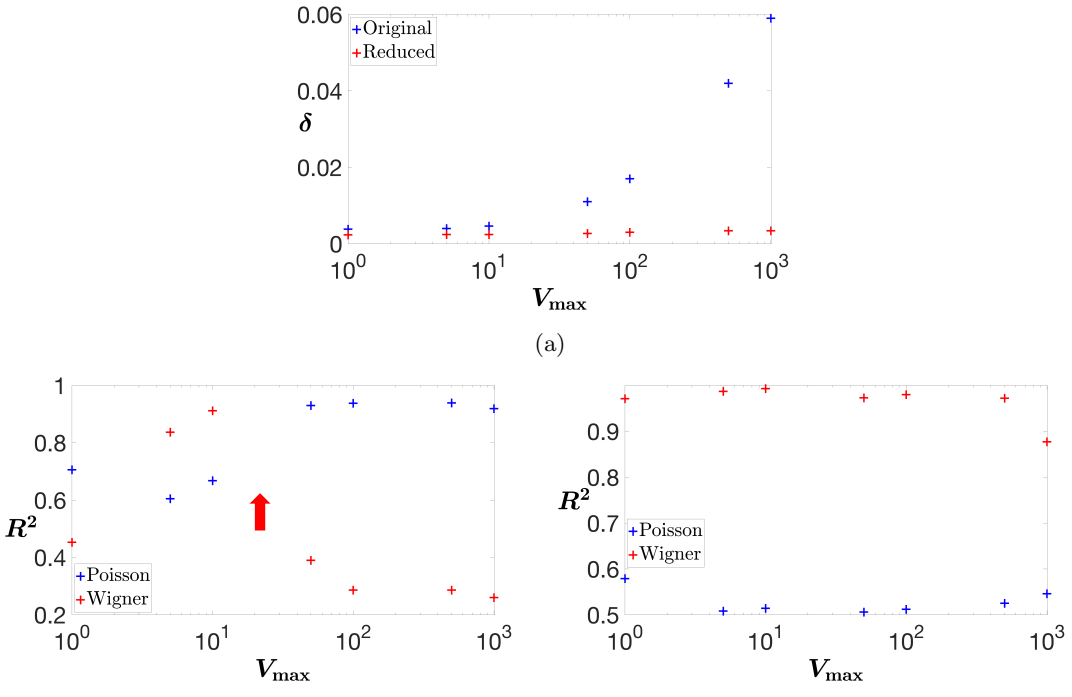

(a) (b) (c)

Figure 4.26: The values found for δ and R^2 for the various potential strengths. (a) δ. (b) R^2 for the original equation. The arrow points at the potential strength where the curves cross, which indicates a transition. (c) R^2 for the reduced equation.

	Original			Reduced		
$V_{\max}$	δ	R_P^2	R_W^2	δ	R_P^2	R_W^2
1	$3.8\ 10^{-3}$	0.706	0.453	$2.3\ 10^{-3}$	0.579	0.971
5	$4.0\ 10^{-3}$	0.605	0.837	$2.4\ 10^{-3}$	0.508	0.987
10	$4.6\ 10^{-3}$	0.668	0.912	$2.4\ 10^{-3}$	0.514	0.993
50	$1.1\ 10^{-2}$	0.930	0.390	$2.7\ 10^{-3}$	0.506	0.973
100	$1.7\ 10^{-2}$	0.938	0.286	$3.0\ 10^{-3}$	0.512	0.980
500	$4.2\ 10^{-2}$	0.939	0.286	$3.4\ 10^{-3}$	0.525	0.972
1000	$5.9\ 10^{-2}$	0.919	0.260	$3.4\ 10^{-3}$	0.546	0.877

Table 4.6: Summary of the values found for δ and R^2.

IV.2.b The energy spacings ratios

We have reiterated the analysis of the energy spacings conducted before but this time computing the energy spacings ratios. We consider the exact same parameters. The results, which are summarized in Figure 4.27 and in Figure 4.28 are much more conclusive than for those for the energy spacings. Indeed, we can clearly see that the average value $\langle r \rangle$ of the energy spacings ratios of the eigenvalues of the original equation remains at around 0.53 (which corresponds to delocalized eigenstates) before dropping to around 0.38 (which corresponds to localized eigenstates) for potential strengths above 50. Additionally, for the reduced equation, this average value $\langle r \rangle$ does not vary significantly and stays are around 0.53, which corresponds to delocalized eigenstates. This suggests that the eigenfunctions of the reduced equation remain delocalized regardless of the potential strength.

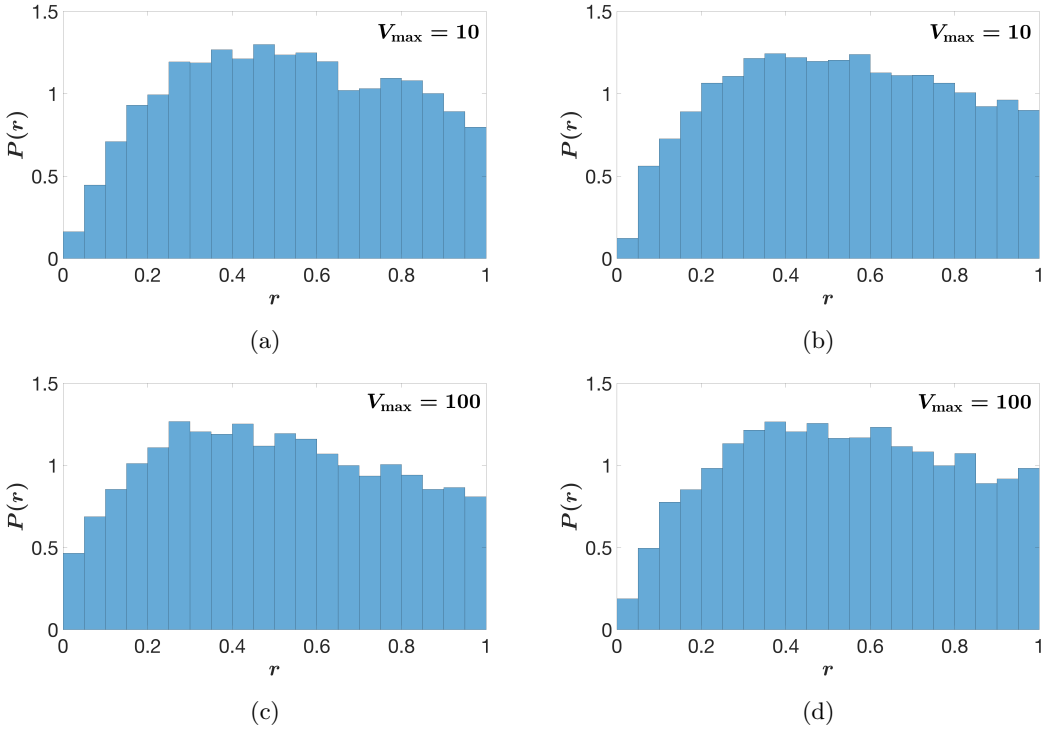

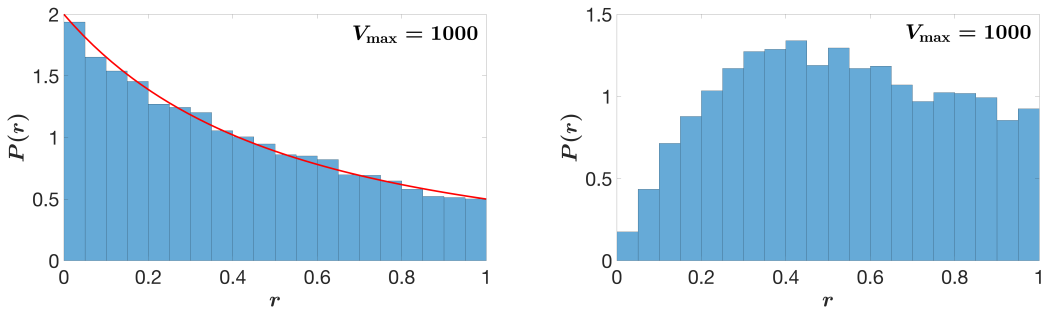

(e) (f)

Figure 4.27: Statistics of the energy spacing ratios of the first 10000 eigenvalues (in blue bars) for different parameters. We have also displayed the $2/(1+r)^2$ distribution in red when appropriate. (a) Original equation and $V_{\max} = 10$. (b) Reduced equation and $V_{\max} = 10$. (c) Original equation and $V_{\max} = 100$. (d) Reduced equation and $V_{\max} = 100$. (e) Original equation and $V_{\max} = 1000$. (f) Reduced equation and $V_{\max} = 1000$.

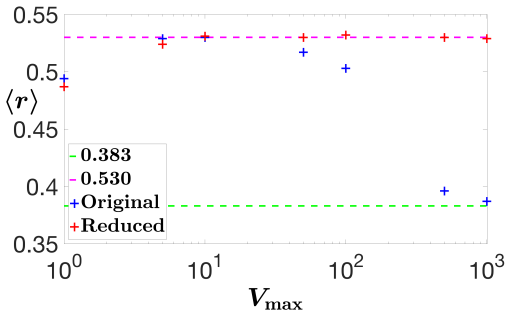

Figure 4.28: The values found for $\langle r \rangle$ and R^2 for the various potential strengths

	Original	Reduced
$V_{\max}$	$\langle r \rangle$	$\langle r \rangle$
1	0.494	0.487
5	0.529	0.524
10	0.530	0.531
50	0.517	0.530
100	0.503	0.532
500	0.396	0.530
1000	0.387	0.529

Table 4.7: Summary of the values found for $\langle r \rangle$.

IV.3 Highlighting the transition: finite-size scaling analysis

In the previous subsections, we have observed through various numerical simulations that in 3D for strong enough random potentials, the eigenfunctions of the original equation are localized under a certain energy, and delocalized over it, while the eigenfunctions of the reduced equation are all delocalized. The issue with this analysis is that we have not shown whether the eigenfunctions of the reduced equation are truly delocalized, or if they are just localized with a very large localization length.

To examine more closely the possible delocalization/localization transition, we implement a finite-size scaling procedure [11, 28, 29, 30]. We start this analysis by computing an eigenfunction ψ close to a

certain energy E. We then cut up the domain in boxes of size ℓ^3. There are $(L/\ell)^3 \equiv \lambda^{-3}$ such boxes. We then compute the probability of finding ψ in each box k:

$$\mu_k = \sum_{i \in k} |\psi_i|^2. \tag{4.8}$$

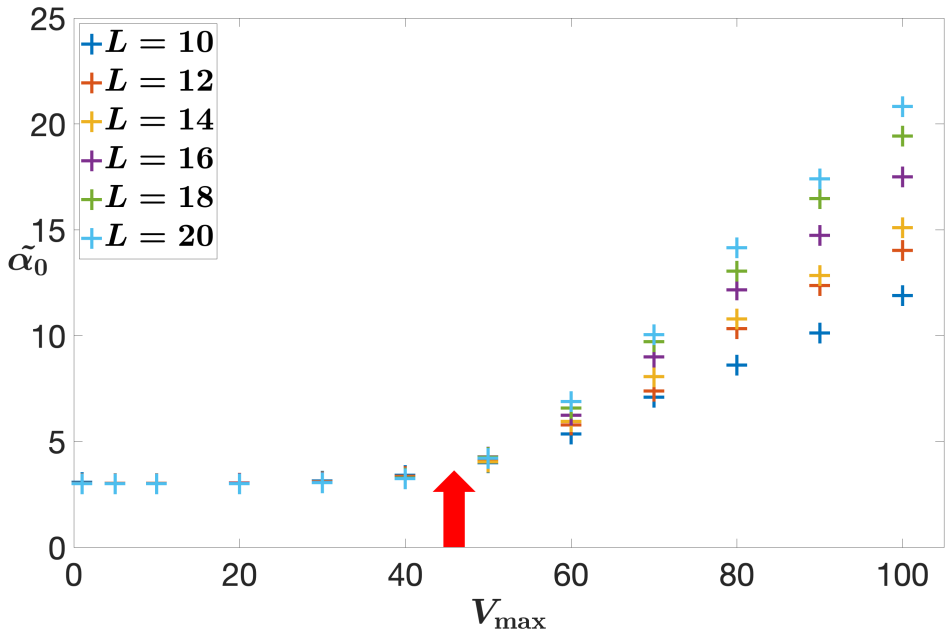

(a)

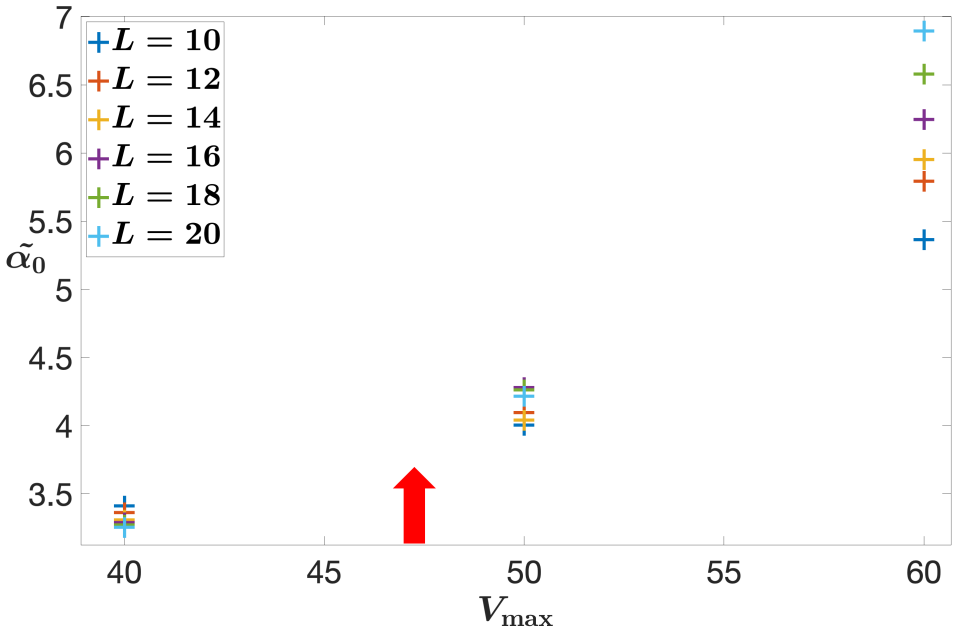

(b)

Figure 4.29: The multifractal analysis for the original eigen equation. $\tilde{\alpha_0}$ is calculated for different values of the potential strength ($V_{\max} = 1, 5, 10, 20, 30, 40, 50, 60, 70, 80, 90,$ and 100) and for different domain sizes (domain side-length $L = 10, 12, 14, 16, 18,$ and 20). We computed $\tilde{\alpha_0}$ for a certain sample by averaging all the eigenfunctions in an interval $[19.5, 20.5]$ over five different samples of random disorder. (a) All the points computed. (b) A close up at the transition.

We define these boxes (coarse-graining) in order to compare systems of different sizes. Indeed, by fixing λ, the distributions μ_k are all the same size regardless of the domain size. It can be shown that the distribution:

$$\tilde{\alpha_k} \equiv \log \mu_k / \log \lambda \tag{4.9}$$

at fixed λ does not depend on the system size at the critical point. We use the mean value of this distribution $\tilde{\alpha_0} \equiv \langle \log \mu_k \rangle / \log \lambda$ as a dimensionless finite-scaling observable. If we assume the following finite-size scaling law:

$$\tilde{\alpha_0}(L, V_{\max}) = f((V_{\max} - V_{\max,c}) L^{1/\nu}) \tag{4.10}$$

where $V_{\max,c}$ is the critical potential strength (under which all the eigenfunctions are delocalized, and over which the lowest eigenfunctions are localized), ν is the critical exponent, and f is some universal function, then when plotting α vs. $V_{\max}$, the curves should intersect at the critical point. Figure 4.29 shows this transition. When increasing the domain side-length L, the curves become steeper and exhibit a more abrupt transition. In Figure 4.29b, we have zoomed on the small values of potential strength. We can see that $\tilde{\alpha_0}$ is larger for smaller domain sizes at these potential strengths, while the opposite is true for large potential strengths (for $V_{\max}$ over 50). This indicates that all the curves should intersect at a single point corresponding to $V_{\max,c}$.

For our simulations we have fixed the coarse-graining parameter $\lambda = 0.2$. We sampled $V_{\max}$ over $\{1, 5, 10, 20, 30, 40, 50, 60, 70, 80, 90, 100\}$ and L over $\{10, 12, 14, 16, 18, 20\}$. $\tilde{\alpha_0}$ was averaged over all the eigenfunctions in the interval $[19.5, 20.5]$, and over five different samples of random disorder. We chose this interval so as to be sure that no matter the potential strength we would have some eigenfunctions.

The goal of these computations is not to determine the values of the critical potential strength or of the critical exponent, but to merely to show the presence of a transition in the case of the original equation.

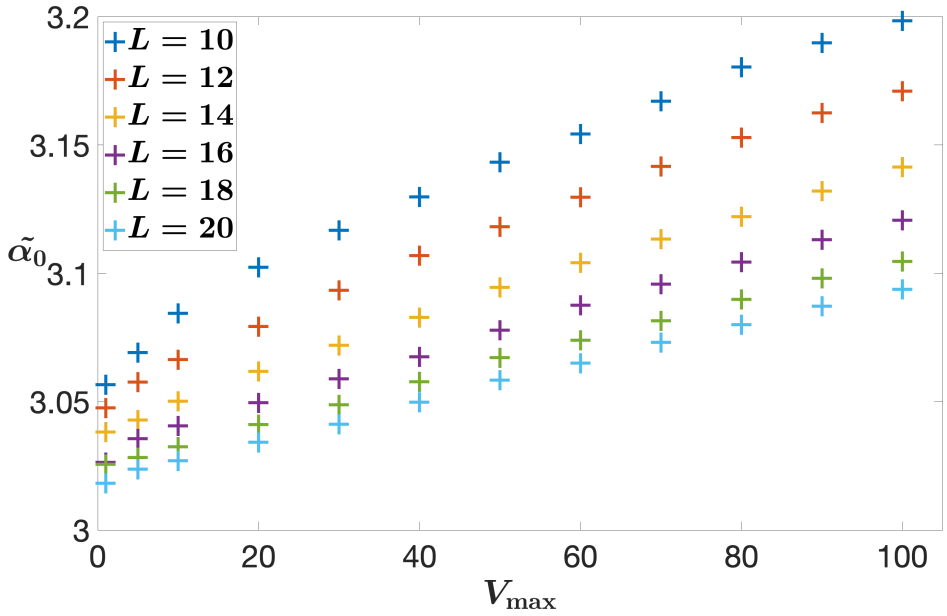

Figure 4.30: The multifractal analysis for the reduced eigen-equation. $\tilde{\alpha_0}$ is calculated for different values of the potential strength ($V_{\max} = 1, 5, 10, 20, 30, 40, 50, 60, 70, 80, 90,$ and 100) and for different domain sizes (domain side-length $L = 10, 12, 14, 16, 18,$ and 20). $\tilde{\alpha_0}$ is computed for a certain sample by averaging all the eigenfunctions in an interval $[4.5, 5.5]$.

We have repeated this exact procedure for the eigenfunctions of the reduced equation. Instead of the intervals $[19.5, 20.5]$ we chose the interval $[4.5, 5.5]$ since the spectrum always starts at 0 for the reduced equation. The results are displayed in Figure 4.30. The curves do not intersect in a single point like they do for the eigenfunctions of the original equation when there is a transition. We therefore conclude that

the eigenfunctions of the reduced equation do not appear to exhibit any critical behavior: there is no phase transition. Our initial observations in the previous subsections suggested that the eigenfunctions of the reduced equation were delocalized. Furthermore, the values found for $\tilde{\alpha_0}$ for the eigenfunctions of the reduced equation are consistent with those found for the eigenfunctions of the original equation with low potential strengths (see Figure 4.29b), i.e. around 3.0. According to these simulations, no matter the potential strength, the eigenfunctions are always delocalized.

V Conclusion and Outlook

In this chapter, we have presented substantial evidence using various methods that the differential term in the reduced equation $-\frac{1}{u^2}\boldsymbol{\nabla}\cdot\left(u^2\boldsymbol{\nabla}\phi\right)$ can be sufficient to localize eigenfunctions, without the presence of a confining potential. We showed this first by looking at the eigenfunctions, then by studying their localization lengths by analyzing their participation ratios as well as the the statistics of the distributions of the energy spacings of the eigenfunctions and their ratios, and finally by using multifractal analysis. We have seen that in 1D and 2D, the removal of the effective confining potential term does not modify the localization properties of the eigenfunctions. However in 3D without this term, there is no phase transition between localizing and delocalizing phases, which, alongside the fact that the distributions of the energy spacings and their ratios exhibit all the characteristics of delocalization, indicates that the eigenfunctions of the 3D require the confining potential for them to localize.

We therefore hypothesize that the differential term is responsible for localization at high energies in 1D and 2D. However we still do not understand by which mechanisms this term induces localization, and why these mechanisms break down for dimensions greater than 2. Understanding this mechanism would be a future topic of research to investigate.

Bibliography

[1] E. Abrahams, P. W. Anderson, D. C. Licciardello, and T. V. Ramakrishnan. Scaling theory of localization: Absence of quantum diffusion in two dimensions. *Phys. Rev. Lett.*, 42:673–676, 1979. doi:10.1103/PhysRevLett.42.673.

[2] G. W. Anderson, A. Guionnet, and O. Zeitouni. *An Introduction to Random Matrices*. Cambridge Studies in Advanced Mathematics. Cambridge University Press, 2009. doi:10.1017/CBO9780511801334.

[3] D. N. Arnold, G. David, M. Filoche, D. Jerison, and S. Mayboroda. Computing spectra without solving eigenvalue problems. *SIAM J. Sci. Comput.*, 41:B69–B92, 2017. URL: https://arxiv.org/abs/1711.04888.

[4] D. N. Arnold, G. David, M. Filoche, D. Jerison, and S. Mayboroda. Localization of eigenfunctions via an effective potential. *Commun. Part. Diff. Eq.*, 44(11):1186–1216, 2019. doi:10.1080/03605302.2019.1626420.

[5] D. N. Arnold, G. David, D. Jerison, S. Mayboroda, and M. Filoche. Effective confining potential of quantum states in disordered media. *Phys. Rev. Lett.*, 116:056602, 2016. doi:10.1103/PhysRevLett.116.056602.

[6] Y. Y. Atas, E. Bogomolny, O. Giraud, and G. Roux. Distribution of the ratio of consecutive level spacings in random matrix ensembles. *Phys. Rev. Lett.*, 110:084101, Feb 2013. doi:10.1103/PhysRevLett.110.084101.

[7] Y. Y. Atas, E. Bogomolny, O. Giraud, P. Vivo, and E. Vivo. Joint probability densities of level spacing ratios in random matrices. *Journal of Physics A: Mathematical and Theoretical*, 46(35):355204, 2013. doi:10.1088/1751-8113/46/35/355204.

[8] S. Balay, S. Abhyankar, M. F. Adams, J. Brown, P. Brune, K. Buschelman, L. Dalcin, V. Eijkhout, W. D. Gropp, D. Kaushik, M. G. Knepley, D. A. May, L. C. McInnes, R. T. Mills, T. Munson, K. Rupp, P. Sanan, B. F. Smith, S. Zampini, H. Zhang, and H. Zhang. PETSc users manual. Technical Report ANL-95/11 - Revision 3.9, Argonne National Laboratory, 2018.

[9] S. Balay, W. D. Gropp, L. C. McInnes, and B. F. Smith. Efficient management of parallelism in object oriented numerical software libraries. In E. Arge, A. M. Bruaset, and H. P. Langtangen, editors, *Modern Software Tools in Scientific Computing*, pages 163–202. Birkhäuser Press, 1997.

[10] D. Braun and G. Montambaux. Spectral correlations from the metal to the mobility edge. *Phys. Rev. B*, 52:13903–13909, Nov 1995. doi:10.1103/PhysRevB.52.13903.

[11] T. Devakul and D. A. Huse. Anderson localization transitions with and without random potentials. *Phys. Rev. B*, 96(214201), 2017. doi:http://dx.doi.org/10.1103/PhysRevB.96.214201.

[12] M. Filoche and S. Mayboroda. Universal mechanism for Anderson and weak localization. *Proc. Natl. Acad. Sci. USA*, 109(37):14761–14766, 2012. doi:10.1073/pnas.1120432109.

[13] M. Filoche and S. Mayboroda. *The landscape of Anderson localization in a disordered medium*, volume 601, pages 113–121. Contemp. Math., 2013. doi:10.1090/conm/601/11916.

[14] M. E. Fisher and M. N. Barber. Scaling theory for finite-size effects in the critical region. *Phys. Rev. Lett.*, 28:1516–1519, 1972. doi:10.1103/PhysRevLett.28.1516.

[15] V. Gasparian. Determinant approach to the scattering matrix elements in quasi-one-dimensional and two-dimensional disordered systems. *Phys. Rev. B*, 77:113105, 2008. doi:10.1103/PhysRevB.77.113105.

[16] V. Gasparian and A. Suzuki. Localization length in two-dimensional disordered systems: Effects of evanescent modes. *Journal of physics. Condensed matter : an Institute of Physics journal*, 21:405302, 10 2009. doi:10.1088/0953-8984/21/40/405302.

[17] L. Gong and K. Ma. Comparison of higher-order level spacing ratios signatures localization-delocalization transitions in one-dimensional single-electron lattice systems. *Physics Letters A*, 384(15):126298, 2020. doi:https://doi.org/10.1016/j.physleta.2020.126298.

[18] T. Guhr, A. Müller–Groeling, and H. A. Weidenmüller. Random-matrix theories in quantum physics: common concepts. *Phys. Rep.*, 299(4):189 – 425, 1998. doi:https://doi.org/10.1016/S0370-1573(97)00088-4.

[19] V. Hernandez, J. E. Roman, and V. Vidal. SLEPc: A scalable and flexible toolkit for the solution of eigenvalue problems. *ACM Trans. Math. Software*, 31(3):351–362, 2005. doi:https://doi.org/10.1145/1089014.1089019.

[20] M. Kappus and F. Wegner. Anomaly in the band centre of the one-dimensional Anderson model. *Z. Phys.*, 45(1):15–21, 1981. doi:10.1007/BF01294272.

[21] B. Kramer and A. MacKinnon. Localization: theory and experiment. *Rep. Prog. Phys.*, 56(12):1469–1564, 1993. doi:10.1088/0034-4885/56/12/001.

[22] R. C. Kuhn, O. Sigwarth, C. Miniatura, D. Delande, and C. A. Müller. Coherent matter wave transport in speckle potentials. *New J. Phys.*, 9(6):161–161, 2007. doi:10.1088/1367-2630/9/6/161.

[23] A. MacKinnon and B. Kramer. One-parameter scaling of localization length and conductance in disordered systems. *Phys. Rev. Lett.*, 47:1546–1549, 1981. doi:10.1103/PhysRevLett.47.1546.

[24] S. A. Molčanov. The structure of eigenfunctions of one-dimesional unordered structures. *Mathematics of the USSR-Izvestiya*, 12(1):69–101, 1978. doi:10.1070/im1978v012n01abeh001841.

[25] N. Mott. Electrons in disordered structures. *Adv. Phys.*, 16(61):49–144, 1967. doi:10.1080/00018736700101265.

[26] N. F. Mott and E. A. Davis. *Electronic Processes in Non-Crystalline Materials*. Oxford University Press, 1979.

[27] V. Oganesyan and D. A. Huse. Localization of interacting fermions at high temperature. *Phys. Rev. B*, 75:155111, 2007. doi:10.1103/PhysRevB.75.155111.

[28] A. Rodriguez, L. J. Vasquez, and R. A. Römer. Multifractal analysis with the probability density function at the three-dimensional Anderson transition. *Phys. Rev. Lett.*, 102:106406, 2009. doi:10.1103/PhysRevLett.102.106406.

[29] A. Rodriguez, L. J. Vasquez, K. Slevin, and R. A. Römer. Critical parameters from a generalized multifractal analysis at the Anderson transition. *Phys. Rev. Lett.*, 105:046403, 2010. doi:10.1103/PhysRevLett.105.046403.

[30] A. Rodriguez, L. J. Vasquez, K. Slevin, and R. A. Römer. Multifractal finite-size scaling and universality at the Anderson transition. *Phys. Rev. B*, 84:134209, 2011. doi:10.1103/PhysRevB.84.134209.

[31] J. E. Roman, C. Campos, E. Romero, and A. Tomas. SLEPc users manual. Technical Report DSIC-II/24/02 - Revision 3.10, D. Sistemes Informàtics i Computació, Universitat Politècnica de València, 2018.

[32] B. Shklovskii, B. Shapiro, B. Sears, P. Lambrianides, and H. Shore. Statistics of spectra of disordered systems near the metal-insulator transition. *Phys. Rev. B*, 47:11487–11490, 1993. doi:10.1103/PhysRevB.47.11487.

[33] D. Thouless. Introduction to localization. *Phys. Rep.*, 67(1):5 – 8, 1980. doi:https://doi.org/10.1016/0370-1573(80)90072-1.

[34] Z. Zhang. How many numerical eigenvalues can we trust? *Journal of Scientific Computing*, 65, 2013. doi:10.1007/s10915-014-9971-5.

Chapter 5

The Aubry-André Model

I Introduction

This final chapter is dedicated to the study of the Aubry-André model, a deterministic model mimicking some features of disordered systems. The previous chapters have delved into what information the localization landscape provides on the spatial structure of the eigenfunctions (Chapter 2) and on their spectral structure (Chapters 3 and 4). We now investigate how the Aubry-André model, which has been presented already in the introduction, can be studied using the localization landscape formalism. There are various experimental [19, 17, 12] and numerical [9, 20] setups that use this model, making it an interesting case study.

The Aubry-André model is unique in that it displays properties associated to randomness while being completely deterministic [3, 16, 14, 6]. This allows us to study localization in a frame containing analytical equations, which is not possible usually with disordered or random potentials. As it is a tight-binding model, the localization landscape equation reduces to a simpler relation, as opposed to the eigen-equation, and we will show that the landscape can be obtained through an exact closed formula.

In this chapter, we investigate the localization landscape for the one dimensional Aubry-André model, using results from the lattice landscape [18]. Our goal is to provide a base framework in the Aubry-André model to ease the study of more general quasiperiodic potentials, at greater dimensions for instance.

II The Aubry-André landscape

II.1 The Aubry-André model

The Aubry-André model is a tight-binding model of a quantum particle inside a periodic potential whose periodicity is incommensurate with that of the lattice. We recall the one-dimensional Aubry-André equation which reads:

$$H_\omega^{\lambda,\alpha}\psi_n = \psi_{n+1} + \psi_{n-1} - 2\lambda\cos\left[2\pi\left(\omega + n\alpha\right)\right]\psi_n = E\psi_n \tag{5.1}$$

with three different parameters, $\lambda > 0$ the potential's strength, $\alpha \in [0;1]$ the frequency (which is taken to be irrational in order to obtain an incommensurate potential) and $\omega \in [0;1]$ an additional phase. The "$\psi_{n+1}+\psi_{n-1}$" term represents the hopping term in a tight-binding nearest neighbor model. The hopping term can also be likened to the Laplacian term in what would be a continuous equation. We also recall that there are three different regimes for this equation:

- $\lambda > 1$: the eigenfunctions are all localized (pure point spectrum).
- $\lambda < 1$: the eigenfunctions are delocalized (absolutely continuous spectrum).

- The $\lambda = 1$ case is the critical regime where the spectral measure of the operator is zero, i.e. it is singular continuous [7]. The spectrum has a fractal and self-similar structure (the Hofstadter butterfly seen in the introduction).

In this chapter we study the localizing regime of the operator, i.e. for $\lambda > 1$. Since this is a discrete system, the spectrum can only take values in the interval $[-2\lambda - 2, 2\lambda + 2]$. In order to work only with positive eigenvalues, we apply a constant shift $(2\lambda + 2)$ to the potential which does not modify the spatial structure of the eigenfunctions nor the structure of the spectrum. We also chose to multiply the cosine term by -1 which once again does not change any of the results. The consequence is that the potential vanishes at $n = 0$ which makes finding the fundamental mode easier since the global minimum of the potential is at $n = 0$. Figure 5.1 displays two examples of Aubry-André potentials (5.1a and 5.1b) as well as two corresponding eigenfunctions (5.1c and 5.1d). The second example was chosen so that the irrational frequency is close to $1/2$, making the potential seem almost periodic to the naked eye. The frequency of the first example was chosen to be "highly irrational", in practice far away from the "simplest" fractions $(1/2, 1/3, 1/4, 1/5,$ etc.) so that patterns in the potential are more difficult to discern, and so that it seems more "random". The pseudo-random potentials exhibit regularly spaced peaks and valleys, but the values they take are never repeated. The eigenfunctions exhibit several peaks spaced out at specific intervals in a hierarchical structure.

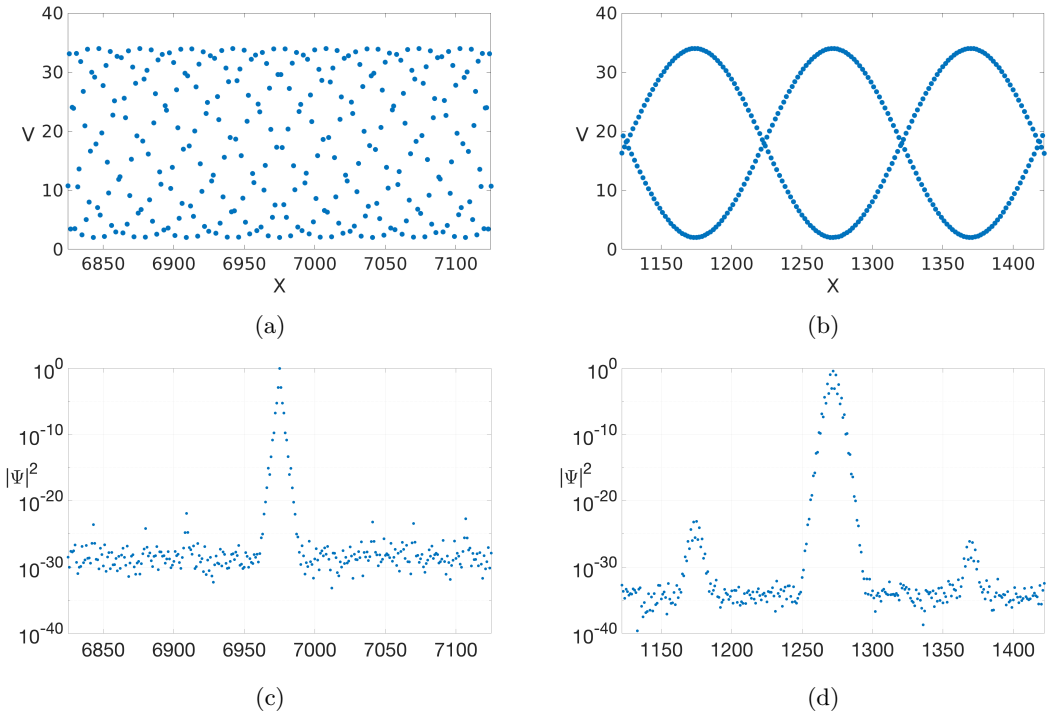

Figure 5.1: (a) Aubry-André potential for $\lambda = 8$ and $\alpha = 3000/7919 \approx 0.379$ (b) Aubry-André potential for $\lambda = 8$ where $\alpha = 4000/7919 \approx 0.505$. (c) An eigenfunction of eigenvalue $E = 1.93$ corresponding to the potential of $\alpha = 3000/7919 \approx 0.379$. (d) An eigenfunction of eigenvalue $E = 1.91$ corresponding to the potential of $\alpha = 4000/7919 \approx 0.505$.

In order to simulate a pseudo-random potential numerically we have to design a finite-system-size approximation of Eq. (5.1) [9]. To mimic an infinite domain, we use periodic boundary conditions, which means that $\alpha L \in \mathbb{Z}$ so that $V_{n+L} = V_n$, L being the domain size. Furthermore, for the potential to be incommensurate, we also require that no value is to be repeated, which demands that $V_n \neq V_{n'}$ from which follows that $\gcd(\alpha L, L) = 1$ (where $\gcd(a, b)$ is the greatest common divisor between a and b). In practice, taking the domain size L to be a prime number and defining the frequency as $\alpha = \frac{n_\alpha}{L}$ with n_α an integer between 1 and L is sufficient to properly approximate equation 5.1.

II.2 The localization landscape of the Aubry-André model: extensions of the landscape properties in the discrete setting

Although initially designed for continuous systems, one can also derive a discrete version of the localization landscape [18]. It is obtained by solving the analogous landscape equation:

$$u_{n+1} + u_{n-1} + (2\lambda + 2 - 2\lambda \cos[2\pi(\omega + n\alpha)])\, u_n = 1. \tag{5.2}$$

Most of the properties of the landscape have been proven in the continuous case. In this subsection we will express the discrete versions of these properties. One of the first ones is a control inequality that provides an upper bound for the eigenfunctions' amplitude:

$$|\psi_n| < E u_n. \tag{5.3}$$

The fundamental inequality (5.3) has been explicitly confirmed. As seen in Chapter 2, this relation means that the eigenfunctions' amplitude has to be small in regions where the landscape is small as well. However, this conclusion only holds when $u_n < \frac{1}{E}$ since the eigenfunctions are L^∞ normalized in the inequality. In Figure 5.2, we have displayed the four first eigenfunctions of a tight-binding Hamiltonian with a potential following a uniform random law with values in $[2t; 4t]$ alongside the localization landscape. We can see that the latter predicts the regions where localization occurs.

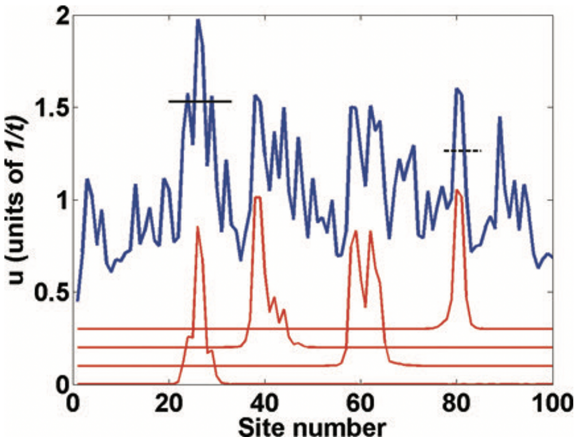

Figure 5.2: Four first eigenstates of a tight-binding Hamiltonian with a potential following a uniform random law with values in $[2t; 4t]$. The system is of size $L = 100$. The localization landscape is plotted in blue, while in red are the 4 first eigenstates. Reprinted from [18].

Since this is a discrete system, localization also occurs at the top of the spectrum. In Figure 5.3, we can see that the last eigenstates at the top of the spectrum oscillate with a frequency equal to the inverse of the lattice parameter. We can study their envelope by transforming the eigenfunction and removing the high frequency contribution: $\psi_n = (-1)^n \varphi_n$. The eigen-equation then becomes:

$$(\varphi_{n+1} + \varphi_{n-1}) + (2\lambda + 2 - 2\lambda \cos[2\pi(\omega + n\alpha)])\, \varphi_n = E\varphi_n \tag{5.4}$$

There is a symmetry by change of sign of the hopping amplitude (here set at 1) which reverses the order of the eigenstates (the low energy eigenfunctions become high energy and vice-versa). We apply a shift to the potential so that all the eigenvalues are positive again. We can then define a dual landscape that has similar properties to that of the original localization landscape except applied to the envelopes of the original high energy eigenstates (that are now low energy with this transformation):

$$-(u^*_{n+1} + u^*_{n-1}) + (V_{\text{shift}} + 2\lambda + 2 - 2\lambda \cos[2\pi(\omega + n\alpha)])u^*_n = 1, \tag{5.5}$$

where u^* is the dual landscape. The new confining inequality reads $\varphi_n < u^*_i(V_{\text{shift}} - E^*)$.

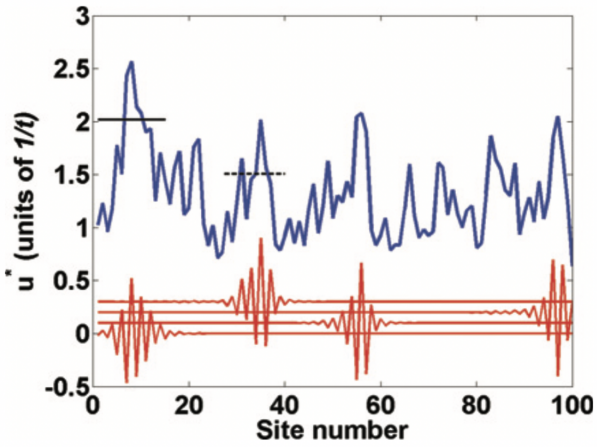

Figure 5.3: Four last eigenstates of a tight-binding Hamiltonian with a potential following a uniform random law with values in $[2t; 4t]$. The system is of size $L = 100$. The dual landscape is plotted in blue, while in red are the 4 last eigenstates. Reprinted from [18].

As mentioned before in the continuous case, the localization landscape defines an effective confining potential $W \equiv 1/u$ [2] which is a smoothed version of the original potential. This effective confining potential allows for approximations of not only the fundamental eigenvalue of each localized sub-region, but also its corresponding eigenfunction. The estimate for the fundamentals in each sub-region is $E_0^{(m)} \approx \left(1 + \frac{d}{4}\right) \min_{\Omega_m} W$, where d is the dimensionality of the system [1, 11]. It also enables us to define an Agmon distance:

$$\rho_E(\vec{r_1}, \vec{r_2}) = \min_{\gamma} \left(\int_{\gamma} \sqrt{(W(\vec{r}) - E)_+} ds \right). \tag{5.6}$$

Although there was no mathematical proof of a discrete counterpart of the continuous Agmon distance, a natural extension of this notion to the tight-binding model would be:

$$\rho_E(n_1, n_2) = \min_{\gamma} \sum_i \sqrt{(W_i - E)_+}. \tag{5.7}$$

Extending from the continuous result, an eigenfunction centered at n_0 is therefore expected to decay as $\psi_i \lesssim e^{-\rho_E(n_0, n_i)}$.

Very recently, an exact discrete version of the Agmon distance has been proven [22]:

$$\rho_E(n_1, n_2) = \inf_{\gamma \in \mathcal{P}(n,m)} \sum_{j=1}^{k(\gamma)} \ln \left(1 + \sqrt{\min \left[(W_{\gamma_j} - E)_+, (W_{\gamma_{j+1}} - E)_+ \right]} \right), \tag{5.8}$$

where $\mathcal{P}(n, m)$ is the collection of paths going from n to m and γ a path. Eq. (5.7) is a good approximation of Eq. (5.8), which allows us to use the former expression.

The asymptotic behavior of the integrated density of states can be determined using Weyl's law. This law uses the potential in its expression:

$$N_V(E) \propto \int_{V(x)<E} \sqrt{(E - V(x))_+} dx. \tag{5.9}$$

In disordered systems, replacing the potential with the effective confining potential in Weyl's law has been found to give better approximations:

$$N_W(E) \propto \int_{W(x)<E} \sqrt{(E - W(x))_+} dx, \tag{5.10}$$

which translates to:

$$N_W(E) \propto \sum_{W_i<E} \sqrt{E - W_i}. \tag{5.11}$$

Recent research on the integrated density of states for random potentials in localization landscape theory has led to upper and lower bounds of the counting function [8]. We recall the landscape law counting function (3.4) defined in Chapter 1.

$$N_u(E) = \frac{1}{|\Omega|} \times \left(\text{the number of cubes } Q \in \{Q\}_{\kappa\mu^{-1/2}} \text{ such that } \min_Q \frac{1}{u} \leq E \right) \tag{5.12}$$

as well as the following inequality with constants the C_4, C_5, and C_6:

$$C_5 N_u(C_6 E) \leq N(E) \leq N_u(C_4 E), \tag{5.13}$$

We now have all the tools necessary to study tight-binding Hamiltonians with the localization landscape. We display some examples of the localization landscape calculated for Aubry-André potentials to provide visual examples. Doing so, we show qualitatively that the effective confining potential is a good predictor of the localization sub-regions.

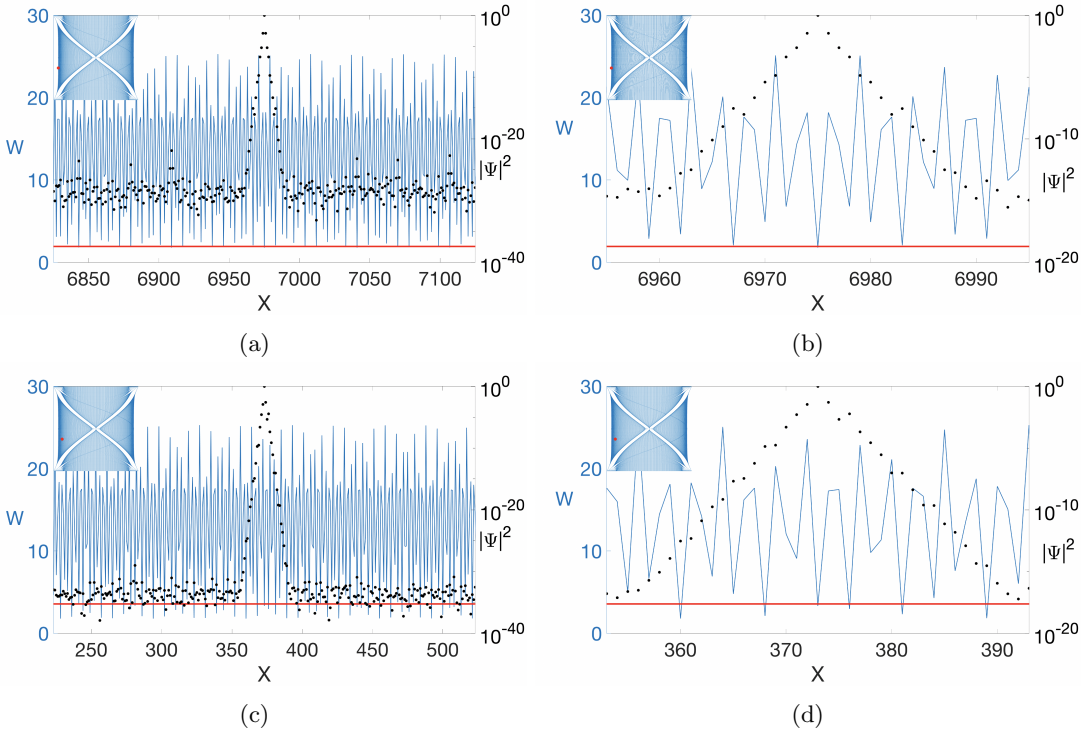

Figure 5.4: Eigenfunctions displayed over the effective confining potential. The parameters of the Aubry-André potential are: $\lambda = 8$ and $\alpha = 3000/7919 \approx 0.379$. The red line corresponds to the energy of the eigenfunction. In the top left of each figure is displayed the the position of the eigenvalue in the energy-frequency graph. (a) $E = 1.93$ (b) Zoomed in version of (a). (c) $E = 3.57$ (d) Zoomed in version of (c).

We start by displaying for two different localized eigenfunctions for two different irrational frequencies ($\alpha = 3000/7919 \approx 0.379$ and $\alpha = 0.505$) and with $\lambda = 8$ (localized regime) (see Figures 5.4 and 5.5). We have selected the two same irrational frequencies as for our first examples in Figure 5.1, and two eigenfunctions whose energy is at the bottom of the spectrum, as can be seen in the energy-frequency graphs displayed in the top right corner of each eigenfunction plot.

In Figures 5.4b, 5.4d, 5.5b, and 5.5d, one can see that the maximum of the eigenfunction occurs on the lattice point where its energy intersects the effective confining potential. The eigenfunctions then decay from this maximum, but re-increases on lattice points where their energy is greater than W.

The minima of the effective confining potential predict where the eigenfunctions will be maximal, and W also indicates how the eigenfunctions decay.

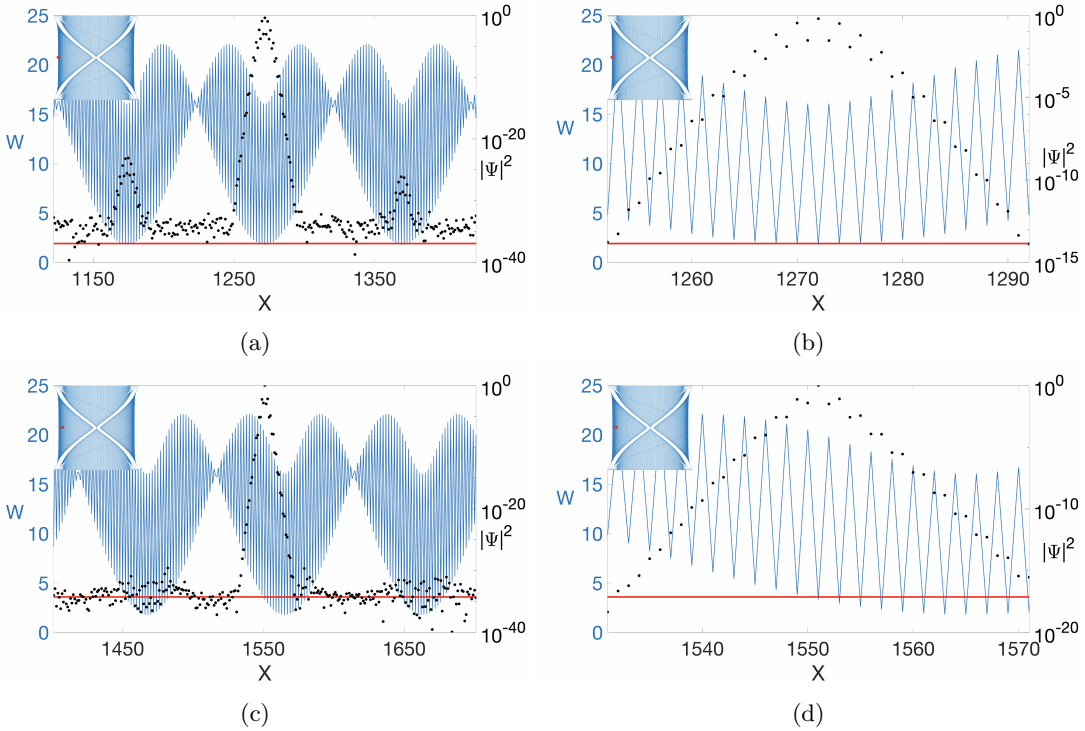

Figure 5.5: Eigenfunctions displayed over the effective confining potential. The parameters of the Aubry-André potential are: $\lambda = 8$ and $\alpha = 4000/7919 \approx 0.505$. The red line corresponds to the energy of the eigenfunction.In the top left of each figure is displayed the the position of the eigenvalue in the energy-frequency graph. (a) $E = 1.91$ (b) Zoomed in version of (a). (c) $E = 3.58$ (d) Zoomed in version of (c).

III A closed formula for the localization landscape

It turns out that an exact closed formula can be derived for the localization landscape in finite sized systems, by exploiting the fact that in one-dimension, the Aubry-André localization landscape equation reduces to a second order recurrence equation, which we will present in this section.

First we will directly calculate the localization landscape by using the forward sweep or Thomas algorithm, which is presented in the appendix 5.A.1. We will then use the fact that numerical results shown in Figures 5.4 and 5.5 suggest that the solution to this equation is the sum of sines and cosines. We therefore search for a solution using the discrete Fourier transform (DFT) of the localization landscape.

III.1 Direct calculation

We start by simplifying the equation to make it more manageable. Since we have periodic boundary conditions and because we have $\alpha = n_\alpha/N$, the potential V_k is symmetric and even: $V_k = V_{N-k}$ and $V_k = V_{-k}$. The same is therefore true for the landscape. We only need to solve the second order recurrence equation on half the lattice points thanks to this symmetry.

Defining $g_k = 2\lambda + 2 - 2\lambda\cos\left(\frac{2\pi(k-1)n_\alpha}{N}\right)$, the system reduces to:

$$\text{if } N \text{ is odd: } H = \begin{pmatrix} g_k & -2 & ... & 0 \\ -1 & ... & ... & 0 \\ ... & ... & ... & ... \\ 0 & ... & -1 & g_{\frac{N+1}{2}} - 1 \end{pmatrix} \tag{5.14}$$

$$\text{if } N \text{ is even: } H = \begin{pmatrix} g_k & -2 & ... & 0 \\ -1 & ... & ... & 0 \\ ... & ... & ... & ... \\ 0 & ... & -2 & g_{\frac{N}{2}} \end{pmatrix} \tag{5.15}$$

One introduces the vectors U_k and X_k defined as: $U_k = u_{k-1}$ and $X_k = 1$. From this

$$HU = X \tag{5.16}$$

In the same way, we can define two sequences c_k and e_k:

$$\begin{aligned} &c_1 = g_1 = 2 \qquad c_k = g_k - \frac{1}{c_{k-1}} = g_k - \frac{1}{g_{k-1} - \frac{1}{...-1}} \\ &e_1 = 1 \qquad e_k = 1 + \frac{e_{k-1}}{c_{k-1}} = 1 + \frac{1}{c_{k-1}} + \frac{1}{c_{k-1}c_{k-2}} + ... = 1 + \sum_{j=1}^{k-1} \prod_{l=j}^{k-1} \frac{1}{c_l} \end{aligned} \tag{5.17}$$

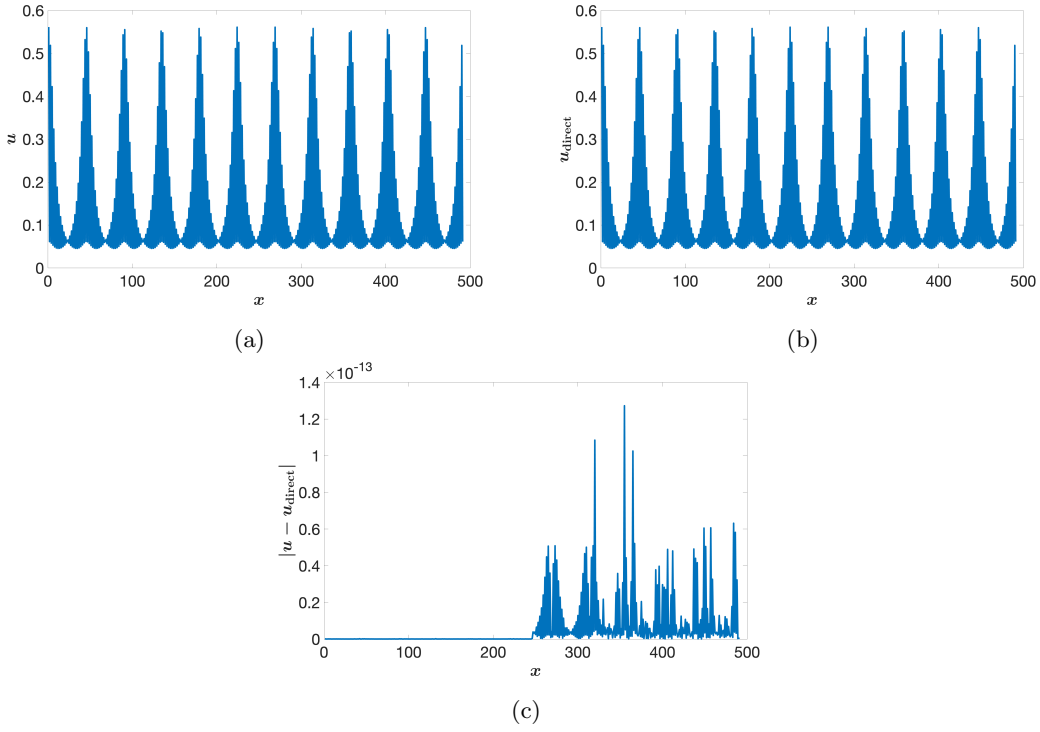

Figure 5.6: (a) The localization landscape computed numerically with the following parameters: $N = 491$ and $\alpha : 251/491 \approx 0.511$. (b) The localization landscaped computed using the direct formula 5.18. (c) Difference between the landscape computed using numerical methods and the closed formula 5.18.

And then, using the Thomas algorithm presented in the appendix 5.A.1, the localization landscape is given by:

$$
\begin{aligned}
U_{\frac{N+1}{2}} &= \frac{e_{\frac{N+1}{2}}}{c_{\frac{N+1}{2}}} = \sum_{j=1}^{\frac{N+1}{2}} \prod_{l=j}^{\frac{N+1}{2}} \frac{1}{c_l} \\
U_k &= \frac{e_k + U_{k+1}}{c_k} = \frac{e_k}{c_k} + \frac{1}{c_k}\frac{e_{k+1}}{c_{k+1}} + ... + \frac{1}{c_k ... c_{\frac{N-1}{2}}}\frac{e_{\frac{N+1}{2}}}{c_{\frac{N+1}{2}}} \\
U_k &= \sum_{j=1}^{k}\prod_{l=j}^{k}\frac{1}{c_l} + \frac{1}{c_k}\sum_{j=1}^{k+1}\prod_{l=j}^{k+1}\frac{1}{c_l} + ... + \frac{1}{c_k ... c_{\frac{N-1}{2}}}\sum_{j=1}^{\frac{N+1}{2}}\prod_{l=j}^{\frac{N+1}{2}}\frac{1}{c_l} = \sum_{m=k}^{\frac{N+1}{2}}\left(\prod_{m'=k}^{m-1}\frac{1}{c_{m'}}\right)\left(\sum_{j=1}^{m}\prod_{l=j}^{m}\frac{1}{c_l}\right)
\end{aligned}
\tag{5.18}
$$

Figure 5.6 compares the localization landscape computed numerically and the one obtained through the direct formula (5.18) (top left and right respectively), as well as the difference between this computational method and traditional numerical methods (bottom frame). The difference is very small (which are of the order of 10^{-13}) when compared to the values of the landscape (of the order of 0.1 as can be seen in Figures 5.6a and 5.6b). Interestingly, the difference is larger in the second half of the domain. This is most likely because the direct method exploits the symmetry of the localization landscape while the numerical computational method does not.

While this formula gives results that are essentially identical to the real landscape, it is not very interpretable, and does not give any information on the structure of the landscape.

III.2 Discrete Fourier Transform

We now move on to the second method using the discrete Fourier Transform for determining a closed formula for the localization landscape. As mentioned before, the structure of the landscape is very periodic. For instance, in Figure 5.5, the landscape seems to be the product of three cosines: one with a wavelength equal to the lattice spacing, another with a wavelength equal to about 200, and a last one with a wavelength of around 100. It therefore makes sense to search for a solution using the discrete Fourier Transform.

We define the inverse discrete Fourier transform (DFT) as:

$$
u_n = \frac{1}{N}\sum_{k=0}^{N-1}\tilde{u}_k e^{\frac{2\pi i}{N}kn} \tag{5.19}
$$

The method of calculation is quite similar to what was done in the previous subsection. The reader should refer to the appendix 5.A.2 for more details. In the direct calculation, the terms in relation to one another are the adjacent ones. What we mean by this is that u_k is expressed with u_{k+1} and u_{k-1}. Once the landscape equation has been rewritten for its Fourier coefficients, the coefficients that are in relation to one another are no longer the adjacent ones, but those n_α apart. It is therefore necessary to reorder these coefficients in order to apply the Thomas algorithm. We define: $\tilde{U}'_{k+1} = \tilde{u}_{k\,n_\alpha}$ as the reordered Fourier coefficients.

In the case of odd N, we define the sequences b_k and d_k:

$$
\begin{aligned}
b_1 &= 1 \qquad b_k = f_k - \frac{1}{b_{k-1}} = f_k - \frac{1}{f_{k-1} - \frac{1}{...-1}} \\
d_1 &= \frac{N}{2\lambda} \qquad d_k = \frac{d_{k-1}}{b_{k-1}} = \frac{\frac{N}{2\lambda}}{b_{k-1}...b_1}.
\end{aligned}
\tag{5.20}
$$

We can then express the reordered Fourier coefficients as:

$$\begin{aligned}
\tilde{U}'_{\frac{N+1}{2}} &= \frac{d_{\frac{N+1}{2}}}{b_{\frac{N+1}{2}}} = \frac{\frac{N}{2\lambda}}{b_{\frac{N+1}{2}}...b_1} \\
\tilde{U}'_k &= \frac{d_k}{b_k} + \frac{\tilde{U}'_{k+1}}{b_k} = \frac{N}{2\lambda}\left(\frac{1}{b_1...b_k} + \frac{1}{b_1...b_k^2 b_{k+1}} + ... + \frac{1}{b_1...b_k^2...b_{\frac{N+1}{2}-1}^2 b_{\frac{N+1}{2}}}\right)
\end{aligned} \tag{5.21}$$

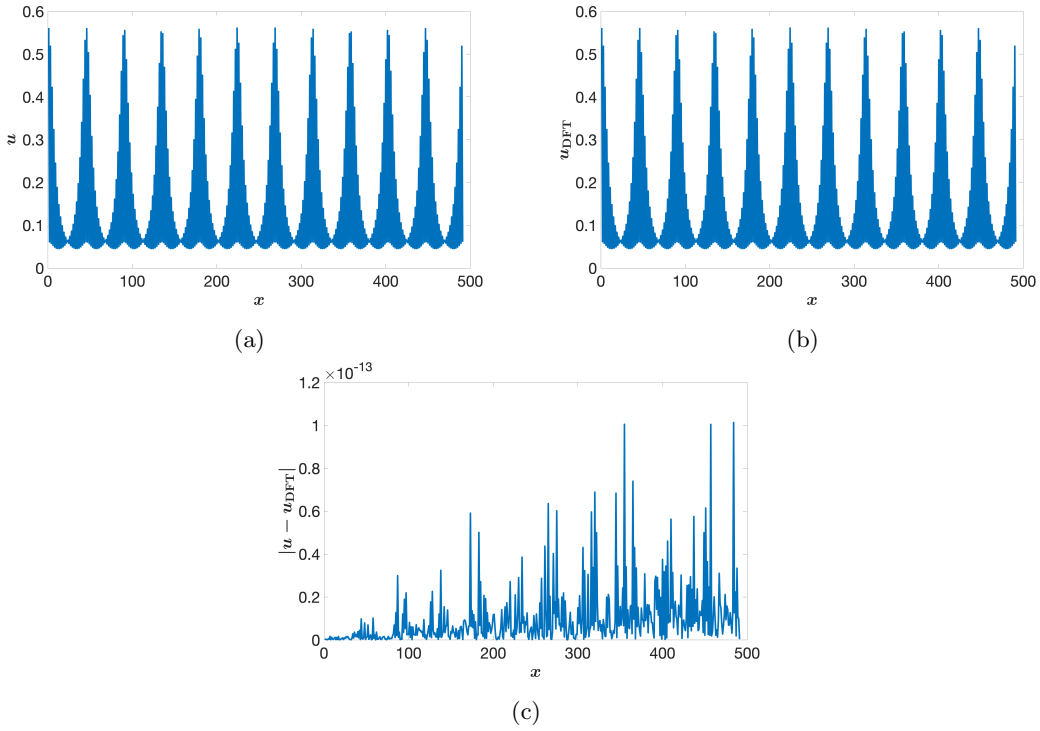

Figure 5.7: (a) Localization landscape computed numerically with the following parameters: $N = 491$ and $\alpha : 251/491 \approx 0.511$. (b) Localization landscaped computed using the DFT method. (c) The difference between the landscape computed using numerical methods and the DFT method.

This allows for an iterative method to calculate the Fourier coefficients directly starting from the last reordered Fourier coefficient and then computing the rest by backwards iteration. In Figure 5.7 we can see that this method produces very accurate results. The first two figures show an example of localization landscape calculated with the same parameters ($N = 491$ and $n_\alpha = 251$) using numerical methods (on the left) and the iterative formula (on the right). The bottom figure shows the difference between these two methods (of the order of 10^{-13}).

The various computations of $\tilde{U}'_k$ in Figure 5.8 suggest that the reordered Fourier coefficients decrease. In Figure 5.8a, the increase and decrease of the Fourier coefficients follow a regular pattern that is difficult to discern, whereas in Figure 5.8b, where the terms have been rearranged, consecutive terms clearly decrease regularly.

We have unfortunately been unable to prove that the reordered Fourier coefficients decrease, but all of our numeric evidence suggests it. In Figure 5.9, we have plotted a histogram of the distribution of the values of $\tilde{U}'_{k+1}/\tilde{U}'_k$ for $N = 491$ and for all values of n_α. These ratios are all strictly between 0.5 and 1, which shows that the reordered Fourier coefficients are always decreasing. The rate at which the coefficients decrease depends on the value of n_α, and the distribution of these rates does not have a well defined shape. Nonetheless, if we assume that on average the rate at which the coefficients decreases is equal to the mean of the distribution of the ratios $\tilde{U}'_{k+1}/\tilde{U}'_k$, i.e. 0.624, then on average the 11^{th} coefficient will be around $0.624^{10} \approx 0.01$ times the value of the first coefficient.

The agreement is very good between both closed formulae we have derived and the numerical computations. Unfortunately, the method we have just described to derive these formulae does not generalize at

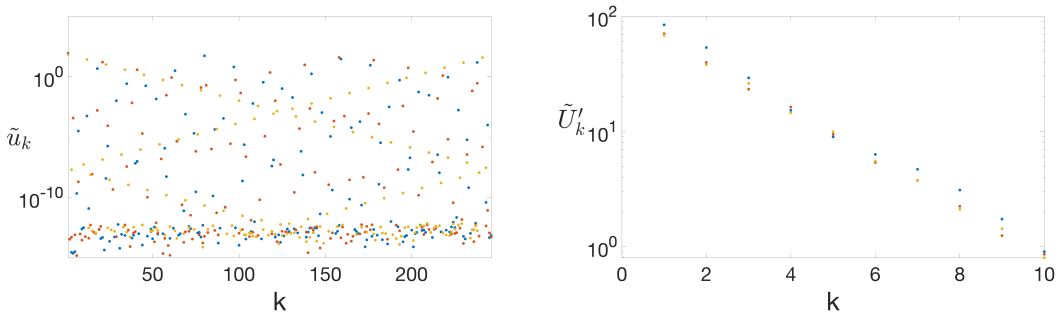

(a) (b)

Figure 5.8: (a) The Fourier coefficients of the localization landscape calculated for $N = 491$ and 3 different values of $n_\alpha = \{79, 157, 251\}$ in logarithmic scale. (b) First terms of the reordered Fourier coefficients $\tilde{U}'_k$ for the same N and n_α.

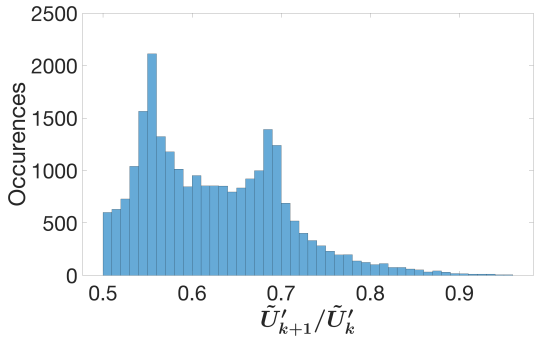

Figure 5.9: Histogram of the distribution of the values of $\tilde{U}'_{k+1}/\tilde{U}'_k$ for $N = 491$ and for $n_\alpha \in \{1, 490\}$. For each value of n_α, we computed the ratio for the 51 first reordered Fourier coefficients. The maximum value of this distribution is 0.955, the mean is 0.624, and the minimum is 0.5.

all at higher dimensions.

IV Structure of eigenfunctions and eigenvalues

The structure of the eigenfunctions is already well understood: in the localization regime the exact asymptotics of the eigenfunctions determined by the continued fraction of the frequency are known [4, 15]. The goal in this section is to assess whether the properties of the localization landscape presented before remain true for Aubry-André potentials.

IV.1 Structure and localization of the eigenfunctions

To begin with, the Agmon distance already presented in section II.2 and defined via the effective confining potential, controls the decay of the exponentially localized eigenfunctions [2]. In Figure 5.10 we have displayed an eigenfunction and its Agmon estimate for two different potentials. The estimate is calculated by computing the Agmon distance between the maximum of the eigenfunction and each point. We see that the Agmon estimate controls the exponential decay of the eigenfunction, but does not account for the resonances of the eigenfunctions. According to the definition of the Agmon distance (5.6), it is a decreasing function from its starting point, whereas the eigenfunction can increase again (this is particularly apparent in Figure 5.10d).

To study localization, an essential issue is to be able to identify quantitatively whether eigenfunctions are localized or delocalized. We have used the inverse participation ratio (IPR), which we have presented

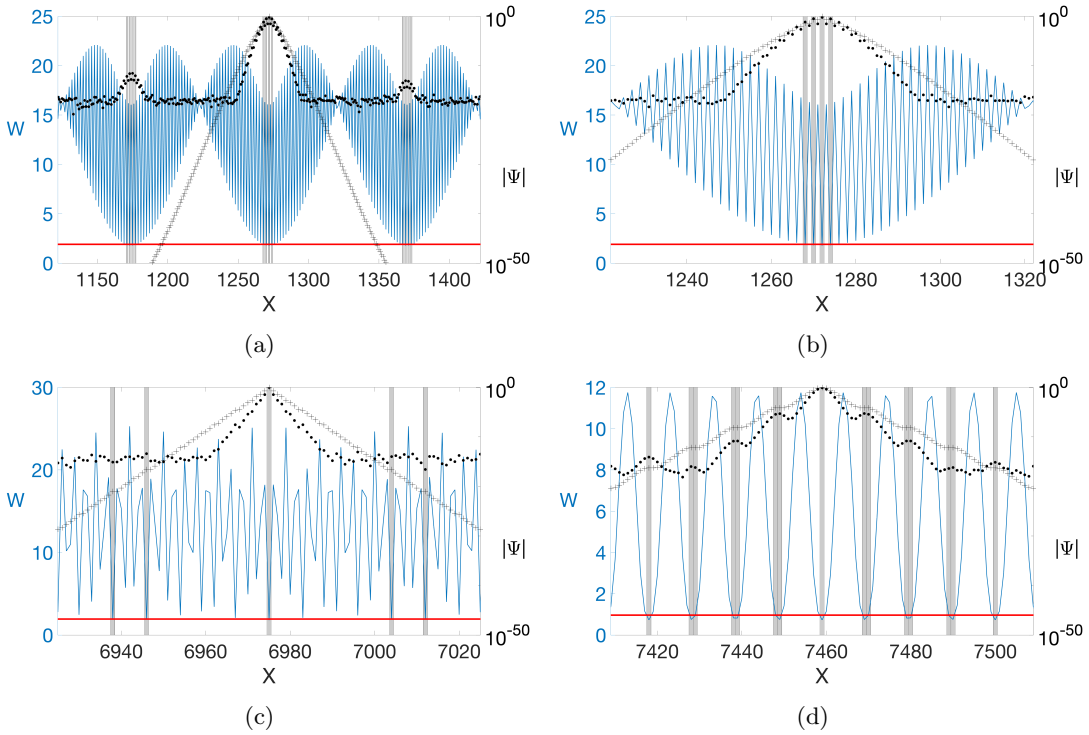

Figure 5.10: In each figure is displayed the effective confining potential for a certain set of parameters N, λ and α, alongside an eigenfunction (in dots) and its Agmon estimate (in crosses). The red horizontal line corresponds to the energy of the eigenfunction. The grayed out areas correspond to points where the eigenvalue is greater than the effective confining potential. (a) The potential's parameters are: $N = 7919$, $\lambda = 8$ and $\alpha = 4000/7919 \approx 0.505$. The eigenvalue is $E = 1.91$. (b) Same as (a) but zoomed in. (c) The potential's parameters are: $N = 7919$, $\lambda = 8$ and $\alpha = 3000/7919 \approx 0.379$. The eigenfunction is of energy $E = 1.93$. (d) The potential's parameters are: $N = 7919$, $\lambda = 3$ and $\alpha = 773/7919 \approx 0.0976$. The eigenfunction is of energy $E = 0.96$. In this case the eigenfunction increases again on the lattice points where its energy is less than W (the grayed out areas).

before in Chapter 2, to measure the localization of eigenfunctions. We recall the definition of the IPR as:

$$\text{IPR} = \frac{\left(\sum_n |\psi_n|^4\right)}{\left(\sum_n |\psi_n|^2\right)^2}. \tag{5.22}$$

We also remind the reader that a completely localized eigenfunction which only exists in one point has an inverse participation ratio of 1. Contrarily, a delocalized eigenfunction has an inverse participation equal to $1/N$, which tends towards 0 in the limit of the infinite system size.

We then replace the eigenfunction in the expression of the inverse participation ratio by the Agmon estimate defined before in order to determine whether this estimate is accurate in determining if the eigenfunctions are localized or not.

As expected, as can be seen in Figure 5.11, in the low energy part of the spectrum, the approximation derived from the Agmon distance given by the localization landscape provides a result that is in accord with what the eigenfunctions would give. We define r as the absolute difference between the IPR computed from both methods used to obtain it. We show this absolute difference in the bottom part of Figure 5.11. In the more localizing regimes, at the bottom of the spectrum, the difference between the IPRs approaches 0 in the interval $\alpha \in [0.1, 0.9]$. For the $\lambda = 8$ case, in this frequency interval, the average absolute difference for the 50 first eigenfunctions is $\langle r \rangle = 0.049$, and for 82% of the eigenfunctions the r is less than 0.1. In the $\lambda = 3$ case, the error for frequencies close to 0.25, 0.33, 0.5, 0.66, and 0.75 are greater compared to all the other frequencies. In Figure 5.12 we have zoomed in on Figure 5.11b and drawn arrows pointing at the areas where the error is greater. These frequencies correspond to where the potential resembles

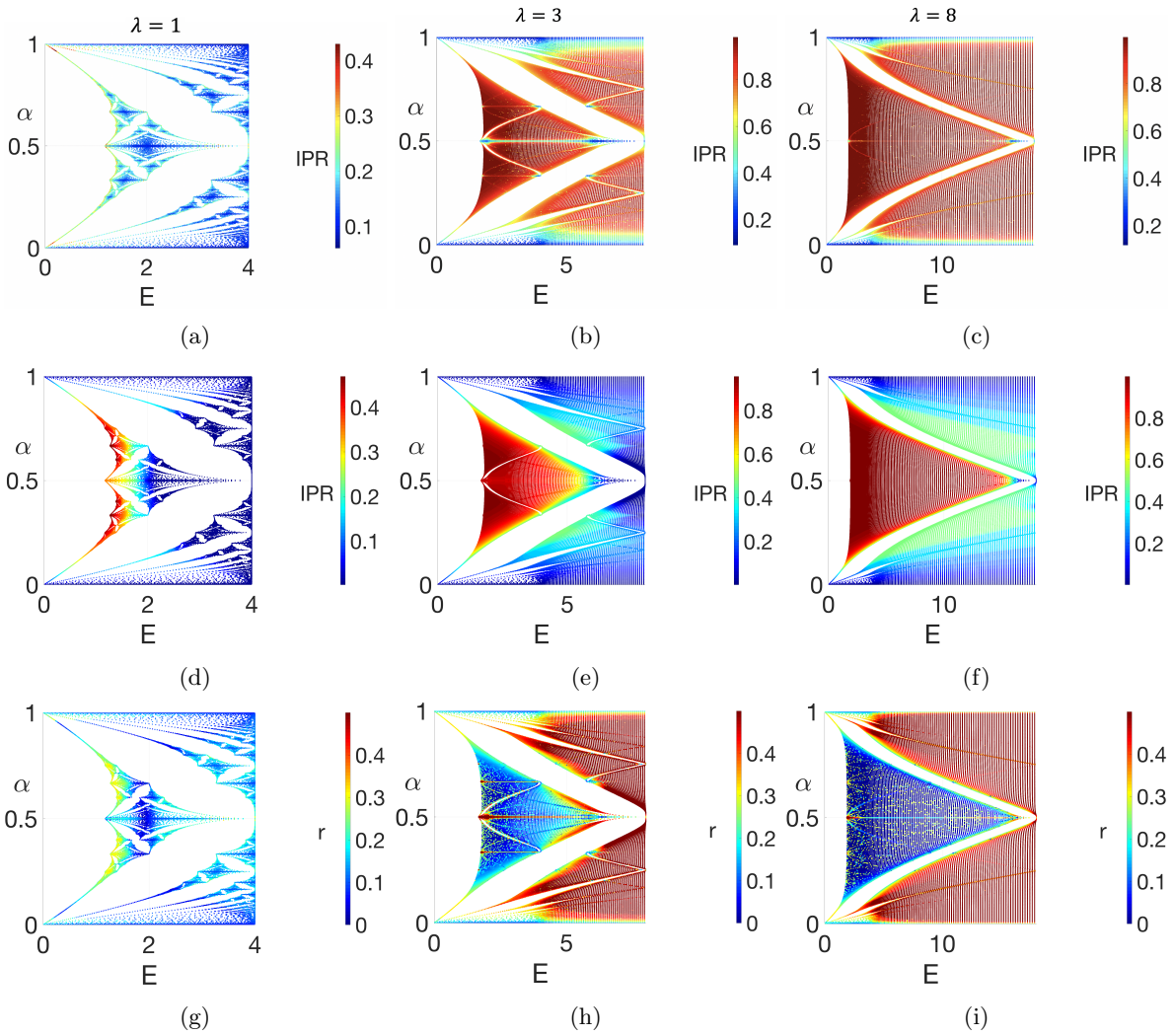

Figure 5.11: The low energy part of the energy-frequency graphs. Top row: color representation of the inverse participation ratio of the eigenfunctions for three different values of $\lambda = 1, 3$ and 8 (See Eq. (5.22)). Middle row: color representation of the inverse participation ratio calculated from the Agmon estimate for three different values of $\lambda = 1, 3$ and 8 ($\psi_i \approx e^{-\rho_E(n_0,n_i)}$). Bottom row: color representation of the absolute difference of the exact IPR of the eigenfunctions and the IPR computed using the Agmon estimate for three different values of $\lambda = 1, 3$ and 8.

the most a periodic potential, meaning the eigenfunctions are slightly more delocalized, as can be seen in Figure 5.11b. This behavior is not captured by the Agmon distance approximation of the IPRs.

To summarize, the Agmon distance and the approximation derived from it provide an accurate estimate of the eigenfunctions at the bottom of the spectrum, granted that the eigenfunctions are localized (which is not so much the case when the frequency of the potential gets close to certain rational frequencies).

IV.2 Relationship between minima of effective confining potential and eigenvalues

The ratio between the minima of the effective confining potential and the first eigenvalues has been measured consistently around (1+d/4) in the continuous case for many types of disordered potential [1]. In this subsection, we investigate whether this still holds in the Aubry-André model. We computed the first eigenfunctions, their eigenvalues, and their respective minimum of the effective confining potential for different potential strengths and irrational frequencies. We compared these eigenvalues and these minima in order to study the relationship between them.

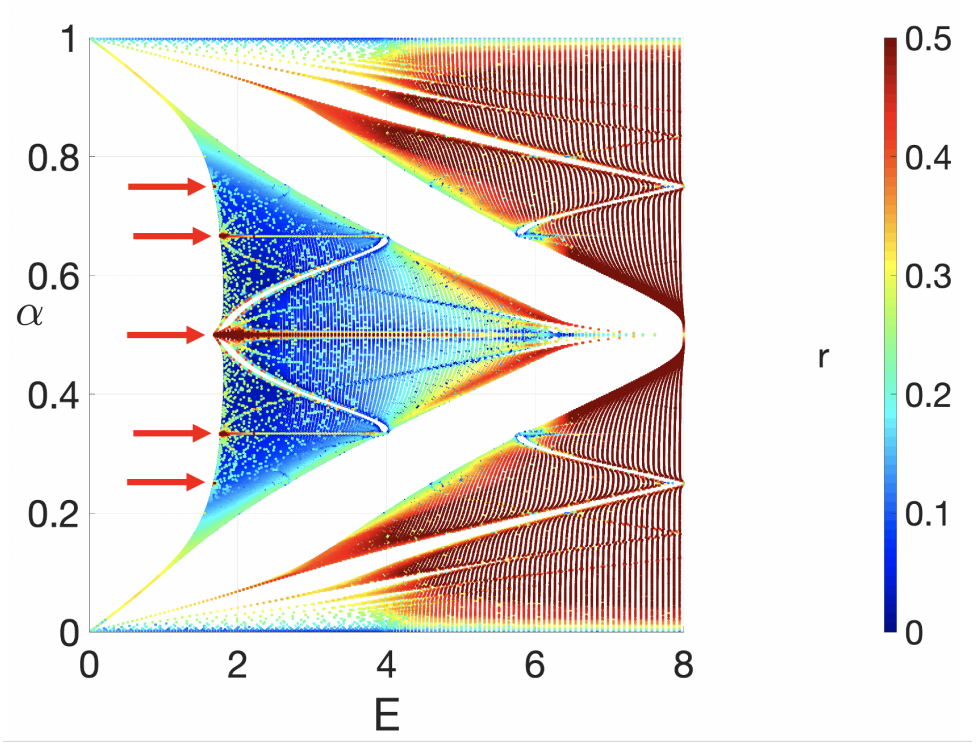

Figure 5.12: A closer look at a color representation of the absolute difference of the IPR calculated using both methods for $\lambda = 3$. The arrows point at areas of the low energy spectrum where the error is large.

In Figure 5.13, we have displayed the first 500 eigenvalues versus their corresponding minima values of the effective confining potential as well as their ratios for a strongly localizing Aubry-André potential. We have repeated this study for all values of α and different values of λ (different potential strengths). Figure 5.14 shows the range of values the ratios can take for different irrational frequencies. Figure 5.15 shows the average of these ratios for each frequency, while Figure 5.16 shows the standard deviation of the distribution of the ratios.

Our first observation in Figure 5.13 is that these ratios remain remarkably constant for frequencies in the interval [0.1 0.9]. This is where the standard deviation of the distribution of ratios is the closest to 0 ($\sigma < 0.015$) according to Figure 5.16. Furthermore the standard deviation decreases when the potential strength is larger. This makes sense as the eigenfunctions are more localized on individual sites when the potential is stronger.

Our second observation from Figure 5.13 is that the average of the ratio between the eigenvalues and the corresponding minima value is not $(1 + d/4)$, but varies depending on the frequency and the potential strength. For $\lambda = 8$, the average ratio goes from 1.27 at $\alpha \approx 0.1$ to 1.07 at $\alpha \approx 0.4$ before going back up to 1.1 at $\alpha \approx 0.5$. For $\lambda = 3$, it goes from 1.30 at $\alpha \approx 0.1$ to 1.17 at $\alpha \approx 0.4$ before going to 1.12 at

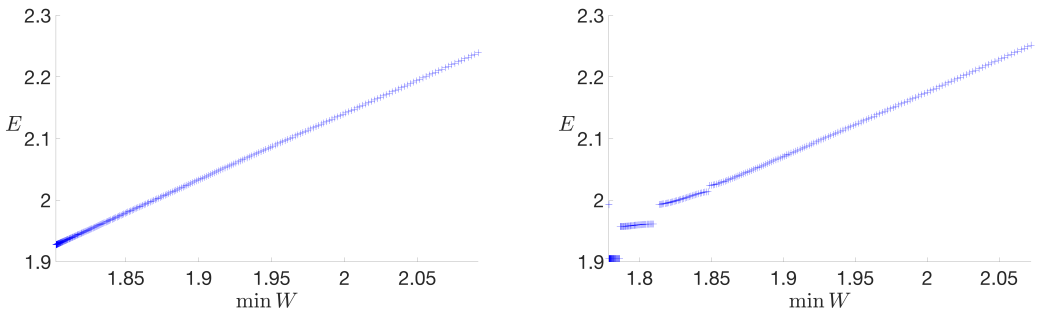

(a) (b)

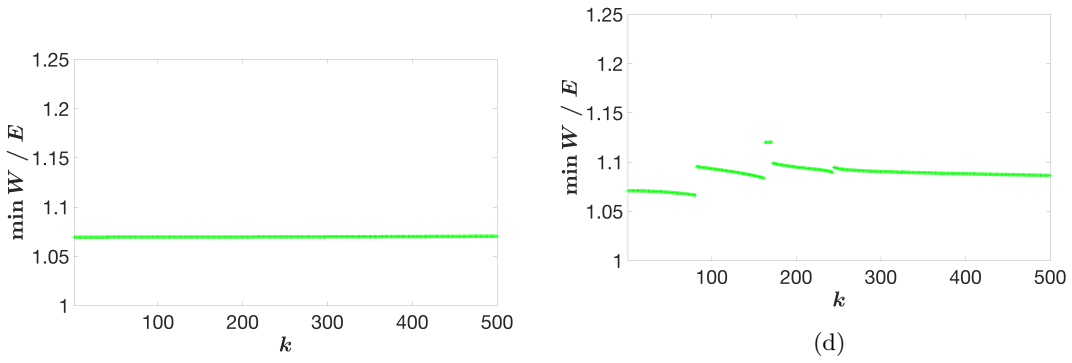

Figure 5.13: Top: the first 500 eigenvalues versus their corresponding minima values of the effective confining potential. (a) $N = 7919$, $\lambda = 8$ and $\alpha = 3000/7919 \approx 0.379$. (b) $N = 7919$, $\lambda = 8$ and $\alpha = 4000/7919 \approx 0.505$. Bottom: the ratios between the first 500 eigenvalues and their corresponding minima values of the effective confining potential: (c) $N = 7919$, $\lambda = 8$ and $\alpha = 3000/7919 \approx 0.379$. The average of the distribution of the ratios between the two values is $\langle E_i / \min W \rangle \approx 1.07$ and its standard deviation is $2.84\ 10^{-4}$. (d) $N = 7919$, $\lambda = 8$ and $\alpha = 4000/7919 \approx 0.505$. The average of the distribution of the ratios between the two values is $\langle E_i / \min W \rangle \approx 1.09$ and its standard deviation is $9.26\ 10^{-3}$.

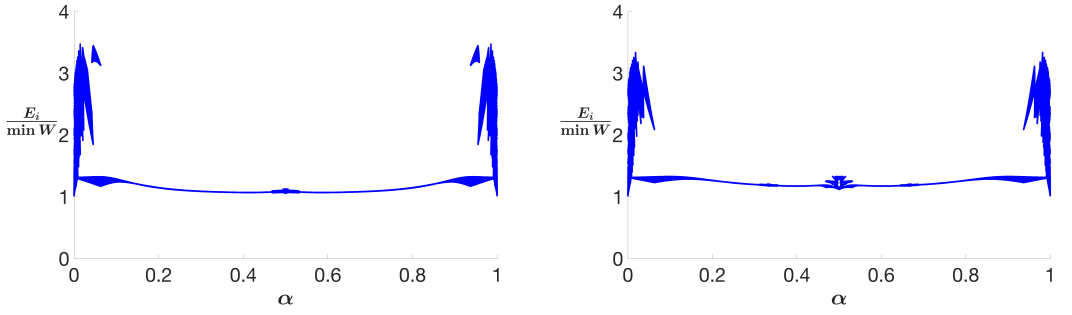

Figure 5.14: Scatter plot of the ratio between the first 500 eigenvalues and their corresponding minima values of the effective confining potential for all values of α and for $N = 7919$. (a) $\lambda = 8$. (b) $\lambda = 3$.

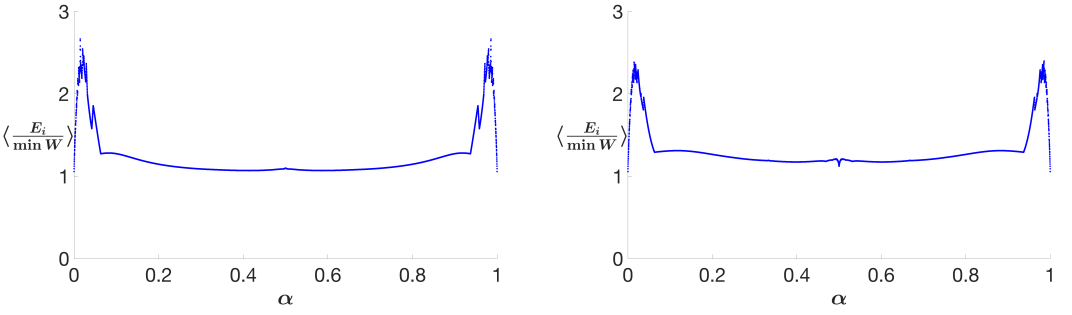

Figure 5.15: The average of the ratio between the first 500 eigenvalues and their corresponding minima values of the effective confining potential for all values of α and for $N = 7919$. (a) $\lambda = 8$. (b) $\lambda = 3$.

$\alpha \approx 0.5$. We remind the reader that the spectrum is symmetric with respect to the point $\alpha = 0.5$. The same spectrum is produced for $\alpha = 0.5 + \alpha'$ and $\alpha = 0.5 - \alpha'$.

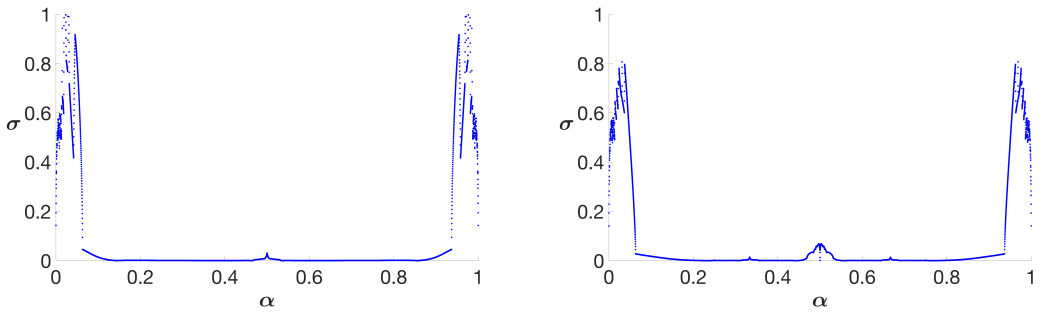

(a) (b)

Figure 5.16: The standard deviation of the distribution of the ratios between the first 500 eigenvalues and their corresponding minima values of the effective confining potential for all values of α and for $N = 7919$. (a) $\lambda = 8$. (b) $\lambda = 3$.

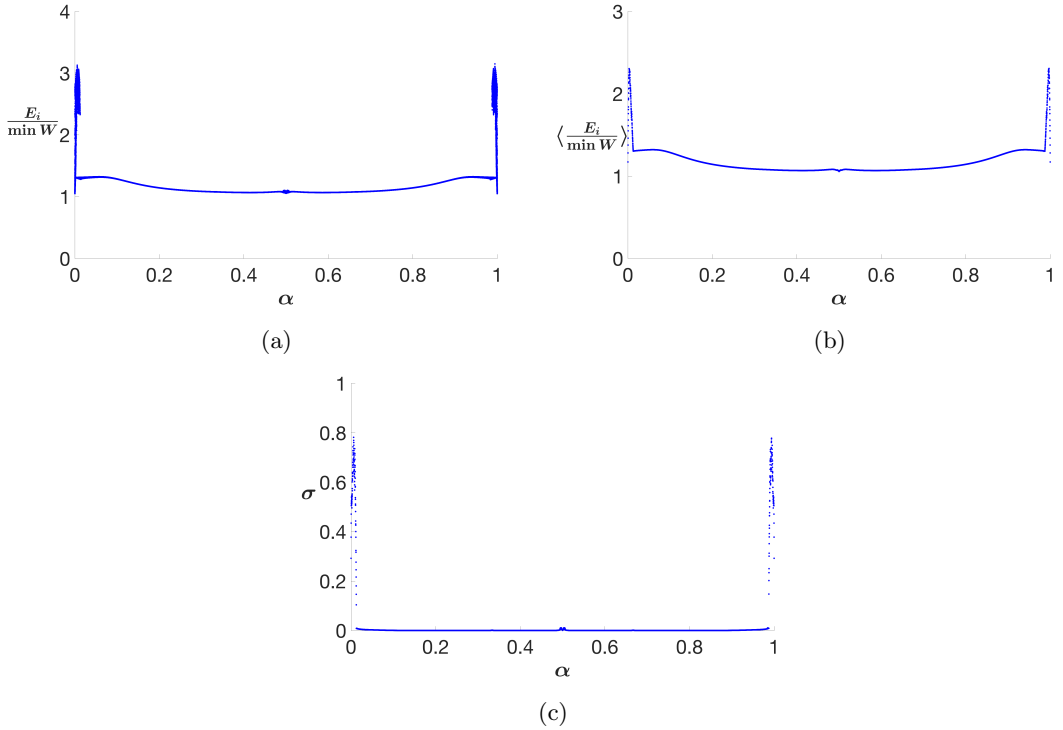

(a) (b)

(c)

Figure 5.17: (a) Scatter plot of the ratio between the first 100 eigenvalues and their corresponding minima values of the effective confining potential for all values of α for $N = 7919$ and $\lambda = 8$. (b) The average of the ratio between the first 500 eigenvalues and their corresponding minima values of the effective confining potential for all values of α for $N = 7919$ and $\lambda = 8$. (c) The standard deviation of the distribution of the ratios between the first 500 eigenvalues and their corresponding minima values of the effective confining potential for all values of α for $N = 7919$ and $\lambda = 8$.

These results indicate that in the same vein as the continuous case, in a large interval of frequencies, the ratios between the eigenvalues and their corresponding local minima are almost constant (around 1.1) which means that the localization landscape estimates are very good predictors of the eigen-energies of the localized eigenfunctions. However, this ratio is not the same as in the continuous case, and seems to break down for very low and high frequencies. A possible explanation for this is that at low frequencies, the potential forms very few but very large "wells". Since there are less local minima, there are less local fundamental modes. Symmetry dictates that the same is true at very high frequencies. Because the relation we are trying to establish relates the local fundamentals with their respective local minima of the effective confining potential, if we consider more eigenfunctions than there are of local fundamentals,

we will be counting higher energy local modes for which the relation should not work. In Figure 5.17, we have repeated the same figures as before but considering only 100 eigenfunctions this time. The range of frequencies for which the standard deviation is low and ratios remain constant has increased. It goes now from about $\alpha = 0.01$ to $\alpha = 0.99$.

These results suggest that there is a relationship between the energy of the eigenfunctions and their respective local minima of the effective confining potential. This relation varies from about 1.3 for frequencies close to 0 and 1, to around 1.07 for frequencies close to 0.5. It also depends on the potential strength. In Table 5.1, we have summarized the average ratios across all frequencies for different potential strengths. The ratios decrease as the potential strength increases. So while there is no universal relationship between the local minima of the effective confining potential and the eigenvalue of the associated localized eigenfunction like in the continuous case, the ratio varies depending on the parameters of the potential.

	$\lambda = 1$	$\lambda = 3$	$\lambda = 5$	$\lambda = 8$	$\lambda = 10$
$\langle E_i / \min W \rangle_{i,\alpha}$	1.33	1.22	1.17	1.12	1.10

Table 5.1: Summary of the values found for the average of the ratios across all frequencies for different potential strengths λ.

IV.3 Hofstadter's butterfly, the energy-frequency graphs and its gaps

Fixing the potential strength λ and plotting the spectra of the Aubry-André Hamiltonians for various values of the frequency α in the (E, α)-plane (which we will call the energy-frequency graphs) reveals interesting figures. For $\lambda = 1$, the object created is a fractal, and the spectrum is of measure 0. It is known in the litterature as Hofstadter's butterfly [13].

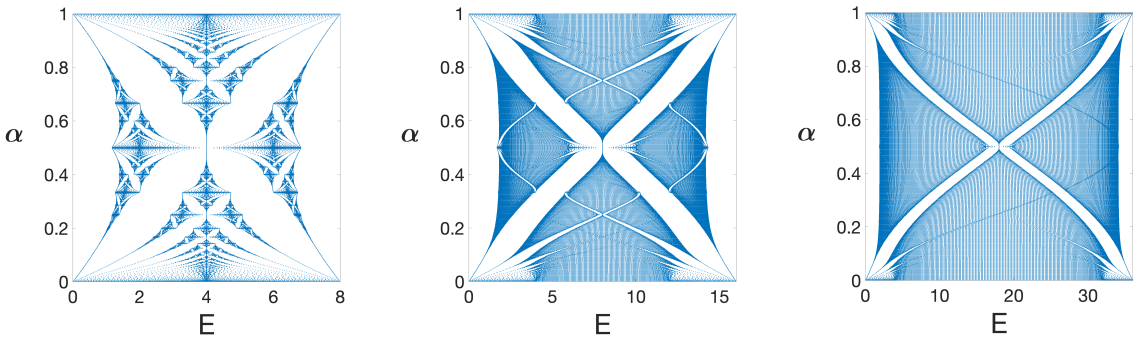

(a) (b) (c)

Figure 5.18: The structure of the eigenvalues E versus the frequency of the pseudo-random potential α for three different values of the potential intensity ($\lambda = 1, 3, 8$ respectively).

Is the localization landscape able to replicate these unique structures? To reproduce the low energy half of the energy-frequency graphs, we employ the approximation for the eigenvalues we have just determined in the previous subsection. We saw in the previous section that the coefficient that relates the eigenvalues and the local minima depends on the frequency, but we will be using the average values over all frequencies found in Table 5.1 for different potential strengths.

Similarly, for the high energy half of the energy-frequency graphs, we exploit the same estimation using the dual landscape defined in equation (5.5) and defining a dual effective confining potential. We compute the dual landscape using this equation as well as the eigenvalues of the dual equation E_i^*, and retrieve the eigenvalues of the original equation by applying the shift: $E_i = V_{\text{shift}} - E_i^*$. The dual effective confining potential is defined as the reciprocal of the dual landscape: $W^* \equiv 1/u^*$.

From the previous subsection, the approximations given by the localization landscape are more accurate when estimating low energy eigenvalues and when the potential is higher in intensity. Comparing figures 5.18 and 5.19, the outline of the low energy part of the energy-frequency graphs is kept when using

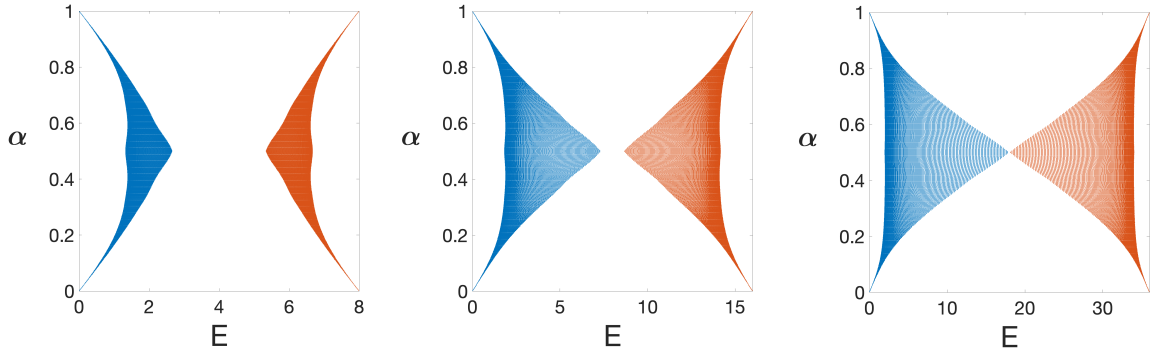

Figure 5.19: The structure of the eigenvalues E approximated using the localization landscape versus the frequency of the pseudo-random potential α for three different values of the potential intensity ($\lambda = 1, 3, 8$ respectively).

the landscape approximation, while the finer details especially present for $\lambda = 1$ are absent. Moreover, the gaps that appear in the energy-frequency graphs (which are most visible in Figure 5.18b) are not always replicated when using the localization landscape approximation, but this is to be expected since the estimate using the local minima of W is only applicable for the local fundamental modes inside a confining potential well, and not for the local excited states of these same wells.

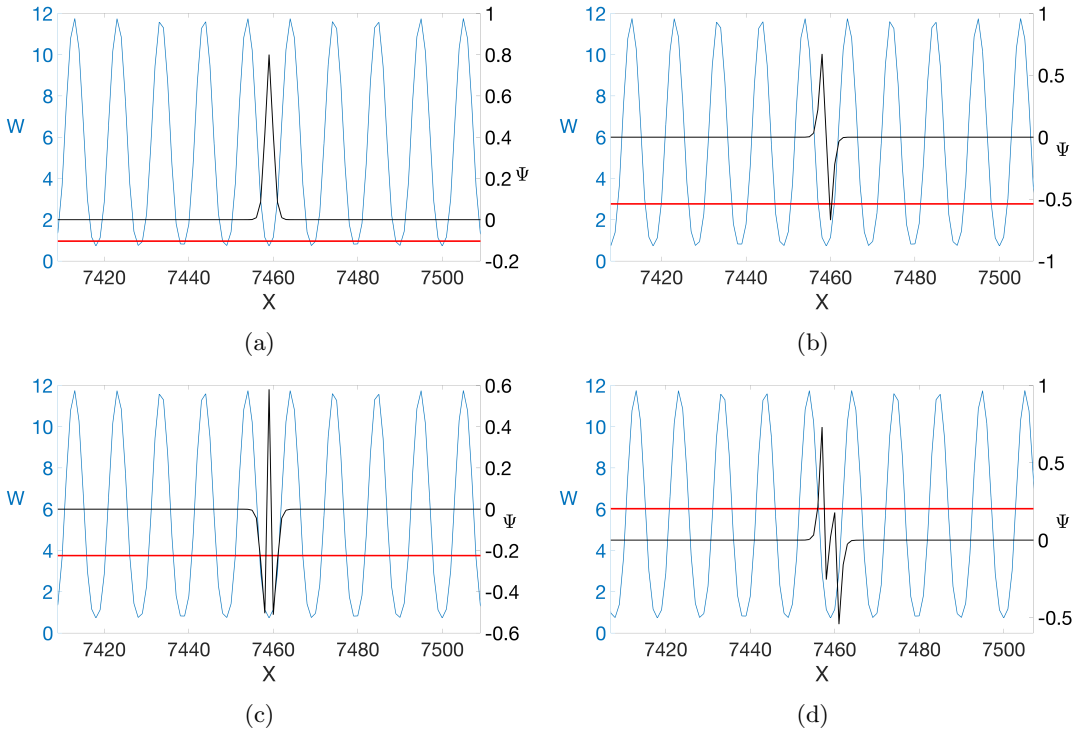

Figure 5.20: The potential's parameters are: $N = 7919$, $\lambda = 3$, and $\alpha = 773/7919 \approx 0.0976$. (a) An eigenfunction localized at the lattice point 7459 of energy $E = 0.96$. (b) An eigenfunction localized at the same local minimum but at higher energy: $E = 2.77$. It is the first excited state. (c) The second excited state with $E = 3.75$. (d) The third excited state with $E = 6.02$.

What causes these gaps to appear ? We have seen in subsection II.2 that the eigenfunctions localize in the local minima of the effective confining potential. The first eigenvalues are therefore determined by the distribution of the minima of W. If the local minima are deep enough, the next eigenstate localized in that site will be that local minimum's first excited state. For example, Figure 5.20 depicts four consecutive eigenfunctions in the same local minimum of W. At this value of α (around 0.1), all local minima of W

are around the same value. The jump in energy between each subsequent eigenvalue causes the presence of gaps in the energy-frequency graphs.

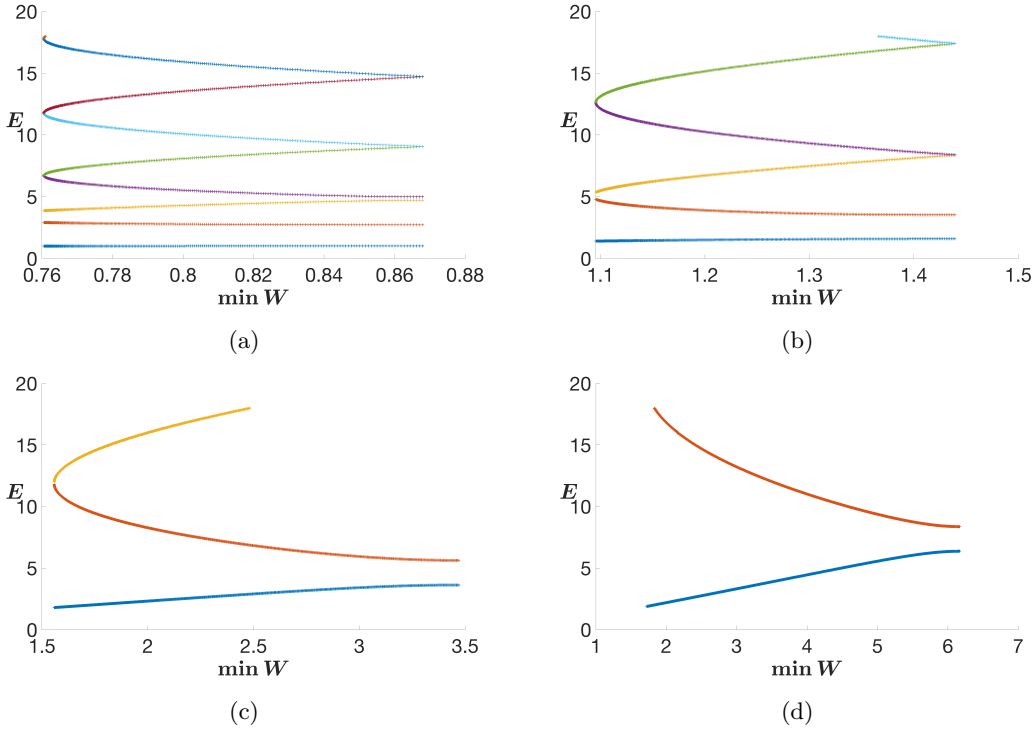

Figure 5.21: We display the energy of the eigenfunctions versus the value of their respective local minimum of the effective confining potential for domains of size $N = 7919$ and different values of α. Each color represents the number of the local eigenstate (blue is the local fundamental, orange is the local first excited state, etc.). (a) $\alpha = 491/7919 \approx 0.0620$. There are 491 sub-regions. (b) $\alpha = 773/7919 \approx 0.0976$. There are 773 sub-regions. (c) $\alpha = 1483/7919 \approx 0.187$. There are 1483 sub-regions. (d) $\alpha = 2137/7919 \approx 0.270$. There are 2137 sub-regions.

The domain is divided up in intervals delimited by the successive local maxima of the effective confining potential. These are sub-regions of localization. Each interval contains one local minimum of W. For all the eigenstates in the first half of the spectrum, we determine their maximum and associate them to a local minimum of W/sub-region of localization. In Figure 5.21, we display a scatter plot of the energy of the eigenfunctions versus their associated local minimum of W for different values of α. We see that the number of sub-regions is equal to n_α, and therefore increases with α (until $\alpha = 0.5$). The less sub-regions there are, the more local excited states. Interestingly, the local fundamentals are related linearly to the local minima, as we have shown before. However, according to Figure 5.21a, the energy of the local first excited states increases as the local minima decreases. Then the opposite occurs, and so forth. For every value of α, there is always a jump in energy between the local fundamentals and the local first excited states, which explains the gaps that occur in the energy-frequency graphs, such as in Figure 5.18c.

In conclusion while the relationship between the local minima and the energies of the eigenfunctions is less straightforward (there is a constant ratio in the continuous case), the structure of the effective confining potential (of its minima) is not only a good predictor of the local fundamentals but also of the higher local modes.

V The density of states

V.1 Weyl's law

We remind the reader that in the continuous setting, Weyl's law provides an asymptotic at higher energy for the integrated density of states. However, as discussed before, in disordered systems, a more accurate version of Weyl's law can be found by replacing the potential by the effective confining potential [2]. This modified version of Weyl's law has been shown to be effective even at low energies. The updated Weyl's law using the effective confining potential for discrete systems that we will study is:

$$N_W(E) = \frac{1}{\pi} \sum_{W_i < E} \sqrt{(E - W_i)_+}, \tag{5.23}$$

as it is a good approximation of the exact equation (5.8).

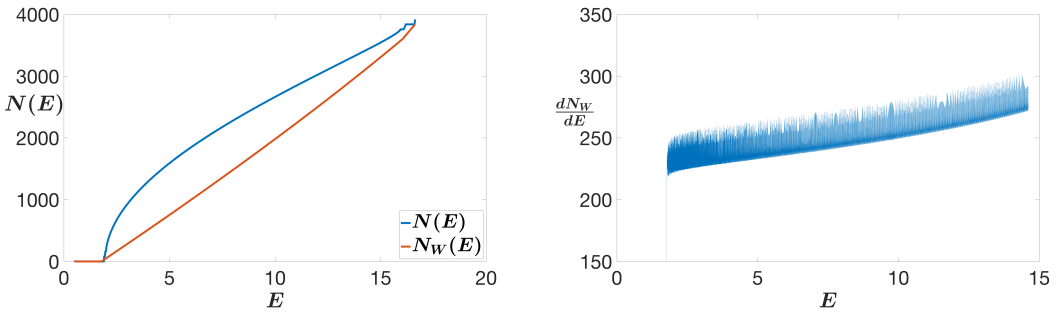

(a) (b)

Figure 5.22: (a) The counting function $N(E)$ is displayed in blue for $\lambda = 8$ and $\alpha = 0.505114$. The approximation given by Weyl's law using the effective confining potential is in red. (b) The derivative of $N_W(E)$ is not constant and is slightly increasing.

In Figure 5.22a we have displayed the counting function alongside the estimate of the counting function derived from Weyl's law using the effective confining potential. The estimate seems to be linear, but in Figure 5.22b we have plotted its derivative (the density of states, DOS) which is not constant, showing that it is slightly superlinear. Regardless, the updated Weyl's law does not describe the counting function well. This is not surprising since Weyl's law originally is meant to give the asymptotic behavior of the counting function for continuous systems. Here we are using it for a discrete system and for the low energy part of the counting function.

V.2 The landscape law

We then turn to the recent landscape law that we have already studied in the previous chapter for a more accurate approximation of the integrated density of states [8]. Our hope is that, similarly to our previous study in Chapter 3 on the Lifshitz tails, the general aspect of N_u is very close to the real counting function. We will then determine the sharpest values for the constants C_4, C_5, and C_6.

We recall the basis of our analysis to determine the sharpest values of the constants. First, we compute the landscape law counting function by dividing the domain in boxes of size $1/\sqrt{E}$ and then counting all the boxes where $W < E$. We then compute the ratio $N_u(CE)/N(E)$ for many different values of C and determine C_4 by finding the smallest value of C for which this ratio is always grater than 1. C_6 is determined by finding the value of C for which the standard deviation of the ratio $N_u(CE)/N(E)$ is the smallest. C_5 is defined by the maximum of the ratio $N_u(C_6E)/N(E)$, and $C_{5,\text{fit}}$ is the average of that ratio.

In Figures 5.24 we have displayed the results of the analysis we have just detailed. The parameters of the potential are: $\lambda = 8$ and $\alpha = 4000/7919 \approx 0.505$. Figure 5.23 shows that the landscape law captures not only the asymptotic behavior of the integrated density of states, but also the behavior at the beginning

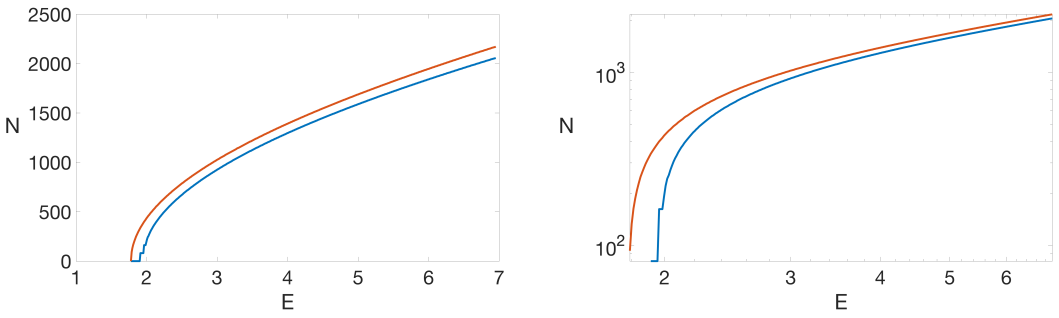

Figure 5.23: The counting function N has been calculated and displayed in blue for $\lambda = 8$ and $\alpha = 0.505114$. The approximation given by the landscape law is in red. On the left is a linear plot, while on the right is a loglog plot.

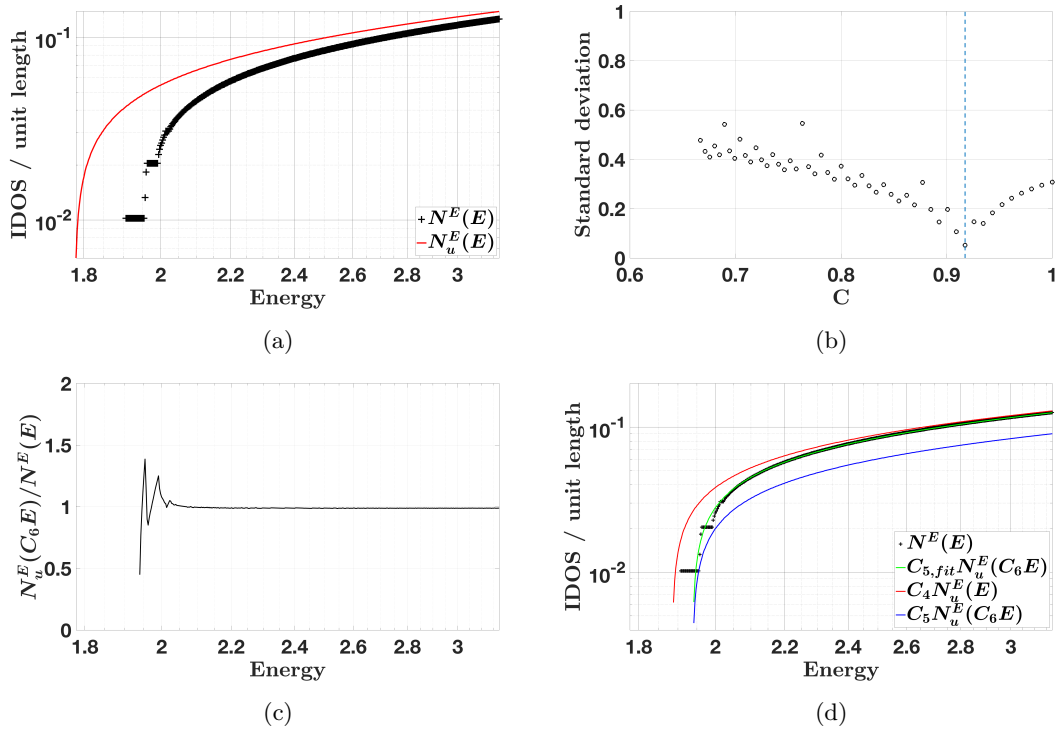

Figure 5.24: The parameters are $L = 7919$, $\alpha = 0.505114$ and $\lambda = 8$. (a) Standard deviation of the distribution of $\ln(N_u^E(CE)/N^E(E))$ for various values of C. The minimum corresponds to the sharpest value of C_6. (b) The ratio $(N_u^E(C_6E)/N^E(E))$. The maximum yields the sharpest value of C_5, the best fit for $N(E)$ is deduced from the average of this ratio. (c) The corresponding fit by the landscape law of the integrated density of states divided by unit length.

of the spectrum. The sharpest values for the constants C_4, C_5, and C_6 determined by this method are: $1/C_4 \approx 1.08$, $1/C_5 \approx 1.4$, $1/C_{5,\text{fit}} \approx 1.0$, and $1/C_6 \approx 1.09$. Interestingly, the values are not exactly the same as in our previous study (we do not find $1/C_4 \approx 1/C_6 \approx 1.25$) but this not necessarily surprising. Indeed, in the preceding section, we showed that the relationship between the minima of the effective confining potential and the eigenvalues is not the same as in a traditional Anderson system, and in fact the values we have found here are more consistent vith the ratios between the energies and the local minima of W we obtained previously. The fit of the counting function by the landscape law counting function with the constants $C_{5,\text{fit}}$ and C_6 is remarkably accurate throughout the spectrum as can be seen in Figure 5.24d. We have repeated this fit with different parameters of λ and α in Figure 5.25, and given a summary of the results in Table 5.2.

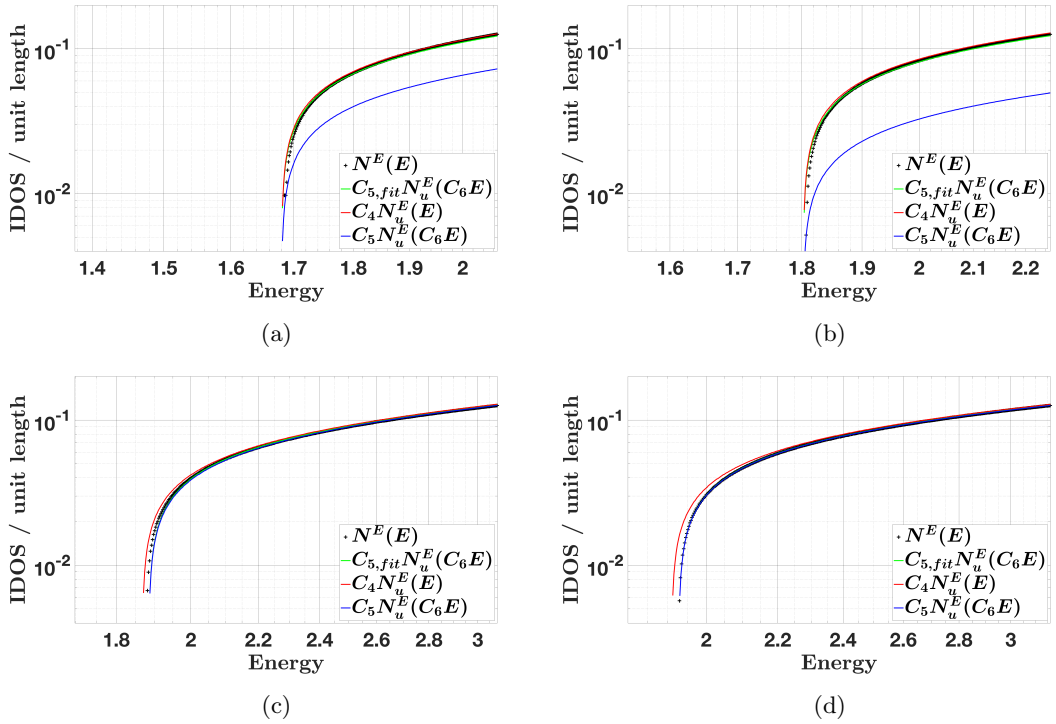

(a) (b) (c) (d)

Figure 5.25: Comparison between the Landscape Law and the the integrated density of states (per unit length) for different values of λ and α. The summary of the sharpest values is given in Table 5.2. (a) $\lambda = 3$ and $\alpha = 1999/7919 \approx 0.252$. (b) $\lambda = 3$ and $\alpha = 3000/7919 \approx 0.379$. (c) $\lambda = 8$ and $\alpha = 1999/7919 \approx 0.252$. (d) $\lambda = 8$ and $\alpha = 3000/7919 \approx 0.379$.

λ	α	$1/C_4$	$1/C_5$	$1/C_{5,\text{fit}}$	$1/C_6$
3	0.252	1.22	1.75	1.04	1.22
	0.379	1.17	2.60	1.05	1.17
8	0.252	1.1	1.01	0.99	1.11
	0.379	1.04	1.01	1.00	1.06

Table 5.2: Summary of the values found for the constants C_4, C_5, $C_{5,\text{fit}}$, and C_6 found in Figures 5.25.

We have reiterated this analysis for all possible α and for different values of λ: 1, 3, 5, 8, and 10 in Figures 5.26. The main takeaway is that these sharpest values are not constant, and depend on the parameters α and λ. However at constant α, the sharpest values of C_4 and C_6 converge towards a specific value as the potential strength increases. Another interesting observation is that the shape of the curves for the values of C_4^{-1} and C_6^{-1} in the strongly localizing regime ($\lambda \geq 5$) is reminiscent of the shape of the curve of the ratio between the eigenvalues and their corresponding local minima of the effective confining potential (Figure 5.14). For instance, for $\lambda = 8$, the ratio goes from 1.27 at $\alpha \approx 0.1$ to 1.07 at $\alpha \approx 0.4$ before going back up to 1.1 at $\alpha \approx 0.5$. For these same parameters, C_6^{-1} goes from 1.25 at $\alpha \approx 0.1$ to 1.07 at $\alpha \approx 0.4$ before going back up to 1.09 at $\alpha \approx 0.5$, which are all very close to the values of the ratios.

To summarize, the fact that these sharpest values are not constant with respect to λ and α is not surprising, as the ratios between the eigenvalues and their respective minima of the effective confining potential are not constant as well. The landscape law is nonetheless effective in approximating the counting function using the values of C_6 and $C_{5,\text{fit}}$.

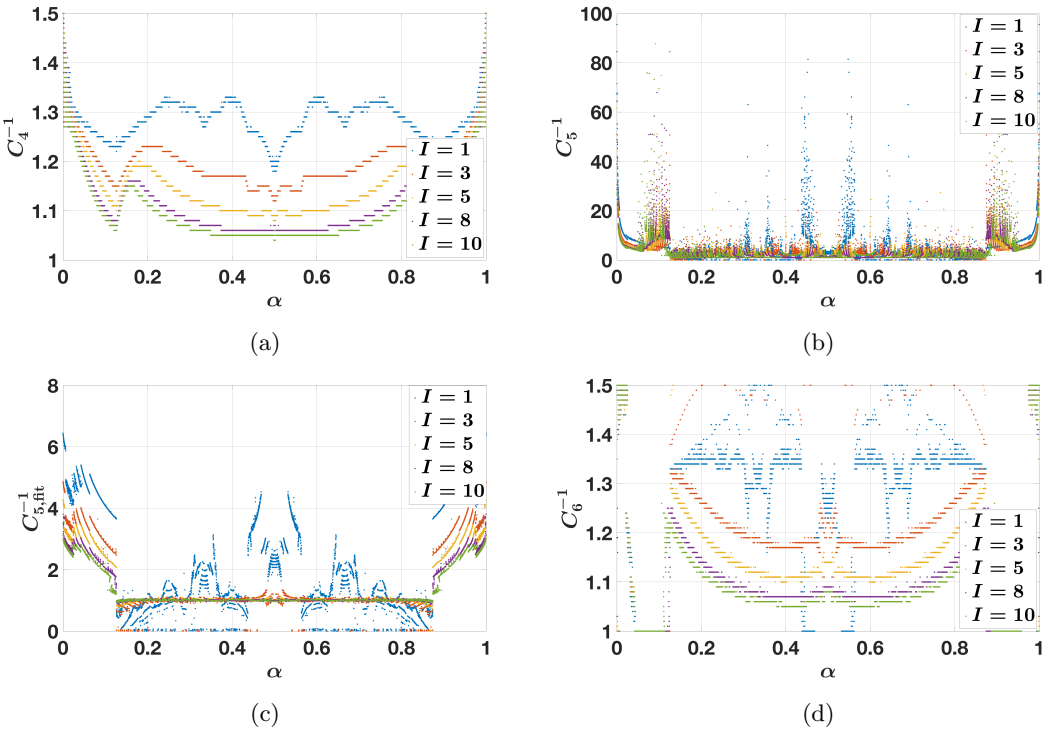

Figure 5.26: The sharpest values have been calculated for a system of size $N = 7919$ for five different values of λ: 1, 3, 5, 8, and 10, and for all possible α. (a) Sharpest values of C_4. (b) Sharpest values of C_5. (c) Sharpest values of $C_{5,\mathrm{fit}}$. (d) Sharpest values of C_6.

VI Conclusion

We have introduced the localization landscape for the Aubry-André model. We have shown that some of the essential properties of the localization landscape were conserved even though most of them pertained to continuous systems. Notably, the reciprocal of u (which we have called W) possesses similar properties to the effective confining potential defined in the continuous setting. W allows for a prediction of the eigenvalues and of the localization regions. Moreover, we can define an Agmon distance from W that correctly controls the initial exponential decay of the eigenfunctions, but not the resonances that occur throughout the domain. The discrete nature of the tight-binding model induces another localization at the top of the energy band. Another localization landscape (called dual landscape) can be defined that allows to generalize the properties of the landscape given for low energies to high energies. Finally, the new landscape law captures the aspect of the integrated density of states.

Moreover we have established a closed formula for the localization landscape for these quasi-periodic potentials. Although we were unable to clearly demonstrate it, the Fourier coefficients of the discrete Fourier transform of the localization landscape seem to decrease exponentially in a very specific pattern which can be linked to the hierarchical structure of the eigenfunctions [4, 15]. Unfortunately, the methods we have used for these calculations should not work for higher dimensional systems, so generalizing these formulae is most likely not possible.

Several properties of the localization landscape theory are no longer valid for Aubry-André potentials. Interestingly, the linear relationship between the eigenvalues of the localized eigenfunctions and the minima of the effective potential is conserved. However, the ratio is not the one found in the continuous setting. For a large interval (about [0.1 0.9]), it is practically constant, but increases for both low and high α. For this reason, the sharpest values for the constants C_4, C_5, and C_6 also depend on these two parameters contrarily to the values of the constants for the Anderson tight-binding model we have studied in Chapter 3.

While the spatial structure of the eigenfunctions and their spectral structure was already well understood in one-dimension [15], there remain questions concerning for instance the localization/delocalization transition in higher dimensions [9, 24] and in interacting systems [10, 23]. The localization landscape formalism could potentially open the way for new methods to study these problems, especially considering there have been recent breakthroughs extending this formalism to many-body systems [5].

5.A Details for closed formula calculations

5.A.1 Forward sweep or Thomas algorithm

The Thomas algorithm is a special case of the Gaussian elimination algorithm for tridiagonal matrices [21]. For a matrix M of size n, an unknown vector X, and a known vector D, we assume the following notation: where $(a_i)i \in \{2...n\}$ (sud-diagonal terms), $(b_i)i \in \{1...n\}$ (diagonal terms), $(c_i)i \in \{1...n-1\}$ (superdiagonal terms), $(d_i)i \in \{1...n\}$ (known elements), and $(x_i)i \in \{1...n\}$ (unknown elements):

$$\begin{pmatrix} b_1 & c_1 & & & 0 \\ a_2 & b_2 & c_2 & & \\ & a_3 & b_3 & \ddots & \\ & & \ddots & \ddots & c_{n-1} \\ 0 & & & a_n & b_n \end{pmatrix} \begin{pmatrix} x_1 \\ x_2 \\ x_3 \\ \vdots \\ x_n \end{pmatrix} = \begin{pmatrix} d_1 \\ d_2 \\ d_3 \\ \vdots \\ d_n \end{pmatrix} \tag{5.24}$$

The first step of the algorithm is to proceed with a forward sweep. For $i = 2, 3, ..., n$ we redefine:

$$b_i := b_i - \frac{a_i}{b_{i-1}} c_{i-1} \tag{5.25}$$

$$d_i := d_i - \frac{a_i}{b_{i-1}} d_{i-1}. \tag{5.26}$$

The second step is a backwards substitution going from n to 1:

$$x_n = \frac{d_n}{b_n} \tag{5.27}$$

$$x_i = \frac{d_i - c_i x_{i+1}}{b_i} \tag{5.28}$$

The algorithm is considerably simplified if the elements are simple enough ($0s$ or $1s$ for example, as in out case).

5.A.2 Details for Discrete Fourier Transform calculation

We recall that we are calculating the Fourier coefficients $\tilde{u}_k$ of the localization landscape. Inserting the definition of the coefficients in the Aubry-André equation gives:

$$\sum_{k=0}^{N-1} \tilde{u}_k \left(-e^{\frac{2\pi i}{N} k(n+1)} - e^{\frac{2\pi i}{N} k(n-1)} (2\lambda + 2 - 2\lambda \cos(\frac{2\pi n_\alpha n)}{N})) e^{\frac{2\pi i}{N} kn} \right) = N \tag{5.29}$$

Rearranging terms we obtain:

$$\sum_{k=0}^{N-1} e^{\frac{2\pi i}{N} kn} \left((-e^{\frac{2\pi i}{N} k} - e^{\frac{-2\pi i}{N} k} + (2\lambda + 2)) \tilde{u}_k - \lambda(\tilde{u}_{k+n_\alpha} + \tilde{u}_{k-n_\alpha}) \right) = N \tag{5.30}$$

with $k \in \mathbb{Z} \setminus N$. Defining $\omega_n = e^{-\frac{2\pi i}{N} n}$:

$$\sum_{k=0}^{N-1} \omega_n^k \left(\tilde{u}_k (2\lambda + 2 - \omega_1^k - \omega_1^{-k}) - \lambda \tilde{u}_{k+n_\alpha} - \lambda \tilde{u}_{k-n_\alpha} \right) = N \tag{5.31}$$

We can therefore write the previous equation in matrix form:

$$VC\tilde{U} = NX, \tag{5.32}$$

where V is a symmetric Vandermonde matrix: $V_{kl} = \omega_{k-1}^{l-1}$, C a matrix defined by: $C_{kl} = (2\lambda + 2 - \omega_1^k - \omega_1^{-k})\delta_{kl} - \lambda(\delta_{k(l+n_\alpha)} + \delta_{k(l-n_\alpha)})$, and X a vector with all of its elements equal to one.

Noticing that:

$$\sum_{j=0}^{N-1} \bar{\omega}_j^k \omega_l^j = N\delta_{kl}, \tag{5.33}$$

we can determine the inverse of V which is: $V^{-1} = \frac{1}{N}\bar{V}$ where $\bar{}$ stands for the complex conjugation operation.

Therefore we have:

$$C\tilde{U} = \frac{1}{N}\bar{V}X \tag{5.34}$$

In the same way, noticing that

$$\sum_{k=0}^{N-1} \omega_i^k = \delta_{i0} \tag{5.35}$$

the matrix equation is equivalent to:

$$(2\lambda + 2 - \omega_1^k - \omega_1^{-k})\tilde{u_k} - \lambda(\tilde{u}_{k+n_\alpha} + \tilde{u}_{k-n_\alpha}) = N\delta_{k0} \quad \forall k \in \mathbb{Z} \setminus N. \tag{5.36}$$

We will now reorder the terms in order to obtain a tridiagonal system. By defining a new vector $\tilde{U}'_{k+1} = \tilde{u}_{kn_\alpha}$, the previous system becomes a tridiagonal system:

$$C' = \begin{pmatrix} 2\lambda + 2 - 2\cos\left(\frac{2\pi k n_\alpha}{N}\right) & -\lambda & ... & -\lambda \\ -\lambda & ... & ... & 0 \\ ... & ... & ... & ... \\ -\lambda & ... & -\lambda & 2\lambda + 2 - 2\cos\left(\frac{2\pi(N-1)n_\alpha}{N}\right) \end{pmatrix} \tag{5.37}$$

and

$$\tilde{U}' = \begin{pmatrix} \tilde{U}'_1 \\ ... \\ \tilde{U}'_k \\ ... \\ \tilde{U}'_N \end{pmatrix} \qquad X' = \begin{pmatrix} N \\ 0 \\ ... \\ ... \\ 0 \end{pmatrix} \tag{5.38}$$

give us:

$$C'\tilde{U}' = X'. \tag{5.39}$$

Since the solution u is real, the Fourier coefficients verify $\tilde{u}_k = \tilde{u}_{N-k}$ (which translates to $\tilde{U}'_{k+1} = \tilde{U}'_{N-k+1}$). We therefore only need to solve for twice as less unknowns. The first equation for example gives us $\tilde{U}'_1 = \tilde{U}'_2 + \frac{N}{2\lambda}$. However now we need to separate the cases where N is odd or even for the last equation.

If N is odd, only $\tilde{U}'_1$ is unique, thus we now have $\frac{N+1}{2}$ terms. The last equation of the matrix links terms $\tilde{U}'_{\frac{N+1}{2}-1}$, $\tilde{U}'_{\frac{N+1}{2}}$ and $\tilde{U}'_{\frac{N+1}{2}+1}$. The new matrix has the following form:

$$\text{if } N \text{ is odd: } C' = \begin{pmatrix} 2\lambda + 2 - 2\cos\left(\frac{2\pi(k-1)n_\alpha}{N}\right) & -2\lambda & ... & 0 \\ -\lambda & ... & ... & 0 \\ ... & ... & ... & ... \\ 0 & ... & -\lambda & \lambda + 2 - 2\cos\left(\frac{\pi(N-1)n_\alpha}{N}\right) \end{pmatrix} \tag{5.40}$$

If N is even, $\tilde{U}'_1$ and $\tilde{U}'_{\frac{N}{2}+1}$ are unique, thus we have $\frac{N}{2}+1$ terms. The last equation this time links $\tilde{U}'_{\frac{N}{2}}$, $\tilde{U}'_{\frac{N}{2}+1}$ and $\tilde{U}'_{\frac{N}{2}+2}$. The matrix has the following form:

$$\text{if } N \text{ is even: } C' = \begin{pmatrix} 2\lambda + 2 - 2\cos\left(\frac{2\pi(k-1)n_\alpha}{N}\right) & -2\lambda & ... & 0 \\ -\lambda & ... & ... & 0 \\ ... & ... & ... & ... \\ 0 & ... & -2\lambda & 2\lambda + 2 - 2\cos\left(\pi n_\alpha\right) \end{pmatrix} \tag{5.41}$$

Dividing by λ equation 5.36 (2λ for the first equation), as well as defining special functions $f_k = \frac{2\lambda+2-2\cos\left(\frac{2\pi(k-1)n_\alpha}{N}\right)}{\lambda}$ simplifies the expression further. The new C' matrix is now :

$$\text{if } N \text{ is odd: } C' = \begin{pmatrix} 1 & -1 & ... & 0 \\ -1 & f_k & ... & 0 \\ ... & ... & ... & ... \\ 0 & ... & -1 & f_{\frac{N-1}{2}} - 1 \end{pmatrix} \tag{5.42}$$

and

$$\text{if } N \text{ is even: } C' = \begin{pmatrix} 1 & -1 & ... & 0 \\ -1 & f_k & ... & 0 \\ ... & ... & ... & ... \\ 0 & ... & -2 & f_{\frac{N}{2}} \end{pmatrix} \tag{5.43}$$

Using the forward sweep that is presented in the appendix 5.A.1 again, we can solve this system. We will look only at the case where N is odd but the procedure is quite similar if N is even. If we define sequences b_k and d_k as

$$\begin{aligned} b_1 &= 1, \qquad b_k = f_k - \frac{1}{b_{k-1}} = f_k - \frac{1}{f_{k-1} - \frac{1}{...-1}} \\ d_1 &= \frac{N}{2\lambda}, \qquad d_k = \frac{d_{k-1}}{b_{k-1}} = \frac{\frac{N}{2\lambda}}{b_{k-1}...b_1}, \end{aligned} \tag{5.44}$$

then the U_k terms can be rewritten:

$$\begin{aligned} \tilde{U}'_{\frac{N+1}{2}} &= \frac{d_{\frac{N+1}{2}}}{b_{\frac{N+1}{2}}} = \frac{\frac{N}{2\lambda}}{b_{\frac{N+1}{2}}...b_1} \\ \tilde{U}'_k &= \frac{d_k}{b_k} + \frac{\tilde{U}'_{k+1}}{b_k} = \frac{N}{2\lambda}\left(\frac{1}{b_1...b_k} + \frac{1}{b_1...b_k^2 b_{k+1}} + ... + \frac{1}{b_1...b_k^2...b_{\frac{N+1}{2}-1}^2 b_{\frac{N+1}{2}}}\right) \end{aligned} \tag{5.45}$$

Bibliography

[1] D. N. Arnold, G. David, M. Filoche, D. Jerison, and S. Mayboroda. Computing spectra without solving eigenvalue problems. *SIAM J. Sci. Comput.*, 41:B69–B92, 2017.

[2] D. N. Arnold, G. David, D. Jerison, S. Mayboroda, and M. Filoche. Effective confining potential of quantum states in disordered media. *Phys. Rev. Lett.*, 116:056602, 2016.

[3] S. Aubry and G. André. Analyticity breaking and Anderson localization in incommensurate lattices. *Ann. Isr. Phys. Soc.*, 3:133–164, 1980.

[4] A. Avila. The absolutely continuous spectrum of the almost mathieu operator, 2008.

[5] S. Balasubramanian, Y. Liao, and V. Galitski. Many-body localization landscape. *arXiv*, 2019.

[6] J. Bourgain. Anderson localization for quasi-periodic lattice Schrödinger operators on $\mathbb{Z}^d$, d arbitrary. *Geo. and Func. Anal.*, 17(682), 2007.

[7] D. Damanik. The spectrum of the almost Mathieu operator. *Lecture Series in the CRC 701*, 2008.

[8] G. David, M. Filoche, and S. Mayboroda. The landscape law for the integrated density of states. *arXiv*, 2019.

[9] T. Devakul and D. A. Huse. Anderson localization transitions with and without random potentials. *Phys. Rev. B*, 96(214201), 2017.

[10] E. V. H. Doggen and A. D. Mirlin. Many-body delocalization dynamics in long aubry-andré quasiperiodic chains. *Phys. Rev. B*, 100:104203, 2019.

[11] M. Filoche, M. Piccardo, Y.-R. Wu, C.-K. Li, C. Weisbuch, and S. Mayboroda. Localization landscape theory of disorder in semiconductors. I. Theory and modeling. *Phys. Rev. B*, 95:144204, 2017.

[12] V. Goblot, A. Štrkalj, N. Pernet, J. L. Lado, C. Dorow, A. Lemaître, L. Le Gratiet, A. Harouri, I. Sagnes, S. Ravets, and et al. Emergence of criticality through a cascade of delocalization transitions in quasiperiodic chains. *Nat. Phys.*, 16(8):832–836, 2020.

[13] D. R. Hofstadter. Energy levels and wave functions of Bloch electrons in rational and irrational magnetic fields. *Phys. Rev. Lett.*, 14(6), 1976.

[14] S. Jitomirskaya. Metal-insulator transition for the almost Mathieu operator. *Ann. of Maths.*, 150(3), 1999.

[15] S. Jitomirskaya and W. Liu. Universal hierarchical structure of quasiperiodic eigenfunctions. *Ann. of Maths.*, 187(3), 2018.

[16] M. Johansson and R. Riklund. Self-dual model for one-dimensional incommensurate crystals including next-nearest-neighbor hopping, and its relation to the Hofstadter model. *Phys. Rev. B*, 43(16), 1991.

[17] Y. Lahini, R. Pugatch, F. Pozzi, M. Sorel, R. Morandotti, N. Davidson, and Y. Silberberg. Observation of a localization transition in quasiperiodic photonic lattices. *Phys. Rev. Lett.*, 103:013901, 2009.

[18] M. L. Lyra, S. Mayboroda, and M. Filoche. Dual landscapes in Anderson localization on discrete lattices. *EPL*, 109:47001, 2015.

[19] G. Roati, C. D'Errico, L. Fallani, M. Fattori, C. Fort, M. Zaccanti, G. Modugno, M. Modugno, and M. Inguscio. Anderson localization of a non-interacting Bose-Einstein condensate. *Nature*, 453(7197):895–U36, 2008.

[20] A. Szabó and U. Schneider. Non-power-law universality in one-dimensional quasicrystals. *Phys. Rev. B*, 98:134201, 2018.

[21] J. Tu, G.-H. Yeoh, and C. Liu. Chapter 5 - cfd techniques: The basics. In J. Tu, G.-H. Yeoh, and C. Liu, editors, *Computational Fluid Dynamics (Third Edition)*, pages 155 – 210. Butterworth-Heinemann, third edition edition, 2018.

[22] W. Wang and S. Zhang. The exponential decay of eigenfunctions for tight binding hamiltonians via landscape and dual landscape functions, 2020.

[23] S. Xu, X. Li, Y.-T. Hsu, B. Swingle, and S. Das Sarma. Butterfly effect in interacting aubry-andre model: Thermalization, slow scrambling, and many-body localization. *Phys. Rev. Res.*, 1:032039, 2019.

[24] Q.-B. Zeng, Y.-B. Yang, and Y. Xu. Higher-order topological insulators and semimetals in generalized aubry-andré-harper models. *Phys. Rev. B*, 101:241104, 2020.

Chapter 6

Conclusion and perspectives

Throughout this thesis, we have expanded upon the already numerous properties of the localization landscape, which helps the study of the spatial and spectral structure of eigenfunctions in disordered media. In its first iterations, the localization landscape was seen as an effective tool for predicting the sub-regions of localization. However more and more evidence points towards the fact that it is an unavoidable underlying structure.

In a first part, we have developed the localization landscape and especially the effective confining potential's role in the confinement of the low energy eigenstates. We accounted for the wave-like nature of the localized eigenfunctions to perfect the watershed algorithm that defines the various sub-regions of localization. We have also shown how the localization landscape is used in defining the landscape law for approximating the Lifshitz tails (the near 0 asymptotic behavior of the integrated density of states). These two methods could prove to be instrumental in future computation techniques that look to approximate the counting function for low energy eigenstates without solving the eigen-equation for either systems that are very large or of high dimensionality.

We then moved on to the high energy localization, and have shown that when the Hamiltonian is rewritten to reveal the effective confining potential and the differential term $\frac{1}{u^2}\boldsymbol{\nabla}\cdot\left(u^2\boldsymbol{\nabla}\right)$, this latter term is capable of localizing eigenfunctions at higher energies in 1D and 2D, but not at higher dimensions. While we have presented evidence that the differential term can be a source of localization, we do not yet have any clear understanding on its mechanism. The question whether this term could explain the emergence of localization/delocalization transition at higher dimension remains open to conjecture.

And finally we used the Aubry-André model as a case study for the localization landscape, and established some closed formula for the landscape. Nonetheless, many of the properties of localization landscape theory in the continuous setting were interestingly not reproduced as such in Aubry-André potentials. It is not yet clear whether the reason behind this is because of the discrete or pseudo-random nature of the potential. The implication is that these incommensurate potentials should really be treated as a distinct case and not be grouped with random potentials. Localization in Aubry-André potentials is a different phenomenon from Anderson localization.

Through the works we have presented in this thesis, the localization landscape offers many new opportunities in the study of localization. We have already suggested how it can help answer questions concerning high energy localization and the localization/delocalization transition. The next direction that should be taken is in addressing the question of many-body localization as that is the field with the most open questions as of now. There have been a few attempts in trying to develop the landscape to include interactions, but there is still work to be done in simplifying the theory and making it more manageable.

Acknowledgments

I would like to thank my supervisor, Marcel Filoche, for his guidance throughout these last few years as well as for his patience. His great attention to detail and scrupulousness have pushed me beyond my capabilities and made me a better scientist. I would also like to thank many of the professors and researchers in the WAVE collaboration: Svitlana Mayboroda, Guy David and David Jerison for the in depth mathematical discussions, Douglas Arnold for his help in everything related to numerics, Alain Aspect and Sir Richard Friend for their fascinating lectures, and James Speck who despite being very busy would always make time for everyone. I would like to thank the Simons Foundation which has allowed me to meet all these fantastic people and travel in amazing places, among these Minneapolis, Cambridge, and New York City.

I thank all the members of my laboratory PMC, which was my home for the past couple years. A special thanks to, Claude Weisbuch who was my first contact there and was always available and willing to spend time with students. But also Mathis Plapp, the director of the lab, who was attentive to all of our troubles. I could not forget my coworkers in my office, Alistair Rowe and Anne-Chantal Gouget, who despite fighting for the control of the office thermostat all the time would always be available for friendly conversations which were enjoyable distractions from the day to day work. A special thanks to Julien Monguillon who is no longer part of the lab, but who worked tirelessly to help me compile and install obscure C++ libraries that did not always produce the desired outcome. And of course I thank all my fellow PhD students: Weibke Hahn for our great discussions on cultural differences between France and Germany, Sylvain Chevalier and Elodie Chaudan for their help during my brief stint as PhD representative at the lab council, Jean-Marie Lentali and Yannis Cheref for all the fantasy and sci-fi conversations, Ivan Pacheco-Bubi for all the NBA conversations, Mylène Sauty, Pierre Pelletier, and Abel Thayil with whom I've been on most of the Simons trips (and I wish them good luck for their own PhDs), Fabian Cadiz for his help in my first teaching assignments, Cassiana Andrei who is always so sweet and nice with everyone, and Capucine Cleret de Langavant, Alexandre da Silva, Mathilde Bouvier, and Louise Daugas for their companionship during our coffee breaks.

I could not forget my friends with whom I shared the arduous task of accomplishing a PhD: Lilian Chabrol, Thibaut Coudarchet and Alexandre Feller who were always interested in discussing theoretical physics, Delphine Geyer, the best teacher I know, Pierre Soulard who let me in his dojo close to where I live when we first started writing our manuscripts, Christopher Madec for his companionship during our "breaks", Sami Jouaber for his insight in programming, and Celine Boucly and Lucile Favreau, my old roommates, who despite not wanting to watch *Alien* are terrific people. Of course I also have normal friends that did not pursue PhDs: Anthony Troger and his fiancée Marie Janssen-Langenstein who despite their busy schedule always found time to see the rest of us, Clémence Testelin (or should I say Soulard now?) my semi-regular gym buddy, Baptiste Rosell my SSBU buddy, Guillaume Fabre who is always in a good mood, and Jim Eisenberg one of my oldest friend who possible talks too much but I always enjoy listening to.

And finally I would like to thank my family for their support throughout my life: my sister Sarah who lives far away but on whom I can always count on, my mother Fabienne for her unconditional love and support as well as her partner Jean-Pierre, my father François-Xavier that I am very proud of following in his footsteps, and his partner Nathalie who has always done everything to make me feel welcome in their home.

ECOLE
DOCTORALE

Titre : Analyse des structures spatiales et spectrales des fonctions propres dans les modèles d'Anderson via la théorie du paysage de localisation

Mots clés : localisation d'Anderson, paysage de localisation, désordre

Résumé : Dans un solide désordonné ou aléatoire, les fonctions d'onde des états électroniques peuvent s'écarter des états de Bloch étendus et au contraire, être localisées de manière exponentielle dans l'espace. Ce changement radical de la structure spatiale des fonctions d'onde a une forte influence sur les propriétés de transport du système et peut, par exemple, être responsable de la transition métal/isolant dans les alliages désordonnés. Dans les années récentes, un nouvel outil théorique appelé le *paysage de localisation* a émergé pour l'étude de cette localisation induite par le désordre. Dans cette thèse, nous utilisons la théorie du paysage de localisation afin d'étudier divers aspects de la localisation des ondes. Tout d'abord, nous montrons comment extraire efficacement la structure spatiale de localisation à n'importe quelle dimension en adaptant l'algorithme dit de *watershed*. Puis nous passons à l'analyse des propriétés spectrales et calculons la distribution des valeurs propres (la densité intégrée des états) dans des modèles d'Anderson en *tight-binding* en utilisant de nouvelles approximations dérivées du paysage de localisation. Nous étudions ensuite comment le paysage de localisation permet de comprendre l'existence d'un seuil de mobilité à plus haute énergie, en fonction de la dimension. Enfin, nous nous intéressons à un potentiel déterministe de désordre, le modèle d'Aubry-André, et explorons quelles informations sur le système peuvent être déduites du formalisme de localisation du paysage.

Title : Analysis of the spatial and spectral structures of localized eigenfunctions in Anderson models through the localization landscape theory

Keywords : Anderson localization, localization landscape, disorder

Abstract : In a disordered or random solid, the wave functions of electronic states can depart from the extended Bloch states and on the contrary be instead exponentially localized in space. This dramatic change of the spatial structure of the wave functions has a strong influence on the transport properties of the system, and for instance, can be responsible for the metal/insulator transition in disordered alloys. In the recent years, a new theoretical tool called the *localization landscape* has emerged to study this disorder-induced localization. In this thesis, we use the localization landscape theory to study various aspects of wave localization. First, we show how to extract efficiently the spatial structure of wave localization in any dimension by adapting the so-called *watershed* algorithm. Turning to the spectral properties, we compute the distribution of eigenvalues (the integrated density of states) in tight-binding Anderson models using new approximations derived from the localization landscape. We then investigate how the localization landscape can shed a new light on the existence of a dimension-dependent mobility edge at higher energy. Finally, we take a case study of a deterministic potential mimicking disorder, the Aubry-André model, and explore which information on the system can be deduced from the localization landscape formalism.

Institut Polytechnique de Paris
91120 Palaiseau, France